Optimal GPS/GALILEO GBAS methodologies with an application to troposphere

Alizé Guilbert

THÈSE

En vue de l'obtention du

DOCTORAT DE L'UNIVERSITÉ DE TOULOUSE

Délivré par : *l'Institut National Polytechnique de Toulouse (INP Toulouse)*

Présentée et soutenue le *1 Juillet 2016* **par :**

Alizé GUILBERT

Optimal GPS/GALILEO GBAS Methodologies with an Application to Troposphere

---

JURY

Bernd Eissfeller	Professeur	Rapporteur
Frank Van Graas	Professeur	Rapporteur
Christophe Macabiau	Docteur	Directeur de thèse
Carl Milner	Docteur	Co-Directeur de thèse
Pierre Ladoux	Ingénieur	Invité

École doctorale et spécialité :
MITT : Signal, Image, Acoustique et Optimisation

Unité de Recherche :
Ecole Nationale de l'Aviation Civile - Laboratoire TELECOM/SIGNAV

Directeur de Thèse :
Christophe Macabiau

Rapporteurs :
Bernd Eissfeller et *Frank Van Graas*

ABSTRACT

In the Civil Aviation domain, research activities aim to improve airspace capacity and efficiency whilst also tightening safety targets and enabling new more stringent operations. This is achieved through the implementation of new Communications, Navigation, Surveillance and Air Traffic Management (CNS/ATM) technologies and processes. In the navigation domain, these goals are met by improving performance of existing services whilst also expanding the services provided through the development of new Navigation Aids (Navaids) or by defining new operations with existing systems. One such developmental axe for enabling expansion towards new such operations is the provision of safer, more reliable approach and landing operations in all weather conditions.

The Global Navigation Satellite System (GNSS) has been identified as a key technology in providing navigation services to civil aviation users [1] [2] thanks to its global coverage and accuracy in relation to conventional Navaids. This global trend can be observed in the fitting of new civil aviation aircraft since a majority of them are now equipped with GNSS receivers. The GNSS concept includes the provision of an integrity monitoring function by an augmentation system to the core constellations. This is needed to meet the required performance metrics of accuracy, integrity, continuity and availability which cannot be met by the stand-alone constellations. Three such augmentation systems have been developed within civil aviation: the GBAS (Ground Based Augmentation System), the SBAS (Satellite Based Augmentation System) and the ABAS (Aircraft Based Augmentation System).

The Ground Based Augmentation System (GBAS) is currently standardized by the ICAO to provide precision approach navigation services down to Category I using the GPS or GLONASS constellations [3]. Research and standardisation activities are on-going with the objective to extend the GBAS concept to support Category II/III precision approach operations with a single protected signal (GPS L1 C/A), however some difficulties have arisen regarding ionospheric monitoring that threaten to limit availability of this solution.

With the deployment of Galileo and BeiDou alongside the modernization of GPS and GLONASS, it is envisaged that the GNSS future will be multi-constellation (MC) and multi-frequency (MF). European research activities within the SESAR program have focused on the use of GPS and Galileo. The service commitments for this last constellation is expected to be in place in the medium term. The use of two protected frequency bands enables the mitigation of ionospheric errors at the expense of multipath and noise inflation, whilst the improved geometry of two constellations may be used to counter this resulting inflation and enable Cat II/III for worse performing aircraft. Therefore the MC/MF GBAS concept should lead to increased availability, stronger robustness to unintentional interference (due to the use of two protected frequency bands), better ground

segment monitoring capabilities, better modelling of **atmospheric effects** and improved measurement accuracy from modernized signals. However, several challenges and key issues must be resolved before the potential benefits may be realized.

This PhD has addressed two key topics relating to GBAS, the **provision of corrections data** within the MC/MF GBAS concept and the **impact of tropospheric ranging biases** on both the SC/SF and MC/MF GBAS concepts. Due to the tight constraints on GBAS ground to air communications link, the VHF Data Broadcast (VDB) unit, a novel approach is needed when expanding to a MC/MF corrections service [4]. One of the proposals discussed in the PhD project for an updated GBAS VDB message structure is to separate message types for corrections with different transmission rates. Furthermore, This PhD argues that atmospheric modelling with regards to the troposphere has been neglected in light of the ionospheric monitoring difficulties and must be revisited for both nominal and anomalous scenarios. The thesis focuses on how to compute the worst case differential tropospheric delay offline in order to characterize the threat model before extending previous work on bounding this threat in order to protect the airborne GBAS user.

This previous work led by Ohio University for assessing differential tropospheric delays [5] [6] [7] is based on GPS data collection which is inherently subject to undersampling. Furthermore, the bounding methodology was constrained by restricting the scope to SF GPS GBAS and an already defined data message format. In the scope of MC/MF GBAS development, an alternative approach was needed. Therefore, in this PhD project, Numerical Weather Models (NWMs) are used to assess fully the worst case horizontal differential range component of the troposphere (differential tropospheric delay between aircraft and ground assuming aircraft and ground are at the same altitude). An innovative worst case horizontal differential range tropospheric gradient search methodology is used to determine the induced differential ranging biases impacting aircraft performing Cat II/III precision approaches with GBAS. This provides as an output a worst case differential ranging bias as a function of elevation for two European regions (low-elevation coastal and high-elevation mountainous). The range vertical differential component (differential tropospheric delay between aircraft and ground assuming aircraft and ground are not at the same altitude but are at the same latitude and longitude) is also modelled by statistical analysis by comparing the truth data to the GBAS standardized model for vertical tropospheric correction up to the height of the aircraft. A model of the total uncorrected differential ranging bias is generated which must be incorporated within the nominal GBAS protection levels.

In order to bound the impact of the troposphere on the positioning error and by maintaining the goal of low data transmission, different solutions have been developed which remain conservative by assuming that ranging biases conspire in the worst possible way. Through these techniques, in order to protect the user against tropospheric ranging biases, it has been shown that a minimum of 3 parameters may be used to characterize a region's model.

The main contributions of this thesis are firstly the development of an **optimal processing scheme** for meeting Cat II/III performance requirements with the MC/MF GBAS trough the derivation of the error budget degradation

when using lower frequency corrections than the current GBAS message correction rate of 2Hz, and the validation of these theoretical analysis with real data. Other contributions deal with the determination and bounding of **differential tropospheric ranging biases** in the **horizontal** and **vertical** directions. Finally, other contributions include the validation of the differential tropospheric ranging biases computation, and the comparison of tropospheric gradients between U.S. data and European data as well as between low relief and high relief regions.

RESUME

Dans le domaine de l'Aviation Civile, les motivations de recherches sont souvent guidées par la volonté d'améliorer la capacité et l'efficacité de l'espace aérien grâce à la modernisation des moyens de navigation aérienne existants et à l'ajout de nouvelles infrastructures. Ces buts peuvent être atteints en développant les services qui permettent des opérations d'approche et d'atterrissage plus robustes et plus fiables quels que soient le lieu et les conditions météorologiques.

La navigation par satellite, grâce au Global Navigation Satellite System (GNSS), a été reconnue comme un moyen performant de fournir des services de navigation aérienne [1] [2]. Depuis quelques années, les systèmes de navigation par satellites sont devenus des moyens de navigation de référence grâce à leur couverture mondiale et à leur précision. En particulier, ce système de navigation est utilisé en aviation civile à bord des avions dont la majorité est équipé de récepteurs GNSS. Le concept du GNSS requiert l'utilisation de moyen d'augmentations pour fournir une fonction de contrôle d'intégrité. Cet appui est nécessaire au vu des exigences [1] concernant la précision, l'intégrité, la disponibilité et la continuité des systèmes GNSS surtout dans les applications critiques de type aviation civile. Trois moyens d'augmentation ont alors été développés: le GBAS (Ground Based Augmentation System), le SBAS (Satellite Based Augmentation System) et le ABAS (Aircraft Based Augmentation System).

Le GBAS est actuellement standardisé par l'OACI pour fournir un service de navigation incluant les approches de précision allant jusqu'à la catégorie I incluse, en utilisant les constellations GPS ou GLONASS [3]. Des travaux de recherches et de développement sont en cours pour permettre d'étendre ce service jusqu'à catégorie II/III avec un seul signal protégé (GPS L1 C/A). Cependant des contraintes limitant la disponibilité de cette solution sont apparues lors de la surveillance de la ionosphère.

Grâce à la modernisation du GPS et GLONASS et à la future implémentation des constellations Galileo et Beidou, les futurs GNSS utilisant de multiples constellations et de multiples fréquences (MC/MF) sont étudiés. En Europe, les activités de recherches dans le cadre du projet SESAR se sont appuyées sur la constellation GPS et sur la disponibilité future de la constellation Galileo. L'utilisation de deux bandes de fréquences protégées permet la réduction des retards ionosphériques tout en augmentant l'impact du bruit et des multi-trajets. Cependant l'amélioration de la géométrie des satellites, grâce aux deux constellations, peut compenser cette augmentation et permettre de réaliser des approches de précision de catégorie II/III. C'est pour cela que le MC/MF GBAS devrait permettre de nombreuses améliorations telles que l'augmentation de la disponibilité du système, la meilleure robustesse face aux interférences, un meilleur modèle des **retards atmosphériques** et une meilleure précision due aux nouveaux signaux de meilleure qualité. Cependant, de nombreux challenges et problèmes doivent être résolus avant d'atteindre les bénéfices potentiels.

Dans ce travail de thèse, deux principaux sujets en rapport avec le GBAS ont été traités, la **transmission des données de corrections** dans le contexte du MC/MF GBAS et **l'impact des biais de mesures troposphériques** dans le cadre du SC/SF GBAS et du MC/MF GBAS. Dû aux strictes contraintes portant sur le format des messages transmis à l'utilisateur via l'unité de VHF (Very High Frequency) Data Broadcast (VDB) [4], une nouvelle approche est nécessaire pour permettre l'élaboration du MC/MF GBAS. Une des solutions proposée dans cette thèse est de transmettre les corrections et les données d'intégrité à l'utilisateur dans des messages séparés à des fréquences différentes. De plus ce travail de thèse remet en question la modélisation de l'atmosphère. En effet, au vue de la difficulté de surveiller les retards ionosphériques, ceux relatifs à la troposphère furent en partie négligés et doivent être réévalués aussi bien dans des conditions nominales que non-nominales. Cette thèse se concentre d'abord sur les moyens de calculer le pire gradient troposphérique pour caractériser la menace troposphérique avant de développer les précédents travaux pour borner cette menace dans le but de protéger l'utilisateur.

Les précédentes études faites par l'Université d'Ohio pour traiter les retards troposphérique différentiels [5] [6] [7] sont basées sur la collecte de données GPS qui est intrinsèquement liée à du sous-échantillonnage. De plus, dans le cadre du SF GPS GBAS, la méthode pour borner l'erreur fut contrainte par le format du message transmis. En vue du futur MC/MF GBAS, une nouvelle approche s'est avérée nécessaire. C'est pour cela que dans ce projet de thèse, des modèles météorologiques numériques (NWMs) sont utilisés pour estimer intégralement la composante horizontale du pire retard différentiel troposphérique (retard différentiel dû à la décorrelation horizontale entre l'avion et la station sol). Une méthode innovante pour rechercher les pires retards différentiels troposphériques horizontaux est utilisée pour déterminer les biais de mesures qu'ils induisent impactant les avions visant une approche de Cat II/III avec le GBAS. Un modèle de ces pires biais de mesure troposphériques différentiels horizontaux dépendant de l'élévation des satellites pour 2 régions européennes (une région côtière à bas-relief et une région montagneuse à haut relief) est alors développé. La composante verticale du pire retard différentiel troposphérique (retard différentiel dû à la différence d'altitudes entre l'avion et la station sol) est aussi modélisée grâce à une étude statistique qui compare les données réelles au modèle standard établi pour le GBAS. Un modèle du biais de mesure différentiel total non corrigé est développé et doit être introduit dans le calcul des niveaux de protections sous des conditions nominales.

Pour borner l'impact de la troposphère sur l'erreur de position tout en se focalisant sur le souhait d'avoir un nombre de données transmises à l'utilisateur faible, différentes solutions ont été développées. Elles restent conservatives en supposant que les biais de mesures se combinent pour engendrer la pire erreur de position verticale. Avec ces méthodes, au minimum 3 paramètres, définis selon leur région géographique d'utilisation, doivent être transmis à l'utilisateur pour le protéger contre ces biais de mesures troposphériques.

Les principales contributions de cette thèse sont le développement **d'un modèle optimal de traitements** pour répondre aux exigences liées à la Cat II/III d'approche avec le MC/MF GBAS. Ceci a été effectué tout d'abord grâce à l'analyse théorique de la possibilité d'avoir des messages transmis à une fréquence plus faible que celle standardisée actuellement à 2 Hz puis par la validation de cette possibilité grâce à l'analyse de données réelles.

Ensuite, les autres apports de cette thèse portent sur les solutions permettant de déterminer et de borner les **biais de mesures troposphériques différentiels** dans les directions **horizontales** et **verticales**. Enfin, d'autres contributions incluent la validation du calcul des biais troposphériques et la comparaison entre les gradients troposphériques apparaissant dans les données américaines et européennes pour une région côtière à bas-relief et une région montagneuse à haut relief.

ACKNOLEDGEMENTS

Tout d'abord, je souhaiterais particulièrement remercier mon directeur de thèse Christophe Macabiau et mon co-directeur de thèse Carl Milner pour leur disponibilité, leur temps, leur patience et leur gentillesse. C'est en grande partie grâce à eux et à leur expertise dans le domaine du GNSS que j'ai pu réussir à valider ce doctorat.

Je voudrais remercier ensuite la Commission Européenne et l'ENAC pour avoir financé mes travaux de thèse au sein du projet SESAR ainsi que toutes les entreprises partenaires de ce projet.

Mes plus vifs remerciements vont également à Henk Veerman du NLR pour m'avoir aidé à travailler sur la Troposphère et de m'avoir permis d'exploiter les données Harmonie de KNMI, ainsi que Météo France avec Pierre Brousseau pour m'avoir fourni les données AROME et pour m'avoir expliqué comment les modèles météorologiques avaient été développés.

I would like to thank Pr. Bernd Eissfeller and Pr. Frank Van Graas for their reviews and for having attended my PhD defense.

Merci aussi à Pierre Ladoux pour son aide et sa disponibilité durant ce projet SESAR et pour avoir accepté d'être membre de mon jury de thèse.

Ensuite, je dois en partie ma réussite de ce doctorat à mes collègues du laboratoire SIGNAV et particulièrement Giuseppe Rotondo qui a partagé mon bureau et qui m'a beaucoup aidé pendant ces 3 ans, Paul Thevenon et Jeremy Vezinet pour leurs précieux conseils, leurs analyses et leurs corrections tout au long de ma thèse.

Enfin, je n'aurais pas pu mener à bien mes travaux de thèse sans le soutien de mes parents Fouzia Bouchareb et Bruno Guilbert, de mon « frérot » Guillaume Guilbert et des autres membres de ma famille. Ils m'ont poussé à faire cette thèse et je leur dois tout.

Je n'oublie pas mes amis qui ont su me soutenir, me supporter, me motiver, me changer les idées tous les jours pendant ces 3 dernières années. Un énorme merci à mes « copines » Charlotte Blanc, Aurélie Deloeil qui étaient présentes lors de ma soutenance.

TABLE OF CONTENTS

*** The Ground Based Augmentation System is presented over these sections**

TABLE OF FIGURES

TABLE OF TABLES

TABLE OF ACRONYMS

GNSS	***Global Navigation Satellite System***
GBAS	***Ground Based Augmentation System***
ABAS	***Aircraft Based Augmentation System***
SBAS	***Satellite Based Augmentation System***
GPS	***Global Positioning Service***
MC	***Multi-Constellation***
MF	***Mult-Frequency***
SESAR	***Single European Sky ATM Research***
ICAO	***International Civil Aviation Organisation***
SC	***Single Constellation***
SF	***Single Frequency***
VDB	***VHF Data Broadcast***
NWM	***Numerical Weather Model***
U.S.	***United States***
C/A	***Coarse/Acquisition***
VHF	***Very High Frequency***
I-free/IF	***Ionosphere Free***
D-free	***Divergence Free***
CNS	***Communication Navigation Surveillance***
ATM	***Air Traffic Management***
GAST	***GBAS Approach Service Type***

WP	***Work Package***
RNP	***Required Navigation Performance***
SSR	***Secondary Surveillance Radar***
RF	***Radio Frequency***
ILS	***Instrument Landing System***
GLS	***GBAS Landing System***
SIS	***Signal In Space***
FAA	***Federal Aviation Administration***
TC	***Tropospheric Correction***
PBN	***Performance Based Navigation***
SARPs	***Standards and Recommended Practices***
NPA	***Non Precision Approach***
APV	***Approaches with vertical guidance***
PA	***Precision Approach***
DH	***Decision Height***
RVR	***Runway Visual Range***
MDA	***Minimum descent Altitude***
MDH	***Minimum Decision height***
DA	***Decision Altitude***
RNAV	***Area Navigation***
TSE	***Total System Error***
PSE	***Path Steering Error***
FTE	***Flght Technical Error***
PDE	***Path Definition Error***

PEE	***Position Estimation Error***
HPL	***Horizontal Protection Level***
VPL	***Vertical Protection Level***
HAL	***Horizontal Alert Limit***
VAL	***Vertical Alert Limit***
LAL	***Lateral Alert Limit***
LPL	***Lateral Protection Level***
TTA	***Time to Alert***
RAIM	***Receiver Autonomous integrity Monitoring***
ARNS	***Aeronautical Radio Navigation Services***
DGNSS	***Differential GNSS***
EGNOS	***European Geostationary Navigation Overlay Service***
LAAS	***Local Area Augmentation System***
WAAS	***Wide Area Augmentation System***
WADGNSS	***Wide Area DGNSS***
GEO	***Geostationary***
ESA	***European Space Agency***
LTP/FTP	***Landing/Ficticious Threshold Point***
GPIP	***Glide Path Intersection Point***
LOC	***Localizer***
MMR	***Multi-Mode Receiver***
GFC	***GBAS Facility Classification***
FAST	***Facility Approach Service Type***
GCID	***GBAS Continuity/Integrity Designator***

APD	***Approach Performance Designator***
AST	***Active Service Type***
SST	***Selected Service Type***
LOS	***Line of Sight***
GGTO	***GPS to Galileo Time offset***
TEC	***Total Electron Content***
STD	***Slant Tropospheric Delay***
CMC	***Code Minus Carrier***
PRC	***PseudoRange Correction***
RRC	***Range Rate Correction***
AD	***Accuracy Designator***
GAD	***Ground AD***
AAD	***Aircraft AD***
PAN	***Position and Navigation***
MT	***Message Type***
PVT	***Position Velocity Time***
LSE	***Least Square Estimation***
FD/FDE	***Fault Detection/Exclusion***
SQM	***Signal Quality Monitoring***
CCD	***Code Carrier Divergence***
DQM	***Data Quality Monitoring***
MDM	***Measurement Quality Monitoring***
MRCC	***Multiple Receiver Consistency Check***
DSIGMA	***Dual Solution Iono Gradient Monitoring Algorithm***

BAM	***Bias Approach Monitor***
RRFM	***Reference Receiver Fault Monitor***
DCMC	***Differential Correction Magnitude Check***
RR	***Reference Receiver***
FAS	***Final Approach Segment***
FASVAL	***FAS Vertical Alert Limit***
HPDCM	***Horizontal Position Differential Correction Magnitude***
IGM	***Iono Gradient Monitor***
RH	***Relative Humidity***
P	***Pressure***
T	***Temperature***
MHM	***Modified Hopfield Model***
ZTD	***Zenith Tropo Delay***
SHD	***Slant Hydrostatic Delay***
SWD	***Slant Wet Dalay***
ADB	***Additional Data Block***
GND	***Ground***
A/C	***Aircraft***
LUT	***Look up Table Transmission***
LDT	***Low Data Transmission***
WSS	***Worst Satellite Subset***

Chapter 1 : Introduction

1.1 Background and Motivation

1.1.1 Background

Nowadays, most of the civil aviation aircrafts are equipped with Global Navigation Satellite System (GNSS) receivers (90% of aircrafts according the EUROCONTROL Survey [8]) and since it was recognized as a key technology in providing accurate navigation services with a worldwide coverage. This GNSS concept was defined by the International Civil Aviation Organization (ICAO) [1] and is today understood to be composed of the core constellations GPS (Global Positioning System) and GLONASS, the future constellations Galileo and BeiDou constellations implementations, as well as approved augmentations. In view of the stringent civil aviation specifications and requirements defined for the use of GNSS within the CNS/ATM system (Communications, Navigation, and Surveillance / Air Traffic Management), a stand-alone core constellation need augmentations systems for meeting requirements specified by ICAO [1] in terms of accuracy, integrity, availability and continuity. Therefore, several augmentation systems able to monitor GNSS integrity have been developed such as GBAS (Ground Based Augmentation System), SBAS (Satellite Based Augmentation System) and ABAS (Aircraft Based Augmentation System).

The Ground Based Augmentation System (GBAS) is currently standardized by the ICAO to provide precision approach navigation services down to Category I using the GPS or GLONASS constellations [3]. Current investigations into the use of GBAS for a Category II/III service type known as GAST (GBAS Approach Service Type) D are ongoing [9] but several constraints have arisen as those linked to the ionospheric monitoring [10].

That is why, Multi-frequency and multi-constellation GBAS solutions known as GAST F solutions are being explored within this PhD in the scope of the European SESAR (Single European Sky ATM Research) program (WP 15.3.7) which addresses these issues. This SESAR project is detailed in the following subsection.

1.1.2 SESAR Project

Contrary to the United States, Europe does not have a single sky, one in which air navigation is managed at the European level. Furthermore, European airspace is among the busiest in the world with over 33,000 flights [11] on busy days and high airport density. This makes air traffic control even more complex.

The EU Single European Sky is an ambitious initiative launched by the European Commission in 2004 to reform the architecture of European air traffic management. It proposes a legislative approach to meet future capacity and safety needs at a European rather than a local level.

The key objectives of the SESAR project are to [11]:

- Restructure European airspace as a function of air traffic flows
- Create additional capacity; and
- Increase the overall efficiency of the air traffic management system

Then, the major elements of this new institutional and organizational framework for Air Traffic Management (ATM) in Europe consist of:

- Separating regulatory activities from service provision, and the possibility of cross-border ATM services.
- Reorganizing European airspace that is no longer constrained by national borders.
- Setting common rules and standards, covering a wide range of issues, such as flight data exchanges and telecommunications.

Furthermore, the activities in the CNS (Communication, Navigation and Surveillance) domain constitute a significant level of investment within the SESAR program [11] and are included in the Work Package 15 (WP15) named *Non Avionic CNS System* Work package. It addresses CNS technologies development and validation also considering their compatibility with the Military and General Aviation user needs.

Key issues linked to CNS activities are described below:

Communication (WP 15.2) [11]

Communication activities focus on developing a reliable and efficient communication infrastructure to serve all airspace users in all types of airspace and phases of flight and on providing the appropriate Quality of Service needed by the most demanding applications.

Navigation (WP 15.3) [11]

Navigation system developments in SESAR focus on the evolution of GNSS-based navigation technologies which will be developed to fulfil navigation performance supporting RNP (Required Navigation Performance) based operations as defined and validated in the operational projects of the program.

The SESAR work program integrates operational projects, which define new PBN (Performance Based Navigation) procedures and concepts, with the technical projects, which develop the Navigation tools and systems according to the operational needs, which are validated by the operational projects. For the underlying navigation sensor and system developments SESAR projects aim to define the medium and long term GNSS baseline including the expected configuration of constellations, signals and augmentation systems (GBAS/ABAS/SBAS). This will drive

the further developments within the program covering evolution from single constellation/single frequency (GPS L1 C/A) to multi-constellation/multi-frequency (GPS L1/L5 and Galileo E1/E5).

This PhD project is included inside this part of the SESAR project and more precisely in the *WP 15.3.7 named Multi GNSS CAT II/III GBAS.*

Surveillance (WP 15.4) [11]

Surveillance activities deal with issues relative to the increasing traffic densities, the pressures on the use of Radio Frequency (RF) spectrum, the new modes of separation and the greater demands on surveillance systems. Indeed, this needs stimulate the use of new surveillance techniques including ADS-B (Automatic Dependent Surveillance Broadcast) and Wide Area Multi-Lateration which can deliver improved performance in terms of accuracy, update rate, coverage and are also potentially more efficient from an RF perspective than traditional Secondary Surveillance Radar (SSR).

1.1.3 Ground Based Augmentation System *[1]

As mentioned above, in view of the stringent civil aviation requirements specified by ICAO [1], augmentations systems were developed for improving performances beyond core constellations performance. In particular, for precision approaches, GBAS (Ground Based Augmentation System) was defined and use the Differential GNSS (DGNSS) technique that significantly improves both the accuracy and the integrity within a local coverage area around the airport. This system is intended to provide an alternative to the already implemented Instrument Landing System (ILS) which suffers from a number of limitations and siting constraints. Then, the term GBAS Landing System (GLS) [12] was assigned to the approach procedure/capability provided by such a system (precision approaches and landing operations).

Today, GBAS installations are standardized to provide precision approaches down to Category I (CAT-I) and are based on GPS and GLONASS using a single frequency (GPS L1 C/A). GBAS CAT II/III service with a single protected signal (GPS L1 C/A) is at an advanced stage of development and standardisation.

It is expected that the evolution of GBAS towards multi-constellation (MC) and multi-frequency (MF) provide better performance and robustness as well as availability of services. In this PhD project and from a European perspective the multi-constellation focus is on GPS/GALILEO.

1.2 Objectives and Contributions

1.2.1 Objectives

In the Civil Aviation domain, research motivations are currently related to the wish to improve airspace capacity, efficiency and safety thanks to the modernization of existing Navigation aids (Navaids), the addition of new infrastructures or addition and modification of user and ground processing. These research motivations will

obviously depend on political motivations. For example, the building of the Galileo constellation in Europe has an impact on European researches and applications about this new element. Consequently motivations will depend on regions where Civil Aviation applications will be applied and developed.That is why, in Europe, research activities within the SESAR project have focused on the use of GPS and Galileo constellations.

As mentioned in the section above, current GBAS is based on GPS and GLONASS constellations and provides precision approach service down to Category I (CAT-I) using a single protected signal (GPS L1 C/A). The evolution of GBAS towards Multi-Constellation (MC) and Multi-Frequency (MF) is expected to provide better performance and robustness as well as availability of services. Several expected improvements [9] are listed below:

- The MC/MF GNSS implementation and particularly the apparition of multiple constellations will provide additional ranging sources thus improving the availability of service (by improving the geometry of the position solution). Furthermore, it will also improve continuity of service that will increase operational robustness and enable advanced applications. Indeed, in some regions ionospheric scintillation can cause loss of service. This issue could be solved with the MC/MF GNSS implementation because with more satellites in view it would be much less likely that scintillation would result in loss of service. So, the availability of additional ranging sources and frequencies will improve the operational robustness.
- With the future implementation of Galileo constellation, MC will provide constellation diversity which limits the dependency from GPS especially in case of a total constellation failure which is a concern of some European institutions and stakeholders. However, from an avionics perspective, greater diversity adds significant complexity to receiver design and thus the associated cost to some stakeholders represents a significant offset to the benefits.
- Future satellites will provide signals for multiple frequencies which allow eliminating errors (or at least mitigating them) caused by the ionospheric threat mitigation during approach and landing operations. Single frequency GBAS L1 CAT III (known as GAST-D) faces demanding constraints linked to requirements for protecting the system against anomalous ionosphere conditions such as equipment & siting requirements, ionosphere threat space, ground and airborne monitoring. Dual-Frequency (DF) processing is expected to overcome at least some of these constraints. [13]
- In addition to DF, new satellites will provide better designed signals [14] (longer codes, higher data rates, message error detection, control methods use of pilot channels, multiplexing) with higher power (much higher with L5 signals) which should provide better accuracy and monitoring performance (noise, multipath, interference rejection). This will lead to better performance of GBAS corrections and also has some impact on particular facility constraints (possibility to have a narrower correlator, a more robust tracking in challenge environment, etc.). [13]

With the introduction of Multi-Frequency, Multi-Constellation SIS (Signal In Space) having different characteristics than GPS L1 C/A SIS, a reconsideration of the current GBAS architecture is required to take the best advantage of the new SIS performance. Indeed, many improvements could be noted by the MF/MC GNSS

such as mitigation of **anomalous atmospheric effects**, increased availability, stronger robustness to unintentional interference and better accuracy performance due to modernized signal. However, several challenges and key issues must be resolved before the potential benefits may be realized, these include: deriving system level requirements, optimizing the MF processing at ground and aircraft sides, **defining VHF Data Broadcast (VDB) transmission and format of the transmitted message from the GBAS VDB unit** [4], management of dual constellation at ground and aircraft sides, Galileo fault modes, ground subsystem monitoring and technology, safety, airborne technology, airborne performance and certification, operational impact, standardization, validation and certification authorities involvement etc.

In this PhD project, some of these key issues are investigated to define an optimal solution for this MC/MF GBAS. Therefore, issues concerning the available space for message transmission from the GBAS VHF Data Broadcast (VDB) unit [4] are examined with the possibility of providing corrections at a lower rate than the current 2Hz. This alternative approach is needed because today corrections and their integrity are provided in combined messages broadcast every half second (2Hz) and with the evolution to multiple correction types, based on the different signals and observables for two or more constellations this could not be applicable anymore. Furthermore, if future signals from the modernized constellations are needed to be used or in view of the possible expansion further than two constellations then no additional transmission space would be available.

Also, in order to meet the most stringent requirements of Cat II/III precision approach operations several challenges and key issues must be solved relating to atmospheric modelling. Indeed, nowadays ionospheric effect is considered as dominant compared to troposphere therefore the ionospheric and tropospheric spatial gradients are considered as a combined threat. However, there are a number of arguments for revisiting this topic. Firstly, recent observations, reported at last ICAO NSP meeting [5], showed unexpected atmospheric behavior. These observations have been confirmed by the FAA (Federal Aviation Administration) [15] and Boeing and have shown that significant spatial gradients with no link to ionosphere activity are likely to appear mainly during warm and sunny days. The source could be related to a non-modelled behavior of the troposphere. Even if the range errors induced by this phenomenon are not significant compared to those due to ionospheric gradients, the combination of these “troposphere” gradients with ionospheric gradients could lead to missed detection or false detection of the ground subsystem’s ionospheric monitor, thus impacting integrity and continuity. Secondly, in the advent of DF GBAS, the ionosphere may feasibly be reduced significantly through the ionosphere-free smoothing technique. Under such a scenario, the troposphere threat model may need to be changed and a means for bounding the potential errors derived.

The spatial differential range tropospheric delay can be decomposed into two components: the horizontal component (differential tropospheric delay between aircraft and ground assuming aircraft and ground are at the same altitude) and the vertical component (differential tropospheric delay between aircraft and ground assuming aircraft and ground are not at the same altitude but are at the same latitude and longitude). Both are represented in the following Figure 1 where the differential range delay between paths 2 and 3 (above the aircraft height) define the horizontal component of the differential range tropospheric delay. The vertical

component of the differential range tropospheric delay is represented by the path 1 and is modelled by the standardized vertical Tropospheric Correction (TC) [16]sent to the aircraft.

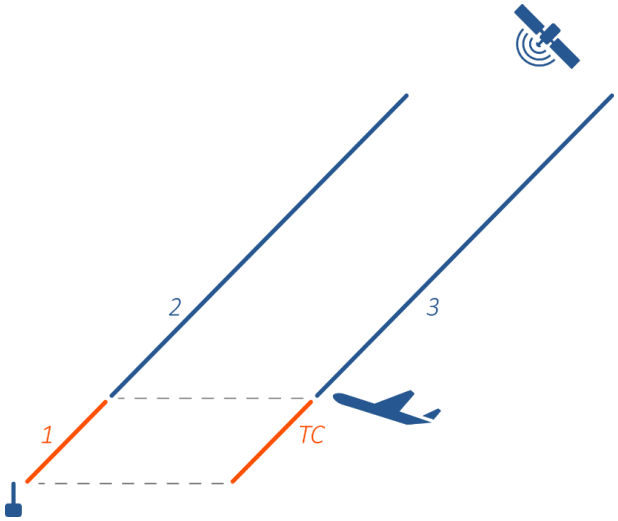

Figure 1-GBAS Troposphere Delay Paths

Previous work undertaken at Ohio University [5] [6] [7] highlighted the need to consider range horizontal troposphere gradients as a possible source of failure.

That is why, this thesis contains a specific analysis of the tropospheric modelling for both nominal and non-nominal cases and the development of an innovative methodology for bounding these errors.

Therefore this PhD work has initiated the process of assessing the troposphere threat by determining the optimal Dual Constellation (DC)/ Dual Frequency (DF) GBAS processing.

1.2.2 Original Contributions

The main contributions of this thesis are summarized below and detailed all along this report. Several subjects have been published in papers and conferences. They are mentioned in the different sections of this document and the bibliography.

- Development of an optimal processing scheme for meeting the Cat II/III with the MC/MF GBAS (Chapter 4)
- Derivation of the error budget degradation when using lower frequency corrections than the current GBAS message correction rate of 2Hz (4.2 and 4.3).
- Real data analysis for validating the theoretical analysis of this error budget degradation (4.3).
- Development of a worst case horizontal differential range tropospheric ranging delay search methodology using a comprehensive 3D meteorological data model (5.4).
- Determination of horizontal differential tropospheric ranging biases impacting Cat II/III GLS operating aircraft using a comprehensive 3D meteorological data model (5.4).

- Model of the worst case horizontal differential tropospheric ranging biases as a function of elevation for two European regions (5.4.4).
- Analysis of GBAS standardized model for vertical Tropospheric Correction (5.5).
- Model of residual vertical differential tropospheric ranging biases (5.5.2.2).
- Analysis and Validation of the differential tropospheric ranging biases computation (5.4.5).
- Development of a bounding methodology for horizontal differential tropospheric ranging biases (6.3.1.2).
- Computation of protection levels accounting for the impact of the potential presence of horizontal and vertical differential tropospheric ranging biases (6.4).
- Comparison of Tropospheric gradients between U.S. data and European data between low relief costal region and a high relief mountainous region (6.4).

1.3 Dissertation Organization

The thesis is organized as follows. Chapter 2 introduces the main Civil Aviation Authorities such as ICAO, RTCA.Inc, EUROCAE, FAA and EASA. Then, an overview of requirements applicable to GNSS for navigation of civil aviation aircraft is given. A following part describes the different phases of flight with an emphasis on approaches. The concept of Performance Based Navigation (PBN) is presented, followed by a section dealing with the operational criteria of ICAO for GNSS based navigation. Finally, the corresponding Signal In Space (SIS) requirements are reminded for each phase of flight with some proposition for CAT-II/III precision approaches.

Chapter 3 highlights the GNSS Processing considered in this PhD work. First, GNSS concept for Civil Aviation is presented with the introduction of the basic principle of satellite positioning. Therefore, the different steps for establishing the position estimation and the navigation solution are described by explaining how the pseudorange measurement is obtained and corrected for being used to estimate the position. This is followed by a brief description of the GNSS and signals currently used or planned to be used for civil aviation applications. Then a detailed part focuses on the Differential GNSS (DGNSS) technique that significantly improves both the accuracy and the integrity of the GNSS. Furthermore, some methodologies enabling to measure the trust on the correctness of this position and system performances are presented by detailing integrity monitoring concepts for GNSS systems.

Then, in the scope of the evolution to the MC/MF GBAS, the Chapter 4 deals with a main constraint which is the available space for message transmission from the GBAS VHF Data Broadcast (VDB) unit. Therefore, the possibility of providing corrections at an optimal correction message rate is examined by developing the GBAS error modelling. Then the specific case of the GBAS tropospheric error modelling is presented for both nominal and non-nominal cases. Furthermore, the properties of the range-rate corrections are essential to understand how an increase in the correction update period will impact the total performance of the system therefore the

current methodology and an innovative one are shown. The total error budget is then derived to quantify the degradation in the corrections as a function of the message update rate. Finally, a performance benefits analysis is realized to evaluate the possibility of an increased update rate.

Chapter 5 highlights key issues relating to anomalous tropospheric modelling. Therefore, first the use of meteorological modelling for estimating the worst differential tropospheric delay is introduced by presenting two solutions: one using a wall model built with GNSS data and the second using Numerical Weather Models which are 3D layered models of meteorological and geographical parameters. Then, some methodologies for estimating tropospheric delays by using these atmospherical parameters are described. This part of the report also addresses how to find the horizontal differential tropospheric range error focusing on the worst case (non-nominal) conditions and evaluates the accuracy of such methodology using NWMs data. This chapter finishes with a part about the modelling of the vertical component of the differential tropospheric range error by introducing the standardized TC and by presenting a statistical analysis based on NWMs.

Finally the Chapter 6 analyses the two possible threats related to the troposphere known as horizontal gradients and vertical gradients. Then a mainly focus is done on the horizontal gradients impacting the differential error with the presentation of means for protecting an aircraft from ranging biases due to horizontal gradients. This is achieved by comparing results using an existing methodology and a novel approach using methodology presented in Chapter 5. Chapter 7 presents the outcomes of this PhD project

Chapter 2 : Navigation Performance Requirements for Civil Aviation

This part of the thesis summarizes the requirements applicable to GNSS use for civil air navigation and integrity monitoring. In order to understand clearly each function, Civil Aviation Authorities such as ICAO, RTCA, Inc., EUROCAE, FAA and EASA are first introduced. Then, in order to clarify where and when requirements are applicable, the different categories of phases of flight are presented according to approaches. After, the concept of Performance Based Navigation (PBN) is described. Finally, the operational criteria of ICAO for GNSS based navigation are defined trough the associated Signal In Space requirements reminded for each phase of flight and several performance requirements for CAT-II/III precision approaches are proposed.

2.1 Civil Aviation Authorities

2.1.1 International Civil Aviation Organization (ICAO)

The International Civil Aviation Organization (ICAO) is the agency of the United Nations, which elaborates all concepts and techniques for international air navigation and organizes the planning and development of international air transport to provide a safe and regulated growth. Its council ratifies standards and recommended practices (SARPs) concerning air navigation, prevention of unlawful interference, and facilitation of border-crossing procedures for international civil aviation. Moreover, the ICAO defines the formalities for air accident investigation followed by authorities in countries which had sign the Convention on International Civil Aviation, commonly known as the Chicago Convention [17].

Furthermore, a main role of the International Civil Aviation Organization (ICAO) is to establish the standards for radio navigation aids, including those concerning Global Navigation Satellite Systems (GNSS). They are defined in the Annex 10 to the Convention on International Civil Aviation.

2.1.2 RTCA, Inc.

RTCA, Inc. is a US private, not-for-profit Corporation that establishes recommendations regarding communications, navigation, surveillance, and air traffic management (CNS/ATM) system issues. RTCA works as

a Federal Advisory Committee. The Federal Aviation Administration (FAA) uses its recommendations as the basis for policy, program, and regulatory decisions and the private sector uses them as the basis for development, investment and other business decisions [18].

Moreover, GNSS systems are treated by the working group SC-159 of RTCA whose function is to elaborate minimum standards that defines the basis for FAA permission of equipment using GPS as primary means of civil aircraft navigation.

2.1.3 EUROCAE

The European Organization for Civil Aviation Equipment (EUROCAE) is an organization which was built to provide a European assembly for resolving technical problems with electronic equipment for air transport. EUROCAE deals only with aviation standardization and related documents which are compulsory for enabling the regulation of aviation equipment and systems [19].

EUROCAE is composed of manufacturers, service providers, aviation authorities as well as users (airlines, airports). EUROCAE can be considered as the European “RTCA”.

In order to create EUROCAE documents, Working Groups (WG) are organized. Indeed, the WG-62 is responsible for the preparation of aviation use of GALILEO and the development of Minimum Operation Performance Specifications (MOPS) for the first GALILEO airborne receivers.

2.1.4 FAA and EASA

FAA and EASA form the authorities which are officially responsible for publishing compulsory requirements to be respected by aircraft manufacturers and airliners to fly an aircraft. The FAA is an agency of the United States Department of Transportation and the EASA is similar to the European Commission. Their aim is to enable a safe civil aviation air traffic.

Most of their published documents refer to the standardization publications established by the previous organisations. It is relevant to mention here publications which are directly related to this PhD project and which are the airworthiness criteria for landing operations. These can be found in FAA Advisory Circular AC 120-28D [16]and EASA CS AWO [20].

After having presented the different organisations which have a role in the elaboration of the standards related to the use of GNSS systems for civil aviation, the standardized phases of flight for civil aircraft flights are presented in the following section.

2.2 Phases of Flight

2.2.1 Categories of flight phases

The flight of an aircraft consists of six major phases [21]:

- ***Take-Off***: From the application of take-off power, through rotation and to an altitude of 35 feet above runway elevation or until gear-up selection, whichever comes first.
- ***Departure***: From the end of the take-off sub-phase to the first prescribed power reduction, or until reaching 1000 feet above runway elevation or the VFR pattern (Visual Flight Rules), whichever comes first.
- ***Cruise***: Any level flight segment after arrival at initial cruise altitude until the start of descent to the destination.
- ***Descent***:
    - Instrument Flight Rules (IFR): Descent from cruise to either Initial Approach Fix (IAF) or VFR pattern entry.
    - Visual Flight Rules (VFR): Descent from cruise to the VFR pattern entry or 1000 feet above the runway elevation, whichever comes first.
- ***Final Approach****:* From the FAF (Final Approach Fix) to the beginning of the landing flare.
- ***Landing***: Transition from nose-low to nose-up attitude just before landing until touchdown.

As this thesis focus in Approaches operations a more detailed description are given in the following section.

2.2.2 Approaches

Categories of aircraft approaches are defined through the level of confidence that can be placed by the pilot into the system he used in order to land the plane safely. They are divided in two main segments: the first one is the aircraft segment which follows the indication provided by the landing system, and the second is the pilot segment which takes over in the final part and controls the aircraft using visual outside information. As the reliability of the aircraft, the crew and the landing system increases, the height of the aircraft over the ground at the end of the interval of use of the information provided by the system can be decreased [22].

Three classes of approaches and landing operation have been defined by the ICAO in the Annex 6 [23] and are classified as follows:

- ***Non Precision Approaches and landing operations (NPA)****:* They are defined by an instrument approach and landing which uses lateral guidance but does not use vertical guidance.
- ***Approaches and landing operations with vertical guidance (APV)****:* They are defined by an instrument approach and landing which uses lateral and vertical guidance but does not meet the requirements established for precision approach and landing operation.
- ***Precision approaches and landing operations (PA):*** They are defined by an instrument approach and landing which uses precision lateral and vertical guidance with minima defined by the category of operation.

The different phases of flight and type of approaches are represented on the Figure 2 with the type of GNSS augmentations which enable navigation operations for civil aviation during the corresponding phase of flight.

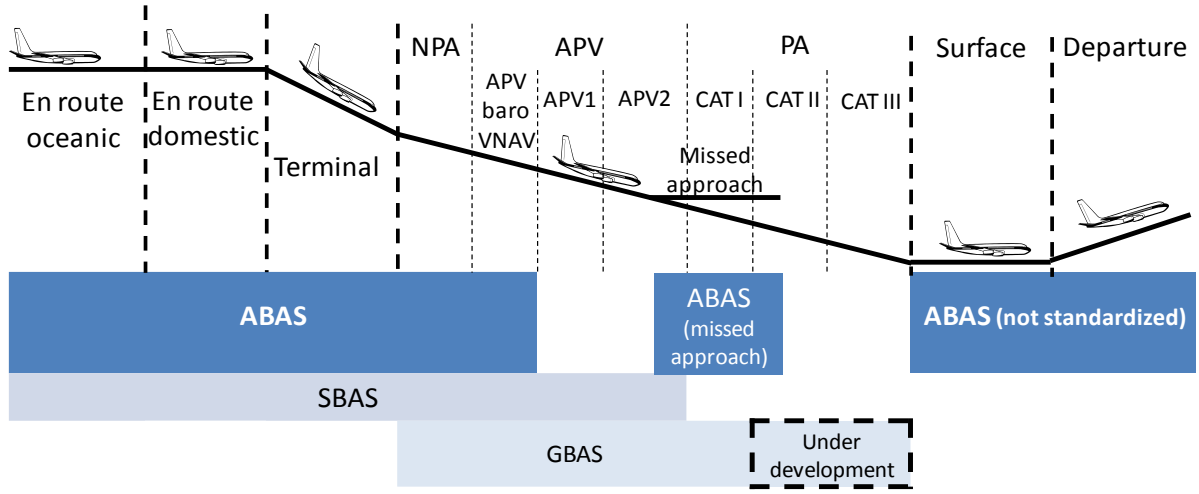

Figure 2-Phases of flight and GNSS augmentations [24]

Three different operational parameters are usually used to define these approaches: the Decision Height (DH), the Distance of Visibility and the Runway Visual Range (RVR). They are defined as follows [25]:

- ***Decision Height (DH)*** is the minimal height above the runway threshold at which as missed approach procedure must be executed if the minimal visual reference required in order continuing the approach has not been established.
- ***Distance of Visibility*** is the greatest distance, determined by atmospheric conditions and expressed in units of length, at which it is possible with unaided eye to see and identify, in daylight a prominent dark object, and at night a remarkable light source.
- ***Runway Visual Range (RVR)*** is the maximum distance in the landing direction at which the pilot on the centre line can see the runway surface markings, runway lights, as measured at different points along the runway and in particular in the touchdown area.

The links between these parameters and the approach categories are represented in the following table defined by the ICAO.

Category	**Minimum Descent Altitude (MDA)** **Minimum Descent Height (MDH)** **Decision Altitude (DA)** **Decision Height (DH)**	**Visual requirements**
NPA	MDA ≥ 350 ft	Depending on the airport equipment
APV	DA ≥ 250 ft	
LPV 200	DH ≥ 60 m (200ft)	

Precision Approaches	CAT – I		DH ≥ 60 m (200ft)	Visibility ≥ 800 m Or RVR ≥ 550 m
	CAT – II		30 m (100ft) ≤ DH ≤ 60 m (200ft)	RVR ≥ 300 m
	CAT – III	A	0 m ≤ DH ≤ 30 m (100ft)	RVR ≥ 175m
		B	0 m ≤ DH ≤ 15 m (50ft)	50 m ≤ RVR ≤ 175 m
		C	DH = 0 m	RVR = 0 m

Table 1 - Decision heights and Visual requirements [23]

The criterion for the CAT – III - A, B, C selection is the conditions in which operations are intended to be conducted.

2.3 Performance Based Navigation – PBN

The *Performance Based Navigation (PBN)* is a concept which specifies that aircraft Area Navigation (RNAV) system performance requirements are defined with the terms of accuracy, integrity, availability, continuity and functionality, which are selected for the intended operations in the context of a particular airspace concept. The PBN concept is different from sensor-based navigation. Indeed, performance requirements are identified in navigation specifications, which also identify the choice of navigation sensors used to meet the performance requirements. These navigation specifications are defined at a sufficient level of detail to enable a global harmonization by providing specific implementation guidance for all states and operators [17].

PBN offers several advantages compared to the sensor-specific method of developing airspace and obstacle clearance criteria [26] such as:

- Reducing the need to maintain sensor-specific routes and procedures, and their associated costs
- Avoiding the need for developing sensor-specific operations with each new evolution of navigation systems, which would be cost-prohibitive
- Allowing for more efficient use of airspace (route placement, fuel efficiency and noise abatement)
- Clarifying how RNAV systems are used
- Simplifying the operational approval process for operators by providing a limited set of navigation specifications intended for global use.

The concept of PBN relies on RNAV systems and *Required Navigation Performance (RNP)* procedures and key terms and definitions are reminded here [17]:

- ***Area Navigation (RNAV)****:* A method of navigation which permits aircraft operation on any desired flight path within the coverage of station-referenced navigation aids or with the limits of the capability of self-contained aids, or a combination of these.
- ***Area Navigation Equipment****:* Any combination of equipment used to provide RNAV guidance.
- ***Required Navigation Performance (RNP) Systems***: An RNAV system which supports on-board performance monitoring and alerting.
- ***Required Navigation Performance (RNP)****:* A statement of the navigation performance necessary for operation within a defined airspace.

According to [17] the RNP can be defined by the Total System Error (TSE) which is illustrated in the following figure:

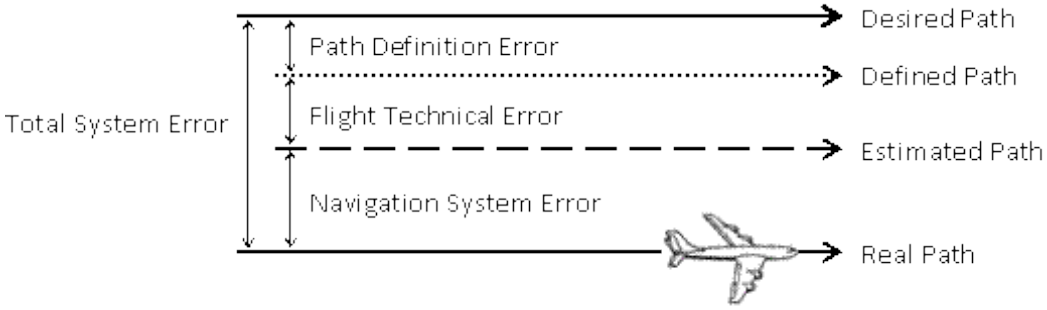

Figure 3-Total System Error [17]

Where important terms are defined below:

- ***Defined Path****:* The output of the path definition function.
- ***Desired Path****:* The path that the flight crew and air traffic control can expect the aircraft to fly, given a particular route or leg or transition.
- ***Estimated Position***: The output of the position estimation function.
- ***Path Steering Error (PSE)****:* The distance from the Estimated Position to the Defined Path. The PSE includes both FTE and display error.
- ***Flight Technical Error (FTE)****:* The accuracy with which the aircraft is controlled as measured by the indicated aircraft position with respect to the indicated command or desired position.
- ***Path Definition Error (PDE)****:* The difference between the Defined Path and the Desired Path at a specific point.
- ***Position Estimation Error (PEE)****:* The difference between the true position and Estimated Position.
- ***Total System Error (TSE)****:* The difference between true position and Desired Position. This error is equal to the vector sum of the Path Steering Error, Path Definition Error, and Position Estimation Error.

To support the PBN concept a reduced set of performance criteria have been identified so as to characterize the performance of navigation equipment. These criteria are presented in the next section.

2.4 Operational Criteria for Navigation Performance

Required operational requirements for GNSS based navigation are defined by four criteria/metrics which are accuracy, availability, continuity and integrity. The corresponding definitions which are reminded here can be found in [1].

2.4.1 Accuracy

Accuracy is the degree of conformance between the estimated or measured position and/or velocity of a platform at a given time and its true position and/or velocity. For characterizing the accuracy on the estimated quantity, ICAO has defined a 95% confidence level. It means that for any estimated position at a specific location, the probability that the position error is within the former requirement should be at least 95%.

2.4.2 Availability

The availability of a navigation system is the ability of the system to provide the required function and performance at the initiation of the intended operation. The availability of GNSS is characterized by the portion of time the system is used for navigation and during which reliable navigation information is presented to the crew, autopilot, or other system managing the flight of the aircraft.

2.4.3 Continuity

The continuity of a system is the capability of the total system (comprising all elements necessary to maintain aircraft position within the defined airspace) to perform its function without interruption during the intended operation. Continuity relates to the capability of the navigation system to provide a navigation output with the specified accuracy and integrity throughout the intended operation, assuming that it was available at the start of the operation. The occurrence of navigation system alerts, either due to rare fault-free performance or to failures, constitute continuity failures. For En-route operations, since the durations of these operations are variable, the continuity requirement is specified as a probability on a per-hour basis. For both approach and landing operations, the continuity requirement is stated as a probability for a short exposure time.

2.4.4 Integrity

Integrity is a measure of the trust that can be placed in the correctness of the information supplied by the total system. Integrity includes the ability of a system to provide timely and valid alerts to the user when the system must not be used for the intended operation (or phase of flight).

Integrity requirements are defined with three parameters described below:

- ***Integrity risk****:* It is the probability of providing a signal that is out of tolerance without warning the user in a given period of time.
- ***Time-to-Alert***: It is the maximum allowable elapsed time from the onset of a positioning failure until the equipment annunciates the alert.
- ***Alert limits***: For each phase of flight, to ensure that the position error is acceptable, alert limits (Horizontal (or Lateral for approaches with vertical guidance) and Vertical) are defined and represent the largest position error which results in a safe operation. More details are given below:
    - The *Horizontal Alert Limit (HAL/LAL)* is the radius of a circle in the horizontal plane (the local plane tangent to the WGS-84 ellipsoid), with its centre being at the true position, that describes the region that is required to contain the indicated horizontal position with the required probability for a particular navigation mode.
    - The *Vertical Alert Limit (VAL)* is half the length of a segment on the vertical axis (perpendicular to the horizontal plane of WGS-84 ellipsoid), with its centre being at the true position, that describes the region that is required to contain the indicated vertical position with the required probability for a particular navigation mode.

The probability of non-integrity detection quantifies the integrity risk. It represents the probability that an error exceeds the alert limit without the user being informed within the time to alert.
The values assigned to these three parameters depend on the specific application and intended operation, and are determined by the ICAO.

2.5 Annex 10 [3] SIS Performance Requirements

2.5.1 Existing requirements

The Signal in Space (SIS) is the combination of guidance signals arriving at the antenna of an aircraft [27] .The combination of GNSS elements and a fault-free GNSS user receiver shall meet the SIS requirements defined in the following Table 2.

The fault-free receiver is assumed to be a receiver with nominal accuracy and time-to-alert performance. The concept of a fault-free user receiver is applied only as a means of defining the performance of combinations of different GNSS elements .Such a receiver is assumed to have no failures that affect the integrity, availability and continuity performance [1].

Typical operation	Accuracy Horizontal 95%	Accuracy Vertical 95%	Integrity (Note 2)	Time-to-alert (Note 3)	Continuity (Note 4)	Availability (Note 5)

	(Notes 1 and 3)	(Notes 1 and 3)				
En-route	H 3.7km	N/A	$1-10^{-7}/h$	5 min	$1-10^{-4}/h$ to $1-10^{-8}/h$	0.99 To 0.99999
En-route, Terminal	H 0.74km	N/A	$1-10^{-7}/h$	15 s	$1-10^{-4}/h$ to $1-10^{-8}/h$	0.99 To 0.99999
Initial approach, Intermediate approach, NPA, Departure	H 220m	N/A	$1-10^{-7}/h$	10 s	$1-10^{-4}/h$ to $1-10^{-8}/h$	0.99 To 0.99999
Approach operations with vertical guidance (APV-I)	H 16m	V 20m	$1-2.10^{-7}/app$	10 s	$1-8.10^{-6}/15\ s$	0.99 To 0.99999
Approach operations with vertical guidance (APV-II)	H 16m	V 8m	$1-2.10^{-7}/app$	6 s	$1-8.10^{-6}/15\ s$	0.99 To 0.99999
Cat-I precision approach	H 16m	4≤V≤6 m	$1-2.10^{-7}/app$	6 s	$1-8.10^{-6}/15\ s$	0.99 To 0.99999

Table 2-SIS performance requirements [1]

Typical operation	Horizontal alert limit	Vertical alert limit
En-route (oceanic/continental low density)	7.4 km (4 NM)	N/A

En-route (continental)	3.7 km (2 NM)	N/A
En-route, Terminal	1.85 km (1NM)	N/A
NPA	556 m (0.3 NM)	N/A
APV – I	40 m (130 ft)	50 m (164 ft)
APV – II	40 m (130 ft)	20 m (66 ft)
CAT – I precision approach	40 m (130 ft)	35 to 10 m (115 to 33 ft)

Table 3-Alert Limits associated to typical operations [1]

Notes associated to previous tables [1]

1. The 95th percentile values for GNSS position errors are those required for the intended operation at the lowest height above threshold (HAT), if applicable.

2. Integrity requirement includes an alert limit against which the requirement can be assessed. For Category I precision approach, a vertical alert limit (VAL) greater than 10 m for a specific system design may only be used if a system-specific safety analysis has been completed. Further guidance on the alert limits is provided in [1] *Attachment D. These alert limits are defined in 3.*

3. The accuracy and time-to-alert requirements include the nominal performance of a fault-free receiver.

4. Ranges of values are given for the continuity requirement for en-route, terminal, initial approach, NPA and departure operations, as this requirement is dependent upon several factors including the intended operation, traffic density, and complexity of airspace and availability of alternative navigation aids. The lower value given is the minimum requirements for areas with low traffic density and airspace complexity. The higher value given is appropriate for areas with high traffic density and airspace complexity. Continuity requirements for APV and Category I operations apply to the average risk (over time) of loss of service, normalized to a 15-second exposure time.

5. A range of values is given for the availability requirements as these requirements are dependent upon the operational need which is based upon several factors. The lower values given are the minimum availabilities for which a system is considered to be practical but are not adequate to replace non-GNSS navigation aids. For en-route navigation, the higher values given are adequate for GNSS to be the only navigation aid provided in an area. For approach and departure, the higher values given are based upon the availability requirements at airports with a large amount of traffic assuming that operations to or from multiple runways are affected but reversionary operational procedures ensure the safety of the operation.

6. A range of values is specified for Category I precision approach. The 4.0 m (13 feet) requirement is based upon ILS specifications and represents a conservative derivation from these specifications.

7. The terms APV-I and APV-II refer to two levels of GNSS approach and landing operations with vertical guidance (APV) and these terms are not necessarily intended to be used operationally.

2.5.2 CAT II/III

GNSS performance requirements for Category II and III precision approach operations are under development by the different authorities and have not yet been harmonized. However, several methods have been proposed and used to derive the required performance for CAT-II/III precision approaches as it is illustrated in [28]. Two methods are described the ‘‘ILS (Instrument Landing System) Look-Alike Method’’ defined by EUROCAE and the ‘‘Autoland Method’’ defined by RTCA.

The first method named “ILS Look-Alike Method” is based on the concept of matching the performance of the ILS at the Navigation System Error (NSE) level through linearization of current specifications at a given height. The figure below explains this method

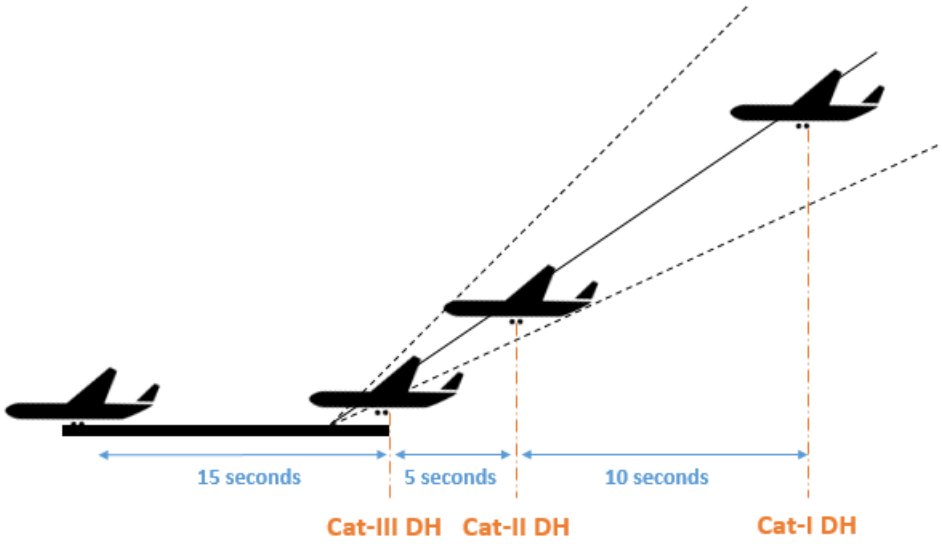

Figure 4-ILS Look-Alike Method

The second one called “Autoland Method” is based on the need to protect the safety of a landing operation using the current specification for the probability to land in a given landing box. The following figure described this method.

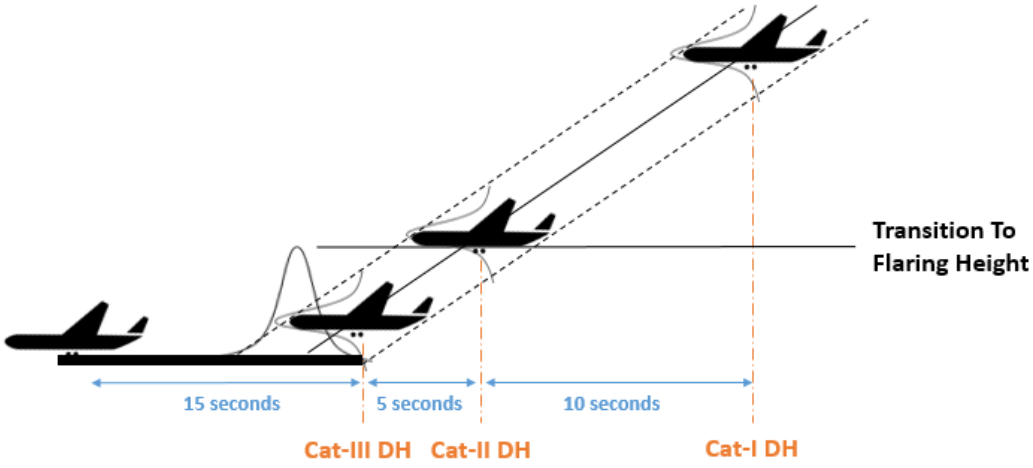

Figure 5-Autoland Method

The following table summarized the SIS Performance Requirements for the different phases of aircraft operation for each method. These are defined, as for all approaches using vertical guidance, with Vertical and Lateral performances requirements.

Cat - III		ILS Look-Alike (EUROCAE)	Autoland (RTCA)
Accuracy	**SIS Accuracy (2σ)**	3.6 m (L) 1.0 m (V)	6.2 m (L) 2.0 m (V)
Integrity	**Alert Limit**	10.4 m (L) 2.6 m (V)	15.5 m (L) 10.0 m (V)
	Integrity Risk	10^{-9} per 30s (L) 10^{-9} per 15s (V)	10^{-9} per 30s (L) 10^{-9} per 15s (V)
	Time-to-Alert (TTA)	2s	2s
Continuity	**Continuity Risk**	2×10^{-6} per 30s (L) 2×10^{-6} per 15s (V)	2×10^{-6} per 30s (L) 2×10^{-6} per 15s (V)
Availability	**Probability of Availability**	0.99-0.99999	0.99-0.99999

Table 4-SIS Performance Requirements for the various phases of aircraft operation [28]

This is important also to notice that requirements such as Decision Height and Visual requirements for these categories are defined in Table 1

Chapter 3 : GNSS Processing

3.1 The Civil Aviation GNSS Concept

3.1.1 Introduction

The Global Navigation Satellite System (GNSS) concept was introduced and developed by ICAO (International Civil Aviation Organization) and more precisely by the FANS (Future Air Navigation Systems) committee. It is included in the CNS/ATM concept (Communication Navigation Surveillance/Air Traffic Management) established by ICAO in 1983 and adopted in 1991. The operational plan of this latter was adopted by ICAO in 2003 and remains set around the world. [29]

GNSS is defined by ICAO as a system capable of estimating position and time and composed of one or several satellites constellations, aircrafts embedded receivers and an integrity monitoring function. GNSS was inspired by GPS and GLONASS systems but whilst similar in principle, the ICAO requirements (as described above in section 2.5) are so stringent in terms of accuracy, integrity, availability and continuity (their concepts were introduced in section 2.4) that GPS standalone receivers cannot be used without augmentation by an integrity monitoring solution.

The basic principle of satellite positioning is to measure ranges and radial velocities between satellites with a known trajectory and user receivers. In fact, range measurements are propagation time measurements of a signal between the satellite antenna and user antenna and velocity measurements are measurements of Doppler deviations of the carrier of the received signal. These range measurements are so called *pseudorange* measurements since they include an offset between satellite clock and user clock realizations used to generate the correlated signal codes. Therefore, these pseudorange measurements enable the user to estimate his position, his velocity, and to synchronize his local oscillator with the GPS reference time. That is why GPS is defined as a PVT (position, velocity, time) estimation mean.

The different steps for establishing the position estimation and the navigation solution are described in all parts of this section. Indeed, at first, how the pseudorange measurement is obtained and corrected for being used to estimate the position is explained, then a brief description of the GNSS and signals currently used or planned to be used for civil aviation applications is given. Finally, due to stringent civil aviation requirements a more detailed part will focus on the Differential GNSS (DGNSS) which is a technique that significantly improves both the accuracy and the integrity of the GNSS.

3.1.2 Principle of Satellite Positioning [29]

Satellites transmit signals with modulated codes whose chip transitions are synchronized with the satellite atomic frequency standard. The receiver measures the signal propagation time through correlation of the incoming signal with another replica code copy generated with respect to the receivers own oscillator. The tracking function of the receiver has the function to continually update the best estimate of the propagation delay by tracking the correlation peak.

Since the correlation process involves two input signals generated with reference to different oscillators (satellite and receiver) which are not synchronized, a deviation between "satellite time" and "receiver time" will appear in the propagation time measurement. A pseudorange measurement denoted ρ and expressed in meters is obtained by multiplying this propagation time by the propagation velocity c.

The pseudo range measurement ρ^i (in meters) is described by the following equation:

$$\rho^i = c \times t^i + c \times \Delta t_u^i + e^i$$

Equation 1 - Pseudorange model

Where the parameter t^i is the propagation time between the antenna of the satellite i and the receiver antenna, Δt_u^i is the deviation between the satellite clock and the receiver clock and $\Delta t_u^i = \Delta t_u - \Delta t^i$ by setting Δt_u as the deviation between receiver clock and GPS time and Δt^i as the deviation between satellite clock and GPS time. The signal propagation delays and measurements errors are gathered in e^i.

This pseudo range measurement can be corrected by $\Delta \hat{t}^i$ which is a correction of the deviation between satellite clock and GPS time given by the satellite signal and applied to each ρ^i . [30]

So corrected measurements ρ_c^i are affected by the same bias which is the receiver clock bias and a new relation can be obtained:

$$\rho_c^i = \rho^i + c \times \Delta \hat{t}^i + n^i = c \times t^i + c \times \Delta t_u + e^i$$

Equation 2 -Corrected pseudorange model

The propagation time t^i represents the propagation time of the signal from the satellite to the receiver. It depends on the desired receiver u position defined through its 3 coordinates: X_u , Y_u, Z_u and on the satellite position which is assumed to be known and defined by its 3 coordinates : X^i, Y^i, Z^i:

$$c \times t^i = r^i = \sqrt{(X^i - X_u)^2 + (Y^i - Y_u)^2 + (Z^i - Z_u)^2}$$

Equation 3 –Range

So the corrected pseudo range measurement model can also be expressed as:

$$\rho_c^i = \sqrt{(X^i - X_u)^2 + (Y^i - Y_u)^2 + (Z^i - Z_u)^2} + c \times \Delta t_u + e^i$$

Equation 4 -Corrected pseudorange measurement model

A user can estimate their position (3 unknown coordinates) and the receiver clock bias Δt_u using a minimum of 4 simultaneous corrected pseudorange measurements ρ_c^i (see section 3.3. for more details).

3.1.3 Planning of GNSS implementation in Civil Aviation

GNSS is composed of existing constellations of navigation satellites and complementary satellite systems for improving performances like the augmentation system EGNOS in Europe or ground complements systems like Differential GNSS. They are presented in this part of the report.

3.1.3.1 Operational Satellite Positioning Systems (GPS/GLONASS)

3.1.3.1.1 GPS

Regarding principles of satellite positioning described in 3.1.1 that have an impact on the GPS structure concerning satellites, ground stations and timing. Therefore, the GPS is composed of three segments defined as Space Segment, User Segment and Control Segment.

The space segment [29] is the satellite part of the positioning system. The United States' Global Positioning System (GPS) [31] space segment consists of up to 32 (MEO) satellites in six different orbital places, with the exact number of satellites varying as older satellites are retired and replaced. GPS became operational in July 1995 with the following noteworthy modifications:

- Modernization of GPS II : GPS L2C since the end of 2005, GPS L5 in 2010
- With the adding of L1C, GPS III could be operational in 2021
- New military signal M-code on L1 and L2

Each of the GPS signal is composed of one carrier to transmit the signal at the desired frequency, a navigation message which contains some useful data for the user such as orbit information, $\Delta\hat{t}^i$ (explained in 3.1.2 which is a correction of the deviation between satellite clock and GPS time) and a PRN code which is a random binary sequence different for all satellite which enables to recognize them.

Today, several signals are available for civil aviation application named GPS L1 C/A and GPS L5 (in the future L1C will be available and is described only for information purpose in this part). These signals are the GNSS signals located in the specific frequency bands named Aeronautical Radio Navigation Services (ARNS). ARNS bands are reserved for aeronautical systems and particularly protected from in-band interference by regulation authorities.

The characteristics of these available GPS signals for Civil Aviation (frequency occupation, structure) are described in the following table extracted from [32].

Constellation	Signal	Modulation	Code Length (ms)	Chip rate (Mcps)	Navigation Data (sps)	Secondary Code Length
GPS	L1 C/A	BPSK(1)	1023	1.023	50	No
	L1C-I	TMBOC(6,1,4/33)	10230	1.023	100	No
	L1C-Q		10230	1.023	Pilot	1800 bits
	L5-I	QPSK(10)	10230	10.23	1000	NH-10 (10bits)
	L5-Q		10230	10.23	Pilot	NH-20 (20 bits)

Table 5-GPS signals for civil aviation

The User Segment [33] includes millions of GPS receivers (military or civilians). These receivers can be static on Earth, or mobile in a vehicle on Earth, in an aircraft or a spacecraft. They permanently collect GPS signals and process them to compute the position and velocity of the user.

The role of the Control Segment [33] is to ensure the surveillance of the received signal characteristics, to compute the ephemeris data and the satellites clock corrections, and to download the navigation message into the satellites payload. Therefore, the control segment is composed of 4 major subsystems: the Master Control Station (MCS, soon replaced by a New Master Control Station) located in Colorado which is responsible for constellation command and control, a Back-up Master Control Station (BMCS, soon replaced by an Alternate Master Control Station), a network of 4 ground antennas and a network of monitor stations globally-distributed.

As mentioned in introduction, under the GPS SPS specifications [33], the probability of failure is less than $10^{-5} per\ hour$ and *per satellite* and therefore an integrity monitoring function is needed to meet the integrity risk requirement for aviation operations of the order of 10^{-7}.Indeed, such standalone receivers (GPS, GLONASS or BeiDou) cannot be used without spatial, regional, local augmentation which improve accuracy and/or integrity. Also a RAIM algorithm could be used for providing integrity information for some approaches and landing operations such as NPA. These regional GNSS are briefly presented below and a more detailed section 3.1.4 concerns other augmentation techniques.

3.1.3.1.2 GLONASS [34]

The formerly "Soviet Union" , and now *Global'naya Navigatsionnaya Sputnikovaya Sistema* (Global Navigation Satellite System), or GLONASS, was a fully functional navigation constellation in 1995. After the Collapse of the Soviet Union, it fell into disrepair, leading to gaps in coverage and only partial availability, but the full orbital constellation has since been restored in 2011.

3.1.3.2 Navigation Satellite Systems in development (GALILEO/ BeiDou /QZSS/IRNSS)

3.1.3.2.1 GALILEO [35]

The European Union and European Space Agency agreed in March 2002 to introduce their own alternative to GPS, called the Galileo positioning system. At an estimated cost of EUR 3.0 billion, the system was originally scheduled to be operational in 2010 but the updated calendar is currently defined as:

- 1999 : Definition of Galileo
- 2002 : Start of the Project
- 2005 : First satellite was launched for testing
- 2011 : The 2 first Galileo Satellites was launched
- 2015 : 12 satellites are in orbit
- 2020 : Constellation completed

Today, several signals are available for civil aviation application by similitude with GPS named Galileo E1 and Galileo E5a (in the future E5b will be available and is described only for information purpose in this part). These signals are the GNSS signals located in the specific frequency bands named Aeronautical Radio Navigation Services (ARNS). ARNS bands are reserved for aeronautical systems and particularly protected from in-band interference by regulation authorities.

The characteristics of these available Galileo signals for Civil Aviation (frequency occupation, structure) are described in the following table extracted from [32].

Constellation	Signal	Modulation	Code Length (ms)	Chip rate (Mcps)	Navigation Data (sps)	Secondary Code Length
GALILEO	E1B	CBOC(6,1,1/11)	4092	1.023	250	No
	E1C		4092	1.023	Pilot	Primary x 25 (100 ms)
	E5A-I	QPSK(10)	10230	10.23	50	Primary x 20 (20 ms)
	E5A-Q		10230	10.23	Pilot	Primary x 100

						(100 ms)
	E5B-I	QPSK(10)	10230	10.23	250	Primary x 4 (4 ms)
	E5B-Q		10230	10.23	Pilot	Primary x 100 (100 ms)

Table 6-Galileo signals for civil aviation

3.1.3.2.2 BeiDou Navigation Satellite System (BDS or BeiDou-2) [36]

China has expand their experimental regional navigation system known as BeiDou-1 which consists of four satellites (three working satellites and one backup satellite) into a global navigation system BeiDou Satellite Navigation Experimental System called BeiDou-2 (also known as COMPASS).

This new system is under construction as of January 2015 and is planned to be a constellation of 35 satellites by 2020.In-mid 2015, China started the build-up of the third generation BeiDou system (BDS-3) in the global coverage constellation. The first BDS-3 satellite was launched 30 September 2015 and in March 2016, 4 BDS-3 in-orbit validation satellites have been also launched.

3.1.3.3 Regional GNSS

3.1.3.3.1 QZSS [34]

The Quasi-Zenith Satellite System (QZSS), is a proposed regional positioning system. It is not required to work in standalone mode but to enhance GPS covering Japan. The first demonstration satellite was launched in September 2010. In 2011 the Government of Japan has decided to accelerate the QZSS deployment in order to reach a 4-satellite constellation by 2018 while aiming at a final 7-satellite constellation in the future.

3.1.3.3.2 IRNSS [35]

The Indian Regional Navigational Satellite System (IRNSS) is an independent regional satellite navigation system being developed by Indian Space Research Organisation (ISRO) which would be under the total control of Indian Government. Five satellites are already placed in orbit and the IRNSS constellation of seven satellites is expected to operate from June 2016.

These regional GNSS can therefore be used to enhance systems. Another technique to meet the stringent ICAO requirements for GNSS is the Differential GNSS. The following section details its principle.

3.1.4 Differential GNSS in Civil Aviation

Differential GNSS (DGNSS) is a technique that significantly improves both the accuracy and the integrity (if monitoring systems are defined) of the GNSS. DGNSS uses *reference receivers* at known locations to estimate the errors for use at receivers at unknown locations. Since the reference receiver positions are known, it is possible to compute the geometric range between each satellite and the reference station. Indeed, by comparing the satellite range measurement and the true geometric range measurement, a correction is computed for each satellite tracked by the ground station. This correction is broadcast to DGNSS users on a convenient communications link. The accuracy improvement arises because the largest GNSS (GPS) errors vary slowly with time and are strongly correlated over distance (atmospheric errors, satellite orbit and clock errors). Also a DGNSS can also significantly improves the *integrity* of GNSS for all classes of users if some monitors are implemented (on ground and/or user sides), indeed that will reduce the probability that a GNSS user would suffer from an unacceptable position error attributable because it to an undetected system fault.

In order to use DGNSS, several constraints exist [29]:

- The user must employ only satellites for which corrections have been received from the reference station
- The user must apply the corrections with a small time lag

The main advantage of using DGNSS is the reduction of the correlated errors noted above but an important drawback of using DGNSS is the fact that non-correlated errors like noise and multipath are amplified as illustrated by the following figure.

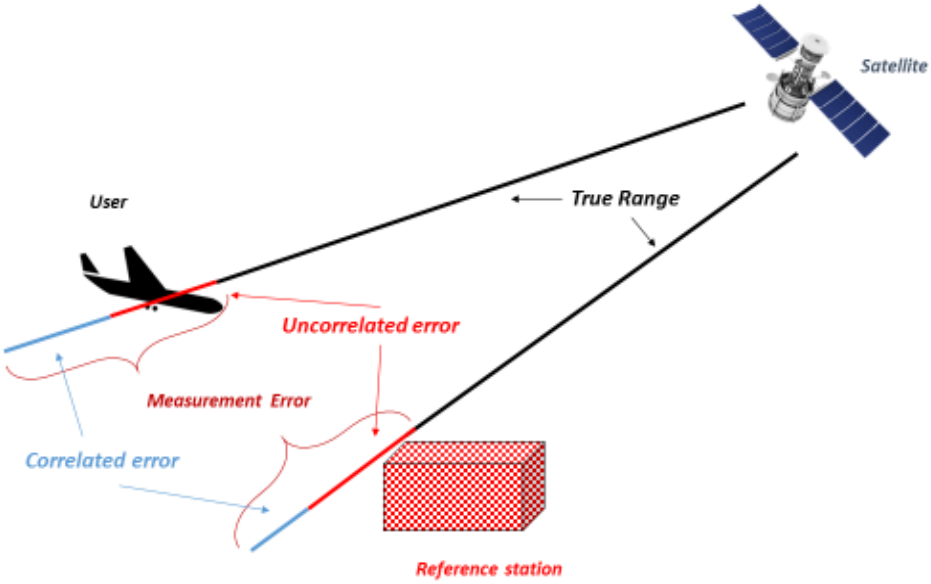

Figure 6-DGNSS principle

However, performance of this system will depend of the correlation between measurements errors at the reference station and at the user location: spatial separation and temporal separation Indeed, the more this errors are correlated in space and time the more such a system performs well.

When the coverage area is small, only a single reference station is required and this form of DGNSS is named Local Area DGNSS (LADGNSS). Otherwise, when the coverage area is large, a network of reference stations is necessary and is known as Wide Area DGNSS (WADGNSS).

Other solutions exist and use the DGNSS principles but with some differences such as PPP (Precise Point Positioning) which uses precise reference satellite orbit and clock products or RTK (Real Time Kinematic) which computes double difference of ranges and send directly corrected range (not only corrections).

3.1.4.1 Wide Area Differential GNSS

3.1.4.1.1 Introduction

In the Civil Aviation context, Wide Area Differential GNSS (WADGNSS) is conceptualised as the Satellite Based Augmentation System (SBAS). In the USA this system is deployed and named Wide Area Augmentation System (WAAS) and in Europe, the equivalent system is known as EGNOS (European Geostationary Navigation Overlay Service).

3.1.4.1.2 SBAS Architecture

SBAS transmits differential corrections and integrity messages for navigation satellites tracked by a network of reference receivers, typically deployed for an entire continent. Depending on the architecture of the system and the required performance level, between 20 and 35 reference receivers are needed to cover a continent. Reference Stations track the GPS signal and some stations allow to collect GPS data such as orthography of satellites, allow to determine ephemeris and clock corrections and allow to estimate the ionospheric delays throughout the whole service area. Then measurements are sent to redundant master stations.
The roles of master stations is to calculate the clock and orbits differential corrections, to calculate satellite integrity parameters, to compute the ionospheric corrections and to transmit them to the users through the SBAS navigation messages. SBAS also provides real time error bounding data for these corrections. These corrections and error data are both valid over the continental area defined by the reference network and so they are broadcast to suitably equipped aircraft using Geostationary Earth Orbit (GEO) satellites.

There are four major differences between the SBAS and GBAS concepts [37].First of all, for SBAS, the frequency band of the data link is identical to that of the GPS signals. Next, the use of geostationary satellites in SBAS enables messages to be broadcast over very wide areas. The third difference is the fact that The GEO satellites used in SBAS can also transmit ranging measurements, as if they were GPS satellites. Finally, the main difference is the fact that SBAS provides vectorial corrections such as clock, ionosphere and ephemeris corrections while GBAS transmits scalar ones (pseudorange corrections).

Considering some limitations dealing with the number of control stations and operation costs, it is believed [38] that the best performance level currently attainable by the SBAS corresponds to APV I or II performance approaches.

As mentioned in the introduction of this section, several SBAS are currently implemented:

- The Wide Area Augmentation System (WAAS), operated by the United States Federal Aviation Administration (FAA).
- The European Geostationary Navigation Overlay Service (EGNOS), today operated by the European Space Agency (ESA) and then operated by the ESSP (European Satellite Service Provider) from the beginning of the year 2009.
- The Multi-functional Satellite Augmentation System (MSAS) system, operated by Japanese Civil Aviation Bureau (JCAB).

3.1.4.1.3 Dual Frequency/ Multi Constellations SBAS

By the adding of new constellations such as GLONASS and the future GALILEO, a modernization of SBAS is under investigation [39] and at an advanced stage of development. Indeed, the new concept of Dual-Frequency (DF)/Multi-Constellation (MC) SBAS was proposed and a standardization is expected to be available for 2021/2022. This development contains different tasks such as: an identification of operational benefits and the technical requirements, a prototyping and some flight tests of DF/MC SBAS receiver opportunity. Such a DF/MF receiver is planned to be certified in Europe after 2025. [40]

3.1.4.2 Local Area Differential GNSS

Within civil aviation the LADGNSS implementation is known as the Ground Based Augmentation Systems (GBAS). It's primary purpose is to support precision approach operations. In the USA, the FAA version of this kind of system is known as the Local Area Augmentation System (LAAS). [41]

3.1.4.2.1 GBAS Introduction *[2]

As introduced before, GBAS is a local area differential system that strengthen standalone GNSS to support civil aviation operations around the airport. Indeed, the maximum coverage range is currently 23NM and it defines the GBAS coverage volume which is the region within the GBAS is required to meet the accuracy, integrity and continuity requirements (section 2.4). This coverage volume is illustrated in a plan view and profile view in the following figure where LTP/FTP design the Landing/Fictitious Threshold Point and GPIP, the Glide Path Intersection Point.

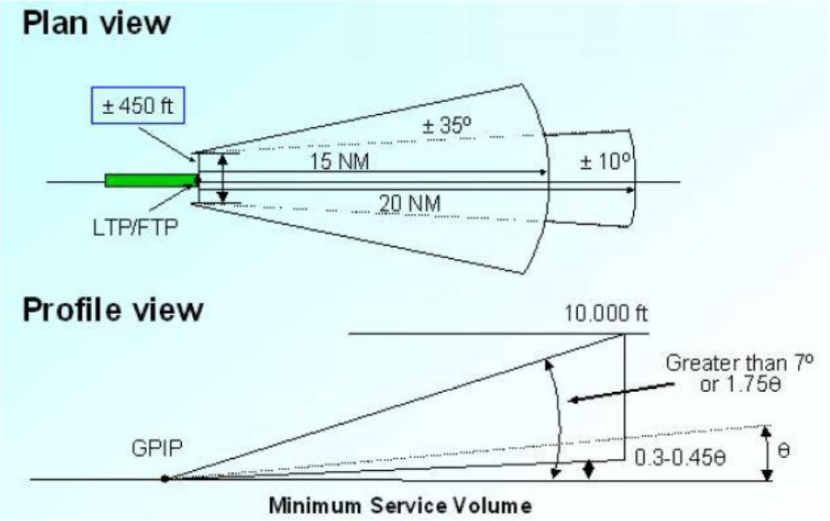

Figure 7-GBAS volume Coverage [1]

Users of such a system receive the augmentation information directly from a ground-based transmitter and use differential corrections valid in this local area. GBAS supports all phases of approach, landing, departure, and surface operations within its coverage volume. As explained in section 2.5, GBAS approach services are currently defined through GASTs A, B, C and D (more details in 3.1.4.2.3) which correspond respectively to GBAS for APV I, APV II, CAT I and CAT II/III approaches. [42]

The already implemented Instrument Landing System (ILS) consists of two independent sub-systems, one providing lateral guidance (LOC) and the other vertical guidance (Glide Path)to aircraft approaching a runway. ILS has a siting constraints as it has to be installed at each runway end instead of GBAS for which the station may cover multiple runways at a single airport and data which may be used for nearby airports and heliports as well. Also, based on ILS an aircraft will suffers from so-called critical areas and could have constraints on possible trajectories for approaching an airport [43].

Even if ILS remains the primary source of guidance in major airports, GBAS is expected to play a key role in maintaining existing all-weather operations capability at CAT I, II and III airports.

Furthermore with the evolution of GBAS towards multi-constellation (MC) and multi-frequency (MF) by the adding of the Galileo constellation, some improvements in terms of technical performance are hoped such as: mitigation of anomalous ionospheric effect, stronger robustness to unintentional interference, constellation diversity which limits the dependency from GPS, better availability due to the adding of satellites and a therefore an improvement of the continuity of service.

3.1.4.2.2 GBAS Architecture *[3]

As described by the following figure, GBAS infrastructure is composed of three subsystems: The Satellite Subsystem, the Ground Subsystem and the Aircraft Subsystem.

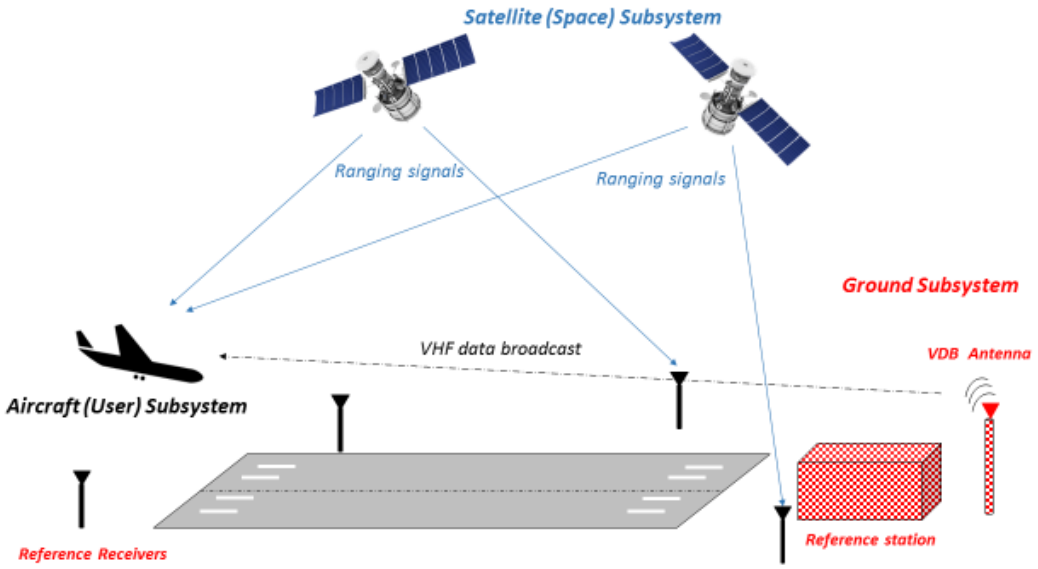

Figure 8-GBAS architecture

- The *Satellite Subsystem* which produces ranging signals. It consists on GNSS satellites from the core constellations (called ranging sources). This Space Segment is mainly composed of satellites from GNSS constellations explained above (GPS/GALILEO/GLONASS) but could be also added by some SBAS satellites. This subsystem provides satellite status, position and timing signal and need to have a sufficient number of satellites to determine the user position

In this PhD project, only GPS and Galileo constellations are used, therefore this thesis only deals with the limited case of available L1C/A, L5, E1 and E5a signals as described in the previous sections 3.1.3.1.1 and 3.1.3.2.1.

- The *Ground Subsystem* installed at the airport premises is responsible for transmitting to the user: pseudorange corrections, integrity data of various satellites in view, database for the final approach segment and other relevant information. It is composed of 2-4 reference receivers with a ground station and a VHF transmitter which provides VDB (VHF Data Broadcast) messages containing data which will be applied at the user subsystem.

- The *Aircraft Subsystem* receives and processes the GNSS signal in space in order to compute and output the position solution. Indeed, this subsystem applies broadcast pseudorange corrections to its measurements in order to compute a position with a corrected pseudorange, then it computes deviations from broadcast approach path and finally it determines if a GBAS approach is safe by computing protection levels. Due to the ICAO precision approach transition strategy, a Multi-Mode Receiver (MMR) is needed to enable a mix of systems possible (ILS/ GLS-GBAS Landing System). This system offers a great flexibility to users therefore when GBAS corrections cannot be applied, this receiver can work in GPS mode for instance.

The GBAS signal in space is defined as the combination of the satellite signals from the core satellite constellations and the VDB signal.

Several GBAS ground subsystem configurations are possible according to the GNSS Standards [27] which support GAST A,B,C and D. GAST A, B and C are intended to support typical APV I, APV II and Cat I operations respectively as defined in 2.5.1. GAST D has been introduced to support landing operations in lower visibility conditions including Cat III operations.

For information purpose, it can be added that other configurations are currently investigate but not defined in standards such as:

- GBAS ground subsystem configurations which support Cat III precision approach using GALILEO and GPS based on dual-frequency data (known as GAST-F)
- And the GBAS ground subsystem configurations which supports GAST D, and GAST-C using GPS, GLONASS or GALILEO, as well as the positioning service using any combination of these constellations.

Some main configuration options exists and enables to define a GBAS ground subsystem classification named GBAS Facility Classification (GFC) [27].

A GFC is made according different elements such as : the Facility Approach Service Type (FAST) which is a collection of letters from A to F indicating the Service Types that are supported by the ground subsystem, the Ranging Source Types which indicates what ranging sources are augmented by the ground subsystem (noted G1/G3/G4/G5+ for GPS/SBAS/GLONASS/Galileo/ future Ranging Sources respectively), the Facility Coverage which defines the horizontal coverage of the GBAS positioning service (coded as 0 for Ground facilities that do not provide the Positioning Service and as the value of the radius of the GBAS coverage volume expressed in NM) and finally the Polarization of the VDB signal (coded E for elliptical and H for horizontal polarization)

Then the general form for defining the GFC is Facility Approach Service Type/Ranging Source Type /Facility Coverage/Polarization.

The following section describes in details the services providing by GBAS and corresponding classification levels.

3.1.4.2.3 GBAS Service Type *[3]

GBAS provides two types of services defined below:

- The GBAS Approach service which provides vertical and lateral deviation guidance for FAS (Final Approach segments) in Cat I/II/III precision approach, APV, and NPA within the operational coverage area.

- The GBAS Positioning service which provides horizontal position, velocity and time information to support RNAV operations within the service area.

GBAS Approach Services are also differentiated into multiple types known as GBAS Approach Service Types (GAST) [13]. A GAST is defined as the matched set of airborne and ground performance and functional requirements that are intended to be used in order to provide approach guidance with quantifiable performance.

As introduced in sections above, four types of approach service, GAST A, GAST B, GAST C and GAST D are currently defined. GAST A, B and C are intended to support typical APV I, APV II and Cat I operations respectively as defined in 2.5.1. GAST D has been introduced to support landing operations in lower visibility conditions including Cat III operations. This GAST D concept resulted from a PBN approach which defines system performance requirements in terms of the accuracy, integrity, availability, continuity and functionality (described in 2.3) relying on the aircraft capabilities to use the GBAS service to reach CAT II/III minima, instead of putting all the constraints on the Signal in Space. In this innovative approach, there will be a transfer of responsibility from the ground station to the on-board equipment, unlike GAST A/B/C. Mostly because of this responsibility transfer, some concepts are different between GAST D and GAST C. The complexity of this new system in term monitoring or architecture definition is one of the reason which could explain why the airborne functional requirements for GAST D are not standardized yet. More details on changings relative to the GAST D introduction especially about integrity concept is given in 3.3.2.2.3.2.

Furthermore, as it is indicated in [44] for GAST D, the mandatory coverage volume 3.1.1 is intended to be increased for by the possible addition of new broadcast parameters [45].

Other future approach services GAST E and GAST F are supposed to be defined as mentioned in [46] :

- GAST-E is intended to support either Cat II performance operations or Cat III operations with L5/E5a with integration assumptions.
- GAST-F is intended to support Cat III performance level through the provision of MC/MF corrections

GBAS service levels are listed in the following table extracted from [27]:

GBAS Service Level	Typical operation(s) which may be supported by this level of service
A	Approach operations with vertical guidance (performance of APV-I designation)
B	Approach operations with vertical guidance (performance of APV–II designation)
C	Precision Approach to lowest Category I minima
D	Precision Approach to lowest Category IIIb minima, when augmented with other airborne equipment
E	Precision Approach to lowest Category II/IIIa minima
F	Precision Approach to lowest Category IIIb minima

Table 7-GBAS service levels [27]

It is important to note that several service types can be supported simultaneously by a GBAS ground subsystem. Two types of ground subsystems exist: those that support multiple types of approach service and those that do not. The types of services supported for each approach are indicated in the Approach Performance Designation (APD) field in a FAS data block within the Type 4 message (described in3.2.3.4.3). A GBAS Continuity/Integrity Designator (GCID) parameter in the Type 2 message (described in3.2.3.4.3) indicates whether a GBAS ground subsystem is currently supporting multiple types of approach service. [13]

This GCID classification is illustrated by the following table extracted from [27] :

GCID	GSL Supported by Ground Station Contribution of Continuity and Integrity
0	(reserved for service levels less stringent than A)
1	GSL A,B,C
2	GSL A, B, C, D
3	GSL A, B, C, D, E
4	GSL A, B, C, D, E, F
5	(reserved for service levels less stringent than A)
6	(reserved for service levels less stringent than A)
7	No Approach Service available

Table 8-GCID classification [27]

Airborne equipment that can support multiple service types will first check the GCID value to determine if the GBAS ground subsystem can also support them and then will check the APD field to see which types of service are supported by the ground segment. Finally, the airborne equipment will choose which approach service to select regarding the APD, the current status of GCID and the airborne equipment type [13].

Based on this approach, the highest type of service supported by both is at first automatically selected by the GBAS airborne equipment. If the desired type of service is not available, the airborne equipment may select the next lower available type of service and annunciate this appropriately. Therefore, during a GBAS operation, there is the Selected Service Type (SST) and the Active Service Type (AST). The first one is the service type that the airborne equipment would use if it were available, and can be no higher than the highest type of service offered

by the ground segment for the selected approach. But The AST is the service type that the airborne equipment is actually using at a particular time.

The airborne equipment annunciates both the SST and AST so that proper action may be taken in the context of the airborne integration and operational procedures. [13]

3.2 Measurement Model

In GNSS, the pseudorange measurement is a fundamental measurement as presented in 3.1.1 it could be achieve by the receiver signal processing step as illustrated in the following figure. Indeed in this step, first satellites transmit signals with modulated codes whose chip transitions are synchronized with the satellite atomic frequency standard. Then the receiver measures the signal propagation time through correlation of the incoming signal with another replica code copy generated with respect to the receivers own oscillator. The tracking function of the receiver has the function to continually update the best estimate of the propagation delay by tracking the correlation peak.

Since the correlation process involves two input signals generated with reference to different oscillators (satellite and receiver) which are not synchronized, a deviation between “satellite time” and “receiver time” will appear in the propagation time measurement. A pseudorange measurement expressed in meters is obtained by multiplying this propagation time by the propagation velocity c.

However, this pseudorange measurement is also impacted by several error sources within the three segments (space, control, and user) such as:

- Delays induced by the propagation of the signal through the atmosphere
- Multipath
- Receiver errors and in particular thermal noise
- Satellite orbit and clock errors
- Inter-frequency and inter-code biases
- Relativist effects
- Signal deformation
- Interference
- Antenna group delay variations as a function of arrival angle

The following figure illustrates the main processing steps to get the final measurements used to compute a position in GNSS receiver.

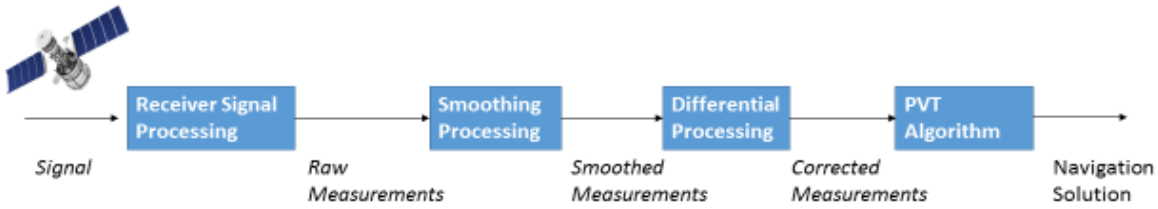

Figure 9-GBAS processing scheme

Then, in the following sections these different quantities are presented and the error models used to represent the impact of errors affecting GNSS signals are detailed.

First, assuming the receiver signal processing step already realized, the models used for the raw measurement are described. Then, the models used to represent the errors affecting the measurements used with GPS/GALILEO standalone are presented as well as several measurement processing models applied for GPS/GALILEO standalone. The differential processing concept is detailed with a further analysis about GBAS case and finally the methodology to obtain the navigation solution is explained.

3.2.1 Raw Measurements

After having received the signal and processed it as mentioned in the introduction of this section, the receiver makes two main measurements named code pseudorange and carrier phase measurements. This last measurements is integrated Doppler frequency shift measurement.

These measurements made by a single frequency receiver u for a given satellite i at epoch k can be modelled respectively as [29]:

$$\rho^i(k) = r^i(k) + c\left(\Delta t_u(k) - \Delta t^i(k)\right) + c\left(I^i(k) + J^i(k)\right) + n_\rho^i(k)$$

Equation 5 - Code pseudorange measurement model

$$\phi^i(k) = r^i(k) + c\left(\Delta t_u(k) - \Delta t^i(k)\right) - c\left(I^i(k) - J^i(k)\right) + \lambda N^i + n_\phi^i(k)$$

Equation 6 -Carrier phase measurement model

Where ρ^i and ϕ^i define respectively the code pseudorange and the carrier phase measurements (both in meters), r^i represents the geometrical distance between the receiver and the satellite i. c is the speed of light in vacuum which is multiplied by the delay of receiver clock Δt_u and the delay of the satellite clock Δt^i. Atmospheric propagation delays such as ionospheric and tropospheric delays are denoted respectively I^i and J^i (both in seconds). Then, λ is the carrier wavelength and N^i is the carrier phase measurement ambiguity which is assumed to be constant over time . Terms denoted n_ρ^i and n_ϕ^i are respectively the code and carrier phase thermal noise and multipath propagation errors.

Indeed, followings parts mainly reminds some models used for error affecting measurements. Then a section dealing on measurement processing 3.2.3.3, introduces the differential measurement model and more particularly the GBAS measurement model.

3.2.2 Measurement Error Model

As mentioned in the previous section, both code and phase measurements are affected by several errors. They need to be modelled in order to correct in the most efficient way these measurements and to quantify performances. Models of each component affecting them are detailed in this section.

3.2.2.1 Satellite Ephemeris and Clock Errors

3.2.2.1.1 Satellite Ephemeris Error

A satellite ephemeris error with a component in the Line-Of-Sight (LOS) direction will induce an error in the estimation of the geometric range between the satellite and the user at each iteration in the least squares position estimation procedure 3.3.1.

The model for satellite position estimation based on the broadcast ephemeris is briefly reminded [47] and it highlights the possible impact of the different terrestrial reference frames on the satellite position estimation. As mentioned in [47], the time of transmission ($\widehat{t^i}$)shall be determined before computing the satellite position (which is useful for building the geometry matrix in 3.3.1) taking into account the satellite clock error, the relativistic effect, and the instrumental delays.

Reminding results presented in [47], in the context of study of PhD project , only the following equations are relevant and have to be taken into account:

At first for SF users:

	$\widehat{t^i}$
L1 C/A	$t_u - \frac{r^i}{c} - \left(\widehat{\Delta t^i} + \Delta t_{rel} - \tau_{GD} + ISC_{L1,CA}\right)$
L5	$t_u - \frac{r^i}{c} - \left(\widehat{\Delta t^i} + \Delta t_{rel} - \tau_{GD} + ISC_{L5,Q}\right)$
E1	$t_u - \frac{r^i}{c} - \left(\widehat{\Delta t^i} + \Delta t_{rel} - \tau_{BGD15}\right)$
E5a	$t_u - \frac{r^i}{c} - \left(\widehat{\Delta t^i} + \Delta t_{rel} - \left(\frac{f_1}{f_5}\right)^2 \tau_{BGD15}\right)$

Then for Dual frequency users (GPS and/or Galileo) [47] [48] [49]:

	$\widehat{t^i}$
L1CA/L5	$t_u - \frac{r^i}{c} - \left(\widehat{\Delta t^i} + \Delta t_{rel} - \tau_{GD} + \frac{ISC_{L5,Q} - \gamma_{15} ISC_{L1,CA}}{1 - \gamma_{15}}\right)$

E1/E5A	$t_u - \frac{r^i}{c} - \left(\widehat{\Delta t^i} + \Delta t_{rel}\right)$

Where $\widehat{t^i}$ is the time of transmission of the measured signal (in GPS time), r^i is the geometric range, t_u is the reception time of the measurement (in receiver time), $\widehat{\Delta t^i}$ is the satellite clock correction, Δt_{rel} is the relativistic effect correction, τ_{GD} is the instrumental delay correction, ISC is the inter-signal correction (for GPS L1C/A, L5) $ISC_{Li,x} = \tau_{L1,PY} - \tau_{Li,x}$ (L1PY is taken as a reference for ISC computation), τ_{BGD15} is the broadcast group delay (for Galileo E1-E5a). And $\gamma_{ij} = \frac{{f_{Li}}^2}{{f_{Lj}}^2}$ and $\tau_{GD} = ISC_{L2,PY}/1 - \gamma_{12}$ (L1PY and L2PY iono-free combination is taken as a reference for TGD computation)

Then, GPS satellite position coordinates in ECEF (WGS84) at $\widehat{t^i}$ are computed from the broadcast orbit model according to Table 20 in [1]. The refined frame WGS84(G1150) was introduced in 2002, which agrees with ITRF2000 at the centimetre level .Galileo satellite position coordinates in GTRF at $\widehat{t^i}$ are computed according to Table 7.3 in [50] (same equations than for GPS but few differences in constants definition). Although different reference frames are used between GPS and Galileo, the Galileo requirements state that the three-dimensional differences of the position compared to the most recent ITRF should not exceed 3 cm (2-sigma).

An error in the broadcast ephemeris which can be denoted $\Delta \boldsymbol{r_u^i}$, including differences between terrestrial reference frames (explained above), will lead to an error in the satellite position ($\Delta \boldsymbol{x^i}$) which will yield to an error in the estimation of the geometric range. This error is the projection of the 3-D error onto the Line-Of-Sight (LOS) between the receiver and the satellite **[47]**.

For the GPS case, the error in the satellite position due to broadcast GPS ephemeris error is of the order of a few meters. According to International GNSS Service (IGS) **[51]**, this accuracy is of the order of 1m at 1-σ and according the GPS SPS specifications **[33]** about the error budget for the L1 C/A code UERE, the contribution of this error is about 2m at 95%,The accuracy of the Galileo ephemeris was investigated in the specialized subtask (ST 3.3.4) of the SESAR project **[11]** and is expected to be similar to GPS.

The ephemeris error and the effect of different terrestrial reference frames have a high temporal and spatial correlation and the range error due to the ephemeris error can be corrected by the ground station corrections as in GBAS (3.1.4.2). The error after differential correction mainly depends on separation between ground station and user. A model for the residual ephemeris error after application of differential corrections was developed in [52] [27]. A bounding relationship between 3-D satellite orbit error was defined as:

$$\Delta r_u^i < \frac{b \left\| \Delta x^i \right\|}{r^i}$$

Equation 7 –Bounding between $\Delta \boldsymbol{r_u^i}$ and a 3-D satellite orbit error

Where $\boldsymbol{b}$ is the distance between the ground station and the aircraft and $\boldsymbol{r^i}$ is the true geometric range for satellite i .

3.2.2.1.2 Satellite Clock Error

The atomic clocks of the satellites contain both noise and drift errors that have a direct impact on the observations as shown in the code and phase measurement models in Equation 5 and Equation 6. The broadcast ephemerides include a second order polynomial used to evaluate the satellite clock errors. The model is the same for both GPS and Galileo but with different time scales. This estimated satellite clock correction $\widehat{\Delta t^i}$ for the satellite i is given by the equation below [47]:

$$\widehat{\Delta t^i} = \boldsymbol{a_0} + \boldsymbol{a_1}(\boldsymbol{t} - \boldsymbol{t_{toc}}) + \boldsymbol{a_2}(\boldsymbol{t} - \boldsymbol{t_{toc}})^2$$

Equation 8 - Estimated satellite clock correction

Where t represents the time of transmission from the satellite i and in the appropriate reference system (GPS time or GST) and t_{toc} the reference time of the clock model in the time reference system (GPS time or GST). Parameters a_0, $a_1$and a_2 are respectively the satellite clock bias, drift and drift-rate according to the valid satellite ephemeris. Their values are respectively in the order of 10^{-3}seconds, 10^{-11}seconds/second and 0 seconds/seconds² [53].

The remaining clock error can be characterized by a Gauss-Markov process [47](or random walk). During the validity time of the model (approximatively 2h), the accuracy of the model is of few meters according IGS and GPS SPS [51] [33].This error is fully spatially correlated and highly correlated in time. Therefore, in GBAS (3.1.4.2) these correlations can be captured by the pseudorange corrections (PRC described in 3.2.3.3.2), which accounts for the spatial correlation, and the range rate correction (RRC described in 3.2.3.3.2), which accounts for the temporal variation of the error due to the latency of the corrections [47].

The model is the same for both GPS and Galileo. However, they assume different time scales. Therefore, in order to take into account the different time scale, in case of multi constellations use, Galileo satellites broadcast the GGTO [47] (GPS to Galileo time offset) model which consists in a first order polynomial. In this PhD project, as assumed in the SESAR project, the GGTO is not used, instead a fifth state is estimated in the Navigation Solution as described in3.3.1.

3.2.2.2 Ionospheric delay

The ionosphere is a dispersive medium which is located between 60 km and 1000 km above the earth's surface, in the atmosphere. In this area ultraviolet rays coming from the sun ionize a portion of gas molecules and thus, releases free electrons which have an influence on the propagation of electromagnetic waves such as GNSS signals [54]. Indeed, phenomena such as reflection, refraction, dispersion or diffraction can appear during this signal propagation. But some frequencies are more vulnerable than others. For example, signal with a frequency

superior to $1MHz$ will be able to cross the ionosphere and signal with frequencies under $1MHz$ will be reflected in the ionosphere [55].

Therefore concerning GNSS signals without reflection phenomena (L-Band frequencies are superior to $1GHz$) propagation velocity through the ionosphere depends on their frequency and the Total Electron Content (TEC, in e/m2) integrated along the signal path. It represents the number of free electrons in a 1 m² column along the LOS. It can be modelled as [54]:

$$TEC = \int_{signal\ path} N_e . dS$$

Equation 9 – TEC expression

With N_e the local electron density expressed in units of electron per cubic meters and dS is the length of the signal path.

With the TEC expression, the ionospheric group delay can be approximated at the first order as [54]:

$$I_P \approx \frac{40.3}{f^2} TEC \quad m$$

Equation 10 – First order approximation of the group delay

The ionospheric delay is the one of the most challenging source of error in civil aviation applications (could be multipath in urban environment) and it is difficult to model accurately. Thanks to frequency dependency shown in Equation 10 (more details given in following section 3.2.3.2.4), its effects on GNSS measurements can be partially removed when dual frequency measurements are available.

Unfortunately for single frequency users, this first order approximation of the group delay in Equation 10 is not sufficient to model the total ionospheric delay, but some algorithms exist to model it more precisely according the GNSS used.

In the case of GPS, the model specified in [56] or [57] is called the Klobuchar algorithm. This model is known to reduce the root mean square of the total ionospheric error by roughly a half.

In the case of GALILEO, a more recent model should be used which is called the Nequick algorithm [58]. It is expected to have better performance than Klobuchar algorithm correcting for 70% of the ionospheric delay when operating on E5a, E5b, and E1 frequencies [59].

For both models, a trade-off has to be found between the percentage ionospheric correction and the complexity of the computations required. The following table which summarizes the two models main characteristics extracted from [60] can be used to select the more appropriate.

	Klobuchar	NeQuick
Model type	Single layer model	Electron density model
Percentage of ionospheric error estimated over the world during one year	50% of the error estimated	70% of the error estimated
Iono effect covered	Ionospheric delay	Ionospheric delay
Constellation concerned	GPS	Galileo
Accuracy	Long term (> 1 year)	Seasonal (4 months)
Seasonal variations	No	Yes
Large scale spatial variations	Medium	Good except near the Equator
Reactivity	Iono parameters broadcasted every 12.5 minutes Iono information updated once a day (best case) Every 6 days (worst case)	Iono parameters broadcasted every 1.64 seconds in F/NAV message and every 0.328 seconds in I/NAV message Iono coefficients updated by ground segment every 24 hours Disturbance flags updated by ground segment every 100 minutes
Complexity	Simple cosine function: low complexity	Epstein formulation of different layers and seasonal variations, sunspots number: high complexity

Table 9-Comparison between Klobuchar and Nyquist models

In the SBAS case, the chosen option is to use a grid-based model [38] for enabling the estimation of the ionospheric delay.

Finally for the GBAS case, more information about the chosen model is given in Chapter 4.

3.2.2.3 Tropospheric delay

Troposphere is a non-dispersive medium for L-band signals (dispersive above 15GHz) which means that its effects does not depend on the GNSS signal frequencies. It is the lowest part of the Earth's atmosphere and it is composed of dry gases and water vapour. These two elements have an impact on the signal propagation velocity

which results in range errors for pseudorange measurements. Water vapour density varies widely with position and time and is difficult to predict.

The Slant Tropospheric Delay (STD) for a satellite signal received at any elevation angle can be computed by using following equation defined in [61] and [62]:

$$STD = 10^{-6} \int N ds$$

Equation 11-STD

Where N defines the refractive index and ds is the differential form of path length over which the integration is performed. The integration is over the entire signal path length, although the tropospheric delay is obviously understood to be zero for the path outside the troposphere.

The impact of the propagation of GNSS signals through troposphere can be modelled as defined in standards. The model used in civil aviation GPS receivers to correct the tropospheric delay can be found in [63]. Moreover, for civil aviation GALILEO receivers, it is specified in [64] that the GALILEO receiver shall apply a tropospheric correction which is at least as good as the one defined in [63].Consequently, this model is a reference for both GPS and GALILEO receivers.

Since tropospheric delay is a local phenomenon, according standards [63] each user shall compute its own tropospheric delay and the one related to the satellite i can be modeled with $\widehat{J^i}$ as [63]:

$$\widehat{J^i} = -\left(d_{hyd} + d_{wet}\right).O(\theta_i)$$

Equation 12 -Model of tropospheric delay related to the satellite i

Where d_{hyd} and d_{wet} are the estimated vertical range delay (i.e. for a satellite at 90° elevation angle) induced respectively by gases in hydrostatic equilibrium and water vapour (in meters), θ_i represents the elevation angle of the satellite i, and $O(\theta_i)$ is a mapping function (also named obliquity factor) that scales the delays to the actual satellite elevation angle

A simplified expression for the mapping function for satellite elevation angle > 4°can be found in [63]

$$O(\theta_i) = \frac{1.001}{\sqrt{0.002001 + \sin^2(\theta_i)}}$$

Equation 13 -Mapping function

It is important to notice that d_{hyd} and d_{wet} are computed from the receiver height and estimates of meteorological parameters as described in [63].

Some other models can be used to model or mitigate the troposphere. Indeed, either empirical approaches exist that derive surface atmospherical parameters and correlate them to tropospheric delays such as Hopfield [65],

Saastamoinen [66] or Ifadis models [67]. Then, advanced models were developed using complex meteorological data (Numerical Weather Models as Arome in 5.2.2.2and Harmonie in 5.2.2.3) such as the one developed by Jan Dousa and presented in [68]. Another methodology is to use some local corrections as in GBAS.

A deeper analysis about this tropospheric delay is done in this report in sections 4.2.1.1.4 and 4.2.2, Chapter 5 and Chapter 6 where more details could be found.

3.2.2.4 Multipath

The impact of multipath on the GNSS signal observables during aircraft approaches is analysed in this section. Indeed, the combination of the direct and reflected signals at the receiver antenna output induces a biased measurements not only representing the direct signal. [22]

For illustration purpose, following figures illustrates the impact of in-phasemultipath on the output of the correlator and on the output of the discriminator (EMLP) (detailed in following section 3.2.2.6)

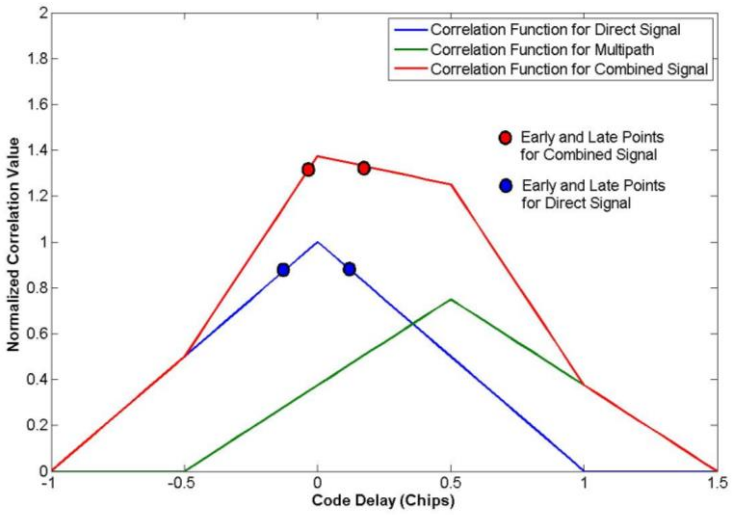

Figure 10-Impact of in phase multipath on the output of the correlator

As it is shown that there is a shift of the early and later points, indeed the symmetry between both positive and negative code delays is not present any more therefore that would have an impact on the measurement error [22]

The impact on the discriminator output which is fed by these previous correlator outputs is represented on the following figure.

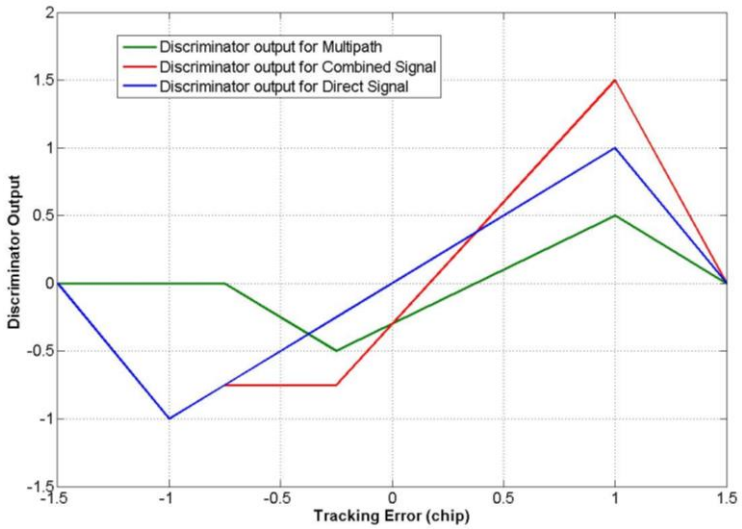

Figure 11-Impact of multipath on discriminator output

As it could be seen by the previous figure, a tracking error will appear at the output of the discriminator by the presence of multipath.

It is important to remark that the multipath error is not symmetric therefore this won't lead to an averaging to zero after smoothing processing (3.2.3.2.)

As shown in the following figure extracted from [69] for L1 C/A signal, raw code tracking error is really impacted by multipath but reduced after the smoothing processing (detailed in 3.2.3.2.)

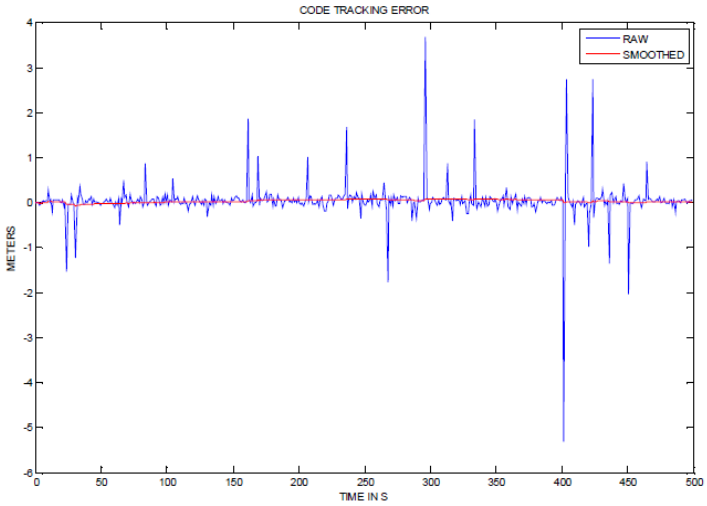

Figure 12-Raw and smoothed tracking error [68]

The multipath modelling is not an easy work because of errors caused by this phenomenon depends on the environment, the antenna and the receiver. Indeed, the geographic environment is very complex to model.

However, different researches as explained in [70] and [71] have been led to compute statistics of the error due to multipath in order to properly taking it into account into the error budgets.

The ICAO adopted a standard curve for GPS L1 C/A code users as defined in SARPs which states the standard deviation of the error due to multipath as a function of the GPS satellite elevation angle [69].This equation curve is presented further in this document dealing with the residual errors (Chapter 4). The work done to validate this standard multipath error expression is described in [70].

The more recent model developed by DLR which enables to determine the impact of multipath on new GNSS signals is the High Resolution Aeronautical Channel model as it is explained in [72].This model can be used to generate three multipath components :

- Path 0: A direct path
- Path 1: A refractive component of the direct path
- Path 2: A strong echo on the fuselage that is changing very slowly
- Path 3: A quickly changing ground echo

Results about this model use have shown that smaller results can be expected for new signals [69].

3.2.2.5 Antenna Group Delay

According the updated MOPS [73], the airborne GPS antennas exhibit biases due to group delays that are function of the signal arrival direction. These errors were not addressed during the GBAS standardization instead they were incorporated into the airborne multipath and noise error budget. In view of the results shown in [73], the group delay errors are much larger than airborne multipath. Furthermore, these group delays are considered bias like errors while multipath is considered noise like, that is why some literature documents [74] worked out this subject and proposed to treat them separately in the aircraft position protection level computation.

3.2.2.6 Noise

As for multipath, it is really difficult to model the receiver noise on pseudorange but some studies [22] had generated the associated correlated noise on the correlator outputs.

The correlator outputs expressions for Early, Late, Prompt In-Phase and Quadra-Phase channels are reminded in the following equation with the Doppler residual considered null assuming that the acquisition is successfully achieved:

$$\begin{cases} I_E(k) = \frac{A}{2}.d(k).\widetilde{K}_c\left(\varepsilon_\tau + \frac{C_s}{2}\right).\cos(\varepsilon_\varphi) + n_{I_E}(k) \\ I_P(k) = \frac{A}{2}.d(k).\widetilde{K}_c(\varepsilon_\tau).\cos(\varepsilon_\varphi) + n_{I_P}(k) \\ I_L(k) = \frac{A}{2}.d(k).\widetilde{K}_c(\varepsilon_\tau - \frac{C_s}{2}).\cos(\varepsilon_\varphi) + n_{I_L}(k) \\ Q_E(k) = \frac{A}{2}.d(k).\widetilde{K}_c(\varepsilon_\tau + \frac{C_s}{2}).\sin(\varepsilon_\varphi) + n_{Q_E}(k) \\ Q_P(k) = \frac{A}{2}.d(k).\widetilde{K}_c(\varepsilon_\tau).\sin(\varepsilon_\varphi) + n_{Q_P}(k) \\ Q_L(k) = \frac{A}{2}.d(k).\widetilde{K}_c(\varepsilon_\tau - \frac{C_s}{2}).\sin(\varepsilon_\varphi) + n_{Q_L}(k) \end{cases}$$

Equation 14-Correlator outputs expressions

Where, $\widetilde{K}_c$ is the correlation function between the locally generated spreading code with the filtered incoming spreading code. $\varepsilon_\varphi = \varphi - \hat{\varphi}$ represents the carrier phase error between the incoming carrier phase φ and the locally generated carrier phase $\hat{\varphi}$, $\varepsilon_\tau = \tau - \hat{\tau}$ is the code delay error between the incoming code delay τ and the locally generated code delay $\hat{\tau}$and ε_f is the frequency error between the incoming carrier and the locally generated carrier. T_I is the correlation time, C_s is the chip spacing. $n_{I_E}(k)$, $n_{I_P}(k)$, $n_{I_L}(k)$ are respectively the Early, Prompt and Late In-Phase post-correlation thermal noise components and $n_{Q_E}(k)$, $n_{Q_P}(k)$, $n_{Q_L}(k)$ are respectively the Early, Prompt and Late Quadra-Phase post-correlation thermal noise components. These parameters are uncorrelated with In-Phase thermal noise components.

The power of the prompt thermal noise components can be computed as [22] [26]:

$$Var[n_{I_P}] = Var[n_{Q_P}] = \frac{N_0}{4T_I}\beta$$

Equation 15-Power of the prompt thermal noise components

Where $N_0/2$ is the equivalent double-sided thermal noise PSD at the correlator input, $\beta = \int_{-\infty}^{+\infty}|H(f)|^2\,|F_L(f)|^2 df$ is the loss of noise power due to the front-end filter, H is the equivalent front-end filter transfer function and $F_L(f)$ is the Fourier transform of the locally generated code sequence.

Then these values are fed into a code delay discriminator that will them to estimate the code delay tracking error. Two types of discriminator are used in GNSS receiver : The Early-Minus Late Power (EMLP) and the Dot-Product (DP). Further details are given in [22] [26].The error variance of the code tracking loop will depend on the discriminator chosen and are found in [75]:

$$\sigma_{\tau,EMLP} = \sqrt{\frac{B_{DLL}\int_{-B/2}^{B/2} G(f)sin^2(\pi f C_s)df}{\frac{C}{N_0}\left(2\pi\int_{-B/2}^{B/2} fG(f)sin(\pi f C_s)df\right)^2}\left(1 + \frac{\int_{-B/2}^{B/2} G(f)cos^2(\pi f C_s)df}{\frac{C}{N_0}T_{DLL}\left(\int_{-B/2}^{B/2} G(f)cos(\pi f C_s)df\right)^2}\right)}\ (m)$$

Equation 16 – Error Variance for EMLP discriminator

$$\sigma_{\tau,DP} = \sqrt{\frac{B_{DLL}\int_{-B/2}^{B/2} G(f)sin^2(\pi f C_s)df}{\frac{C}{N_0}\left(2\pi\int_{-B/2}^{B/2} fG(f)sin(\pi f C_s)df\right)^2}\left(1+\frac{1}{\frac{C}{N_0}T_{DLL}\left(\int_{-B/2}^{B/2} G(f)df\right)}\right)}\ (m)$$

Equation 17- Error Variance for DP discriminator

Where B is the RF front-end filter bandwidth (Hz), C the received signal power over infinite signal bandwidths (W), N_0 represents the power spectral density of the noise (W/Hz), $G(f)$ is the power spectral density of the processed signal, T_{DLL} is the coherent integration time of the DLL (s), Δ is the chip spacing (s) and B_{DLL} is the DLL filter bandwidth (Hz).

The following typical parameterization can be used for nominal cases as expressed in [26]:

	GPS L1	GPS L5	GALILEO E1	GALILEO E5A
B (MHz)	4	24	10	24
T_{DLL} (ms)	20	20	100	100
B_{DLL} (Hz)	1	1	1	1
Cs (chip)	0.2	0.25	0.2	0.25
C/N_0(dBHz)	35	29	36.5	29.7

Table 10-Parameters for DLL tracking error variance computation

Note that the worst (minimum) C/N_0 are given from [64] and are not typical values.

In this section another phenomenon is presented: The Interference phenomenon. It is defined as any undesired signal that interferes with the reception of radio waves and can be interpreted as noise. Low power levels used in GNSS leave aircraft susceptible to unintentional interference in their frequency bands. Even if a large number of mitigation techniques have been investigated to improve the performance of the GNSS receivers, civil aviation system may remain vulnerable. Some of interference can be intentional to GNSS signals, it is called jamming. The method of digital beam-steering could be used at ground and airborne installations in order to protect against intentional and unintentional jamming. This phenomenon can be considered as Carrier wave interference.

Indeed, the three main unintentional interferences are:

- Carrier Wave interference which is a sinusoidal waveform with a high power which can be harmful to GNSS receivers when it is located close to the central frequency of the GNSS signals.
- Wideband interferences which are modelled as white noise with limited bandwidth.

- Pulsed interferences which are provoked by equipment that are already radiating in L5 band and which are DME/TACAN on E5a and Radars on E5b for example.

If combined with the received useful signal, some interfering signal may have the following three impacts on measurements: [32]

- Some additional noise affects the measurements
- A bias affects one or several measurements
- Some or all of the measurements are no longer available

This section has presented some error modelling but measurement processing exists which can mitigate them. Therefore the following section presents some of them for both Single Frequency and Dual Frequency cases applied to standalone systems and also differential systems.

3.2.3 Measurement Processing *4

3.2.3.1 Introduction

This section presents the particular measurement processing techniques of GBAS utilising the observables [29] presented in section 3.2.1 and the fact that error such as ionospheric delay has a frequency dependency. These techniques are employed in other GNSS systems and applications. For simplifying notations, the following measurement model is used in this section

$$\rho = r + b + J + \iota + \eta_\rho$$

Equation 18- Simplified code measurement

$$\phi = r + b + J - \iota + N + \eta_\phi$$

Equation 19- Simplified phase measurement

Where r is the geometric range, ρ is the code pseudorange measurement, ι is the ionospheric delay, J is the tropospheric delay, b is the satellite clock error, η_ρ is the code-tracking noise and multipath, ϕ is the carrier-phase measurement, N is the range ambiguity and $\eta_\phi$is the carrier-tracking noise and multipath

In these simplified measurement models, the receiver clock error is not represented because it has no impact on the position state (common errors are included in the estimated clock bias).

Figure 8 illustrates the GBAS processing which leads to the observables used to compute a position in the GBAS airborne receiver. The inputs of this processing are defined below in following sections.

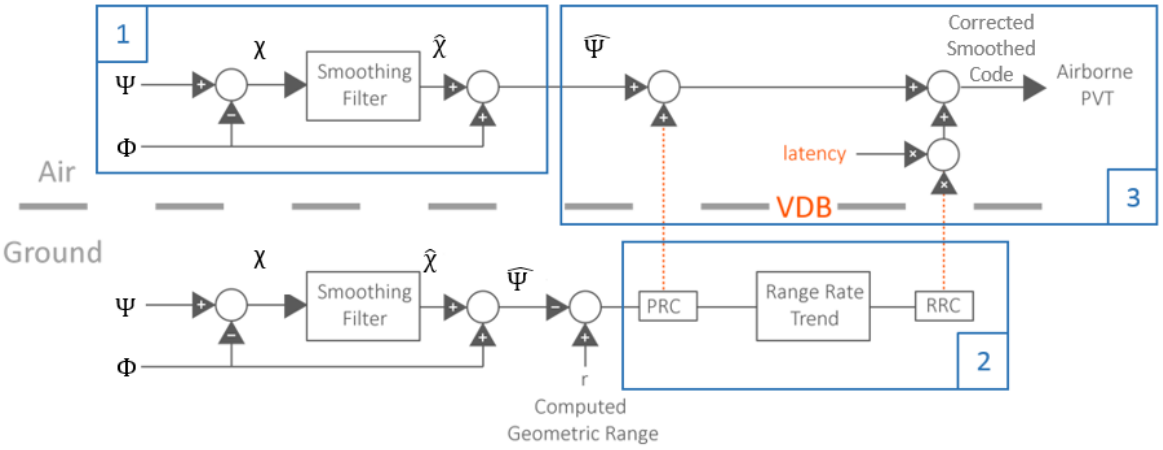

Figure 13-Differential Measurement Processing

In this figure, Φ represents the carrier phase observable, Ψ represent the code observable. Then χ denotes the Code-Minus Carrier observable usually denoted CMC which is presented in 3.2.3.2, then the smoothing filter output named the smoothed CMC is denoted $\hat{\chi}$ and finally $\widehat{\Psi}$ represents the smoothed code observable. All these parameters are detailed below in further sections.

The first box which is identical for ground and aircraft, corresponding to the smoothing processing is explained in a first section 3.2.3.2. Then the second box, representing the Pseudo Range Correction and the Range Rate Correction computed at ground is detailed in the second part of this section. Finally, the last box dealing with the differential processing properly is described with the particular case of GBAS.

3.2.3.2 Smoothing Processing

3.2.3.2.1 Introduction

The smoothing process, also named code-carrier smoothing is a method used to reduce the impact of code noise and multipath on the measurements. It can be used either in single frequency receivers or in dual frequency receivers. In order to achieve this, a complementary filter is used as presented below.

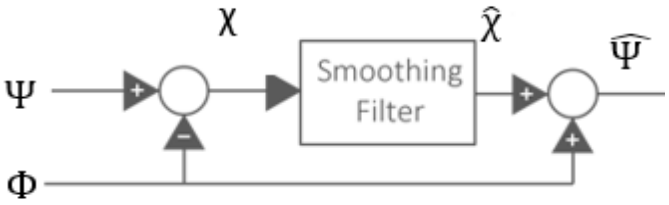

Figure 14-Carrier Smoothing Block Diagram

The carrier smoothing filter takes the Code-Minus Carrier observable usually denoted CMC (denoted χ) as inputs, using the small changes in carrier phase (denoted Φ) to remove the large noise components from the code (denoted Ψ). At the output, the smoothed CMC (denoted $\hat{\chi}$) is then recombined with the phase measurement to obtain the smoothed code (denoted $\widehat{\Psi}$).

This CMC observable can be expressed through the following equation (by using simplified models from Equation 18 and Equation 19:

$$\chi = \Psi - \Phi = 2\iota - N + \eta_\rho - \eta_\phi$$

Equation 20-CMC observable model

The smoothing filter is applied in the discrete time domain, known as the *Hatch filter* and is described in 3.2.3.2.2 but may also be understood from the perspective of continuous time and subsequent transformation into the Laplace domain, in order to simplify the filter theory, as described in 3.2.3.2.3

3.2.3.2.2 Time domain Filter Model

The discrete time model form for the *Hatch filter* is given below [76]. The input variables in this form are the current code measurement, current and previous phase measurements and the smoothed code filter output from the previous epoch. The performance of the filter depends on the time interval between measurements and the smoothing time constant.

$$\widehat{\boldsymbol{\Psi}}_{\boldsymbol{k}} = \frac{\boldsymbol{T}}{\boldsymbol{\tau}}\boldsymbol{\Psi}_{\boldsymbol{k}} + \left(\mathbf{1} - \frac{\boldsymbol{T}}{\boldsymbol{\tau}}\right)\left(\widehat{\boldsymbol{\Psi}}_{\boldsymbol{k-1}} + \boldsymbol{\Phi}_{\boldsymbol{k}} - \boldsymbol{\Phi}_{\boldsymbol{k-1}}\right)$$

Equation 21 - Time Domain filter equation

Where the index k represents the epoch of application of this time model by using observables described in previous section 3.2.3.2.1, T represents the sample interval (time between epochs) and τ, the smoothing time. Finally, the filter initialisation value is $\widehat{\Psi}_0$ and set to equal to Ψ_0 at t_0.

According to [42], if the filter is defined as a variant filter, during the first τ seconds since filter starts the smoothing filter $\frac{T}{\tau}$ is equal to the sample interval T in seconds divided by the time in seconds since filter initialisation. Therefore the definition for the smoothing time τ is as follows:

$$\boldsymbol{\tau} = \begin{cases} \boldsymbol{\tau_c} & \boldsymbol{if\ t > t_0 + \tau_c} \\ \boldsymbol{t - t_0} & \boldsymbol{if\ t < t_0 + \tau_c} \end{cases}$$

Equation 22 - Smoothing time

where $\tau_c$defines the smoothing time constant (typically 100s for GBAS GAST C and 30s for GBAS GAST D, more details are given in the section 3.2.3.4) and $t_0$represents the filter initialisation time.

Once the smoothed code pseudorange obtained, the smoothed CMC is computed.

Therefore, the CMC denoted χ_k at epoch k (in meters) is define through the following equation:

$$\boldsymbol{\chi_k} = \boldsymbol{\Psi_k} - \boldsymbol{\Phi_k}$$

Equation 23 - CMC

The filter equation may then be rearranged to give the following formula:

$$\widehat{\boldsymbol{\Psi}}_{\boldsymbol{k}} = \frac{\boldsymbol{T}}{\boldsymbol{\tau}}\boldsymbol{\chi}_{\boldsymbol{k}} + \left(\mathbf{1} - \frac{\boldsymbol{T}}{\boldsymbol{\tau}}\right)\widehat{\boldsymbol{\chi}}_{\boldsymbol{k-1}} + \boldsymbol{\Phi}_{\boldsymbol{k}}$$

Equation 24 - Filter Equation modified

With $\widehat{\Psi}_k = \hat{\chi}_k + \Phi_k$

Where χ_k is the CMC (in meters) at epoch k and $\hat{\chi}_k$ represents the smoothed CMC (in meters) at epoch k.

The recursive filter Equation 21 can be reformulated in an explicit way (with k ≥ 1):

$$\widehat{\boldsymbol{\Psi}}_{\boldsymbol{k}} = \frac{\boldsymbol{T}}{\boldsymbol{\tau}}\sum_{\boldsymbol{n=1}}^{\boldsymbol{k}}\left(\left(\mathbf{1} - \frac{\boldsymbol{T}}{\boldsymbol{\tau}}\right)^{\boldsymbol{k-n}}(\boldsymbol{\Psi}_{\boldsymbol{n}} - \boldsymbol{\Phi}_{\boldsymbol{n}})\right) + \left(\mathbf{1} - \frac{\boldsymbol{T}}{\boldsymbol{\tau}}\right)^{\boldsymbol{k}}\left(\widehat{\boldsymbol{\Psi}}_{\mathbf{0}} - \boldsymbol{\Phi}_{\mathbf{0}}\right) + \boldsymbol{\Phi}_{\boldsymbol{k}}$$

Equation 25 - Filter equation reformulated

It could be relevant to remark that for large values of k the term $\left(1 - \frac{T}{\tau}\right)^k \left(\widehat{\Psi}_0 - \Phi_0\right)$ becomes close to zero and can be neglected.

In the single frequency case: $\Psi = \rho$ and $\Phi = \phi$ so by substituting the observables Ψ and Φ in Equation 25 with the notations given in the measurement model leads to:

$$\widehat{\boldsymbol{\Psi}}_{\boldsymbol{k}} \approx \frac{\boldsymbol{T}}{\boldsymbol{\tau}}\sum_{\boldsymbol{n=1}}^{\boldsymbol{k}}\left(\left(\mathbf{1} - \frac{\boldsymbol{T}}{\boldsymbol{\tau}}\right)^{\boldsymbol{k-n}}\left(\mathbf{2}\boldsymbol{\iota}_{\boldsymbol{n}} + \boldsymbol{\eta}_{\boldsymbol{\Psi}_{\boldsymbol{n}}} - \boldsymbol{N} - \boldsymbol{\eta}_{\boldsymbol{\Phi}_{\boldsymbol{n}}}\right)\right) + \boldsymbol{r}_{\boldsymbol{k}} + -\boldsymbol{\iota}_{\boldsymbol{k}} + \boldsymbol{J}_{\boldsymbol{k}} + \boldsymbol{b}_{\boldsymbol{k}} + \boldsymbol{N} + \boldsymbol{\eta}_{\boldsymbol{\Phi}_{\boldsymbol{k}}}$$

$$= \boldsymbol{r}_{\boldsymbol{k}} + \boldsymbol{J}_{\boldsymbol{k}} + \boldsymbol{b}_{\boldsymbol{k}} + \boldsymbol{\iota}_{\boldsymbol{k}} + \boldsymbol{N} + \boldsymbol{\eta}_{\boldsymbol{\Phi}_{\boldsymbol{k}}} + \frac{\boldsymbol{T}}{\boldsymbol{\tau}}\sum_{\boldsymbol{n=1}}^{\boldsymbol{k}}\left(\left(\mathbf{1} - \frac{\boldsymbol{T}}{\boldsymbol{\tau}}\right)^{\boldsymbol{k-n}}\left(\boldsymbol{\eta}_{\boldsymbol{\Psi}_{\boldsymbol{n}}} - \boldsymbol{N} - \boldsymbol{\eta}_{\boldsymbol{\Phi}_{\boldsymbol{n}}}\right)\right) + \mathbf{2}\left[\frac{\boldsymbol{T}}{\boldsymbol{\tau}}\sum_{\boldsymbol{n=1}}^{\boldsymbol{k}}\left(\left(\mathbf{1} - \frac{\boldsymbol{T}}{\boldsymbol{\tau}}\right)^{\boldsymbol{k-n}}\boldsymbol{\iota}_{\boldsymbol{n}}\right) - \boldsymbol{\iota}_{\boldsymbol{k}}\right]$$

Equation 26 - SF smoothed code

The last term in this equation is the Ionospheric divergence error introduced by the smoothing process. Since the Ionospheric error rate $\delta\iota$ under nominal ionosphere conditions changes slowly compared to the filter time constant, it can be assumed [47] constant so that with $\iota_k = \iota_n + (k-n)T\delta\iota$ the nominal divergence error can be approximated as [47]:

$$2\left[\frac{T}{\tau}\sum_{n=1}^{k}\left(\left(1 - \frac{T}{\tau}\right)^{k-n}\iota_n\right) - \iota_k\right] \approx -2\delta\iota(\tau - T)$$

Equation 27 - Nominal divergence error

Furthermore, it is relevant to notice here that terms relative to ambiguity N will be totally removed through this smoothing process regarding the Equation 26. Indeed, the smoothing filter will have no impact on the range ambiguity and when the smoothed code is formed the ambiguity term will be removed.

Concerning the smoothed multipath and noise, the following statistical models is assumed for both code and phase terms (with known variances):

$$\eta_{\Psi} \sim N\left(0, \sigma^2_{\eta_{\Psi}}\right) \sim N\left(0, \sigma^2_{\eta_{\rho}}\right)$$

Equation 28 - Code Statistical model

$$\eta_{\Phi} \sim N\left(0, \sigma^2_{\eta_{\Phi}}\right) \sim N\left(0, \sigma^2_{\eta_{\phi}}\right)$$

Equation 29 -Phase Statistical model

Assuming no inter-epoch correlations for the code and phase noise terms, the variance limit in filter steady state results by analysing the Equation 25 as:

$$\sigma^2_{\hat{\Psi},limit} = \frac{T}{2\tau - T}\sigma^2_{\Psi} + 2\frac{(\tau - T)^2}{\tau(2\tau - T)}\sigma^2_{\Phi}$$

Equation 30 - Code and Phase Variance limit

According [77], assuming $\tau \gg T$, the contribution of the phase term is negligible and the noise variance limit can then be approximated by :

$$\sigma^2_{\hat{\Psi},limit} \approx \frac{T}{2\tau}\sigma^2_{\Psi} \approx \frac{T}{2\tau}\sigma^2_{\rho}$$

Equation 31 - Code and phase variance limit approximation

3.2.3.2.3 Laplace domain Filter Model

For the sake of simplicity, the smoothing filter described in previous section is often assumed to be a first order low pass filter acting on continuous time signals presented in previous Figure 14.

The transfer function of this first order low pass filter is as follows:

$$\boldsymbol{F(s)} = \frac{\mathbf{1}}{\boldsymbol{\tau s} + \mathbf{1}}$$

Equation 32 - Laplace filter

Where τ represents the smoothing time constant and s is the Laplace variable

The smoothed CMC is given in that case by applying this transfer function as:

$$\hat{\boldsymbol{\chi}} = \boldsymbol{F\chi}$$

Equation 33 - Laplace smoothed CMC

This approach enables a simple representation of the impact of the filter on the measurement model components, in particular, how the errors react to the filter.

For the single frequency measurement models illustrated before, a model for the CMC variable is obtained:

$$\boldsymbol{\chi = 2\iota - N + (\eta_{\Psi} - \eta_{\Phi})}$$

Equation 34 - SF CMC

So the smoothed CMC variable can be obtained and given:

$$\boldsymbol{\hat{\chi} = 2F\iota - N + F(\eta_{\Psi} - \eta_{\Phi})}$$

Equation 35 - SF smoothed CMC

It is important to note that in this case a steady state is assumed such that transient terms as a result of the phase ambiguity have decayed. Finally the smoothed code pseudorange may then be expressed as:

$$\boldsymbol{\hat{\Psi} = r + (2F - 1)\iota + J + b + F\eta_{\Psi} + (1 - F)\eta_{\Phi}}$$

Equation 36- SF smoothed code

Sereral notations are introduced for clarification. $I = (2F - 1)\iota$ and $\epsilon = F\eta_{\Psi} + (1 - F)\eta_{\Phi}$ are respectively the smoothed ionospheric term and the smoothed noise term (noise and multipath).

These terms are introduced in the Equation 36

$$\hat{\Psi} = r + J + b + I + \epsilon = r + J + b + 2(F - 1)\iota + \epsilon$$

Equation 37 - SF smoothed code simplified

It is relevant to notice that the the ionospheric divergence error introduced by the smoothing process is approximately given by [47] (see also Equation 27):

$$2(F - 1)\iota \approx -2\delta\iota(\tau - T)$$

Equation 38 - Ionospheric divergence error

3.2.3.2.4 Dual Frequency

In this section the smoothing technique is presented for dual frequency users. This dual-frequency processing takes the advantage of dual frequency measurements to remove partially or totally the effect of the ionosphere.

Two main techniques are presented in this section: the Divergence-free (D-free) smoothing and the Ionosphere-free (I-free) smoothing [77]. Both use the same concept as for single frequency presented above but with different inputs for the smoothing filter. The D-free smoothing presents the advantage of keeping the noise as same level as for single frequency case but the disadvantage of not removing totally the ionosphere effect. Whereas the I-free technique removes totally the ionosphere effects but an increasing of the noise compared to SF case appears.

3.2.3.2.4.1 Divergence-free

This section presents the processing models for D-Free processing. In this PhD project, the measurements used by the ground receivers are the L1 C/A (or L1C) and L5 code pseudorange from the GPS constellation and the E1 and E5a code pseudorange from the Galileo constellation, both denoted ρ_1 for the L1 or E1 and ρ_5 for L5 or E5a and ϕ_1 and ϕ_5 for carrier phase measurements respectively.

The code pseudorange and carrier phase measurements models are given below reminding the Equation 18 and Equation 19 :

$$\rho_1 = r + b + J + \iota_1 + \eta_{\rho_1}$$

Equation 39- Code Pseudorange Measurement L1/E1

$$\phi_1 = r + b + J - \iota_1 + N_1 + \eta_{\phi_1}$$

Equation 40 - Carrier Phase Measurement L1/E1

$$\phi_5 = r + b + J - \iota_5 + N_5 + \eta_{\phi_5}$$

Equation 41 - Carrier Phase Measurement L5/E5a

Due to the fact that the ionospheric delay being proportional to the inverse square root of the frequency such as :

$$i = \frac{K}{f^2}$$

Equation 42- Relation between ionospheric delay and frequency

This previous equation is an approximation as higher order terms exist but are smaller than 5cm.

The following equation is derived

$$\boldsymbol{i_1 - i_5 = \left(1 - \frac{{f_1}^2}{{f_5}^2}\right) i_1 \equiv \alpha i_1}$$

Equation 43 - Relation between ionospheric delays L1/L5

The inputs to the D-free smoothing filter Ψ_{DFree1} and Φ_{DFree1} (lead by L1 in this derivation but could equivalently by replaced by L5) are then defined by:

$$\Psi_{DFree1} = \rho_1$$

$$\Phi_{DFree1} = \phi_1 - \frac{2}{\alpha}(\phi_1 - \phi_5) = r + b + J + \iota_1 - N_{DFree1} + \eta_{DFree1}$$

Equation 44 - Inputs of D-Free filter

where

$$N_{DFree1} = N_1 - \frac{2}{\alpha}(N_1 - N_5)$$

$$\eta_{DFree1} = \eta_{\phi 1} - \frac{2}{\alpha}(\eta_{\phi 1} - \eta_{\phi 5})$$

The ground receivers perform CMC smoothing as described in section 3.2.3.2. The smoothed D-Free code pseudorange is computed as follows (at epoch k):

$$\widehat{\boldsymbol{\Psi}}_{\boldsymbol{DFree1_k}} = \frac{\boldsymbol{T}}{\boldsymbol{\tau}}\boldsymbol{\Psi}_{\boldsymbol{DFree1_{k-1}}} + \left(\mathbf{1} - \frac{\boldsymbol{T}}{\boldsymbol{\tau}}\right)\left(\widehat{\boldsymbol{\Psi}}_{\boldsymbol{DFree1_{k-1}}} + \boldsymbol{\Phi}_{\boldsymbol{DFree1_k}} - \boldsymbol{\Phi}_{\boldsymbol{DFree1_{k-1}}}\right)$$

Equation 45 - Smoothed DFree code

The resulting smoothed pseudorange is then derived as for single frequency case in section 3.2.3.2 and the following result is obtained :

$$\widehat{\boldsymbol{\Psi}}_{\boldsymbol{DFree1}} = \boldsymbol{r} + \boldsymbol{b} + \boldsymbol{J} + \boldsymbol{\iota_1} + \boldsymbol{\epsilon_{DFree1}}$$

Equation 46 - Resulting smoothed Dfree pseudorange

With the notation:

$$\epsilon_{DF1} = F\eta_{\rho_1} + (1 - F)\eta_{DFree1}$$

3.2.3.2.4.2 Ionosphere free

This section presents the processing models for I-Free processing. As for D-free case, the measurements used by the ground receivers are the L1 C/A (or L1C) and L5 code pseudorange from the GPS constellation and the E1 and E5a code pseudorange from the Galileo constellation, both denoted ρ_1 for the L1 or E1 and ρ_5 for L5 or E5a and ϕ_1 and ϕ_5 for carrier phase measurements respectively.

The code pseudorange and carrier phase measurements models are given below reminding the Equation 18 and Equation 19

$$\rho_1 = r + b + J + \iota_1 + \eta_{\rho_1}$$

Equation 47- Code Pseudorange Measurement L1/E1

$$\rho_5 = r + b + J + \iota_5 + \eta_{\rho_5}$$

Equation 48- Code Pseudorange Measurement L5/E5a

$$\phi_1 = r + b + J - \iota_1 + N_1 + \eta_{\phi_1}$$

Equation 49 - Carrier Phase Measurement L1/E1

$$\phi_5 = r + b + J - \iota_5 + N_5 + \eta_{\phi_5}$$

Equation 50 - Carrier Phase Measurement L5/E5a

By using the relation Equation 43, the inputs to the I-Free smoothing filter are then defined as:

$$\Psi_{IF} = \rho_1 - \frac{1}{\alpha}(\rho_1 - \rho_5) = r + b + J + \eta_{\Psi IF}$$

$$\Phi_{IF} = \phi_1 - \frac{1}{\alpha}(\phi_1 - \phi_5) = r + b + J + N_{IF} + \eta_{\Phi IF}$$

Equation 51- Inputs of I-free filter

Where:

$$\eta_{\Psi IF} = \eta_{\rho 1} - \frac{1}{\alpha}\left(\eta_{\rho 1} - \eta_{\rho 5}\right)$$

$$\eta_{\Phi IF} = \eta_{\phi 1} - \frac{1}{\alpha}\left(\eta_{\phi 1} - \eta_{\phi 5}\right)$$

$$N_{\mathrm{IF}} = N_1 - \frac{1}{\alpha}(N_1 - N_5)$$

Then, ground receivers perform CMC as described in section 3.2.3.2. The smoothed I- Free observable is computed as follows (at epoch k):

$$\widehat{\boldsymbol{\Psi}}_{\boldsymbol{IF_k}} = \frac{\boldsymbol{T}}{\boldsymbol{\tau_G}}\boldsymbol{\Psi}_{\boldsymbol{IF_{k-1}}} + \left(\mathbf{1} - \frac{\boldsymbol{T}}{\boldsymbol{\tau_G}}\right)\left(\widehat{\boldsymbol{\Psi}}_{\boldsymbol{IF_{k-1}}} + \boldsymbol{\Phi}_{\boldsymbol{IF_k}} - \boldsymbol{\Phi}_{\boldsymbol{IF_{k-1}}}\right)$$

Equation 52 - Smoothed I-free code

The resulting smoothed pseudorange is then derived as for single frequency case in section 3.2.3.2 and the following result is obtained :

$$\widehat{\boldsymbol{\Psi}}_{\boldsymbol{IF}} = \boldsymbol{r} + \boldsymbol{b} + \boldsymbol{J} + \boldsymbol{\epsilon}_{\boldsymbol{IF}}$$

Equation 53 - Resulting smoothed I-free code

With the notation:

$$\epsilon_{IF} = F\eta_{\Psi IF} + (1 - F)\eta_{\Phi IF}$$

3.2.3.3 *Differential Processing* *[5]

This concept of differential processing is illustrated by the second box and the last box in the Figure 13 with the computation of corrections and application of them on the pseudorange measurements at the aircraft. This processing is detailed in this section.

3.2.3.3.1 Presentation

The differential positioning model is based on the principle of spatial and temporal correlation of errors in the section 3.1.4.2 as illustrated by the Figure 6 .A reference station at a fixed and known location is used to estimate errors in the measurements which are likely to be highly correlated to the errors in measurements made at nearby users. These correlated errors are typically atmospherical errors (troposphere/ionosphere) satellite orbit and clock errors. As mentioned before in the DGNSS section 3.1.4.2, the advantage of such a processing is the fact that correlated errors are reduced but an important drawback of using it is that non-correlated errors like noise and multipath at the user side will contain also the uncorrelated errors contribution of the reference station. Therefore there will be an "amplification" of the uncorrelated errors comparing to the use of a standalone processing. When employed in civil aviation applications the reference and user are known as *ground* and *airborne*. The simplest of differential positioning architectures is shown in Figure 15. In this case, the ground computes a pseudorange correction by making the difference $r^G - \widehat{\Psi}^G$ which is applied to the airborne pseudorange measurements to generate a more accurate differentially corrected pseudorange observable $\widetilde{\Psi}^A$. This differentially corrected observable is then used in the PVT computation.

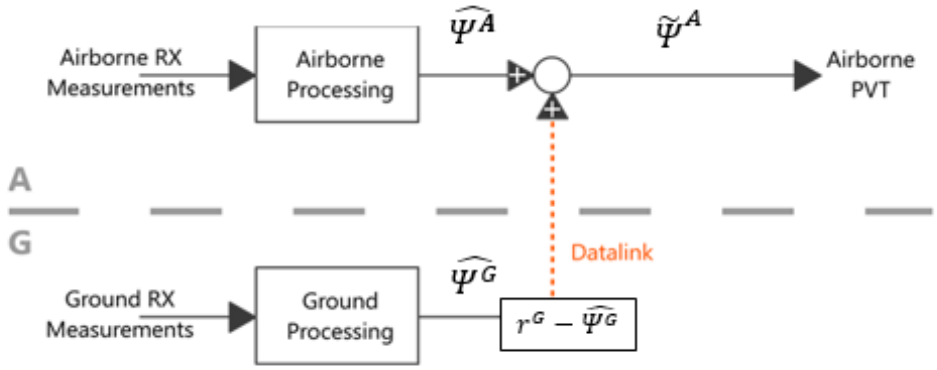

Figure 15-Differential Positioning Architecture

The architecture illustrated in Figure 15 is a simplified architecture because it illustrates the spatial decorrelation between ground and airborne receivers but the impact of latency between aircraft and ground measurement is not shown. Obviously, the degradation in the quality of the pseudorange correction depends on their temporal correlations. Therefore, when this correction is changing rapidly, it must be provided frequently in order to update the airborne pseudoranges. That is why a range rate correction is employed in this PhD project. The following architecture shown that the airborne observables are corrected first with the Pseudorange Correction (noted PRC) and then updated with the introduction of the Range Rate Correction term (noted RRC) which is multiplied by the latency.

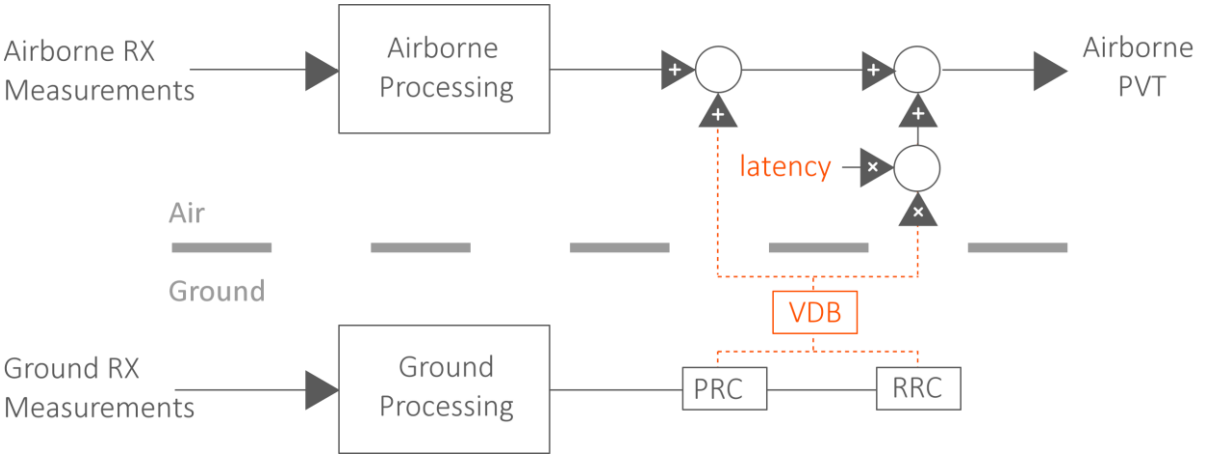

Figure 16-Differential Positioning Architecture with Range-Rate Correction [47]

3.2.3.3.2 PRC/RRC

As introduced in the section 3.2.3.3.1 , corrections are computed at the ground station as described in the following.

Indeed, measurements made by several reference receivers (typically 3 or 4) are averaged together to produce Pseudorange Corrections (PRC) and Range Rate Corrections (RRC) as defined in [78] for all satellites in tracked by the ground receivers. IAlso, "B-values" (3.2.3.3 and 3.3.2.2.3.1.1) are computed to detect and isolate failed reference receivers whose measurements diverge from the consensus of the remaining receivers.

The PRC computation is based on carrier smoothed code measurements and is illustrated by the following figure extracted from [42] [78] [79]:

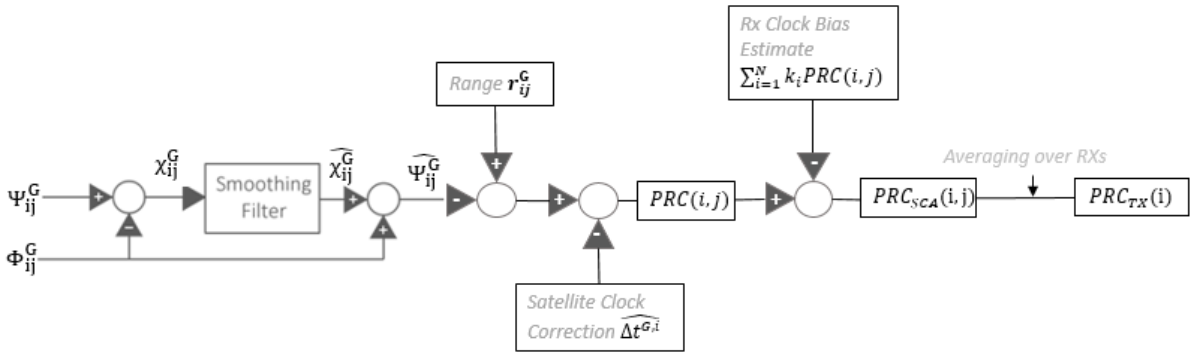

Figure 17-PRC computation

In this figure, it can be noticed that PRC is computed for all receiver j and all satellite i by applying the formula

$$PRC(i,j) = r_{ij}^G - \widehat{\Psi_{ij}^G} - c \times \Delta\hat{t}^{G,i}$$

Equation 54-PRC computation

Because the pseudorange is affected by the receiver clock bias, PRC has to be adjusted by applying the receiver clock bias estimate to define a smoothed clock adjusted PRC (PRC_{SCA}) as :

$$PRC_{SCA}(i,j) = PRC(i,j) - \sum_{i=1}^{N} k_i PRC(i,j)$$

Equation 55- Smoothed Clock Adjsut

The requirement [79] on this formula is to have $\sum_{i=1}^{N} k_i = 1$

Finally, the PRC transmitted (PRC_{TX}) at the user is the average over all receivers (M receivers) therefore:

$$PRC_{TX}(i) = \frac{1}{M(i)} \sum_{j} PRC_{SCA}(i,j)$$

Equation 56- PRC transmitted

In order to protect the user against a faulty measurement the PRC_{SCA} from each receiver are compared each other by computing B-values. They are defined by:

$$B(i,j) = PRC_{TX}(i) - \frac{1}{M(i)-1} \sum_{k \neq j} PRC_{SCA}(i,k)$$

Equation 57-B value

If this B value exceeds the threshold as:

$$B(i,j) > \frac{K_b \sigma_{pr_{gnd,i}}}{M-1}$$

K_b a station configurable parameter between 5 and 6 and $\sigma_{pr_{gnd,i}}$ are extracted from messages (in 3.2.3.4.3)

Then a reference receiver is declared faulty and no B-value for this combination of satellite receiver (i,j) is broadcast. Therefore, if all B-values are below their thresholds the PRC_{TX} is approved and transmitted but if not, some exclusion processes and recalculations are made until all B-values are below it.

The corrected pseudorange is computed as follows: [42].

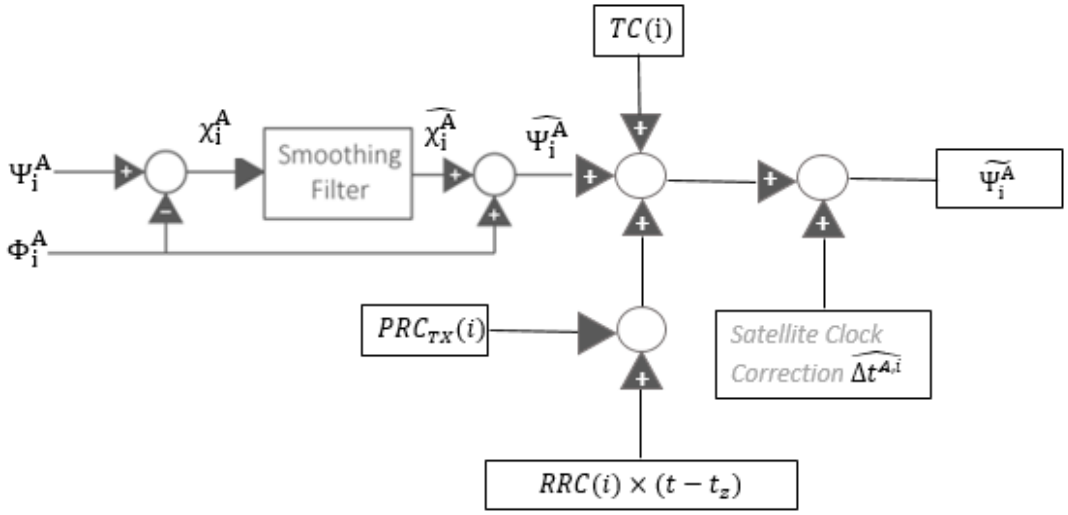

Figure 18-Pseudorange Processing [41]

This figure shows that the corresponding formula for the corrected pseudorange computed at the aircraft is :

$$\widetilde{\Psi_i^A} = \widehat{\Psi_i^A} + PRC_{TX}(i) + RRC(i) \times (t - t_z) + TC(i) + c \times \Delta\hat{t}^{A,i}$$

Equation 58 – Corrected Pseudorange

Where $\widetilde{\Psi_i^A}$defines the corrected pseudorange (in meters) at the current time$t$, $\widehat{\Psi_i^A}$is the smoothed pseudorange (in meters) at the current time t computed at the aircraft. An important value to define is t_z (more information is given in 4.3) and it represents the time of applicability of the PRC given by the appropriate message type as the parameter "Modified Z-count" (more details about messages are given in 3.2.3.4.3). According the requirements [42], $t_{AZ} = t - t_z$ must be inferior to 1.5s in the absence of lost VDB messages and airborne related delays, the examination of the possible of having an higher t_{AZ} is given in section 4.3 . Then, $TC(i)$ represents the tropospheric correction, c is the speed of light (in meters/second) and $\Delta\hat{t}^{A,i}$ is the satellite clock correction (in seconds).

The tropospheric correction TC (detailed in section 5.5) and represented in Figure 1 including mapping function, only based on vertical height difference between aircraft and GBAS ground station for satellite i is described in [42] as:

$$TC(\mathrm{i}) = N_R h_0 \frac{10^{-6}}{\sqrt{0.002 + \sin^2(\theta_i)}}\left(1 - e^{-\frac{\Delta h}{h_0}}\right)$$

Equation 59- Tropospheric Correction

Where N_R is the Refractivity Index, h_0 defines the tropospheric Scale height, θ_i is the elevation for the satellite i and Δh is the height of the aircraft above the GBAS reference location (in meters).Indeed, in differential applications, the interest come from differential tropospheric delay as observed at the reference station and at an aircraft Δh above the reference station.and the vertical delay is modified by an obliquity factor which depend on the elevation θ_i is the elevation for the satellite i.

Details about the computation at the GBAS ground station of parameters such as N_R, h_0 are not given in standards [16]. But a methodology is given by a paper from Van Dierendonck [80] and can be explained by the scheme below:

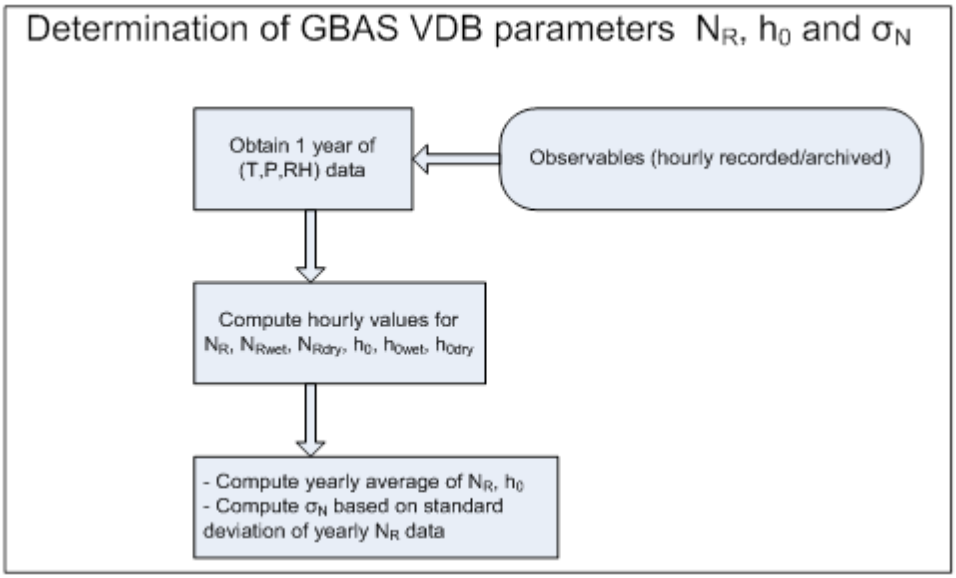

Figure 19-Determination of TC and sigma tropo parameters

It should be noticed that for each parameter the local yearly mean value (normally measured by the GBAS meteo station) is determined and used for broadcast to the aircraft during approach operations.

An alternative approach could be to use data from NWMs to compute these mean values and to derive the corresponding TC and σ_{tropo} for different locations. This work is detailed in the following subsections for Harmonie (presented in 5.2.2.3) and Arome (presented in 5.2.2.2)

3.2.3.3.2.1 Harmonie

In the area of study for Harmonie (presented in 5.2.2.3) an important location is the Schiphol Airport. Therefore, this NWM was used to compute the mean values explained in Equation 59 and Figure 19 for Schiphol and are summarized in the following table:

	N_R(unit-less)	$h_0(m)$	σ_N(unit-less)
Schiphol	320.43	16296	9.3975

Table 11-Yearly mean values for Schiphol

These results were compared to those provided by NLR at the De Bilt Station which is at 35km to Schiphol but more inland.

	N_R(unit-less)	$h_0(m)$	σ_N(unit-less)
De Bilt	327.10	15992	12.71

Table 12-Yearly mean values for De Bilt

By comparing these tables Table 11 and Table 12, it can be notice that h_0 and N_R are comparable but σ_N is quite different. This can be explained by the higher variability of the De Bilt weather. Indeed Schiphol is more near the coast where climate is damped by seawater influence.

Then TC was computed as described in Figure 19 at Schiphol and is represented below as a function of elevation angle.

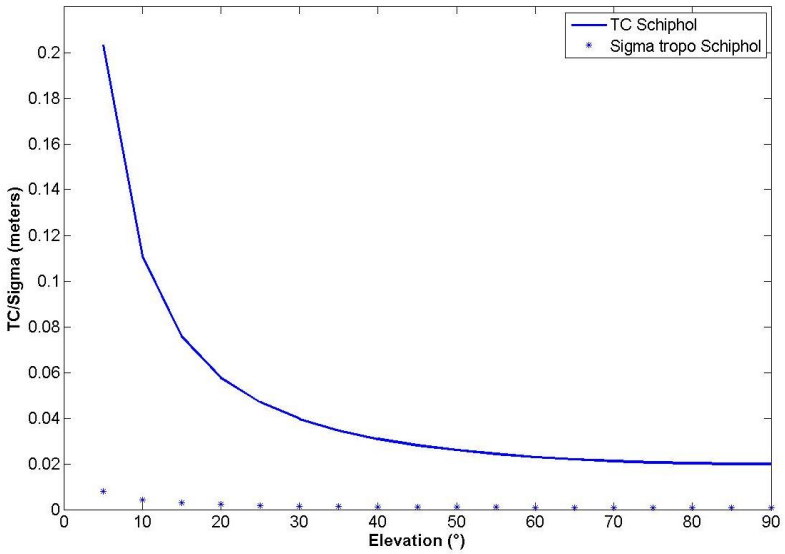

Figure 20-TC and sigma tropo for Schiphol location

3.2.3.3.2.2 Arome

The same process as for Harmonie data in 3.2.3.3.2.1 was also undertaken for Arome (presented in 5.2.2.2).

In this section TC was computed as described above in Figure 19 at Turin Airport and Milan locations for one year of data starting at the 1st January 2014. Arome was used to compute the mean values explained in and in Equation 59 and Figure 19 for Turin and Milan locations and are summarized in the following table:

	N_R(unit-less)	$h_0(m)$	σ_N(unit-less)
Turin	292.26	15980	37.41
Milan	211.46	18120	26.16

Table 13-Yearly mean values for Turin and Milan

Results for TC and the corresponding sigma of the troposphere is provided in the following figure for these 2 locations (Turin in Blue and Milan in Red).

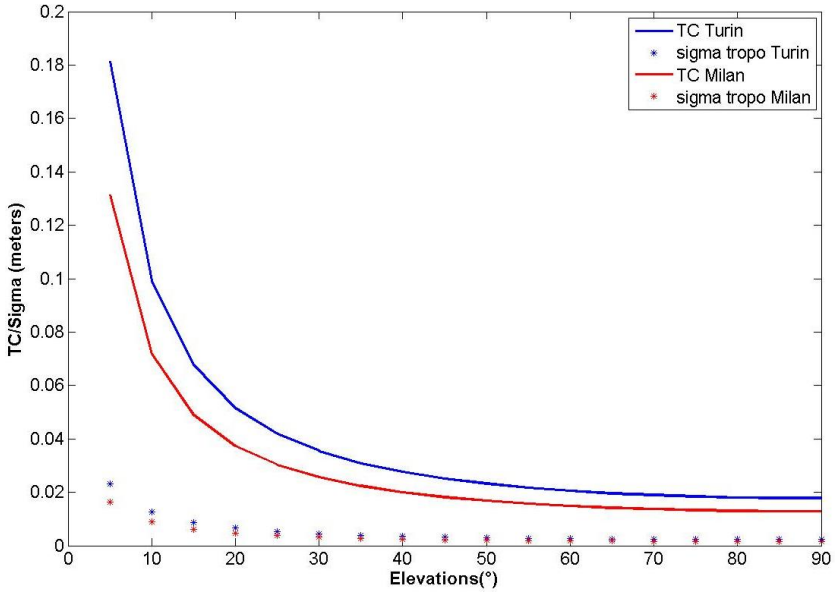

Figure 21-Tropospheric Correction and Sigma tropo at Turin/Milan

3.2.3.3.3 Corrected Smoothed Measurement

In this section, the case of single frequency is treated but it is the same format and computation for the dual frequency cases (more details given in 3.2.3.2.4)

In order to compute the corrected smoothed observables, PRC and RRC (between the epoch k and k-1) are computed at the ground receiver after computation smoothed code observable as shown by Equation 37:

$$\widehat{\Psi^G} = \boldsymbol{r^G + J^G + b^G + I^G + \epsilon^G}$$

$$PRC = r^G - \widehat{\Psi^G} = -b^G - J^G - I^G - \epsilon^G$$

Equation 60 – PRC

Where $\widehat{\Psi^G}$ is the smoothed pseudorange observable, r^G is the geometric range at ground, I^G is the smoothed ionospheric delay, J^G is the troposphere delay, ϵ^G represents smoothed multipath and noise components, b is satellite clock error.

$$RRC_k = \frac{PRC_k - PRC_{k-1}}{T} = -\dot{b}^G - \dot{J^G} - \dot{I}^G - \dot{\epsilon}^G$$

Equation 61 - RRC

T defines the time between two consecutive epochs and ∎ defines the discrete time derivative at t_G the time at ground station. The influence of the PRC-based receiver clock correction has been neglected in as it introduces common mode-like errors which cancel in the airborne position solution.

So at the airborne receiver, the corrections are applied to smoothed pseudorange measurements $\bar{\Phi}^A$ using the following expression:

$$\tilde{\Phi}^A(t_A) = \bar{\Phi}^A(t_A) + PRC + t_{AZ}RRC + TC + c \times \Delta\hat{t}^A$$

Equation 62 - Corrected smoothed measurements

Where $\tilde{\Phi}^A$ is the corrected pseudorange measurement, $\bar{\Phi}^A$ is the smoothed pseudorange measurement and t_{AZ} represents the time between the modified time of correction generation t_z and the time of application at the airborne receiver: $t_{AZ} = t_A - t_z$, Then, TC represents the tropospheric correction, c is the speed of light (in meters/second) and$\Delta\hat{t}^A$ is the satellite clock correction (in seconds).

Equation 62 may be decomposed using Equation 60 and Equation 61 into the error components.

$$\tilde{\Phi}_1^A(t_A) = r^A + \left(-(dr^G + t_{AZ}d\dot{r}^G)\right) + \left(b^A - \left(b^G + t_{AZ}\dot{b}^G\right)\right) + \left(J^A - \left(J^G + t_{AZ}\dot{J^G}\right)\right) + \left(I_1^A - \left(I_1^G + t_{AZ}\dot{I}^G\right)\right) + \left(\epsilon_1^A - (\epsilon_1^G + t_{AZ}\dot{\epsilon}^G)\right)$$

Equation 63 - Smoothed Corrected measurement with error components

Here, dr represents the ephemeris error.

There the following relation can be derived as the input of the Position computation algorithm in 3.3:

$$\tilde{\Phi}_1^A(t_A) - \hat{r}^A = \left(dr^A - (dr^G + t_{AZ}d\dot{r}^G)\right) + \left(b^A - \left(b^G + t_{AZ}\dot{b}^G\right)\right) + \left(J^A - \left(J^G + t_{AZ}\dot{J^G}\right)\right) + \left(I_1^A - \left(I_1^G + t_{AZ}\dot{I}^G\right)\right) + \left(\epsilon_1^A - (\epsilon_1^G + t_{AZ}\dot{\epsilon}^G)\right)$$

Equation 64 – PVT input measurements with error components

Note that terms representing the tropospheric correction and the satellite clock correction are not explicitly represented within Equation 63 and Equation 64 because they are implicitly covered since b and J express the residual errors. Therefore, they won't be represented in following section where this model is used (as Chapter 4)

In this Equation 64, $\hat{r}^A$ is the estimated geometric range from aircraft to satellite and can be expressed by:

$$\hat{r}^A = r^A - dr^A$$

Equation 65 - Estimated geometric range

3.2.3.4 *GBAS Corrected Measurement Model* *[6]

This section presents the Measurement error model after the smoothing processing and application of corrections. Nominal errors will be gathered in the fault-free measurement model whereas non-nominal errors that may cause hazardous positioning failure and which should be detected are described in the faulty measurement model (Figure 32). In this part of the thesis, only the nominal case dealing with fault free measurement model is analysed but the faulty (non-nominal) case is discussed in the section dealing with GBAS integrity monitoring 3.3.2.2.3.

However, in this section the impact of the latency of the pseudorange correction (PRC) due to potentially differing measurement points in time at ground and airborne receivers are not explicitly deriving(as illustrated in Figure 15), therefore in this , the error model is derived by assuming the impact of RRC is covered by these models. This RRC implication in the error model are detailed in another section 4.2.

In all of fault-free case models, the measurement error components are assumed to have a normal distribution with a known variance and a zero mean. The resulting pseudorange error distribution is considered to be the result of the combination of all the errors and therefore, it is supposed to have a normal distribution with zero mean and a variance which is the sum of all error variances. That is why, this section focuses on analysing the different error components distributions.

First, GAST C/D case is presented dealing with Single Frequency case and then GAST F case is illustrated treating the Dual Frequency cases.

3.2.3.4.1 GAST C/D

GAST C and D are discussed together in this section because of their similitude. Their main difference is the fact that, in the GAST D case, time constant into smoothing processing is different. According to [41] in the section 2.3.6.1.1, in addition to the set of smoothed pseudo ranges define for GAST-C with a smoothing constant τ equal to 100s, GBAS equipment supporting GAST D shall produce a second set of smoothed pseudo-ranges by applying the same filter as presented in 3.2.3.2 with τ equal to 30s. This second smoothing time constant is used primarily as part of the mitigation of errors that could be induced by rare ionospheric anomalies. Indeed, the higher the smoothing constant is, the higher the convergence time filter will be therefore that will have an impact on the monitoring [81] of this error. Also by seeing the ionospheric residual uncertainty in Equation 74, the ionospheric error standard deviation will be smaller with a smaller smoothing constant. However, according to [82] the use of 30-second-smoothed pseudoranges has other implications on system performance such as some degradation in accuracy and also some effect on the availability of service. Indeed, it seems that using 30-second-smoothed pseudoranges increase the noise by 30% and ground multipath seems to increase by an empirical factor of 1.4 as it is said in [44].

According to the DLR analysis in [83], for GBAS applications, while comparing GPS standard values extracted from [84] and Galileo error model considered in [85], the error levels seem to be in the same order of magnitude as it is shown in the following figure. So the same GBAS error models as those selected for GPS is used for Galileo.

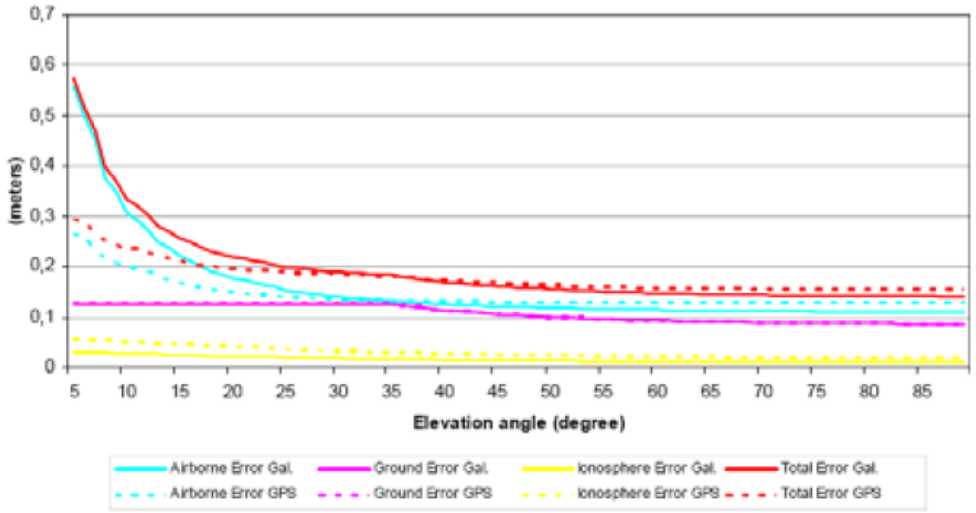

Figure 22-Error budget for Galileo and GPS new signals [83]

In [27], the expressions of the standard deviation of the over bounding distributions of the corrected and smoothed measurement errors in the case of GAST-C are described. The expression of the standard deviation of for ranging source i can be written as:

$$\sigma_i^2 = \sigma_{pr\_gnd,i}^2 + \sigma_{pr\_air,i}^2 + \sigma_{tropo,i}^2 + \sigma_{iono,i}^2$$

Equation 66 – GAST-C standard deviation of the pseudorange measurement error

Where $\sigma_{pr\_gnd,i}^2$ is the post correction fault-free noise term provided by the ground function (via the VDB) for satellite i. Then, $\sigma_{pr\_air,i}^2$ is the variance of the aircraft contribution to the corrected pseudorange error for the i[th] satellite which includes the receiver and airframe multipath contribution. $\sigma_{tropo,i}^2$ represents the variance of the residual tropospheric error for satellite i. Finally, $\sigma_{iono,i}^2$ is the variance of the residual ionospheric delay uncertainty for satellite i, due to spatial decorrelation.

The expressions used to represent these different terms are described below.

3.2.3.4.1.1 SIS pseudorange accuracy

The SIS pseudorange errors model include both errors due to the non-aircraft elements in the GBAS ground segment and other components such the effects of the signal propagation through the atmosphere which are common for all reference receivers(in (a_2)). The root mean square (RMS) of the total non-aircraft contribution to the GBAS ground segment error as a function of satellite elevation angle at the GBAS reference location shall be [27] [86]:

$$\sigma_{pr_{gnd,i}} \leq \sqrt{\frac{\left(a_0 + a_1 e^{-\theta_i/\theta_0}\right)^2}{M} + (a_2)^2}$$

Equation 67 – RMS of the total non-aircraft contribution to the GPS/LAAS error

Where M represents the number of ground reference receiver subsystems, θ_i is the elevation angle for the i^{th} satellite and parameters such as a_0, a_1, a_2 and θ_0 are defined in the following table. a_0 represents components which are not elevation dependant and a_1 those which have an elevation dependency.

These residual errors can include [27] : Thermal Noise (assuming 100-sec smoothing), Ground multipath, Pseudorange acceleration/Data broadcast latency (a_2), Ephemeris(a_2), Ground-to-airborne multipath (a_2), Reference receiver relative survey(a_2),.

The coefficients presented in the following table are derived from a Curve fit to the Root-Sum-Square of the previous components. [27]

Ground Accuracy Designator (GAD)	θ_i (degrees)	a_0 (meters)	a_1 (meters)	θ_0 (degrees)	a_2 (meters)
A	> 5	0.5	1.65	14.3	0.08
B	> 5	0.16	1.07	15.5	0.08
C	> 35	0.15	0.84	15.5	0.04
	≤ 35	0.24	0	-	0.04

Table 14-Non-aircraft Elements Accuracy Requirement [27]

As noticed in this table [27]: three accuracy designators (ADs) are defined for ground installations (GADs) through letters as A, B and C.

GAD-A is intended to represent a level of performance achievable with early and low-cost installations using existing receiver and antenna technologies. GAD-C is intended to represent the performance expected of future CAT-II/III installations, while GAD-B was defined to offer an intermediate level of performance between GAD-A and GAD-C. Furthermore, there is complete interoperability between airborne and ground equipment with different accuracy designations.

The ground accuracy used for GAST-C should not be impacted by changes implied by GAST D since it is supposed to include several error sources and therefore it is assumed to be sufficiently conservative to overbound the errors in the case of GAST-D measurements. However, to take into account advances in GBAS ground station antennae, it is recommended [80]to use also for GAST-D, the C-curve defined in 3.2.3.4.1.1 for elevations between 0 and 35 ° all the way to 90 degrees.

In the SESAR Project, a derivation of a RMS model for 30s smoothing processing was derived [87].Therefore, the proposed RMS model for GAST-D GBAS considering a 30s time constant code carrier smoothing filter is given below:

$$\sigma_{pr\_gnd\_30,i} \leq \sqrt{\frac{\left(a_0 + a_1 e^{-\theta_i/\theta_0}\right)^2}{M} + (a_2)^2}$$

Equation 68 -Proposition for σ_pr_gnd_30

Ground Accuracy Designator (GAD)	θ_i (degrees)	a_0 (meters)	a_1 (meters)	θ_0 (degrees)	a_2 (meters)
C	> 35	0.18	1.01	15.5	0.04
	$\leq$ 35	0.31	0	-	0.04

Table 15-Proposition for Non-aircraft Elements Accuracy GAST D

In this PhD project, the SESAR proposition was not taken into account and for both GAST-C and GAST-D, it was assumed a level of performance defined by GAD-C.

3.2.3.4.1.2 Airborne pseudorange accuracy

The RMS of the total airborne receiver contribution to the error in a corrected pseudorange for a GPS satellite as a function of satellite elevation angle above the local level plane shall be [27]:

$$\sigma_{pr_{air,i}} \leq a_0 + a_1 e^{-\theta_i/\theta_0}$$

Equation 69 - RMS of the total airborne receiver contribution [27]

Where θ_i is the elevation angle for the i^{th} ranging source. And parameters such as a_0, a_1 and θ_0 are defined through the following Table 16 [27]

In comparison with the previous Table 14 dealing with SIS accuracy, two ADs are defined for airborne equipment (AAD): A and B .The current airborne GPS equipment may be able to meet AAD-A standards with appropriate software upgrades, while AAD-B was defined to reflect performance that could be achieved with improved receiver technology. This level AAD-B was chosen in this PhD project.

Airborne Accuracy Designator (AAD)	θ_0 (degrees)	a_0 (meters)	a_1 (meters)
A	6.9	0.15	0.43
B	4	0.11	0.13

Table 16-Airborne Accuracy Designator [27]

According to [27], the same formula as for RMS of the total airborne receiver contribution, is used for multipath with different coefficients presented in the following Table 17 depending on Airframe Multipath Designators (AMDs).

$$\sigma_{mp,i} \leq a_0 + a_1 e^{-\theta_i / \theta_0}$$

Equation 70 – RMS for multipath

The airframe multipath model AMD-A shown in the following table was developed and validated by the community as it appears in [27] and [42].

Airframe Multipath Designator (AMD)	$\boldsymbol{\theta_0}$ **(degrees)**	$\boldsymbol{a_0}$ **(meters)**	$\boldsymbol{a_1}$ **(meters)**
A	10.0	0.13	0.53
B	10.0	0.065	0.265

Table 17-Airframe Multipath Designator [27]

For GAST D, the Airborne accuracy should be multiplied by the factor $\sqrt{100/30}$ to account for the change of carrier smoothing constant leading to [82] [13]:

$$\sigma_{pr_{air_{GASTD},i}} = \sqrt{100/30} \,.\, \sigma_{pr_{air},i}$$

Equation 71 - RMS of the total airborne receiver contribution for GAST D

With $\sigma_{pr\_air}(\theta_i)$ as presented for GAST C in Equation 69

It is the same for the multipath contribution where it should be also multiplied by $\sqrt{100/30}$ to account for the change of carrier smoothing constant:

$$\sigma_{mp_{GASTD},i} = \sqrt{100/30} \,.\, \sigma_{mp,i}$$

Equation 72 - RMS for multipath contribution for GAST D

With $\sigma_{mp}(\theta_i)$ as presented for GAST C in Equation 70

3.2.3.4.1.3 Tropospheric residual uncertainty

The impact of tropospheric error on the total error measurement is expressed through The residual tropospheric uncertainty is defined [42] for both GAST C and GAST D by :

$$\sigma_{tropo,i} = \sigma_N h_0 \frac{10^{-6}}{\sqrt{0.002 + \sin^2(\theta_i)}} \left(1 - e^{-\frac{\Delta h}{h_0}}\right)$$

Equation 73 - Residual tropospheric uncertainty

Where σ_N is the refractivity uncertainty transmitted by ground subsystem, h_0 defines the tropospheric scale height. These parameters can be obtained with the methodology explained in Figure 19 in the section 3.2.3.3 . θ_i is the elevation for the satellite i and Δh is the height of the aircraft above the GBAS reference location (in meters).

More details on tropospheric delays are given in 4.2.2 and Chapter 5.

3.2.3.4.1.4 Ionospheric residual uncertainty

The residual ionospheric uncertainty is defined as [42]:

$$\sigma_{iono,i} = F_{pp} . \sigma_{vert\_iono\_gradient\_x} . (x_{air} + 2 . \tau . v_{air})$$

Equation 74 - Residual ionospheric uncertainty

Where F_{pp} is the vertical-to-slant obliquity factor (unitless) for the given satellite i with the following definition or by using directly the obliquity factor given in the Equation 13

$$F_{pp} = \left[1 - \left(\frac{R_e \cos\theta_i}{R_e + h_I}\right)^2\right]^{-\frac{1}{2}}$$

Equation 75 - F_pp definition

With $R_e = 6378.1363\ km$ as the radius of the earth, $h_I = 350\ km$ is the ionospheric shell height. Then, θ_i is the elevation angle of the satellite and $\sigma_{vert\_iono\_gradient\_x}$ is the Service Type dependent standard deviation of a normal distribution associated with the residual ionospheric uncertainty due to spatial decorrelation. It can be found in the Message types defined in more details in 3.2.3.4.3. x_{air} represents the distance (slant range) between the aircraft and the GBAS reference point (in meters). τ is the Service Type dependent time constant of the smoothing filter and v_{air} is the horizontal speed of the aircraft (meters/sec).

As it is done for tropospheric residual uncertainty some of the parameters necessary to compute ionospheric residual uncertainty which are x_{air} and v_{air} have to be modelled. The assumptions presented in Appendix F of [27] for LAAS availability prediction are used and are reminded in the following table.

	x_{air} (m)	v_{air} (m/s)
GAST C	6000	77
GAST D	5400	72

Table 18-Residual Ionospheric Uncertainty parameters assumptions [27]

Also a velocity profile was developed in the proposal for updated SARPs for GBAS [88] depending on three types of aircraft (Three speed profiles) and is presented in the following figure and table:

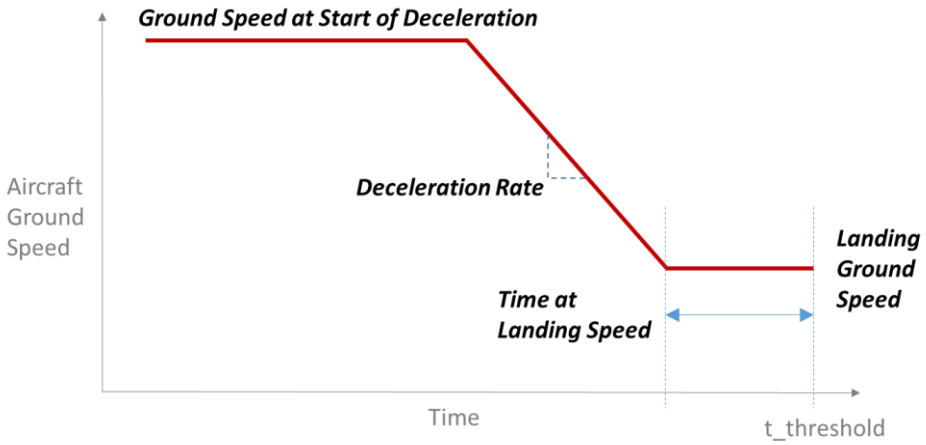

Figure 23-Velocity profile Model [88]

Landing Ground Speed (knots)	Time at Landing Speed (seconds)	Deceleration Rate (knots/s)	Ground Speed at Start of Deceleration (knots)
161	50	1.1	290
148	50	1.1	277
135	50	1.1	264

Table 19-Airborne speed Profile [88]

Also for GAST D, the expression presented by Equation 74 for ionospheric residual error for GAST-C contains explicitly the smoothing constant and $\sigma_{vert\_iono\_gradient\_x} = \sigma_{vert\_iono\_gradient\_D}$. This last value can be found in the Message type with a time constant of 30 seconds as described in 3.2.3.4.3:

$$\sigma_{iono,i} = F_{pp}.\sigma_{vert\_iono\_gradient\_D}.(x_{air} + 2.\tau.v_{air})$$

3.2.3.4.2 GAST F

In this section, GBAS corrected measurement model for Dual Frequency (DF) cases is presented. It is split into two parts according the smoothing technique chosen: D-free smoothing (defined in 3.2.3.2.4.1) and I-free smoothing (defined in 3.2.3.2.4.2).

3.2.3.4.2.1 D-Free

As presented in 3.2.3.2.4.1, this smoothing technique presents the advantage of keeping the noise as same level as for single frequency case but the disadvantage of not removing totally the ionosphere effect.

D-free smoothing is described here for L1 frequency pseudorange by designating the filter inputs as presented in 3.2.3.2.4.1. Therefore, expressions of the standard deviation of the over bounding distributions of the pseudorange measurement errors rely on the same equations as for single frequency cases presented in the previous section 3.2.3.4.1 by the Equation 66. Each components are given in this part and the total measurement error of D-free is derived.

According the analysis in [89], residual noise on the output of D-Free processing is regarded as being of the same magnitude as the noise on the output of SF carrier smoothing.

Indeed, [90] reminds the fact that the smoothed code error ε described in 3.2.3.2.4.1 is mainly composed of code noise and multipath, by denoting $\sigma_{DFree-gnd}$ the standard deviation of ε^G at ground , the noise contribution at ground for D-free can be approximated as [91] [89] [90] :

$$\sigma_{DFree1-gnd} \cong {\sigma_{\rho 1}}^G \sqrt{\frac{T}{2\tau}}$$

Equation 76 - Standard deviation of smoothed code error for D-free

Where T is the output interval of the raw measurement and ${\sigma_{\rho 1}}^G$ is the standard deviation of the raw L1 pseudorange data at ground receiver and τ is the smoothing constant. In the previous equation it is assumed that $\tau \gg T$ and the contribution of the carrier phase errors is negligible.

As it could be noticed by the previous equation, the noise contribution in D-free is equivalent to the one found in SF case in 3.2.3.2 (Equation 31)

In the same way, $\sigma_{DFree1-air}$ is derived for the aircraft side as the standard deviation of ε^A (defined in 3.2.3.2.4.1) [91] [89] [90]:

$$\sigma_{DFree1-air} \cong {\sigma_{\rho 1}}^A \sqrt{\frac{T}{2\tau}}$$

Equation 77 - Airborne receiver error for D-free

Where ${\sigma_{\rho 1}}^A$ is the standard deviation of the L1 code pseudorange data at the airborne.

As it could be noticed by the previous equation, the noise contribution in D-free is equivalent to the one found in SF case in 3.2.3.2 (Equation 31)

Then in D-Free technique, the code-carrier divergence term (in Equation 74) is removed so the sigma value of ionosphere decorrelation $\sigma_{DFree-iono}$ is given as follows [89].

$$\sigma_{DFree-iono} = F_{pp} . \sigma_{vert\_iono\_gradient} . x_{air}$$

Equation 78 - Sigma value of iono decorrelation with D-free

Where x_{air} is the distance between the ground station and the user, $\sigma_{vert\_iono\_gradient}$ is the nominal ionosphere spatial gradient in the vertical (zenith) domain (is generally set to 4 mm/km) and F_{pp} is the obliquity factor corresponding to the elevation angle θ_i (see Equation 13)

In case of Dual-Frequency cases, since troposphere is non-dispersive medium (3.2.2.3), the standard deviation of residual tropospheric error is the same for D-free as for single frequency presented in Equation 73 by $\sigma_{tropo}(\theta_i)$

Therefore:

$$\sigma_{DFree-tropo} = \sigma_{tropo}$$

Equation 79 - Sigma value for tropo error for D-free

In conclusion, the total measurement error of D-Free, σ_{DF} is given by the root-sum-square of these terms according the components described before.

$$\sigma_{DFree} = \sqrt{\sigma^{2}_{DFree-iono} + \sigma^{2}_{DFree-gnd} + \sigma^{2}_{DFree-air} + \sigma^{2}_{DFree-tropo}}$$

Equation 80 - The total measurement error of D-Free

3.2.3.4.2.2 I-Free

As presented in 3.2.3.2.4.2, the main advantage of the I-free technique is that removes totally the ionosphere effects but an increasing of the noise compared to SF case appears.

For this I-free case, the expressions of the standard deviation of the over bounding distributions of the pseudorange measurement errors rely on the same equation as for single frequency cases presented in the previous section 3.2.3.4.1 by the Equation 66 but the first order ionospheric delay is completely removed [90]

Since I-free is not affected by ionosphere, the total measurement error of I-free contains only ground and airborne receiver errors:

$$\sigma_{IF} = \sqrt{\sigma^{2}_{IF-gnd} + \sigma^{2}_{IF-air} + \sigma^{2}_{IF-tropo}}$$

Equation 81 - The total measurement error of I-Free

The standard deviation of errors on I - Free with GPS/GALILEO standalone is expressed as in [90] by determining first the residual noise and multipath error and by setting the variance of ε_{IF} (described in 3.2.3.2.4.2) as in [90]

$$\sigma^{2}_{IF} \cong \left[\left(1-\frac{1}{\alpha}\right)^{2}\sigma^{2}_{\rho 1} + \frac{1}{\alpha^{2}}\sigma^{2}_{\rho 5}\right]\left(\frac{T}{2\tau}\right)$$

Equation 82 -variance of ε_IF for I-free

Where T is the output interval of the raw measurement and $\sigma_{\rho 1}$ is the standard deviation of the raw L1 pseudorange data , and $\sigma_{\rho 5}$ is the standard deviation of the raw L5 pseudorange data and τ is the smoothing constant .

As it could be noticed by the previous equation, the noise contribution in I-free is more important than the one found in SF or D-free case in 3.2.3.2 (Equation 31).

Furthermore remiding 3.2.3.2.4 with the Equation 43

$$\alpha = 1 - \frac{{f_1}^2}{{f_5}^2}$$

Therefore the standard deviation of errors for I-Free smoothing at the ground side is computed as :

$$\sigma_{IF\_gnd} = \left(\frac{T}{2\tau}\right)\sqrt{\left(1-\frac{1}{\alpha}\right)^2\left({\sigma_{\rho 1}}^G\right)^2 + \frac{1}{\alpha^2}\left({\sigma_{\rho 5}}^G\right)^2}$$

Equation 83 - standard deviation of errors on IFree for the ground side

And the standard deviation of errors for I-Free smoothing at the aircraft side is computed as :

$$\sigma_{IF\_air} = \left(\frac{T}{2\tau}\right)\sqrt{\left(1-\frac{1}{\alpha}\right)^2\left({\sigma_{\rho 1}}^A\right)^2 + \frac{1}{\alpha^2}\left({\sigma_{\rho 5}}^A\right)^2}$$

Equation 84 - standard deviation of errors on IFree for the airborne side

Also as for D-free case, since troposphere is non-dispersive medium (3.2.2.3), the standard deviation of residual tropospheric error is the same for I-free as for single frequency presented in Equation 73 by $\sigma_{tropo}(\theta_i)$

Therefore:

$$\sigma_{IF-tropo} = \sigma_{tropo}$$

Equation 85 -Sigma value for tropo error for I-free

By considering that $\sigma_1 = \sigma_5 = \sigma$, the following equations could be considered for L1/L5 or (E1/E5a) I-free [87] [90] in this absence of sufficient knowledge about the L5/E5a multipath and noise performances:

$$\sigma_{IF\_air} \approx 2{,}59\ {\sigma_\rho}^A\sqrt{\frac{T}{2\tau}}$$

$$\sigma_{IF\_gnd} \approx 2{,}59\ {\sigma_\rho}^G\sqrt{\frac{T}{2\tau}}$$

Equation 86 -The simplified measurement error of I-Free

With this last formula, it should be noted that this value is noisier than for D-free smoothing technique.

Although I-Free seems like the optimum solution because the ionosphere delay will be totally removed, the main drawback of this method is the noisy outputs from the smoothing filter (noise and multipath amplification).

3.2.3.4.3 GBAS Messages

This section describes the GBAS messages types and formats sent at the aircraft in order to correct the measurements. The PAN (Position and Navigation subsystem) equipment receives the GBAS messages from ground subsystem that include differential corrections. The GBAS message block contains: the message block header, the message and the message block CRC as defined in [78] by this following table :

Message Block	*Bits*	*Bytes*
Message Block Header	48	6
Message	up to 1696	up to 212
Message Block CRC	32	4

Figure 24-Format of a GBAS message block [78]

A part of the message block header is dedicated to the message type and contains 8 bits. The range of the 8-bit message type field of the message block header allows for up to 256 message types. Messages types 6, 7, 8 and 101 are reserved respectively for possible use to provide differential carrier correction, for military information, for proprietary messages and for GRAS. [78]

The following table lists the allocated message types, and the required broadcast rates to support precision approach and the differential positioning service.

Message Type	*Message Name*	*Minimum Broadcast Rate*	*Maximum Broadcast Rate*
1	Differential Corrections – 100 sec smoothed pseudoranges	For each measurement type: All measurement blocks, once per frame (note 1)	For each measurement type: All measurement blocks, once per slot (note 1)
2	GBAS Related Data	Once per 20 consecutive frames	Once per frame
3	Null Message	N/A	N/A
4	Final Approach Segment (FAS) Construction Data	All FAS blocks once per 20 consecutive frames (note 2)	All FAS blocks once per frame (note 2)
	Terminal Area Path (TAP) Construction Data	(notes 2 and 3)	(notes 2 and 3)
5	Ranging Source Availability (optional)	All impacted sources once per 20 consecutive frames	All impacted sources once per 5 consecutive frames
6	Reserved For Carrier Corrections	-	-
7	Reserved for Military	-	-
8	Reserved for Test	-	-
11	Differential Corrections – 30 sec smoothed pseudoranges	For each measurement type: All measurement blocks, once per frame (note 5)	For each measurement type: All measurement blocks, once per slot (note 5)
101	GRAS Pseudorange Corrections – (As defined in ICAO SARPS Annex 10)	-	-

Table 20-GBAS message types [78]

In this thesis, several message types are more relevant than others and are further described. Indeed, message types 1, 2 and 11 are detailed below:

- Message type 1

As it is explained before in the Table 20, Message Type 1 provides mainly the differential correction data for individual GNSS ranging sources applicable to pseudoranges that are carrier smoothed (see 3.2.3.2) with a time constant of 100 seconds.

In [78], the message type 1 format is defined thanks to this following table:

Data Content	*Bits Used*	*Range of Values*	*Resolution*
Modified Z-count	14	0 – 1199.9 sec	0.1 sec
Additional Message Flag	2	0 – 3	1
Number of Measurements	5	0 – 18	1
Measurement Type	3	0 – 7	1
Ephemeris Decorrelation Parameter (Notes 2, 5)	8	$0 – 1.275 \times 10^{-3}$ m/m	5×10^{-6} m/m
Ephemeris CRC (Notes 2, 5)	8 (most significant byte) (Note 6)	-	-
	8 (least significant byte) (Note 7)		
Source Availability Duration (Notes 4, 5)	8	0 – 2540 sec	10 sec
For N Measurement Blocks:			
Ranging Source ID	8	1 – 255	1
Issue of Data (IOD)	8	0 – 255	1
Pseudorange Correction (PRC)	16	±327.67 m	0.01 m
Range Rate Correction (RRC)	16	±32.767 m/s	0.001 m/s
σ_{pr_gnd} (Note 3)	8	0 - 5.08 m	0.02 m
B_1 (Note 1)	8	±6.35 m	0.05 m
B_2 (Note 1)	8	±6.35 m	0.05 m
B_3 (Note 1)	8	±6.35 m	0.05 m
B_4 (Note 1)	8	±6.35 m	0.05 m

Figure 25-Format of Message type 1 [78]

It is important to note that: 10000000 indicates that the source is not available and 11111111 indicates that the source is invalid and that value is not computed and should not be used.

The PRC/RRC are described in 3.2.3.3.2 and are computed and applied as presented by the Figure 17 and Figure 16.

The "Modified Z-count" parameters inside this previous figure is used to computed the pseudorange corrected as defined in Equation 62. Indeed this parameter is defined as t_z in this equation.

Other parameters such as B-values (3.2.3.3.2 and 3.3.2.2.3.1.1) and Ephemeris parameters (3.3.2.2.3.1.1) are useful for establishing the Navigation Solution in 3.3

- Message type 2

This message type, sent at the rate of 0.1Hz (each 10seconds), identifies the exact location for which the differential corrections provided by the ground augmentation system are referenced. The message also contains

configuration data and parameters needed to compute a tropospheric correction (see Equation 59 and Equation 73), ionospheric delay and other GBAS-related data. In addition, Integrity parameters such as the Ground Station Integrity Designator are included within this message type. Additional data blocks may be appended to the end of this kind of message. In the following sections 3.3.2.2.3 and 4.2 the Additional data block 3 could be useful to defined GAST-D pseudorange measurement error models. It contains missed detection "K" values for ephemeris error and ionospheric parameters.

In [78], the Message Type 2 (MT2) format is defined thanks to this following table :

Data Content	*Bits Used*	*Range of Values*	*Resolution*
Ground Station Reference Receivers	2	2 – 4	-
Ground Station Accuracy Designator	2	-	-
Spare	1	-	-
Ground Station Continuity/Integrity Designator	3	-	-
Local Magnetic Variation	11	± 180°	0.25°
Spare	5	-	-
$\sigma_{vert\_iono\_gradient}$	8	0 – 25.5 x 10^{-6} m/m	0.1 x 10^{-6} m/m
Refractivity Index	8	16 – 781	3
Scale Height	8	0 - 25500 m	100 m
Refractivity Uncertainty	8	0 – 255	1
Latitude	32	± 90.0°	0.0005 arcsec
Longitude	32	± 180.0°	0.0005 arcsec
Reference Point Height	24	± 83886.07 m	0.01 m
Additional data block 1 (if provided)			
Reference station data selector	8	0 to 48	1
Maximum use distance (D_{max})	8	2 to 510 km	2 km
$K_{md\ e\ POS,GPS}$	8	0 to 12.75	0.05
$K_{md\ e\ C,GPS}$	8	0 to 12.75	0.05
$K_{md\ e\ POS,GLONASS}$	8	0 to 12.75	0.05
$K_{md\ e\ C,GLONASS}$	8	0 to 12.75	0.05
Additional data block(s) (if provided, may be included only if Additional Data Block 1 is also provided)			
Repeat for X Additional Data Blocks			
Additional Data Block Length	8	2 to 198	1 byte
Additional Data Block Number	8	2 to 255	1
Data Content	Variable		

Figure 26-Format of the message type 2 [78]

And for the Additional data block 3:

Data Content	*Bits Used*	*Range of Values*	*Resolution*
Additional Data Block Length	8	6	1 byte
Additional Data Block Number	8	3	1
$K_{md\ e\ D,GPS}$	8	0 to 12.75	0.05
$K_{md\ e\ D,GLONASS}$	8	0 to 12.75	0.05
$\sigma_{vert\_iono\_gradient\_D}$	8	0 – 25.5 x 10^{-6} m/m	0.1 x 10^{-6} m/m
Spare	8	-	-

Figure 27-Format of the additional data block 3 [75]

It is relevant to note that in the scope of MC/MF GBAS, this MT2 could be reorganised (as presented in [92]) and modified, therefore other Additional Data Block (ADB) could be introduced and some fields of this MT2 could be re-defined without modifying properly the format of the message. Indeed within the SESAR report [92], the "Spare" field in Figure 26 is modified and an ADB 5 is proposed.

- Message type 11

This message type provides the differential correction data for individual GNSS ranging sources applicable to pseudoranges that are carrier smoothed with a time constant of 30 seconds. The message also includes parameters that describe the distribution of errors in the 30 second smoothed corrections as well as parameters that describe the error in the corresponding 100 seconds smoothed corrections (in type 1 message) as applicable for GAST-D.

In [78], the message type 11 format is defined thanks to this following table:

Data Content	*Bits Used*	*Range of Values*	*Resolution*
Modified Z-count	14	0 – 1199.9 sec	0.1 sec
Additional Message Flag	2	0 – 3	1
Number of Measurements	5	0 – 18	1
Measurement Type	3	0 – 7	1
Ephemeris Decorrelation Parameter (Notes 1 and 3)	8	$0 - 1.275 \times 10^{-3}$ m/m	5×10^{-6} m/m
For N Measurement Blocks:			
Ranging Source ID	8	1 – 255	1
Pseudorange Correction ($PRC_{\tau 30}$)	16	±327.67 m	0.01 m
Range Rate Correction ($RRC_{\tau 30}$)	16	±32.767 m/s	0.001 m/s
$\sigma_{pr\_gnd,100}$ (Note 2)	8	0 - 5.08 m	0.02 m
$\sigma_{pr\_gnd,30}$ (Note 2)	8	0 - 5.08 m	0.02 m

Figure 28-Format of the message type 11

It is important to note that: 11111111 indicates the source is invalid

Then, once pseudorange measurements smoothed and corrected at the airborne, the navigation solution can be estimated and the Position Velocity and Time (PVT) solution established. The following section details this computation and also the performance assessment with the integrity monitoring associated.

3.3 Navigation Solution

Using the measurement models coming from the receiver signal processing module explained and detailed in the previous section, the computation of the position solution estimate can be realized. Moreover, as it was

shown in Chapter 2, it is necessary for civil aviation users to evaluate the system performances. That is why this section also presents the baseline integrity monitoring solution.

3.3.1 Position Computation

3.3.1.1 Distance Computation

In order to compute the position solution estimate, first, the true geometrical distance is introduced. Indeed, the true geometrical distance can be written for the epoch k as:

$$r_i(k) = \sqrt{(X^i(k) - X_u(k))^2 + (Y^i(k) - Y_u(k))^2 + (Z^i(k) - Z_u(k))^2}$$

Equation 87 – True geometrical distance expression

Where the vector (X^i, Y^i, Z^i) defines the Cartesian coordinates of the antenna phase center of the satellite i and $(X_u,\ Y_u,\ Z_u)$ defines the Cartesian coordinates of the antenna phase center of the user receiver u.

Then in the following parts, the computation of the position solution estimate is presented.

3.3.1.2 Least Squares Estimation

The Position Velocity and Time (PVT) computation consists by using a least squares estimation of the position of the aircraft. The standard single constellation algorithm applicable to both GPS and GALILEO is remind here as described in [32]. First, the state vector X is defined as the user receiver position and receiver clock bias:

$$X = \begin{pmatrix} X_u \\ Y_u \\ Z_u \\ b_u \end{pmatrix}$$

Equation 88- State Vector

Where (X_u, Y_u, Z_u) are the Cartesian coordinates of the antenna phase center of the user receiver, b_u represents the user receiver clock bias in meters defined by $b_u = c\Delta t_u$ (with Δt_u is the user receiver clock error in seconds and c the propagation velocity

It is important to note that in the Dual Constellation case (GPS and Galileo constellations) a fifth state will appear in the state vector according choices made on SESAR project for dealing with the second time reference system as mentioned in 3.2.2.1.

The observations used to compute the position are the corrected smoothed pseudorange $\widetilde{\Psi}^A$ in Equation 62 and Equation 63 (presented in 3.2.3.3.3 and 3.2.3.3.3) made by the receiver for each signal.

The input at each iteration of the Least Squares algorithm is defined with the estimated geometric range $\hat{r}^A$ defined in 3.2.3.3.3:

$$p = \widetilde{\Psi}^A - \hat{r}^A$$

By considering that the receiver is tracking at least N satellite signals to be used to compute the position estimate, then N non-linear equations can be obtained relating the observations to the state vector. For example for satellite i the following model is used to describe the input p^i:

$$\mathrm{p}^i(k) = \sqrt{(X^i(k) - X_u(k))^2 + (Y^i(k) - Y_u(k))^2 + (Z^i(k) - Z_u(k))^2} + c\Delta t_u(k) + e^i$$

Equation 89 – Pseudorange measurement for the satellite i

Where (X^i, Y^i, Z^i) defines the Cartesian coordinates of the antenna phase center of the satellite i and e^i is the collection of noise, multipath, and iono, tropo, satellite clock and ephemeris residuals after correction. It can be assumed to be a zero mean Gaussian noise of standard deviation σ^i (representing the total error model as detailed in previous section).

The Least Squares position solution is described in literature such in [32]. The measurement model can be expressed for the epoch k as:

$$P(k) = h\big(X(k)\big) + E(k)$$

Equation 90 – Initial Measurement model

Where $P = \begin{bmatrix} \mathrm{p}^1(k) \\ \vdots \\ \mathrm{p}^N(k) \end{bmatrix}$ represents the measurement vector and $E = \begin{bmatrix} e^1(k) \\ \vdots \\ e^N(k) \end{bmatrix}$ defines the measurement error.

Since the measurements do not linearly depend on the true user position, an iterative least squares estimation technique is used. It implies the linearization of the measurement model around successive estimates of the receiver position.

Let's denote $\hat{X}_0(k)$ an initial estimate of $X(k)$. This initial estimate can be determined using past measurements or can be provided by other navigation means.

Assuming that $X(k) = \hat{X}_0(k) + \Delta X(k)$, the measurement model can be expressed as following:

$$P(k) = h\left(\hat{X}_0(k) + \Delta X(k)\right) + E(k)$$

Equation 91 – Linearized measurement model

Thus the model is linearized around $\hat{X}_0(k)$:

$$P(k) \cong h\left(\hat{X}_0(k)\right) + \frac{\partial h}{\partial X}\left(\hat{X}_0(k)\right) \times \Delta X(k) + E(k)$$

Equation 92 – Linearization around $\hat{\boldsymbol{X}}_{\boldsymbol{0}}(\boldsymbol{k})$ of the measurement model

The first order derivative that appears in this last equation is a $N \times 4$ matrix that can be expressed as:

$$H = \begin{bmatrix} \frac{\partial h^1}{\partial X}\left(\hat{X}_0(k)\right) & \frac{\partial h}{\partial Y}\left(\hat{X}_0(k)\right) & \frac{\partial h}{\partial Z}\left(\hat{X}_0(k)\right) & \frac{\partial h}{\partial b}\left(\hat{X}_0(k)\right) \\ \vdots & \vdots & \vdots & \vdots \\ \frac{\partial h^N}{\partial X}\left(\hat{X}_0(k)\right) & \frac{\partial h^N}{\partial Y}\left(\hat{X}_0(k)\right) & \frac{\partial h^N}{\partial Z}\left(\hat{X}_0(k)\right) & \frac{\partial h^N}{\partial b}\left(\hat{X}_0(k)\right) \end{bmatrix}$$

Equation 93 – First order derivative – Matrix H

These derivatives can be computed using Equation 89 and following expressions are obtained:

$$\frac{\partial h^i}{\partial X}\left(\hat{X}_0(k)\right) = \frac{\hat{X}_0 - X^i(k)}{\sqrt{\left(\hat{X}_0 - X^i(k)\right)^2 + \left(\hat{Y}_0 - Y^i(k)\right)^2 + \left(\hat{Z}_0 - Z^i(k)\right)^2}}$$

$$\frac{\partial h^i}{\partial Y}\left(\hat{X}_0(k)\right) = \frac{\hat{Y}_0 - Y^i(k)}{\sqrt{\left(\hat{X}_0 - X^i(k)\right)^2 + \left(\hat{Y}_0 - Y^i(k)\right)^2 + \left(\hat{Z}_0 - Z^i(k)\right)^2}}$$

$$\frac{\partial h^i}{\partial Z}\left(\hat{X}_0(k)\right) = \frac{\hat{Z}_0 - Z^i(k)}{\sqrt{\left(\hat{X}_0 - X^i(k)\right)^2 + \left(\hat{Y}_0 - Y^i(k)\right)^2 + \left(\hat{Z}_0 - Z^i(k)\right)^2}}$$

$$\frac{\partial h^i}{\partial b}\left(\hat{X}_0(k)\right) = 1$$

Equation 94 – Derivatives expressions

Where $\hat{X}_0(\mathrm{k}) = \begin{pmatrix} \hat{X}_0 \\ \hat{Y}_0 \\ \hat{Z}_0 \\ \hat{b}_0 \end{pmatrix}$

Therefore, the linearized model is written as:

$$P(k) - h\left(\hat{X}_0(k)\right) = H \times \Delta X(k) + E(k)$$

Equation 95- linearized model

Let's denote:

$$\Delta P(k) = P(k) - h\left(\hat{X}_0(k)\right)$$

Equation 96

Then the following formula can be expressed as:

$$\Delta P(k) = H \times \Delta X(k) + E(k)$$

Equation 97

Where $\Delta P(k)$ represents the deviation between the actual measurements and the predicted noiseless measurements that the receiver would have made if its position and clock delay were $\hat{X}_0(k)$.

The least squares estimate of $\Delta X(k)$ is then given by:

$$\Delta\hat{X}(k) = [H^T H]^{-1} H^T \times \Delta P(k)$$

Equation 98 – Least squares estimate

This solution is known as the Least Squares Estimation (LSE). It can be improved by having an a priori knowledge of the statistical distribution of the errors affecting the measurements. In this case, the Weighted Least Squares estimation can be used. This method is explained in the following section.

3.3.1.3 Weighted Least Squares Estimation

As mentioned before, an improvement of the standard LSE can be realized by having an a priori knowledge of the statistical distribution of the errors affecting the measurements. Indeed in previous case these error were assumed to have independent, zero mean distribution with a same variance for all errors, now they are assumed to have have a normal distribution defined as $N(0, \Sigma)$ where Σ is the measurement error covariance matrix $\Sigma = cov(E)$ and with Σ^{-1} named weight matrix. This matrix is defined with the variance of these errors for the N satellites as :

$$\Sigma = \begin{pmatrix} \sigma_1^2 & 0 & \cdots & 0 \\ 0 & \sigma_2^2 & & \vdots \\ \vdots & & \ddots & 0 \\ 0 & \cdots & 0 & \sigma_N^2 \end{pmatrix}$$

Equation 99 – Covariance Matrix

Therefore, the Weighted Least Squares estimation (WLSE) can be used: [32]

$$\Delta\hat{X}(k) = [H^T \Sigma^{-1} H]^{-1} H^T \Sigma^{-1} \times \Delta P(k)$$

Equation 100 – Weighted Least squares estimate

If S denotes the projection matrix:

$$S = [H^T \Sigma^{-1} H]^{-1} H^T \Sigma^{-1}$$

Equation 101 – Projection matrix

Thus,

$$\Delta\hat{X}(k) = S \times \Delta P(k)$$

Equation 102

$\Delta\hat{X}(k)$ is an estimate of $\Delta X(k)$ which is defined as the deviation between the initial estimate $\hat{X}_0(k)$ and $X(k)$. It is then possible to implement an iterative algorithm starting from an initial estimate $\hat{X}_0(k)$ and improving progressively this estimate through the comparison between the measurements and the predicted measurements for each estimated position. The iterative algorithm can be implemented to stop if $\Delta\hat{X}(k)$ has a sufficiently small norm.

The correction measurement variance presented in 3.2.3.4 is the input to the measurement error covariance matrix allowing the use of the Weighted Least Squares algorithm.

It is also possible to express the positioning error as a function of the measurement error by using the Equation 100:

$$\Delta\hat{X} = [H^T\Sigma^{-1}H]^{-1}H^T\Sigma^{-1} \times \Delta P$$

ΔP can be replaced by its expression which is given in Equation 97:

$$\Delta\hat{X} = [H^T\Sigma^{-1}H]^{-1}H^T\Sigma^{-1} \times (H \times \Delta X + E)$$

Equation 103

Then,

$$\Delta\hat{X} = \underbrace{[H^T\Sigma^{-1}H]^{-1}H^T\Sigma^{-1}H}_{I_N}\Delta X + [H^T\Sigma^{-1}H]^{-1}H^T\Sigma^{-1}E$$

Equation 104

With I_N the identity matrix.

Thus,

$$\Delta\hat{X} = \Delta X + [H^T\Sigma^{-1}H]^{-1}H^T\Sigma^{-1}E$$

Equation 105

And finally the positioning error can be expressed with :

$$\Delta X - \Delta\hat{X} = -[H^T\Sigma^{-1}H]^{-1}H^T\Sigma^{-1}E$$

Equation 106 – Positioning error expression

Where: $\Delta X - \Delta\hat{X} = \left(X - \hat{X}_0\right) - \left(\hat{X} - \hat{X}_0\right) = \left(X - \hat{X}\right)$ is the positioning error.

It is important to note that the covariance matrix of the error is defined as $[H^TH]^{-1}$in the LSE and $[H^T\Sigma^{-1}H]^{-1}$ in the weighted case. This quantities are relevant for assessing the performances and characterizing the integrity monitoring concept.

The following part of this report deals with the integrity monitoring concept in civil aviation.

3.3.2 Integrity Monitoring

3.3.2.1 Introduction

As mentioned in Chapter 2, civil aviation is a critical application that needs reliable navigation aids with performance within the requirements standardized by authorities such as ICAO (see 2.5) .Indeed, under the GPS SPS specifications [30], the probability of failure is less than 10^{-5} *per hour* and *per satellite* and therefore an integrity monitoring function is needed to meet the integrity risk requirement for aviation operations of the order of 10^{-7}. Therefore, the integrity monitoring systems have been built to meet the ICAO specifications.
The concept of GNSS integrity, defined as a measure of the trust on the correctness of the information (PVT) supplied by the navigation system, has been defined in this framework of civil aviation. This section presents the integrity monitoring concept.

To be used on aircraft, ICAO requires GNSS signals integrity to be monitored. This GNSS integrity monitoring can be achieved with different ways: [93]

- In an autonomous manner on board
    - Using redundancy on GNSS signals only (RAIM – Receiver Autonomous Integrity Monitoring)
    - Using additional information from other sensors (AAIM – Aircraft Autonomous Integrity Monitoring)
- Using a ground station such as GBAS (see 3.1.4.2)
- Using a network of ground stations such as SBAS (see 3.1.4.1)

These solutions are based on a combination of monitors designed to detect faults by comparing test statistics and thresholds outlined in section 3.3.2.1.1. and performance assessment (3.3.2.1.2) whose role is to guarantee that the integrity requirements is met.

3.3.2.1.1 Faults Monitors

As introduced before, ICAO requires GNSS signal integrity to be monitored. This could be achieved by detecting faults by using a combination of monitors which compare test statistics to thresholds. These monitors could be implemented either on the ground or the aircraft. For example RAIM is performed onboard within ABAS but SQM (Signal Quality Monitoring) within GBAS is performed on the ground. Once fault detection is made, to verify if the integrity requirement is met, performance must be assessed (3.3.2.1.2).

3.3.2.1.2 Performance Assessment

Once the position computed by the algorithm explained in 3.3.1 , it must be checked and the level of trust assessed. Integrity monitoring techniques currently employed in civil aviation are commonly based on checking the compliance with the integrity requirements by calculating statistical bounds of the position error termed protection levels [63].

According to [42], and the following SIS integrity trees in Figure 31 and Figure 32, the total SIS (non Aircraft) integrity risk requirement of 2×10^{-7}per approach (per 150s) is allocated. Then as shown in the figures called integrity trees (Figure 31 and Figure 32) , an allocation may be made between the different system states which depending upon the specific implementation may include a fault-free hypothesis and fault hypothesis relating to ranging sources and ground subsystems failures.

One means to ensure that the allocated integrity budgets are met is to compute a Protection Level. A protection level is a bound with its centre being at the true position that describes the region assured to contain the indicated position within the relevant domain. There are defined for the horizontal domain for operations from en-route down to NPA approaches as HPL, for the lateral and vertical domain for approaches with vertical guidance respectively as LPL and VPL.

Protection Levels are functions of the satellites and user geometry and the expected error characteristics: they are not affected by actual measurements. Their value is predictable given reasonable assumptions regarding the expected error characteristics.

The system assures that, in the absence of an integrity alert, the estimated position is within the volume defined by the HPL/LPL and VPL in compliance with the integrity risk P_{int} defined in 2.4.4 [63]:

$$p\left\{\left[\left(\left|\left(X-\hat{X}\right)_{\mathrm{H}}\right| > \mathrm{HAL/LAL}\right) \text{ or } \left(\left|\left(X-\hat{X}\right)_{\mathrm{v}}\right| > \mathrm{VAL}\right)\right] \text{ and [no alert]}\right\} \leq P_{int}$$

Where $\left(X-\hat{X}\right)_{\mathrm{H}}$and $\left(X-\hat{X}\right)_{\mathrm{V}}$are the horizontal and vertical positioning errors.

When any of the protection levels exceeds the alert limit, the integrity monitoring system is declared unavailable because it is not able to assure that the estimated position is within the volume defined by the HAL (or LAL) and VAL specified in the SIS requirements [63]:

$$(\mathrm{HPL} \leq \mathrm{HAL})\ (\mathrm{or}\ (\mathrm{LPL} \leq \mathrm{LAL})) \text{ and } (\mathrm{VPL} \leq \mathrm{VAL}) \Rightarrow \text{ available integrity monitoring}$$

$$(\mathrm{HPL} > \mathrm{HAL})(\mathrm{or}\ (\mathrm{LPL} > \mathrm{LAL}))\ \text{ or } (\mathrm{VPL} > \mathrm{VAL}) \Rightarrow \text{ unavailable integrity monitoring}$$

The following figure illustrates the relationship between Protection levels and Alert levels.

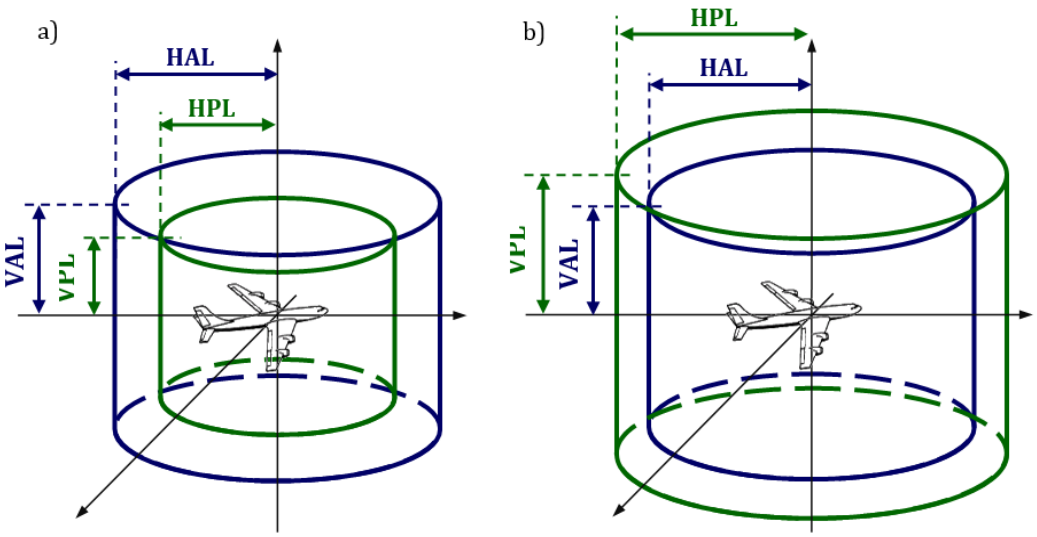

Figure 29-Relationship between alert and protection levels: a) available integrity monitoring system, b) unavailable integrity monitoring system [63]

As already introduced in Chapter 2 and 3.1.3.1, standalone GPS capabilities as described in [1], cannot meet certain civil aviation SIS performance requirements like the accuracy for precision approaches or integrity monitoring for any operation. For this reason different augmentation systems (already presented in 3.1.4) have been implemented to enhance GPS performance and allow its use in civil aviation operations within the ICAO requirements. Among other services, augmentation systems provide GNSS integrity monitoring and their corresponding protection levels are the means for which errors are overbounded [63] [42]. These systems with their Integrity concepts are presented in the following part of this report.

3.3.2.2 Augmentations

Augmentation systems are classified into three types according to the source from which the user receives the augmentation information:

- Aircraft Based Augmentation System (ABAS): the augmentation information is autonomously calculated within the aircraft equipment
- Ground Based Augmentation System (GBAS): the augmentation information is sent from a ground-based transmitter (see 3.1.4.2)
- Satellite Based Augmentation System (SBAS): the augmentation information sent is from a satellite based transmitter (see 3.1.4.1)

3.3.2.2.1 Aircraft Based Augmentation Systems Integrity Concept

ABAS is an augmentation system that uses exclusively information available on board the aircraft. It may employ only GNSS information or provide a hybridized navigation solution that integrates other sensors like bArometric altimeters or inertial navigation systems (INS).

ABAS provides integrity monitoring for the position solution using redundant information that is within the GNSS constellation. Unlike other types of augmentations of the GBAS and SBAS type, ABAS augmentation does not improve positioning accuracy without including any additional systems like inertial sensors. The ABAS integrity monitoring scheme [94], denoted fault detection and exclusion (FDE) is made on-board.

Fault Detection and Exclusion (FDE) is a receiver processing scheme that autonomously provides integrity monitoring for the position solution. The FDE consists of two distinct parts: fault detection and fault exclusion. The fault detection (FD) part detects the presence of an unacceptably large position error for a given mode of flight. It allows to make sure of the integrity of the received signals. Once detection achieved, fault exclusion allows to exclude the source of the unacceptably large position error, thereby allowing navigation to return to normal performance without an interruption in service (continuity of navigation). The fault detection aspects of FDE are referred to as Receiver Autonomous Integrity Monitoring (RAIM). However, FDE also includes the capability to isolate and exclude failed ranging sources so that navigation can continue in the presence of the failure [63].

Both FD and FDE are detailed on the following figure which derives concepts presented in 2.4 about the loss of continuity and the loss of integrity.

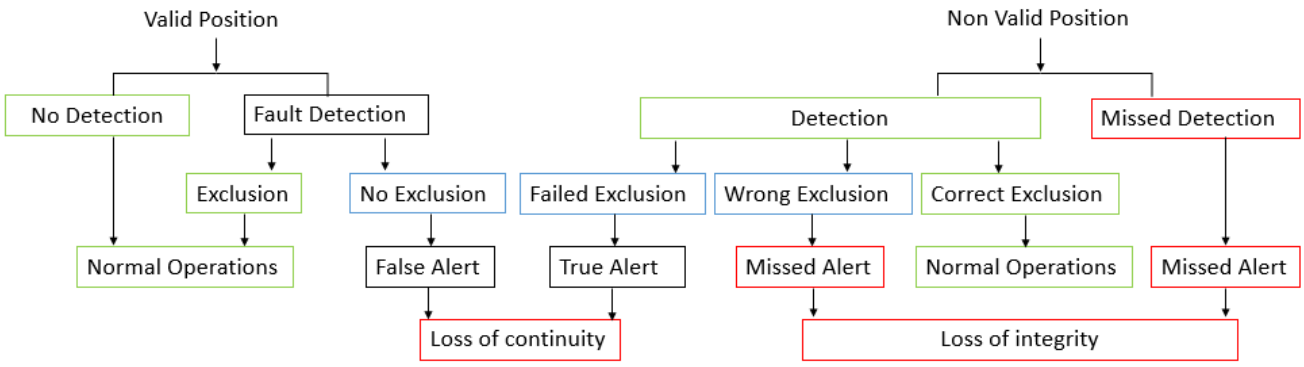

Figure 30-Continuity and Integrity Decision Process

Then the FD function performance regarding the ICAO requirements has to be assessed. Indeed, the FD performances are measured by computing protection levels, it is detailed in the following part of this report.

ABAS are referred as Receiver Autonomous Integrity Monitoring (RAIM) when GNSS information (range measurements) is exclusively used and as Aircraft Autonomous Integrity Monitoring (AAIM) when information from additional on-board sensors (e.g. barometric altimeter, and Inertial Navigation System, INS) is also used. For the performance assessment and determination of protection levels [29], computations are realized on board also.

For this ABAS systems, FD principle assumes that only one range failure may occur at a time (for the SBAS FDE write-up) and without integration with INS) and for designing the integrity monitoring algorithm and evaluating performances some assumptions were identified as the fact as the pseudorange error model, the threat model and the internal probabilities. For evaluating performances, systematic errors are gathered in the fault-free case

(assuming that components (and therefore the resulting pseudorange error) have a normal distribution with a known variance and a zero mean) and the unusual errors (when a large error in range measurement can cause an integrity failure) are gathered in the faulty case. Today the RAIM threat model is defined for Satellite failure and for AAIM the abnormal atmospheric errors or inertial drift have to be accounted too.

3.3.2.2.2 Satellite Based Augmentation Systems Integrity Concept

For the SBAS integrity concept, this is quite different to ABAS because FDE of the signal is performed on the ground. Indeed, The SBAS FDE function is achieved by the ground segment through monitors such as Signal Quality Monitoring, interference monitor, data checks as well as position monitor [37]. For the Performance assessment and determination of protection levels [32], computations are realized on board at each epoch as for ABAS by combining parameters transmitted by the ground segment, airborne parameters and satellites geometry. As shown by the integrity tree [63], the fault-free case integrity concept covered by Protection level computations assumes that there is no satellite failure, no ground system failure and no receiver failure. The ground system integrity cover faulty satellites, corruption of data through GEO link and Hardware network failure.

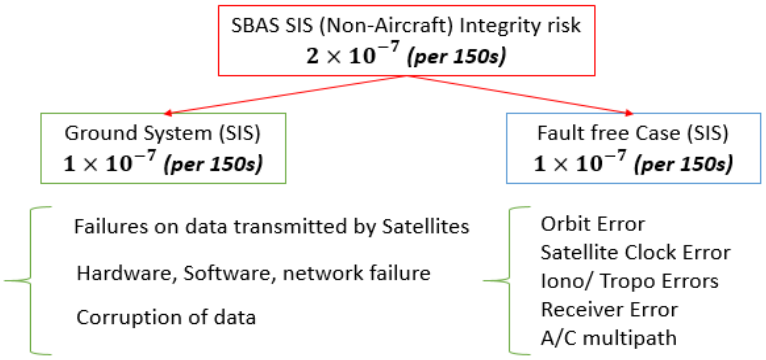

Figure 31-SBAS SIS integrity Tree

It is relevant to remind that integrity messages are received by SBAS users thanks to geostationary satellites (see 3.1.4.1.)

Therefore, SBAS integrity service is supposed to protect users from:

- GPS Satellites and geostationary satellites failures by detecting and excluding faulty satellites thanks to GPS measurements made by reference ground stations.
- Transmission of inaccurate differential corrections due to ground segment failures for example.
- Ionospheric Anomalies

For the Performance assessment, SBAS protection levels computations are standardized and can be found in [63].

3.3.2.2.3 GBAS Integrity Concept *7

As introduced in 3.1.4.2, GBAS integrity monitoring relies on local-area differential corrections computed thanks to the reference receivers, and it is transmitted to the users by the ground transmitter in the VHF frequency band of ILS – VOR systems (108 MHz – 118 MHz). Apart from integrity monitoring, GBAS ground subsystem provides additional information, including the approach path definition and local-area differential pseudorange corrections.

It is important to remind here that in this GBAS case, SIS integrity is monitored by the ground subsystem which checks the quality of all the system signals to allow a timely detection and failure indications that would cause a normal use of the signals to be hazardous for the user [93] [32]. The following integrity tree allocates each probability risk to subsystems [95].

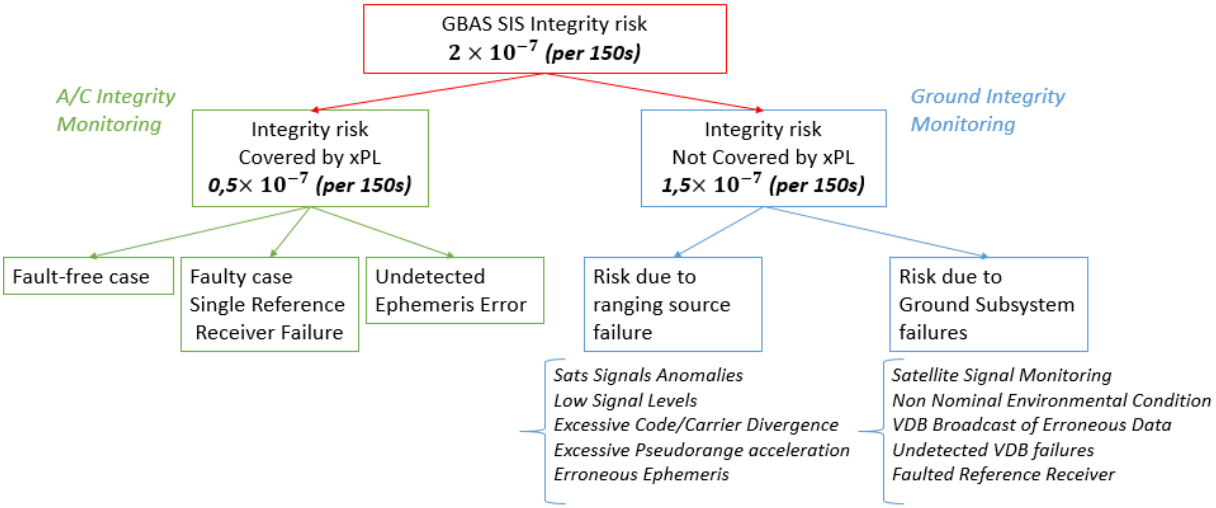

Figure 32-GBAS Integrity tree

Therefore, the VPL and LPL computed by the airborne GBAS receiver assumes two important things: at first the airborne receiver is fault-free therefore pseudoranges corrected by GBAS data are affected by noise only (the other failures being detected by the ground subsystem) and one of the reference receiver may be faulted.

As presented in section 3.2.3.3.2 and in following section 3.3.2.2.3.2, measurements made by several reference receivers are averaged together to produce PRC and RRC for all satellites in view, while “B-values” are computed (3.2.3.3 and 3.3.2.2.3.1.1) to detect and isolate failed reference receivers whose measurements diverge from the consensus of the remaining receivers. In parallel, series of monitors [78] are used to detect potential satellite clock, ephemeris, and signal failures, while specialized monitoring and geometry screening are used to mitigate the threat of ionospheric spatial anomalies that could make GBAS corrections significantly erroneous at nearby user aircraft.

Indeed, during GBAS based operations, irregular temporal and spatial Total Electron Content (TEC) gradients linked to ionospheric delays (see section3.2.2.2) may generate errors on the pseudo range measurements for the following reasons:

- Receivers use code-carrier smoothing filters with a relatively long time constant (30s and 100s) to smooth code pseudo-range measurements during GBAS approaches. Because of the irregular temporal variations of the TEC (and thus of the ionosphere ranging error) These errors on the code pseudo-range measurements may create significant errors in the position domain.
- When radio wave signals cross the ionosphere through spatial TEC gradients they are affected diffently than through a homogenously ionized layer. In the case of augmentation systems that use local differential ionosphere corrections, such as GBAS, if reference receivers and airborne receiver do not experience the same TEC, the correction that the ground subsystem broadcast to the airborne receiver to correct the given ionosphere error will not match the ionosphere error experienced by the aircraft. This creates a residual ranging error on the GBAS corrected pseudo range measurements.

Following sections detail the GAST C integrity monitoring concept and changing relative to the introduction of the GAST D.

3.3.2.2.3.1 GAST C

For GAST C, the ground station is responsible for mitigating all possible integrity threats and for checking if reference receivers are faulty or not by computing B-values (3.2.3.3.2). The airborne receiver has only to check if receivers are faulty or not (with B-values), to apply differential corrections (PRC/RRC) to its own measurements as mentioned in 3.2.3.3 and to compute the ephemeris error position bound. That means that aircraft is only responsible for their own measurement errors. In order to assess performances by computing Protection Levels (PLs) (and Ephemeris Error Position bounds) and comparing them to their corresponding Alert Limits (ALs). If PLs exceeds ALs, then, safety is not ensured and pilot is alerted and has to abort the approach. The approach is simpler for the airborne subsystem than for ground subsystem because this last one has to ensure it can mitigate totally integrity that in order for the ground receiver to be assumed as fault-free when performance assessment is made at user.

Several monitors are compulsory on ground to ensure ranging source integrity [96]:

- SQM (Signal Quality Monitoring): which detects satellite signal deformation, low signal power and Code-Carrier divergence (known as CCD monitoring) .This CCD monitor can also be used to help detect ionospheric fronts but the major disadvantage is that it requires a time history of measurements and cannot detect ionospheric fronts present at satellite acquisition
- DQM (Data Quality Monitoring): which detects anomalies in satellite navigation data (clock/ephemeris data)

- MQM (Measurement Quality Monitoring): Which detects step, ramp and acceleration errors in reference receiver measurements (may be due to satellite or receiver faults)
- MRCC (Multiple Receiver Consistency Check): Which computes B-values that compare measurements among reference receivers and uses them to detect reference receiver failures.
- $\sigma\mu$-Monitor (Sigma-Mean Monitor): Which collects B-values over time and uses them to detect violations of the broadcast pseudo-range correction error (σ_{pr_gnd}) and assumed mean of zero.

Then integrity parameters are broadcasted to the airborne such as B-values (3.2.3.3 and 3.3.2.2.3.1.1).

Reminding from 3.3.2.1.2 and the integrity tree Figure 32, the total SIS integrity risk requirement of 2×10^{-7}per approach is allocated. Then a quarter of this total is split evenly between the fault-free Hypothesis (H0) and the single-receiver fault (H1) Hypothesis [96].

The PLs for both hypothesis and the Ephemeris Error Position Bounds computations are detailed in the following section

3.3.2.2.3.1.1 Protection Levels and Ephemeris Error Position Bound

In this section, both PLs and Ephemeris error position bound are explained. These values are used for integrity monitoring and also for checking the higher level GAST possible.

First, it is important to remind here that the VPL and LPL computed by the airborne GBAS receiver assumes [97]:

- A fault-free airborne receiver
- Pseudoranges corrected by GBAS data affected by noise only (the other failures being detected by the ground subsystem,
- Plus the assumption that one of the reference receiver may be faulted (different from SBAS)

In order to well understand this computation it is important to remind the H_0 and H_1 hypothesis extracted from [42].

- H_0 hypothesis: It assumes the situation where no faults are present in the range measurements used in the ground station to compute the differential corrections.
- H_1 hypothesis: It assumes the situation when a fault is present in one or more range measurement and is caused by one of the reference receivers used in the ground station.

As it is described in detail in [42] lateral and vertical protection levels of the SIS, computed for each Type 1 message, relative to the selected approach segment (VPL_{Apr} and LPL_{Apr}) with the determination of the lateral and vertical protection levels for H_0 and H_1 hypothesis ($VPL_{Apr_{H0}}$, $LPL_{Apr_{H0}}$, $VPL_{Apr_{H1}}$ and $LPL_{Apr_{H1}}$).

$$LPL_{Apr} = max\left[LPL_{Apr_{H0}}, LPL_{Apr_{H1}}\right]$$

$$VPL_{Apr} = max\left[VPL_{Apr_{H0}}, VPL_{Apr_{H1}}\right]$$

Equation 107 – Lateral and vertical protection levels relative to the selected approach segment

Under H_0 hypothesis, it is defined:

$$VPL_{Apr_{H0}} = K_{ffmd}\sqrt{\sum_{i=1}^{N} s^2{}_{Apr_{vert},i}\sigma^2{}_i}$$

$$LPL_{Apr_{H0}} = K_{ffmd}\sqrt{\sum_{i=1}^{N} s^2{}_{Apr_{lat},i}\sigma^2{}_i}$$

Equation 108 - Lateral and vertical protection levels under H_0 hypothesis

Also, by seeing these equations, $\sigma_{Apr\_vert\_H0}$ and $\sigma_{Apr\_lat\_H0}$ are defined through these notations:

$$\sigma^2{}_{Apr\_vert\_H0} = \sum_{i=1}^{N} s^2{}_{Apr_{vert},i}\sigma^2{}_i$$

$$\sigma^2{}_{Apr\_lat\_H0} = \sum_{i=1}^{N} s^2{}_{Apr_{lat},i}\sigma^2{}_i$$

Where K_{ffmd} is the multiplier (unitless) which determines the fault free P_{md} (values can be found in the table 2-16 of [42],Parameters $s_{Apr_{lat},i}$ and $s_{Apr_{vert},i}$ are respectively the projection of the lateral components for the satellite i and the projection of the vertical component and translation of the along track components into the vertical for the satellite I of the S matrix (defined by Equation 101). N is the number of ranging sources used in the position solution and $\sigma^2{}_i$ is the total error measurement model and has been described in detail in previous section: 3.2.3.4. This last parameter will depend on the active Approach Service Type.

Under H_1 hypothesis, the protection level is defined as:

$$VPL_{Apr_{H1}} = max\left|VPL_{Apr_{H1}}[j]\right|$$

$$LPL_{Apr_{H1}} = max\left|LPL_{Apr_{H1}}[j]\right|$$

Equation 109- Lateral and vertical protection levels under H_1 hypothesis

Where $VPL_{Apr_{H1}}$ and $LPL_{Apr_{H1}}$ are computed with:

$$VPL_{Apr_{H1}}[j] = \left|B_{j\_Apr_{vert}}\right| + K_{md}\sigma_{Apr\_vert\_H1}$$

$$LPL_{Apr_{H1}}[j] = \left|B_{j\_Apr_{lat}}\right| + K_{md}\sigma_{Apr\_lat\_H1}$$

Where j defines the ground subsystem reference receiver index, K_{md} is the multiplier (unitless) which determines the P_{md} given when the ground subsystem is faulted. Values can be found in the Table 2-17 of [42].

In the case that receiver is not faulted, that means if B-value exists for it (3.2.3.3.2) ,$B_{j\_Apr_{vert}}$ and $B_{j_Apr_{lat}}$are defined with these equations:

$$B_{j\_Apr_{vert}} = \sum_{i=1}^{N} s_{Apr_{vert},i} B[i,j]$$

$$B_{j\_Apr_{lat}} = \sum_{i=1}^{N} s_{Apr_{lat},i} B[i,j]$$

With $B[i,j]$ is the B value (in meters) for the i^{th} ranging source and j^{th} reference receiver as indicated in the Type 1 message(Table 20) and computing as in3.2.3.3.2 .

In a same way, $\sigma_{Apr\_vert\_H1}$ and $\sigma_{Apr\_lat\_H1}$ are defined through these equations:

$$\sigma^2{}_{Apr\_vert\_H1} = \sum_{i=1}^{N} s^2{}_{Apr_{vert},i} \sigma^2{}_{i\_H1}$$

$$\sigma^2{}_{Apr\_lat\_H1} = \sum_{i=1}^{N} s^2{}_{Apr_{lat},i} \sigma^2{}_{i\_H1}$$

With $\sigma^2{}_{i\_H1} = \left(\frac{M[i]]}{U[i]}\right) \sigma^2_{pr_{gnd\_x,i}} + \sigma^2_{pr\_air,i} + \sigma^2_{tropo,i} + \sigma^2_{iono,i}$, where U[i] is the number of ground subsystem reference receivers whose pseudorange measurements were used to determine the differential correction for the i^{th} ranging source used in the navigation solution, not counting the j^{th} reference receiver. And M[i] is the number of ground subsystem reference receivers whose pseudorange measurements were used to determine the differential correction for the i^{th} ranging source used in the navigation solution (determined from B-values in the Type 1 message). The value $\sigma^2_{pr_{gnd\_x,i}}$ and therefore $\sigma^2{}_{i\_H1}$ depend on the Approach Service type as defined in 3.3.2.2.3.2.3

Then the Ephemeris Error Position Bounds are defined in Vertical and Lateral for the ranging source j as VEB_j and LEB_j respectively.

$$VEB = \max(VEB_j) = \left|s_{Apr_{vert},j}\right| x_{air} P_e + K_{md\ e} \sqrt{\sum_{i=1}^{N} s^2{}_{Apr_{vert},i} \sigma^2{}_i}$$

$$LEB = \max(LEB_j) = \left|s_{Apr_{lat},j}\right| x_{air} P_e + K_{md\ e} \sqrt{\sum_{i=1}^{N} s^2{}_{Apr_{lat},i} \sigma^2{}_i}$$

Where x_{air} is the distance between the aircraft and the GBAS ground station , P_e is the ephemeris decorrelation parameter and depend on the Approach Service type as defined in 3.3.2.2.3.2.3, $K_{md\ e}$ is an Approach Service

Type dependent broadcast multiplier(3.3.2.2.3.2.3) from the probability of missed detection given that there is an ephemeris error in a satellite.

If VEB or VPL exceed the alert limit, the corresponding approach service type C is invalidated. The same is applied for LEB or LPL

In the following section a comparison with GAST D integrity monitoring is made. Indeed, new monitors and new considerations are presented.

3.3.2.2.3.2 GAST D

3.3.2.2.3.2.1 Introduction

As it was said previously, the introduction of the concept of GAST D and the fact that associated requirements are much more challenging to achieve the CAT II/III operation level, lead to an important new consideration that can be seen as a responsibility transfer between the ground station and the airborne part. Indeed, firstly, for this new concept, the ground station protects the aircraft in the range domain instead of protecting it in the position domain (as GAST C) by monitoring each GPS measurement against an acceptable error limit. Secondly, even if the aircraft can take into account integrity alerts with regard to exceeded erroneous measurements it is the airborne receiver which has now the responsibility to select satellite geometry because considering that the aircraft knows its own geometry is less conservative than assuming a degraded geometry at ground as it was made in GAST C. Indeed, this screening was realized through inflation of a broadcast parameter in GBAS whose geometries should not be used. This concept is named “geometry screening”. [98]. Finally, the mitigation of errors induced by anomalous ionospheric condition has been allocated to both the airborne system [42] by adding a Dual Solution Ionospheric Monitoring Architecture (DSIGMA) monitor algorithm and the ground subsystem by implementing the Ionospheric Gradient Monitoring .This transfer of responsibility can take advantages of the benefits obtained by using modern aircraft guidance systems and the airborne receiver better knowledge of the current state of the integrity threats.

Furthermore, the evolution of GAST C to GAST D has involved some changes and additions to monitors and protection levels in the ground and airborne facilities.

For the airborne side, several modifications of existing algorithms and the inclusion of new monitors are required [96] such as : adding some monitors: airborne Code Carrier Divergence(CCD) monitor, a Dual Solution Ionospheric Monitoring Architecture (DSIGMA) monitor, Bias Approach Monitor (BAM), Reference Receiver Fault Monitor(RRFM) and Geometry screening monitor, doing a new Differential Correction Magnitude Check (DCMC), modify the Fault Detection algorithm.

These new monitors are represented by red box in the following figure extracted from MOPS [16]:

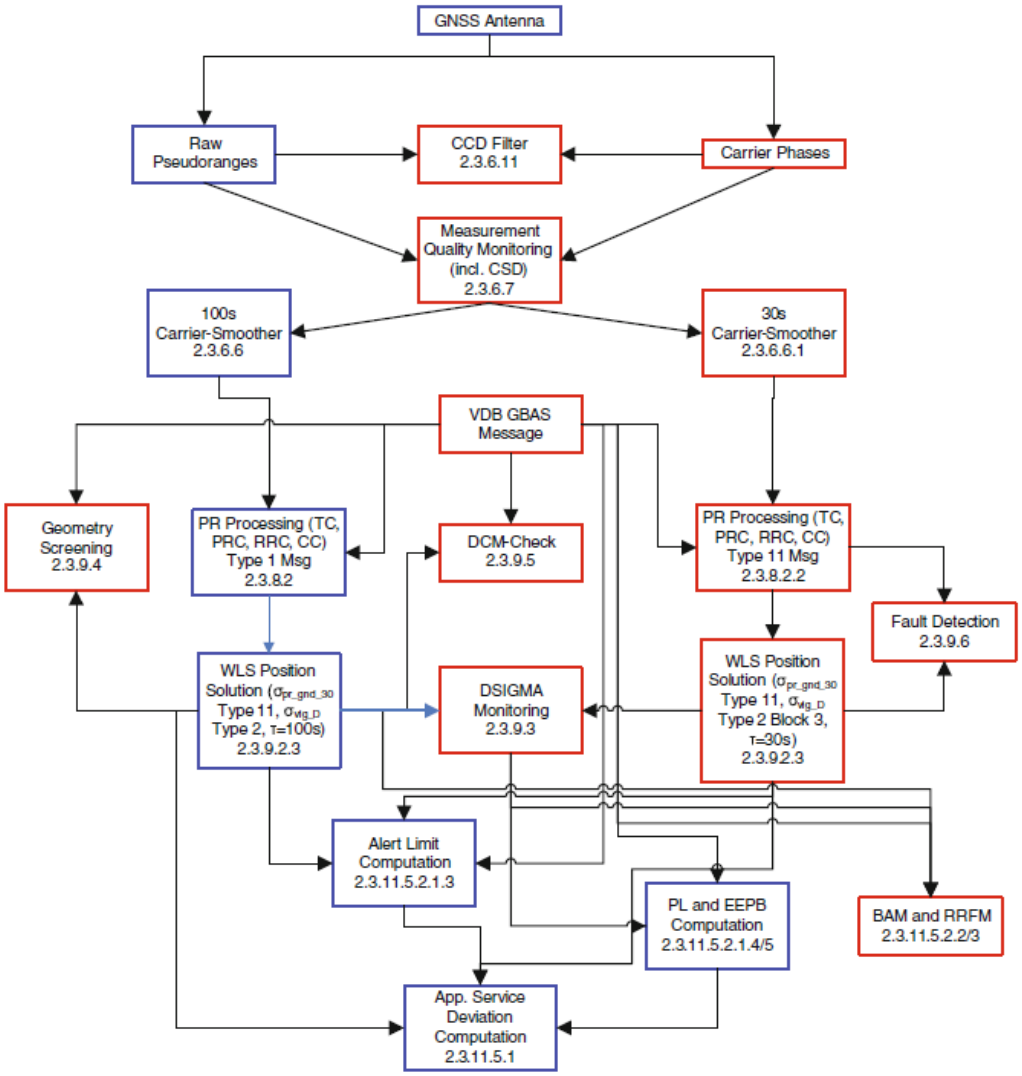

Figure 33-GAST D Aircraft Architecture [16]

For the ground side, other modifications are needed concerning : CCD monitor, Absolute Gradient Monitors (IGM: Ionospheric Gradient Monitor), introduction of pseudorange corrections from 30 seconds smoothed measurements in addition to the standard 100 second corrections and in addition of messages for GAST C : Providing Message type 11 and additional data block in Message type 2 (3.2.3.4.3)

It is important to keep in mind that for GAST D according MOPS [42], it is required that the position used in the elaboration of guidance information comes from the differential PVT using the 30s carrier smoothed corrected measurement.

This section describes some of these new considerations and modifications at the aircraft due to the introduction of the GAST D integrity concept.

3.3.2.2.3.2.2 Airborne Code Carrier Divergence (CCD) Monitor

It is relevant to remind the fact that within the ground facility there is already a CCD monitor but its aim is to detect Code Carrier Divergence resulting from a satellite payload fault. However, it can also be used to detect anomalous ionospheric conditions but it could be enable to do this in some satellite geometries or during ionospheric front movement. So for GAST D, the CCD monitor within the airborne equipment is compulsory. According to [42] in the section 2.3.6.11, the purpose of this monitor is to detect abnormally large gradients in the ionospheric delay that could cause unacceptable errors in the differential position solution. It uses two consecutive code-minus carrier measurements to achieve this. [99]

3.3.2.2.3.2.3 Dual Solution Ionospheric Gradient Monitoring (DSIGMA)

The airborne equipment when supporting GAST D uses this monitor to detect certain errors due to smoothing filter lag and significant ionospheric delay gradients. For this purpose, two smoothing filters (with the two specific smoothing time constant as described in described in 3.2.3.2) are required within both a ground facility and an airborne receiver.

Indeed, as described in [42] the equipment when supporting GAST-D shall compute the difference between the 30s smoothed and the 100s smoothed position solutions. If the absolute value of these differences in the vertical (D_V)or lateral (D_L)direction exceeds 2meters the airborne equipment shall change the active Approach service type to GAST C and outputs associated or use a subset geometry for which this test passes.

The functional architecture of DSIGMA is illustrated by the following figure:

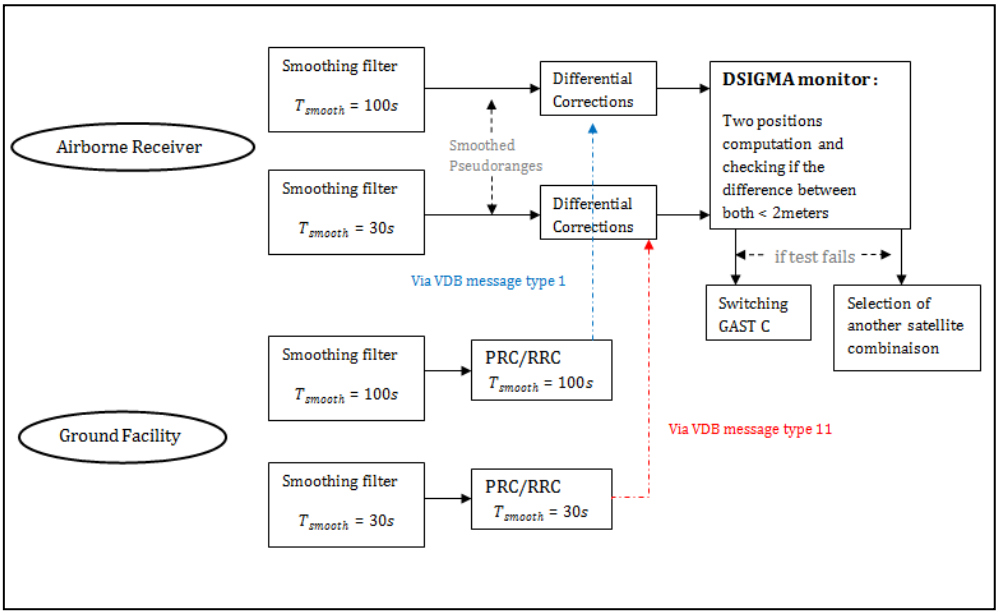

Figure 34-DSIGMA principle

According to [42], the following requirements apply:

- A position solution shall be computed based on 100s smoothed pseudoranges corrected with corrections obtained from message type 1

- A second position solution used to determine deviations shall be computed based on 30s smoothed pseudoranges corrected with corrections obtained from message type 11
- The projection matrix (A) is used for both position solutions. This A is computed based on values computed with values extracted from message Type 11 and Type 2 additional data block 2 using time constant of 30s

3.3.2.2.3.2.4 Reference Receiver Fault Monitor (RRFM)

As it is already presented at the beginning of this section the airborne GBAS receiver assumes that one of the reference receivers may be faulted. For GAST D, the threat of single ground reference receiver (RR) faults (H_1 hypothesis) is mitigated by an error estimation process in the ground station and a monitor at the aircraft [100].

The RRFM is responsible for the detection errors within the reference receiver of the ground facility. To achieve this, it uses the B-values broadcasted by the ground subsystem and checks if they are within the tolerable limits. Details on RRFM evaluations are given in [42].

3.3.2.2.3.2.5 Fault Detection (FD)

According to [42], equipment supporting GAST D shall perform FD for satellite addition (or to detect errors not detected by other monitoring algorithms) at least once after CCD monitor output has converged below its threshold. This is a RAIM-like algorithm (detailed in [42]) that uses redundant satellite measurements to detect faults with a probability of at least 1×10^{-7}per sample. The Satellite measurement shall not be added to the precision approach position solution until the 20-minute observation period required by the airborne CCD monitor has elapsed but this satellite measurement can be added early if the FD allows.

3.3.2.2.3.2.6 Satellite Geometry Screening

As mentioned in the introduction of this section, the airborne receiver in the case of GAST D has the responsibility to select satellite geometry. This is called “geometry screening”. The purpose of this processing is to limit the influence of a single satellite on the total position solution. This ensures that a single satellite measurement cannot result in a hazardous error in the position domain. [99]

Therefore, the aircraft continuously screens geometry of satellites to ensure that the projection of a single pseudorange errors into the position domain does not become too large. This is achieved by limiting the magnitude or elements inside the projection matrix S (Equation 101) to a maximum value S_{max}. Two checks are realized: first individual value of S are checked against the typical value of S_{max} = 4 and then a second check is made for couple of values of S whose addition is compared to 6 [16] .If one of the check appears true (values>limit) the satellite is removed to the geometry and S is rebuilt with a new satellite geometry.

3.3.2.2.3.2.7 Protection Levels

Furthermore, according to the document [42], several modifications have to be taken into account into GAST D for the VPL and LPL computation.

Indeed the $VPL_{Apr_{H0}}$ and $LPL_{Apr_{H0}}$ are modified with the addition of new parameters D_V and D_L as:

$$VPL_{Apr_{H0}} = K_{ffmd}\sqrt{\sum_{i=1}^{N} s^2{}_{Apr_{vert},i}\sigma^2{}_i} + D_V$$

$$LPL_{Apr_{H0}} = K_{ffmd}\sqrt{\sum_{i=1}^{N} s^2{}_{Apr_{lat},i}\sigma^2{}_i} + D_L$$

Equation 110 - Lateral and vertical protection levels under H_0 hypothesis

Under H_1 hypothesis, the new protection level are now defined as:

$$VPL_{Apr_{H1}} = max\left|VPL_{Apr_{H1}}[j]\right| + D_V$$

$$LPL_{Apr_{H1}} = max\left|LPL_{Apr_{H1}}[j]\right| + D_L$$

Equation 111- Lateral and vertical protection levels under H_1 hypothesis

D_V is the magnitude of the vertical projection of the difference between the 30s smoothed position solution and the 100s smoothed position solution (D_V = 0 for GAST C) (see 3.3.2.2.3.2.3) and D_L is the magnitude of the lateral projection of the difference between the 30s smoothed position solution and the 100s smoothed position solution (D_L = 0 for GAST C) (see 3.3.2.2.3.2.3)

It is important here to note that according to [42] [101], for GAST-D the broadcasted values used in $\sigma^2{}_i$ for computing Protection Levels is the one corresponding to 100s smoothing constant for the ground subsystem error contribution$\sigma_{pr_gnd_D} = \sigma_{pr_gnd_100}$. Whereas, the broadcasted value $\sigma_{pr_gnd_30}$is used in the $\sigma^2{}_i$ computation for building the weighted matrix (in Equation 100) and therefore the projection matrix (in Equation 101).

The value $\sigma^2_{pr_{gnd\_x,i}}$ and therefore $\sigma^2{}_{i\_H1}$ are modified for GAST-D because they depend on the Approach Service type as defined in 3.3.2.2.3.2.3

For the ephemeris error position bound computation, the parameters such as P_e and $K_{md\ e}$ will be also changed according this new approach type D.

3.3.2.2.3.2.8 Bias Approach Monitor (BAM)

This new monitor in the airborne side ensures that the projection of the FAS (Final Approach Segment) path realized in the airborne equipment passes within a window defined by the FASVAL(Final Approach Segment Vertical Alert Limit defined as the Vertical Alert Limit for the selected approach in [42]) value with high confidence. This evaluation includes two different checks described in [42]

3.3.2.2.3.2.9 Differential Correction Magnitude Check (DCMC)

The DCMC limits the overall magnitude of all corrections that are applied to the pseudorange measurements. To achieve this, the Horizontal Position Differential Correction Magnitude (HPDCM) of all corrections is limited to a maximum distance of 200 meters.

3.4 Conclusions

This chapter has described how to use the smoothed and corrected measurement models for estimating the position solution. Moreover, some methodologies were presented for measuring the trust on the correctness of this position by detailing integrity monitoring concepts for GNSS systems.

The following chapters focus on the particular case of Multi-Constellations/Multi-frequency GBAS (MC/MF GBAS). Indeed, some investigations into the use GAST D are still ongoing [9]. However, some gaps in performance have been identified and open issues remain [87]. The MC/MF GBAS solutions are studied within the European SESAR program (WP 15.3.7) to address and solve these issues. In this report, optimal processing models and options for this concept are proposed and analysed

Chapter 4 : Optimal Processing Models/Options for MC/MF GBAS

4.1 Introduction

As already mentioned before, after some examinations into the use of GAST-D, several gaps in performance and issues remain [47] [52] such a lack of freedom to account for new signals and new constellations, siting constraints, some validation issues concerning threat model and monitoring concept due to ionospheric disturbance, issues relative to the vulnerability to interference or jamming on L1 frequency and the sensitivity to critical geometries in case of degraded constellation. The Multi-Constellation (MC)/Multi-Frequency (MF) GBAS solutions are under investigation into the SESAR project and intend to solve these issues. The addition of a secondary constellation provides many advantages such as better geometry, robustness against signal outages, relaxing of demanding constraints. In addition, new signals offer the potential to combine measurements on multiple frequencies to mitigate the effects of the ionosphere as presented in 3.2.3.2.4 and 3.2.3.4.2.1.

However, with this evolution to the MC/MF GBAS some constraints appear, a major one deals with the available space for message transmission from the GBAS VHF Data Broadcast (VDB) unit [4]. Indeed, many proposals are currently investigated into the SESAR project to implement these MC/MF GBAS services and to solve these constraints [102]. Several different processing options were investigated within this project and were addressed in this PhD project. The following table reminds them and in which sections of the report they are presented.

Smoothing Types (SF/IF/Dfree)	Smoothing time constants τ	Correction Update Rate t_{AZ}	Measurement interval T	Tropospheric Modelling
3.2.3.2/3.3.2.2.3	3.2.3.2/3.3.2.2.3	4.3	3.2.3.3.2/Chapter 4	4.2.2/Chapter 5/ Chapter 6

Table 21-Differential Processing options

Therefore, these values τ, t_{AZ} and T have an important impact on the GAST-F design.

Moreover, today, corrections and their integrity are provided in combined messages broadcast every half second (2Hz). Extending this approach to multiple correction types, based on the different signals and observables for two or more constellations will not be possible. Furthermore, if future signals from the modernized constellations

are needed to be used or in view of the possible expansion further than two constellations then no additional transmission space would be available. That is why in this report, the possibility of providing corrections at a lower rate than the current 2Hz was examined, with a separate message type dedicated to providing the integrity status of each correction in a manner akin to the SBAS [103].

Also, in order to meet the most stringent requirements of Cat II/III precision approach operations several challenges and key issues must be solved relating to atmospheric modelling. Indeed, there are a number of arguments for revisiting this topic and specifically addressing the tropospheric threat. Firstly, unexpected atmospheric behaviour were observed during GAST-D ground prototypes validation activities [104]. The source could be related to a non-modelled behaviour of the troposphere. Secondly, in the advent of MC/MF GBAS, when using I-free smoothing technique, the main contributor to the atmospheric error will come from the tropospheric delay. That is why, this section contains also a specific analysis to the tropospheric modelling for both nominal and non-nominal cases.

In order to explain the selection of the optimal correction message rate, a number of items must be addressed such as the link between the correction message rate and the RRC, the RRC properties, the error modelling with the explicit application of RRC, the impact of this update rate on performances.

This section first develops the GBAS error modelling which critically contribute to the range-rate corrections in 4.2.1 ,for single frequency case and the proposed MF processing models in the form of the D-free and I-free smoothing techniques. Secondly, in 4.2.2 the specific case of the GBAS tropospheric error modelling is presented for both nominal and non-nominal cases. Then, the properties of the range-rate corrections are essential to understand how an increase in the correction update period will impact the total performance of the system therefore the current methodology and an innovative one are presented in 4.3. The total error budget is then derived which allows a quantification of the degradation in the corrections as a function of the message update rate. Finally, in 4.4, a performance benefits analysis is realized to evaluate the possibility of an increased update rate.

4.2 Error Model

4.2.1 Error Modelling

The GBAS error modelling was already presented in the previous section 3.2.3.4. But the error model was presented without explicitly showing the impact of the latency of the pseudorange correction (PRC). In this section, the impact of RRC is clearly shown and the corresponding error model after smoothing and correction (as illustrated by Figure 16) is detailed for single frequency and I-free cases.

4.2.1.1 Single Frequency Error modelling

4.2.1.1.1 Introduction

For GAST D both Message Type 1 (MT1) and Message Type 11 (MT11) are used to provide corrections with both 100s and 30s smoothing respectively [16] [84] [41].The longer smoothing constant corrections in MT1 mitigate to a greater extent the high frequency components of multipath and noise but suffer from greater ionospheric divergence than the 30s corrections contained in MT11. The measurement model used in this report is the same as the one presented in section 3.2 with Equation 18 and Equation 19and but applied to the ground:

$$\rho_1^G = r^G + b^G + J^G + \iota_1^G + \eta_{\rho_1}^G$$

$$\phi_1^G = r^G + b^G + J^G - \iota_1^G + N_1{}^G + \eta_{\phi_1}^G$$

Equation 112 - Ground error model for GBAS

$$\rho_1^A = r^A + b^A + J^A + \iota_1^A + \eta_{\rho_1}^A$$

$$\phi_1^A = r^A + b^A + J^A - \iota_1^A + N_1{}^A + \eta_{\phi_1}^A$$

Equation 113 – Aircraft error model for GBAS

Where r is the geometric range, ρ is the pseudorange measurement, ι is the ionospheric delay, J is the tropospheric delay, b is satellite clock error, η_ρ is the code-tracking noise and multipath, ϕ is the carrier-phase measurement, N is the range ambiguity and $\eta_\phi$is the carrier-tracking noise and multipath. $\blacksquare_1$ represents a variable for on the L1 signal, $\blacksquare^G$ is used for parameters relating to the ground receivers and $\blacksquare^A$ for those relating to the airborne receiver. Recalling the correction definitions defined in 3.2.3.3.2 and their associated models [16].

$$PRC_1 = r^G - \widehat{\Phi}_1^G = -b^G - J^G - I_1^G - \epsilon_1^G$$

$$RRC_{1,k} = \frac{PRC_{1,k} - PRC_{1,k-1}}{T} = -\dot{b}^G - \dot{J^G} - \dot{I}_1^G - \dot{\epsilon}_1^G$$

Equation 114 - Correction Error models

Where $\widehat{\Phi}_1^G$is the smoothed pseudorange observable, I is the smoothed ionospheric delay, J is the tropospheric delay, T defines the time between two consecutive epochs ϵ represents smoothed multipath and noise components and $\dot{\blacksquare}$ defines the discrete time derivative at t_G the time at ground station. The influence of the PRC-based receiver clock correction has been neglected in equations (4) and (5) as it introduces common mode-like errors which cancel in the airborne position solution. Furthermore, terms representing the tropospheric correction and the satellite clock correction are not represented in this analysis because they have no impact for the study. So at the airborne receiver as it was already mentioned in 3.2.3.3.2 and 3.2.3.3.3, the corrections are applied using the following expression:

$$\tilde{\Phi}_1^A(t_A) = \hat{\Phi}_1^A(t_A) + PRC_1 + t_{AZ}RRC_1$$

Equation 115 - GBAS Aircraft smoothed corrected pseudorange model

Where t_{AZ} represents the time between the modified time of correction generation t_Z and the time of application at the airborne receiver: $t_{AZ} = t_A - t_Z$, $\hat{\Phi}$ is the smoothed pseudorange measurement and $\tilde{\Phi}$ is the corrected pseudorange measurement.

Note by reminding 3.2.3.3.3, that terms representing the tropospheric correction and the satellite clock correction are not explicitly represented in Equation 115 because they are implicitly covered since b and J express the residual errors.

Therefore Equation 115 can be decomposed into error component by using Equation 112, Equation 113 and by reminding results obtained in 3.2.3.3.2:

$$\tilde{\Phi}_1^A(t_A) - \hat{r}^A = \left(dr^A - (dr^G + t_{AZ}d\dot{r}^G)\right) + \left(b^A - \left(b^G + t_{AZ}\dot{b}^G\right)\right) + \left(J^A - \left(J^G + t_{AZ}\dot{J^G}\right)\right) + \left(I_1^A - \left(I_1^G + t_{AZ}\dot{I}^G\right)\right) + \left(\epsilon_1^A - (\epsilon_1^G + t_{AZ}\dot{\epsilon}^G)\right)$$

Equation 116 - Detailed GBAS model for the input of the PVT algorithm

Where $\hat{r}^A$ is the estimated geometric range from aircraft to satellite introduced in 3.2.3.3.3.

Each components of this equation are detailed in following sections.

Indeed,

- $\left(dr^A - (dr^G + t_{AZ}d\dot{r}^G)\right)$ represents the residual differential Ephemeris error
- $\left(b^A - \left(b^G + t_{AZ}\dot{b}^G\right)\right)$ represents the residual differential Satellite Clock error
- $\left(J^A - \left(J^G + t_{AZ}\dot{J^G}\right)\right)$ defines the residual differential Tropospheric error
- $\left(I_1^A - \left(I_1^G + t_{AZ}\dot{I}^G\right)\right)$ defines the residual differential Ionospheric error
- $\left(\epsilon_1^A - (\epsilon_1^G + t_{AZ}\dot{\epsilon}^G)\right)$ represents the residual differential Multipath and Noise errors.

4.2.1.1.2 Residual Ephemeris Error

As presented in the introduction by viewing the Equation 116, the residual differential error due to Residual Ephemeris can be modelled by:

$$\delta dr = dr^A - (dr^G + t_{AZ}d\dot{r}^G)$$

Equation 117 - Residual differential ephemeris error

In order to correctly model the nominal residual ephemeris error and then to properly derive the total error in Equation 116 this previous equation can be decomposed into spatial and temporal components.

$$\delta dr = \underbrace{dr_1^A(t_A) - dr_1^G(t_A)}_{spatial} + \underbrace{dr_1^G(t_A) - \left(dr_1^G(t_G) + t_{AZ}\dot{dr}^G\right)}_{temporal}$$

Equation 118 - Spatial/temporal components of Ephemeris error

Because the RRC corrects for $\dot{dr}^G$, the temporal component is negligible and the mm level spatial error remains.Therefore the nominal residual ephemeris error is assumed to be:

$$\delta dr \approx dr_1^A(t_A) - dr_1^G(t_A)$$

Equation 119- Residual differential ephemeris error Approximation

4.2.1.1.3 Satellite Clock Error

As introduced in Equation 116, the residual differential error due to Satellite Clock can be modelled with a zero-mean Gaussian [52]:

$$\delta b = b^A - \left(b^G + t_{AZ}\dot{b}^G\right)$$

Equation 120 -Residual differential satellite clock error

With $\delta b \sim N(0, {\sigma_b}^2)$ and where σ_b is defined as it is described in details in [52] by the following expression:

$${\sigma_b}^2 = \left(1 + \frac{t_{AZ}}{T}\right) t_{AZ} AVAR(1s)$$

Equation 121 - Std of the residual differential satellite clock error

with $AVAR(1s)$ representing the Allan Variance at the order of 1s. These choice of 1s is done because the focus is made on the short term clock instability and therefore it is the same order of values as for 1s. Furthermore as shown in [52] the 1s case will be the worst case and for being conservative this choice was made.

As it is explained in [52], the residual stochastic satellite clock time error after applying the PRC is a random walk resulting from the sum of independent Gaussian random variables (integration of white noise). Since GBAS provides scalar corrections in the form of the PRC and RRC all the error types are combined. The RRC contains a term that corresponds to the satellite clock error rate, which in the mean will correspond to the deterministic component of the error that was not perfectly estimated by the constellation control segment and modelled by the broadcast clock correction clock error rate term. In [52], the effect of this linear prediction is analyzed. This study concluded by an increasing of the residual satellite clock error by a factor $\sqrt{\left(1 + \frac{t_{AZ}}{T}\right)}$ with respect to the error without applying the linear prediction correction.

By incorporating the impact of the RRC the following Figure 35 representing the residual satellite clock error as a function of t_{AZ} , is obtained ,for the case where $T = 0.5s$.

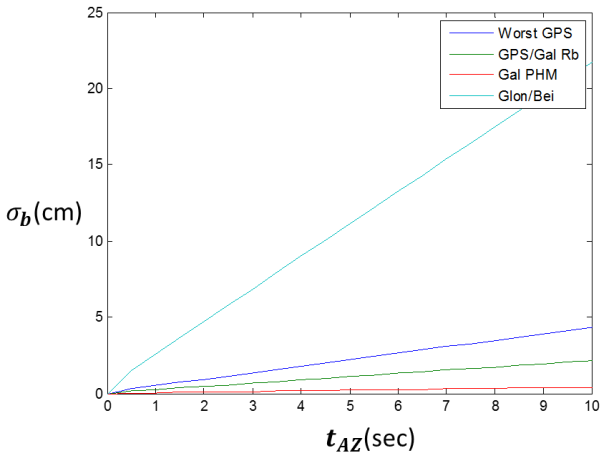

Figure 35-Standard deviation of the Residual Satellite Clock Error over time [51]

Performance for the GPS and Galileo Rb clock are considered as similar as it was analysed in [52].

By analysing this previous figure, the standard deviation rises to a few centimetres for the worst performing GPS satellite (represented by the blue curve) over update periods up to 10s .Also, it shows that with the improved expected performance for the Galileo clock (represented by the red curve) over this time scale only a very small growth in the residual error standard deviation is seen. That is why, with regard to the clock errors, an extension of an update period (increasing of t_{AZ}) to a few seconds appears feasible.

4.2.1.1.4 Troposphere

The troposphere case is treated in further detail in section 4.2.2.

4.2.1.1.5 Ionosphere

The single frequency differential residual error due to the ionospheric delay is expressed as follows:

$$\delta I = I_1^A - \left(I_1^G + t_{AZ}\dot{I}_1^G\right)$$

Equation 122- Residual differential ionospheric error

In order to correctly model the nominal ionosphere error, as for ephemeris error, it may be decomposed into spatial and temporal components.

$$\delta I = \underbrace{I_1^A(t_A) - I_1^G(t_A)}_{spatial} + \underbrace{I_1^G(t_A) - \left(I_1^G(t_G) + t_{AZ}\dot{I_1^G}\right)}_{temporal}$$

Equation 123 - Spatial/Temporal components of the ionospheric error

It is important to notice that in nominal conditions when the smoothing filters (see 3.2.3.2) within the ground and airborne subsystems are in steady states, the term $\dot{I}_1^G$ can be considered as a constant such that the temporal component will be zero and the residual differential ionospheric error will contain only a spatial component. Therefore the residual nominal ionospheric error is considered as :

$$\delta I \approx I_1^A(t_A) - I_1^G(t_A)$$

Equation 124- Residual differential ionospheric error Approximation

4.2.1.1.6 Ground Multipath and Noise

The residual error at the airborne receiver due to smoothed code multipath and noise can be described with the following equation:

$$\delta\epsilon = \epsilon_1^A - (\epsilon_1^G + t_{AZ}\dot{\epsilon}^G)$$

Equation 125-Residual differential multipath and noise error

It is important to note that the term $\dot{\epsilon}^G$ is the error contribution due to the change in the smoothed ground multipath and noise over the interval T at epoch k.

$$\dot{\epsilon}^G = \frac{\epsilon_{1,k}^G - \epsilon_{1,k-1}^G}{T}$$

Equation 126 - Error Contribution due to Change into multipath and noise over T

Under the assumption of uncorrelated raw multipath and noise terms the residual error follows a zero-mean Gaussian distribution defined by:

$$\delta\epsilon \sim N(0, {\sigma_\epsilon}^2)$$

$${\sigma_\epsilon}^2 = {\sigma_{\epsilon^A}}^2 + {\sigma_{\epsilon^G}}^2 + (t_{AZ})^2{\sigma_{\dot{\epsilon}}}^2$$

Equation 127 - STD of the residual differential multipath and noise error

and σ_{ϵ^A} is the standard deviation of the airborne multipath and noise, σ_{ϵ^G}, the standard deviation of the multipath and noise on the pseudorange correction and $\sigma_{\dot{\epsilon}}$the standard deviation of the multipath and noise contribution to the RRC.

This assumption of white noise is made in this analysis for two main reasons. Firstly, if one bias appears on one receiver, this will be handled in the faulty case (H1) otherwise if one bias appears on many receivers that will be covered by the ground as part of the ground station validation (by inflating the sigma) so in both cases it can be assumed that only the noise like part will remain. Secondly, in this part of the work, the focus is made on the change in multipath and noise so assuming white noise (no correlation) is conservative.

The difference over two epochs in smoothed multipath and noise at the ground is then (see [105]for derivation):

$$\epsilon_{1,k}^G - \epsilon_{1,k-1}^G \approx \eta_{1,\rho,k}^G \frac{T}{\tau} + \sqrt{2}\eta_{1,\phi,k}^G$$

Equation 128 - Difference over 2 epochs in smoothed multipath and noise

where $\eta^G_{1,\rho,k}$ is defined as the raw code multipath and noise component, $\eta^G_{1,\phi,k}$ is defined as the phase multipath and noise component and τ as the smoothing time constant, giving:

$$\dot{\epsilon}^G \approx \frac{\eta^G_{1,\rho,k}}{\tau} + \frac{\sqrt{2}}{T}\eta^G_{1,\phi,k}$$

Equation 129 -Derivation of the error contribution due to change in multipath and noise over 2 epochs

The standard deviation of the contribution to the error rate in the smoothed multipath and noise can be expressed as:

$$\sigma_{\dot{\epsilon}} \approx \sqrt{\left(\frac{\sigma_{\eta^G_{1,\rho}}}{\tau}\right)^2 + 2\left(\frac{\sigma_{\eta^G_{1,\phi}}}{T}\right)^2}$$

Equation 130 - STD of the contribution of the error rate into multipath and noise

A conservative bound of 3mm is assumed for the phase noise element of $\sigma_{\eta^G_{1,\phi}}$ (the impact of phase multipath is under review into the SESAR Project). Values of $\sigma_{\eta^G_{1,\rho}}$ as a function of elevation have been obtained from the DLR experimental GBAS installation which is described in [106]. This elevation dependent model appears conservative with respect to an operational station.

4.2.1.1.7 Total Error model

Due to the fact that the total error model results from the sum of independent random variables which follows a zero-mean Gaussian distribution and by viewing all components described in previous subsections, $\tilde{\Psi}^A_1(t_A) - \hat{r}^A$ can be expressed as follows:

$$\tilde{\Psi}^A_1(t_A) - \hat{r}^A \sim N(0, \sigma^2)$$

With

$$\sigma^2(\tau, T, t_{AZ}, \theta)$$

$$= \underbrace{\left(\sigma_\eta(el)T/(2\tau)\right)^2 + (t_{AZ})^2\left(\left(\sigma_{\eta^G_{1,\rho}}(\theta)/\tau\right)^2 + 2\left(\sigma_{\eta^G_{1,\phi}}/T\right)^2\right)}_{gnd\ multipath + noise} + \underbrace{(1 + t_{AZ}/T)t_{AZ}AVAR(1s)}_{SV\ clock}$$

$$+ \underbrace{\sigma_{\epsilon^A}{}^2(\theta)}_{air\ multipath + noise} + \underbrace{\sigma_{iono}(\theta)^2}_{iono} + \underbrace{\sigma_{tropo}(\theta)^2}_{tropo}$$

Equation 131 - STD of the total differential error

Where the elevation angle is represented by θ.

As mentioned in the introduction by the Table 21, values such as τ, T, t_{AZ} have an important impact.Indeed, it could be noted by analysing Equation 131 that variations in time constant will impact σ_{ϵ^A}, σ_η & σ_{iono}. The impact

of the correction update period extension has been derived. The standard deviation of the total error model for the corrected smoothed airborne pseudorange $\tilde{\rho}_1^A(t_A)$ was determined for different processing options using the existing single-frequency smoothed observable and on the I-free (IF) and differing the smoothing constants. In this report, only GPS L1 C/A and GPS L1/L5 IF are presented, though little dependency on constellation clock performance was found. Therefore, these results may be equivalently derived for Galileo observables.

Some simulation where realized in order to evaluate the impact of t_{AZ} on the total error budget modelled by the Equation 131.Therefore, Figure 36 illustrates the impact of elevation and t_{AZ} on the total standard deviation for GPS L1C/A .A GAD – C4 (Table 14) level was used for the ground code multipath component whilst an AAD B (Table 16) level was taken for the aircraft installation [16].

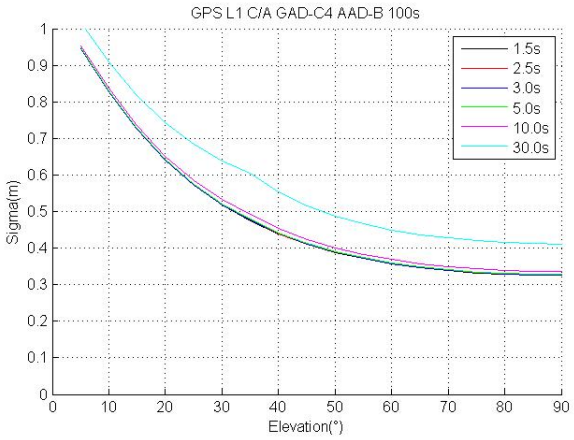

Figure 36-Impact of elevation and t_AZ on the total standard deviation for GPS L1C/A with τ=100s

By analysing results obtained through simulations illustrated by the previous figure, over update periods up to 10s, only a very small growth (2cm of growth for an error from 35cm to 1m) in the residual error standard deviation is seen. That is why, with regard to the single frequency error model, an extension of an update period (increasing of t_{AZ})to a few seconds appears feasible.

4.2.1.2 D-free Smoothing

The D-free PRC and RRC may then be determined in a similar fashion to the GAST D for the single frequency case (3.2.3.3.2) but with the D-free measurement model presented in 3.2.3.2.4.1

$$PRC_{DFree1} = r^G - \hat{\Psi}^G_{DFree1} = -b^G - J^G - \iota_1^G - \epsilon^G_{DFree1}$$

Equation 132 - PRC for D-free

$$RRC_{DFree1} = PRC^{\cdot}_{DFree1} = \frac{\left(PRC_{DFree1,k} - PRC_{DFree1,k-1}\right)}{T}$$

Equation 133 - RRC for D-free

Where $\epsilon^{G}_{DFree1} = F\eta^{G}_{\rho_1} + (1-F)\eta^{G}_{DFree1}$ (3.2.3.2.4.1) with F as the transfer function of the smoothing filter considered in the Laplace domain (see 3.2.3.2.3) or simply the filter operator in the time domain (see 3.2.3.2.2).

If it is assumed the same smoothing technique is applied to the airborne receiver, the corrected model is as follows:

$$\widetilde{\Psi}^{A}_{DFree1} = \widehat{\Psi}^{A}_{DFree1} + PRC_{DFree1} + t_{AZ}RRC_{DFree1}$$

Equation 134 - Expression of the Corrected smoothed D-free pseudorange

Where $\widetilde{\Psi}^{A}_{DFree1}$ represents the corrected smoothed D-Free pseudorange, $\widehat{\Psi}^{A}_{DFree1}$ is the smoothed D-free pseudorange computed at the aircraft side.

Note by reminding 3.2.3.3.3, that terms representing the tropospheric correction and the satellite clock correction are not explicitly represented because they are implicitly covered since b and J express the residual errors.

Therefore, by decomposing the Equation 134 with Equation 132 and Equation 46 this following expression can be derived by reminding results obtained in 3.2.3.3.2 :

$$\widetilde{\boldsymbol{\Psi}}^{\boldsymbol{A}}_{\boldsymbol{DFree}} - \hat{\boldsymbol{r}}^{\boldsymbol{A}} = \left(\boldsymbol{dr}^{\boldsymbol{A}} - \left(\boldsymbol{dr}^{\boldsymbol{G}} + \boldsymbol{t}_{\boldsymbol{AZ}}\,\dot{\boldsymbol{dr}}^{\boldsymbol{G}}\right)\right) + \left(\boldsymbol{b}^{\boldsymbol{A}} - \left(\boldsymbol{b}^{\boldsymbol{G}} + \boldsymbol{t}_{\boldsymbol{AZ}}\,\dot{\boldsymbol{b}}^{\boldsymbol{G}}\right)\right) + \left(\boldsymbol{\iota}^{\boldsymbol{A}}_{\boldsymbol{1}} - \left(\boldsymbol{\iota}^{\boldsymbol{G}}_{\boldsymbol{1}} + \boldsymbol{t}_{\boldsymbol{AZ}}\,\dot{\boldsymbol{\iota}}^{\boldsymbol{G}}_{\boldsymbol{1}}\right)\right)$$
$$+ \left(\boldsymbol{J}^{\boldsymbol{A}} - \left(\boldsymbol{J}^{\boldsymbol{G}} + \boldsymbol{t}_{\boldsymbol{AZ}}\dot{\boldsymbol{J}}^{\boldsymbol{G}}\right)\right) + + \left(\boldsymbol{\epsilon}^{\boldsymbol{A}}_{\boldsymbol{DFree}} - \left(\boldsymbol{\epsilon}^{\boldsymbol{G}}_{\boldsymbol{DFree}} + \boldsymbol{t}_{\boldsymbol{AZ}}\,\dot{\boldsymbol{\epsilon}}^{\boldsymbol{G}}_{\boldsymbol{DFree}}\right)\right)$$

Equation 135 - Decomposition of corrected smoothed D-free input of the PVT algorithm

By considering error models explained for single frequency in section 4.2.1.1, some simulation were realized in order to evaluate the impact of t_{AZ} on the total error budget modelled by the Equation 131.Therefore, Figure 39 illustrates the impact of elevation and t_{AZ} on the total standard deviation for the GPS L1-L5 D-Free case [77] with $\tau = 100s$. A GAD – C4 (Table 14) level is used for the ground code multipath component whilst an AAD B (Table 16) level is taken for the aircraft installation [16].

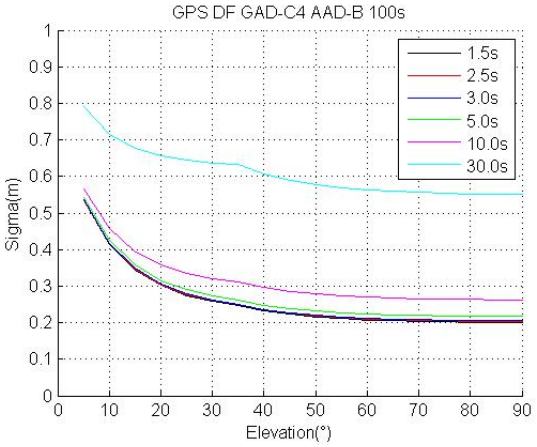

Figure 37-Impact of elevation and t_AZ on the total standard deviation for GPS L1-L5 DFree with τ=100s

By comparing single frequency case illustrated in Figure 36 with the D-free case shown in Figure 37, the error budget seems less inflated when using D-Free.

Results obtained with the 30s smoothing constant are shown in the following figure :

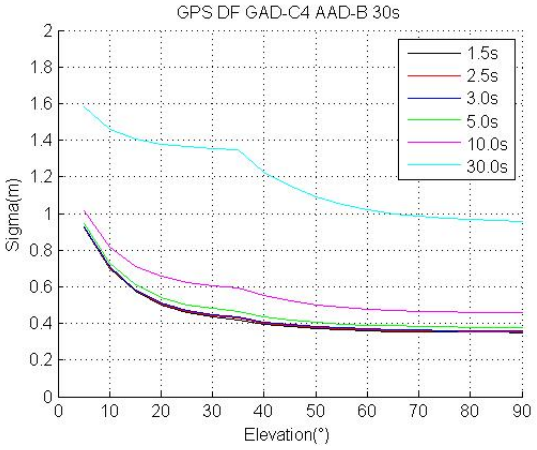

Figure 38-Impact of elevation and t_AZ on the total standard deviation for GPS L1-L5 DFree with τ=30s

Therefore, as guessed, the error budget seems inflated when smoothing constant decreases and the error budget seems as impacted by an increasing of $\boldsymbol{t_{AZ}}$whatever this smoothing constant for D-free.

Therefore, with regard to the total error model for D-free, an extension of an update period (increasing oft_{AZ}) to a few seconds appears also feasible.

4.2.1.3 Ionosphere-free Smoothing

As for D-free, the I-free PRC and RRC may then be determined in a similar fashion to the GAST D for the single frequency case (3.2.3.3.2) but with the I-free measurement model presented in 3.2.3.2.4.2:

$$PRC_{IF} = r^G - \widehat{\Psi}_{IF}^G = -b^G - J^G - \epsilon_{IF}^G$$

Equation 136 - PRC for I-free

$$RRC_{IF} = \dot{PRC}_{IF} = \frac{\left(PRC_{IF,k} - PRC_{IF,k-1}\right)}{T}$$

Equation 137 - RRC for I-free

Where $\epsilon_{IF}^G = F\eta_{\Psi_{IF}}^G + (1-F)\eta_{\Phi_{IF}}^G$ with F as the transfer function of the smoothing filter considered in the Laplace domain (see 3.2.3.2.3) or simply the filter operator in the time domain (see 3.2.3.2.2).

If we assume the same smoothing technique is applied to the airborne receiver, the corrected model is as follows:

$$\widetilde{\Psi}_{IF}^A = \widehat{\Psi}_{IF}^A + PRC_{IF} + t_{AZ}RRC_{IF}$$

Equation 138 - Expression of the Corrected smoothed I-free pseudorange

Where $\widetilde{\Psi}_{IF}^A$ represents the corrected smoothed I-Free pseudorange, $\widehat{\Psi}_{IF}^A$is the smoothed I-free pseudorange computed at the aircraft side.

Note by reminding 3.2.3.3.3, that terms representing the tropospheric correction and the satellite clock correction are not explicitly represented because they are implicitly covered since b and J express the residual errors.

Therefore, by decomposing the Equation 138 with Equation 136 and Equation 53 this following expression can be derived by reminding results obtained in 3.2.3.3.2 :

$$\widetilde{\boldsymbol{\Psi}}_{\boldsymbol{IF}}^{\boldsymbol{A}} - \hat{\boldsymbol{r}}^{\boldsymbol{A}} = \left(\boldsymbol{dr}^{\boldsymbol{A}} - \left(\boldsymbol{dr}^{\boldsymbol{G}} + \boldsymbol{t}_{\boldsymbol{AZ}}\,\dot{\boldsymbol{dr}}^{\boldsymbol{G}}\right)\right) + \left(\boldsymbol{b}^{\boldsymbol{A}} - \left(\boldsymbol{b}^{\boldsymbol{G}} + \boldsymbol{t}_{\boldsymbol{AZ}}\,\dot{\boldsymbol{b}}^{\boldsymbol{G}}\right)\right) + \left(\boldsymbol{J}^{\boldsymbol{A}} - \left(\boldsymbol{J}^{\boldsymbol{G}} + \boldsymbol{t}_{\boldsymbol{AZ}}\dot{\boldsymbol{J}}^{\boldsymbol{G}}\right)\right)$$

$$+\left(\epsilon_{IF}^A - \left(\epsilon_{IF}^G + t_{AZ}\,\dot{\epsilon}_{IF}^G\right)\right)$$

Equation 139 - Decomposition of corrected smoothed I-free Input of the PVT algorithm

By considering error models explained for single frequency in section 4.2.1.1, some simulation were realized in order to evaluate the impact of t_{AZ} on the total error budget modelled by the Equation 131.Therefore, Figure 39 illustrates the impact of elevation and t_{AZ} on the total standard deviation for the GPS L1-L5 IF case [77] with $\tau = 100s$ .A GAD – C4 (Table 14) level is used for the ground code multipath component whilst an AAD B (Table 16) level is taken for the aircraft installation [16].

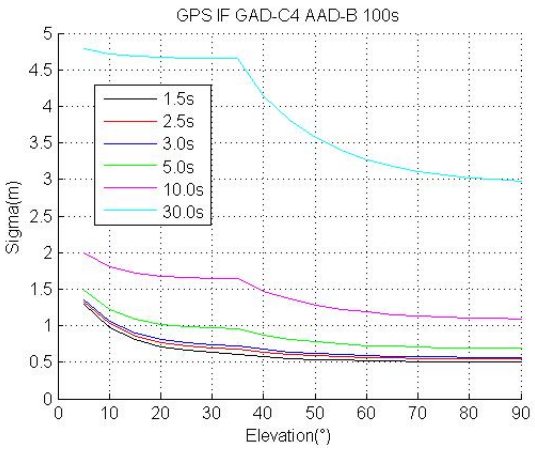

Figure 39-Impact of elevation and t_AZ on the total standard deviation for GPS L1-L5 IFree with τ=100s

This curve represents the impact of elevation and t_{AZ} on the total standard deviation for the GPS L1-L5 IF case with $\tau = 100s$. Results for $\tau = 30s$ are not represented in this report because as for the D-free case presented in the previous section, the sigma should be even more impacted in the 30s smoothing case than for 100s. By comparing single frequency case and D-free case illustrated in Figure 36 and Figure 37 respectively with the I-free case shown in Figure 39, the error budget seems more inflated when using I-Free with 100s than for D-free with 100s smoothing and should be even worst impacted with 30s smoothing constant. But it seems that over update periods up to 5s, a small growth (up to 30cm for an error up to 1.5m) in the residual error standard deviation appears. But whatever the processing modes : single frequency, I-free or D-free, it seems that over update periods up to 5s, a small growth in the residual error standard deviation appears. Therefore, with regard to the total error model, an extension of an update period (increasing of t_{AZ}) to a few seconds appears also feasible.

4.2.2 GBAS Tropospheric Error

In the previous section the total GBAS error modelling by explicitly showing the impact of the range-rate corrections was presented for single frequency case and for the Dual Frequency smoothing cases. By reminding the fact that unexpected atmospheric behaviour, which are supposed to be related to a non-modelled behaviour of the troposphere, were observed during GAST-D ground prototypes validation activities [104] and the fact that in the advent of MC/MF GBAS, when using IF smoothing technique, the main contributor to the atmospheric error will come from the tropospheric delay, a focus was realized in this study about the tropospheric modelling for both nominal and non-nominal cases. This section introduces this analysis.

4.2.2.1 Troposphere

For both single frequency and dual-frequency cases, differential residual error due to the tropospheric delays are expressed as computed in [107] as follows:

$$\delta J = J^A - \left(J^G + t_{AZ}\dot{J^G}\right)$$

Equation 140 - Differential Tropospheric residual error

Where J is the tropospheric delay, t_{AZ} represents the time between the modified time of correction generation t_Z and the time of application at the airborne receiver. The notation $\blacksquare^G$ is used for parameters relating to the ground receivers and $\blacksquare^A$ for those relating to the airborne receiver and $\dot{\blacksquare}$ defines the discrete time derivative at t_G the time at ground station.

As for the ionospheric delay described in the previous section, in order to properly model the effects of the nominal troposphere errors and therefore the total error defined by Equation 116, the Equation 140 can be decomposed into spatial and temporal components.

$$\delta J = \underbrace{J^A(t_A) - J^G(t_A)}_{spatial} + \underbrace{J^G(t_A) - \left(J^G(t_G) + t_{AZ}\dot{J}^G\right)}_{temporal}$$

Equation 141 - Spatial and Temporal components of the differential tropospheric error

It is currently under investigation within SESAR WP 15.3.7 as to whether $\dot{J}^G$ can be considered as a constant. If so the residual differential error due to the troposphere will contain only a spatial component.

4.2.2.1.1 Temporal Component

It is expected that the tropospheric delay variation in nominal condition is likely to be very linear in which case the difference: $J^G(t_A) - \left(J^G(t_G) + t_{AZ}\dot{J}^G\right)$ in the Equation 141, should be negligible.

But even the temporal component of the troposphere delay may be negligible, some changing in time could appear as temporal gradients. That was a subject undertaken by NLR into the SESAR project [108].

Conclusions underlined the fact that high temporal gradients can be expected under severe thunderstorm conditions. These could lead to a differential zenith tropospheric delay in the order of 10 cm which could lead to a meter level in slant direction for a 5° satellite elevations (after applying mapping function). These phenomenon appeared a dozen times per year.

Also, azimuthal variations due to satellite movement at low elevation (meter level for 5° elevation) may lead to sharp tropospheric temporal gradient in the slant direction when GNSS satellites cross sharp cloud edges in the sky.

If this assumption is validated, the residual differential error due to the troposphere will contain only a spatial component which is explained in the following part.

4.2.2.1.2 Spatial Component

As explained before, only the spatial component remains within the residual differential range error due to the troposphere which may be decomposed into horizontal and vertical components.

The previous Figure 1 illustrates the three spatial components which are relevant and critical for GBAS.

As shown in the Figure 1, the total range tropospheric delay observed at the ground station is composed of the delay over paths 1 and 2, which are defined by the aircraft height. However, the aircraft being at a higher altitude is only subject to a delay over path 3. In nominal conditions, the delays over paths 2 and 3 (above the aircraft

height) define the horizontal component of the differential range tropospheric delay and will be highly spatially correlated. This component has been neglected within the standardized models. Horizontal gradients will be treated as non-nominal tropospheric events in this report (in Chapter 6), even though minor such gradients have been observed more frequently than previously thought. [104]

In order to remove the delay over path 1 from the correction, a empirically derived model is used for this Tropospheric Correction (TC) as defined in 3.2.3.3 by the Equation 59 and addressed in the following section 5.5([84] [16]). But, vertical gradients could exist when large differences between path 1 and the TC value occur, these can be also called duct phenomena. If so, errors won't be appropriately bounded by the Gaussian model for the TC error [84] [16].The overbounding Gaussian model for the TC error had been previously validated for nominal and rare conditions [84] [16]. But further investigations were realized for European Meteorological data to validate this model and to assess duct phenomenon. These analysis is described in detail in the following section 5.5.

Then as already mentioned in GBAS integrity concept 3.3.2.2.3, for each threat identified for GBAS, either integrity monitoring approach may be taken or the threat may be incorporated into the nominal modal and overbounded by protection level. For the particular case of the tropospheric threat, GBAS activities have followed the approach of overbounding protection levels. This subject is discuss in detail in further Chapter 6.

4.3 Evolution of Corrections Computation

4.3.1 Presentation

According to the current GAST D requirements [109] based on the 2Hz correction rate, t_{AZ} must be inferior to 1.5s in the absence of lost VDB messages and airborne related delays.

If the update period of the PRC is extended (correction rate inferior to 2Hz), this value of 1.5s will increase. There is then the need to examine the influence of higher t_{AZ}.In order to analyse the influence of an increased correction update period the current extrapolation of PRC of 1.5s was compared to longer extrapolation times t_{ex}. Figure 40 shows at the airborne receiver time t the difference between extrapolated PRC computed using PRC at t.

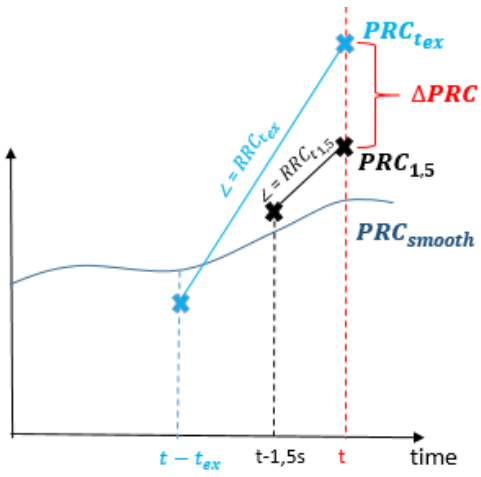

Figure 40-PRC and RRC over time

The following computation expresses the difference in the error using a longer extrapolation period to the current approach.

At first the PRC expressions are derived using Equation 61, for both the current requirement of 1.5s and the longer extrapolation time t_{ex}.

$$PRC_{t_{ex}}(t) = PRC(t - t_{ex}) + RRC(t - t_{ex}) \times t_{ex}$$

Equation 142 - PRC extrapolation with a longer time

$$PRC_{1.5}(t) = PRC(t - 1.5) + RRC(t - 1.5) \times 1.5$$

Equation 143 - PRC extrapolation with the current 1.5s

Then the error made by computing the extrapolated values and the reference 'true' PRC is computed as follows for both extrapolated times.

$$\delta PRC_{1.5}(t) = |PRC_{1.5}(t) - PRC_{smooth}(t)|$$

Equation 144 - Error between extrapolated value of 1.5s and true

$$\delta PRC_{t_{ex}}(t) = \left|PRC_{t_{ex}}(t) - PRC_{smooth}(t)\right|$$

Equation 145 -Error between extrapolated value and true

where PRC_{smooth} is the reference 'true' PRC obtained using a 20 point Gaussian filter (length of the Gaussian window). Then, the set of positive $\Delta PRC_{t_{ex-1.5}}$ is used to derive the statistics as this conservatively relates to the degradations in performance as expressed by :

$$\Delta PRC_{t_{ex-1.5}}(t) = \delta PRC_{t_{ex}}(t) - \delta PRC_{1.5}(t)$$

Equation 146 - Degradations in Performance

The ΔPRC depend upon the statistical properties of the RRC which depend also upon elevations. That is why it was it was relevant to analyze standard deviations for the RRCs from MT1 and MT11 for 5° elevation bins in following section.

4.3.2 RRC Analysis

4.3.2.1 Simulated data analysis

The RRC may be modelled at each epoch as containing a bias term relating to the true linear variation from ephemeris, satellite clock ionosphere and troposphere error rates as well as a stochastic term as a result of the code and phase multipath and noise, the stochastic satellite clock error and other random errors. The VDB data (RRC) obtained by using models presented in previous section 4.2 are represented by Figure 41 and Figure 42. Indeed, they depict the impact of elevation on RRC for both 30s and 100s smoothing constants.

These results were obtained according to the current GAST D requirements [109] based on the 2Hz correction rate which imply that t_{AZ} must be inferior to 1.5s in the absence of lost VDB messages and airborne related delays.

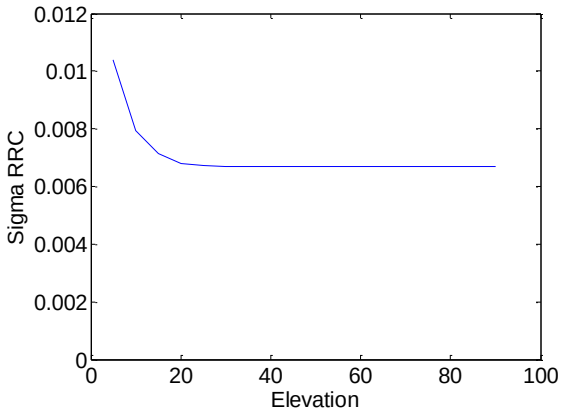

Figure 41-Std for 100s smoothed RRC

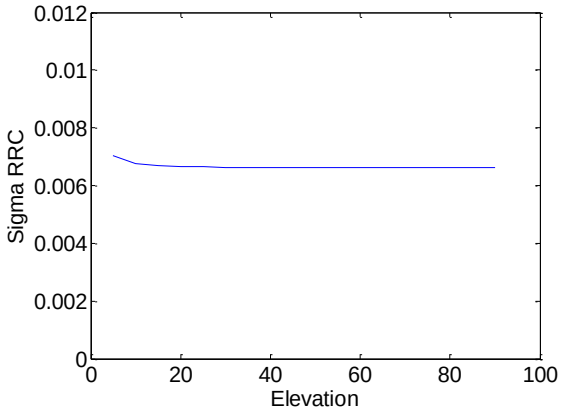

Figure 42-Std for 30s smoothed RRC

By analyzing both Figure 41 and Figure 42, the RRC bias appears negligible with respect to its noise.

4.3.2.2 Real data analysis

Three days of VDB message data obtained from the Thales GAST D prototype ground station installed at Toulouse Blagnac airport were processed. Figure 43 and Figure 44 represented below, show histograms of the RRC over all ranging sources for the MT1 and MT11 corrections. As presented before in this report (3.2.3.4.3) MT1 corrections represent 100s smoothed corrections and MT11 corrections represents 30s smoothed corrections

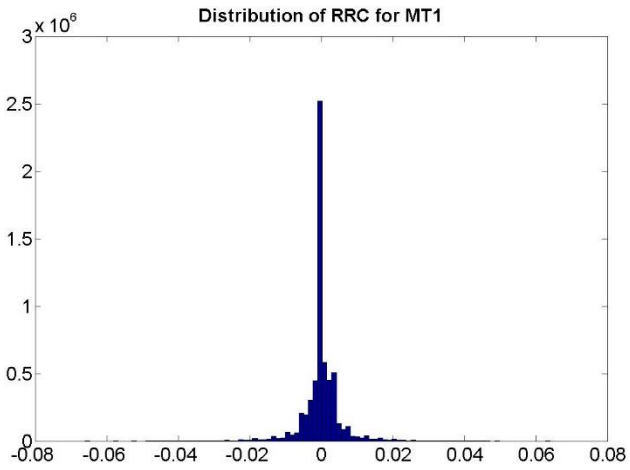

Figure 43-Distribution of RRC for all satellites for MT1 (100s)

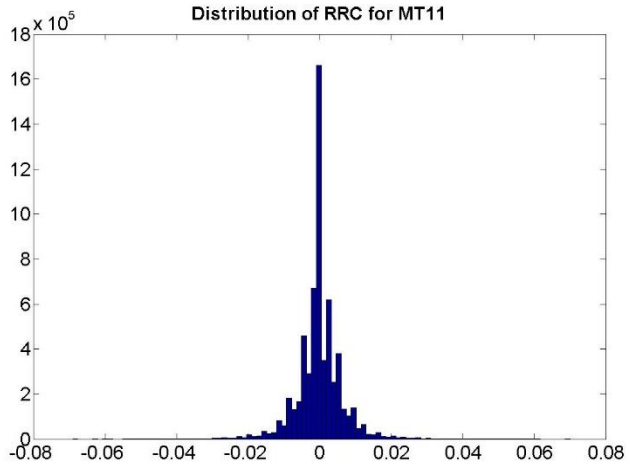

Figure 44-Distribution of RRC for all satellites for MT11 (30s)

By viewing these previous figures for 100s and 30s smoothing constants, it is clear that these RRC distributions are central and in fact contain a high number of zero values (note that the resolution of the RRC is 1mm/s).

Then, a typical one minute interval (with 2Hz for the correction rate) of the RRC are visible in the following Figure 45.

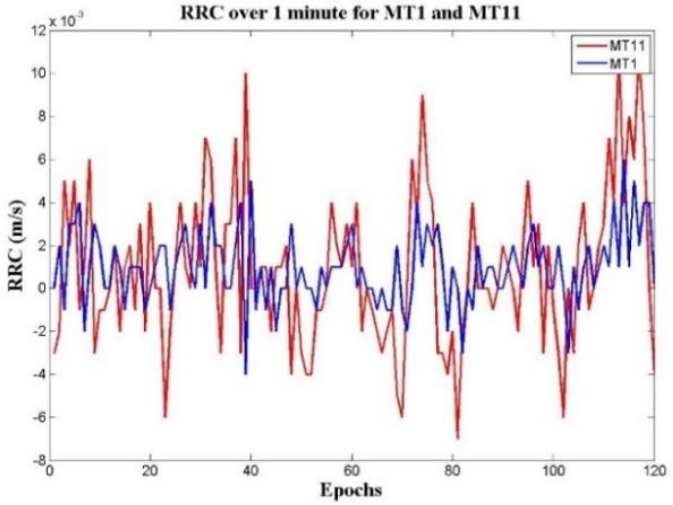

Figure 45-RRC over 1minute

This figure shows the characteristic noise-like nature of the RRC and amplitudes of variations appears higher in the MT11 case than MT1 cases. That could be explain by differences between smoothing constant values

For completed the observations, standard deviations for RRCs from MT1 (100s) and MT11 (30s) were plotted as a function of elevation in Figure 46.

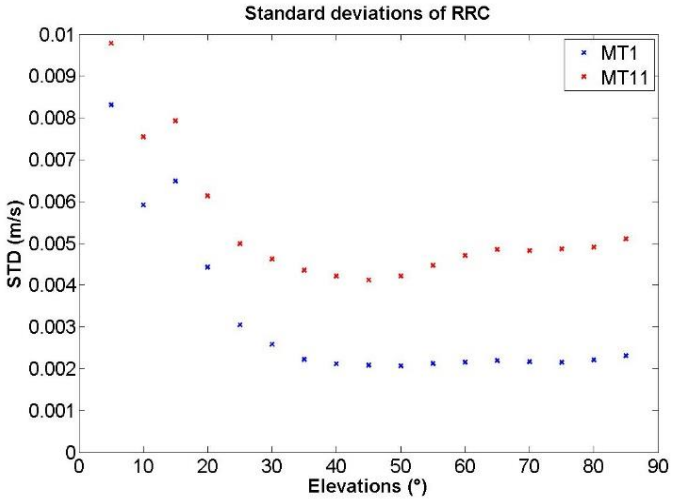

Figure 46-Standard deviation of RRC for MT1 (blue) and MT11 (red)

According to the previous figure, the standard deviation of RRC for 100s smoothing constant takes values from 2-8mm/s and for 30s smoothing constant takes values from 4-10mm/s. These intervals are similar but smaller than those found in theory (represented by Figure 41 and Figure 42) where values are from 7-10mm/s. Therefore, the theory seems enough conservative even the impact of smoothing constant appear more important in real data analysis.

4.3.3 PseudoRange Performances Analysis

4.3.3.1 Simulated data analysis

As presented in the previous section and by applying the methodology explained in 4.3.1, difference in the standard deviation of the corrections for different extrapolation times is analysed by using A GAD – C4 (Table 14) level for the ground code multipath component whilst an AAD B (Table 16) level is taken for the aircraft installation [16]. At first the single frequency case is analysed for both 30s and 100s smoothing constant and then the D-free and I-free cases are treated.

4.3.3.1.1 Single Frequency

In this section, the single frequency case is presented.

Figure 47 represents the standard deviation of the degradation of performance with a 100s smoothing constant.

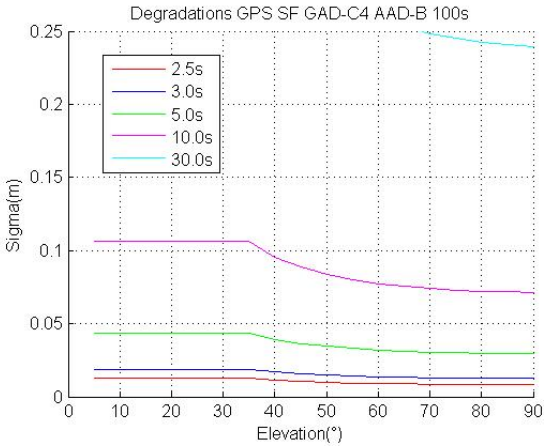

Figure 47-100s Smoothed Error Degradation with Update Period

And, Figure 48 represents the standard deviation of the degradation of performance with a 30s smoothing constant.

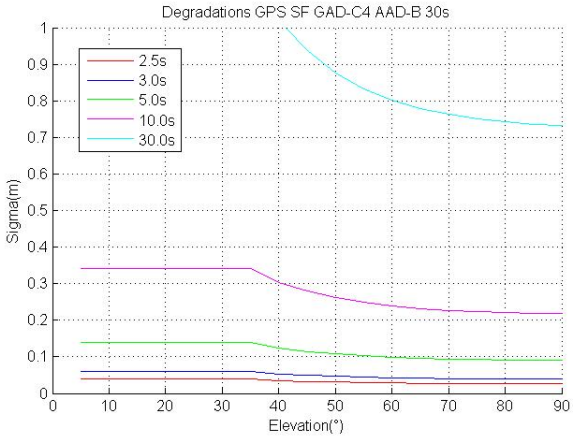

Figure 48-30s Smoothed Error Degradation with Update Period

By comparing these previous figures, the 30s standard deviation is higher than the 100s but in both cases, the highest value is of the order of 20cm for update periods up to 10s. It is relevant to notice that with this simulated data analysis, only a minor difference of a couple of centimetres for update periods up to five seconds appears.

4.3.3.1.2 D-free smoothing

In order to compare each processing mode, the following represents the standard deviation of the degradation of performance with the D-free processing technique with a smoothing constant of 100s.

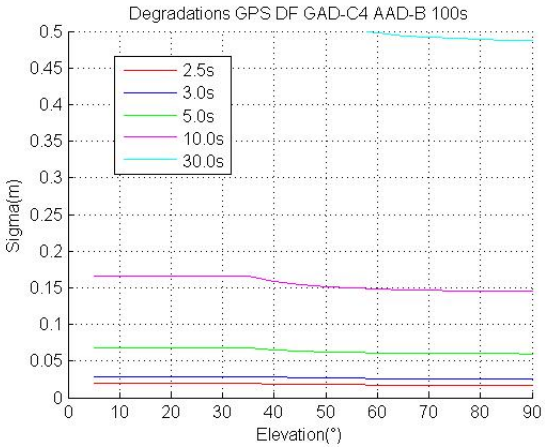

Figure 49-D-free Smoothed Error Degradation with Update Period with τ=100s

By comparing this D-free case in Figure 49 and the previous single frequency represented in Figure 47 and, degradations appear less important when using D-free.

In the following figure, the D-free analysis was realized with a smoothing constant of 30s.

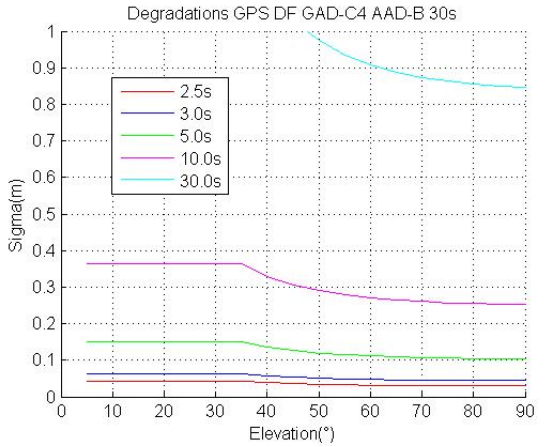

Figure 50-D-free Smoothed Error Degradation with Update Period with τ=30s

As for the error model analysis in 4.2.1.2, the degradation in D-free is more important in the case of a smaller smoothing constant.

But also in this D-free case, it exists only a minor difference of a couple of centimetres for update periods up to five seconds.

4.3.3.1.3 I-free smoothing

As for D-free and single frequency cases, the following Figure 51 represents the standard deviation of the degradation of performance with the I-free processing technique with a smoothing constant of 100s.

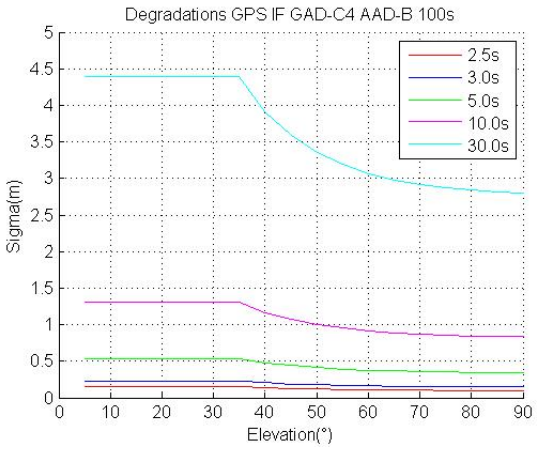

Figure 51-I-free Smoothed Error Degradation with Update Period

Results for 30s smoothing constant with I-free smoothing is be presented in this report because it is guessed that with a smaller smoothing constant in I-free, the degradation will be worst. By comparing this I-free case in Figure 51 with the single frequency and the D-free cases with 100s represented in Figure 47 and Figure 49, degradations appear more important when using I-free than in all cases. But in all processing modes: single frequency, D-free or I-free, it exists only a minor difference of a couple of centimeters for update periods up to five seconds.

These results should be confirmed by the real data analysis presented below.

4.3.3.2 Real Data analysis

As for the RRC analysis (section 4.3.2.2), three days of VDB message data obtained from the Thales GAST D prototype ground station installed at Toulouse Blagnac airport were processed. In this real data analysis, only the Single frequency case is examined.

Figure 52 and Figure 53 present the standard deviations of ΔPRC for MT1 (100s smoothing constant) and MT11(30s smoothing constant) respectively, for different update periods.

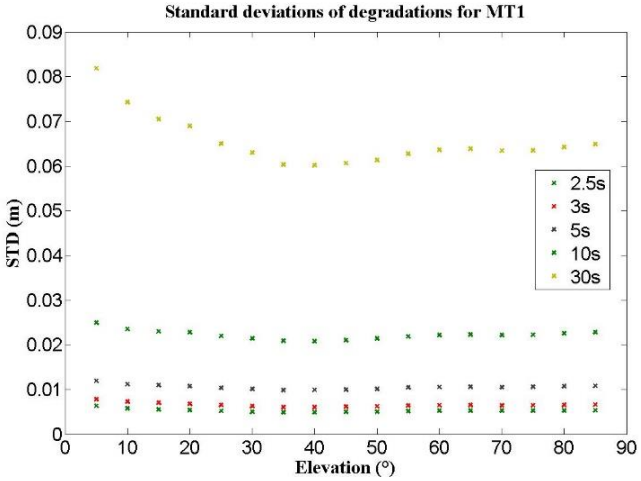

Figure 52-Standard deviation of ΔPRC for different time of extrapolation for MT1

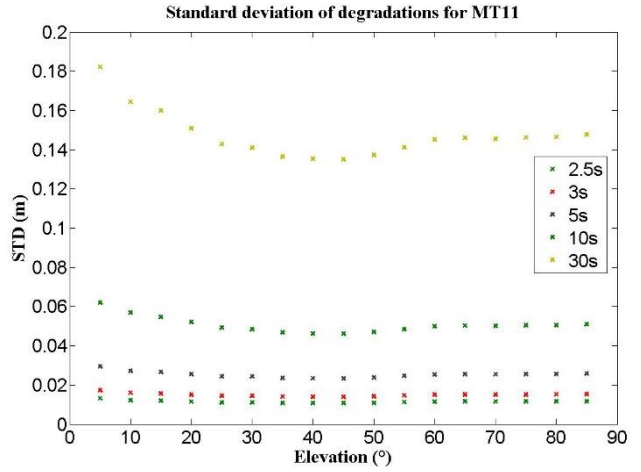

Figure 53-Standard deviation of ΔPRC for different time of extrapolation for MT11

The Figure 52 and Figure 53 show little dependency on elevation as was determined from the theoretical results (Figure 47 and Figure 48) and appears to confirm that the phase noise whose level only has a minor dependence on elevation is the primary contributor.

However, the empirical results (Figure 45, Figure 46, Figure 52 and Figure 53) show a greater influence of the smoothing constant than as determined theoretically (Figure 47 and Figure 48). Indeed, the highest value for standard deviation is around 8cm for MT1 and 18cm for MT11 in the empirical curves and around 18 cm for MT1 and around 20cm for MT11 for the theoretical curves. This analysis suggests that the contribution of code multipath and noise is not sufficiently modelled in the theoretical derivation.

This section has derived in the range domain the total error budget to quantify the degradation as a function of the message update rate for the current MT1 and MT11 corrections based on 100s and 30s smoothing constants

respectively. Theoretically and empirically, the standard deviations rise by a couple of centimeters over update periods up to 10s and thus an extension of the update period from nowadays 0.5s to say 3.5s appears feasible. As seen in the D-free and I-free smoothing analysis, this effect will be inflated when using this Dual frequency case and particularly in I-free case.

4.4 Performance Benefits

4.4.1 Trade-offs

As presented in the introduction of this section with the evolution to the MC/MF GBAS, some constraints appear and a major one deals with the available space for message transmission from the GBAS VHF Data Broadcast (VDB) unit [4]. Any additional corrections and parameters have to be accommodated in this very limited remaining capacity of the VDB.

Furthermore, a new architecture should not be too complex and include too many different processing modes. Many modes would mean a long and expensive development process for the manufacturers and thus complex and expensive user equipment. Additionally, each mode has to be shown to comply with the appropriate requirements and that all different modes would be triggered if necessary. Moreover, also all mode changes have to be investigated which would result in an enormous validation effort. That is why, studies and validation phases are still under investigation within SESAR as there are many trade-offs for finding an agreement about a MC/MF GBAS processing scheme. One possibility was examined in the previous section by decreasing the update rate for sending corrections and some are presented into [102].

Indeed, the corresponding stringent requirements are difficult to achieve since they might require sending corrections at a lower update rate than the currently used 2 Hz. The degradations into the range domain was analysed in the section 4.3.3.

4.4.2 Conclusions

As introduced above, one of the proposals for an updated GBAS VDB message structure is to separate message type for corrections. Indeed, one message type could contain corrections properly with the corresponding sigmas at a lower rate than 2Hz and one message type could contain integrity flags (on 2 bits) at the existing rate of 2Hz. As a matter of fact, in correction message, 3 sigmas should be defined: the first, if 1 missed message is detected, the second if 2 missed messages are detected and the third if no missed message is detected. Therefore, with the integrity message, a check of the 2 bit integrity flag could be realized and then the corresponding sigma could be selected.

In this Chapter 4, the GBAS nominal error modelling was described for SF and DF with a focus on the specific case of the GBAS tropospheric error modelling. After having presented some properties of the range-rate corrections

to understand how an increase in the correction update period will impact the total performance of the system with a current and an innovative methodologies, the total error budget was derived for quantifying the degradation in the corrections as a function of the message update rate. Finally, a performance benefits analysis was realized to evaluate the possibility of an increased update rate.

Therefore this chapter of this thesis has intended to solve a main issue in the scope of the evolution of MC/MF GBAS under nominal conditions. Another key issue within this scope deals with the atmospheric modelling in nominal and non-nominal cases, particularly by considering the troposphere as a threat as it was highlighted in previous work [7]. This other issue is addressed in the following chapters.

Chapter 5 : Anomalous Troposphere Modelling for GBAS

5.1 Introduction

The previous Chapter 4 assessed the GBAS nominal error modelling in the scope of the MC/MF evolution. Moreover, another main issue has to be addressed which deals with the non-nominal atmospheric modelling and particularly the anomalous troposphere modelling. Indeed, the troposphere has been neglected in light of the ionospheric monitoring difficulties and its modelling must be revisited. Indeed, the troposphere should be considered as a threat as it was mentioned in previous studies [7].

Furthermore, as it was mentioned in 3.3.2.2.3, for each threat identified for GBAS integrity monitoring approach shall be taken and the threat to be incorporated into nominal model and overbounded by protection levels. This protection level computation process [110] [111] includes treating the combined threat relating to ionospheric and tropospheric spatial gradients. Therefore, to deal with this non-nominal troposphere assessment, previous work proposed some changings concerning the protection level bounding concept [112] [7] [113] [114].

As presented above by Figure 1 and in section 4.2.2.1.2, two possible anomalies relate to the troposphere which are horizontal and vertical gradients. The overbounding Gaussian model for the Tropospheric Correction (TC) (sections 3.2.3.4 and 5.5) had been previously validated for nominal and rare conditions [84] [16], that means that vertical gradients are supposed to be well modeled by TC defined in [84] [16].

Horizontal gradients are currently neglected by the GBAS integrity concept, where it is assumed that any significant differential errors will be captured by the multitude of ionospheric monitors. However, this requires further investigation following gradients observed in [104] .Furthermore, tropospheric gradients, as a result of their more local nature have the greater potential to impact multiple satellites thus requiring a conspiring ranging biases (ranging errors that combine in such a way that maximize the position error to have the worst possible case) [6]approach and the protection from ionospheric monitors cannot be fully relied on.

Recent observations [104] showed unexpected atmospheric behaviour not previously known. Indeed, differential range errors within the IGM (Ionospheric Ground Monitor) were observed during ground prototypes validation activities for GAST D. Even if their amplitudes are not significant compared to those due to ionospheric gradients, the combination of these tropospheric gradients with anomalous ionospheric gradients in the Ionospheric

Gradient Monitor (IGM) can lead to an unacceptable rate of false alarm. These differential errors are believed to be related to a non-modelled non-nominal behavior of the troposphere. Furthermore, as currently defined in the SARPS it is not a simple problem to distinguish anomalous ionospheric or tropospheric gradients in a single frequency system. Whilst this report does not propose a troposphere monitor to resolve this issue, it is the presence of these previously unknown gradients that suggests the troposphere threat is not sufficiently well known. Finally, in the advent of Dual Frequency (DF) GBAS, the ionosphere may be removed through the Ionosphere-Free (IF) smoothing technique. Under such a scenario, the troposphere threat model should be revisited.

That is why this report and this section focus on the horizontal gradients impacting the differential range error.Therefore, this section first describes the use of meteorological modelling for estimating the worst differential range tropospheric delay by presenting two solutions: one using a wall model built with GNSS data and the second using Numerical Weather Models which are 3D layered models of meteorological and geographical parameters. Then, some methodologies for estimating range tropospheric delays by using these atmospherical parameters are described. A subsection also addresses how to find the differential tropospheric error focusing on the worst case (non-nominal) conditions and finishes by a validation section dealing with the accuracy of such methodology using NWMs data. Finally, this section deals with the modelling of the vertical component of the differential tropospheric range error by introducing the standardized TC and by presenting a statistical analysis based on NWMs.

5.2 Meteorological Modelling

When dealing with non-nominal tropospheric gradient modelling for GBAS, three approaches may be taken. The first one would be to determine the differential errors directly from GNSS data at two reference stations and derive a statistical model. The second approach would be to use a sophisticated meteorological data model which has been obtained using extensive and varied sensors to compute or predict the tropospheric delay on a GNSS signal at two nearby receivers. A compromise can be find between them and is considered here as the third approach.

The first approach has the advantage of requiring only GNSS data processing which assuming that other error sources can be removed ensures no computational error. On the downside, additional error sources can be difficult to remove entirely and may degrade the results. Furthermore, there is an inherent undersampling due to the fact that GNSS measurements can only be obtained from satellites at certain points in the sky at any given time. The advantage of the second approach is that with a detailed data model of the atmosphere, the delay on any line-of-sight vector may be determined, the drawback being the potential for insurmountable computational loads.

The third approach as a compromise between the first two is also available which uses GNSS data to build a simple meteorological model that is then used to estimate worst case differential range delays. Previous work [6] took this third approach to develop a simplified model termed the “Wall model” as shown in the following section by Figure 54.

5.2.1 Weather Wall Model

As presented above, previous work [7] took the approach of using GNSS data to build a simple meteorological model which is then used to estimate worst case differential range delays. Therefore, as shown in the Figure 54 a simplified model termed the “Wall model” was developed.

In this model the troposphere is partitioned by an infinite vertical plane either side of which are defined nominal ‘0’ and worst case ‘w’ weather conditions (as non-nominal conditions) for meteorological parameters such as Temperature (T), Relative Humidity (RH) and Pressure (P).

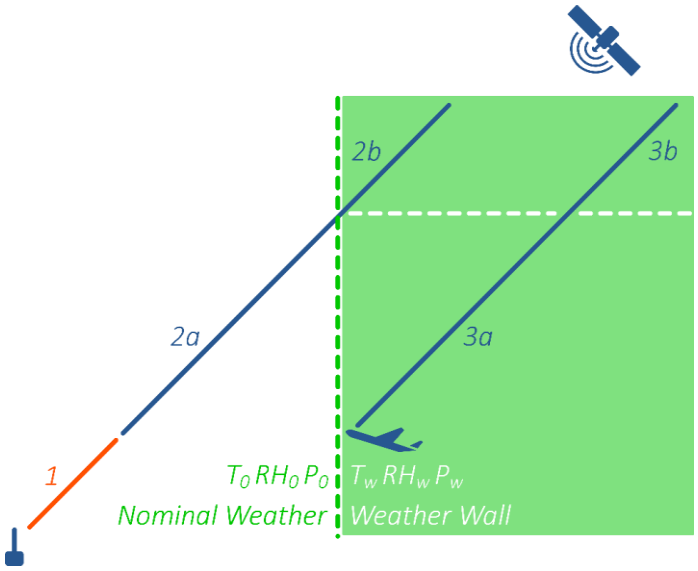

Figure 54-Weather Wall Model to the right of the Ground Station

In Figure 54, the paths 2 and 3 as shown in Figure 1 have been split into parts 2a, 2b, 3a and 3b respectively. The separation is made as the ground station signal leaves the worst case weather wall conditions. Path 3 is thus contained entirely within the worst case weather wall with surface conditions (T_w, RH_w, P_w) whilst path 2 to the ground station experiences different conditions (T_0, P_0, RH_0) during part 2a then (T_w, RH_w, P_w) during part 2b . In this case the wall is represented to the right of the aircraft but it could equivalently also be on the left with no loss of generality. These conditions and particularly atmospherical parameters for both nominal and worst cases need to be set. Therefore, several possibilities exist to parameterize this model. Choices made by ENAC to develop an optimal parameterization is quite different as those found in literature [7]. Following subsections discuss about these different parameterizations.

5.2.1.1 Literature Based parameterization

Following the approach and parameterization taken in [7], the nominal and worst case weather conditions employed for the weather wall model illustrated in Figure 54, are respectively T_0 equal to 15°C, P_0 equal to 1023.25hPa, RH_0 equal to 50% (considered as standards values) and T_w equal to 26°C (+/-5°C), P_w equal to 1023.25hPa, RH_w equal to 75% (+/- 25%). In this Ohio analysis [7], the wall model is implemented using the Modified Hopfield Model ([115]). The constellation chosen was the 24 optimized GPS and the worst case was calculated to appear with 6 satellites (N equal to 6) with a fault free missed detection multiplier of 6 (K_{ffmd} set at 6) with some considerations about the conspiring ranging biases [116]. Another important parameter to define is the distance between the Ground Station and the Runway threshold denoted D_{TH} which is set about 5km according to [7]. Finally, the worst case is assumed to appear when elevation angle is 5°.

5.2.1.2 Optimal parameterization

The weather wall parameterization employed differs from [6] [7] in order to capture the vertical profile of the troposphere. Indeed, some considerations concerning the worst case occurrence change. As for the Ohio analysis [7], the wall model is implemented using the Modified Hopfield Model ([115]) but with the nominal and worst case weather conditions define with respectively T_0 equal to 15°C, P_0 equal to 1023.25hPa, RH_0 equal to 50% (considered as standards values) and T_w set at 26°C, Pw set at 1023.25hPa, RH_w set at 100% with for both cases a temperature lapse rate set to -6.5K/km. The constellations chosen was the 24 optimized GPS constellation and also the 24 GPS added by the 24 Galileo constellation and the worst case was assumed (as in [112] and by seeing the section 6.2.2 with Equation 165 to appear with 12 satellites (N set at 12) for the GPS constellation and N equal to 24 for GPS/Galileo constellations with a fault free missed detection multiplier of 6 (K_{ffmd} set at 6). Some simulations were processed with for comparing with Ohio analysis for N equal to 6 for GPS constellation and N equal to 12 for GPS/Galileo constellation and results are presented in the Appendix A.

Then, two tests were performed with regards to the Ground Facility siting of D_{TH}=5km (as defined in standards [117]) and 10km (in view of the relaxation of constraints for GAST-D or F [45]).

Finally, because the differential range tropospheric delay depend on the distance between the ground station and the aircraft (4.2.2.1 and Figure 82) and by viewing from 6.2.2 that there is a linear dependency between σ_{iono} and x_{air} depending on σ_{vig} and F_{pp}. A modification (inflation) of σ_{vig} was thought and of a worst case mapping function F_{pp} was determined through simulations(more details in 6.2.2). Indeed, this choice was made when testing the methodology of Ohio (explained in detail in 6.2.2) when computing the worst differential range tropospheric delay and the corresponding sigma $\sigma_{\Delta tr}$ (included in the σ_{vig}). The worst case is selected when the σ_{vig} was the highest (therefore $\sigma_{\Delta tr}$ also) by taking into account the mapping function (depending on the elevation angle). Therefore the two following figures illustrates both results obtained with 5° of elevation and 90° of elevation. The main idea (more detailed in 6.2.2) is to find numerically the sigma non-nominal troposphere $\sigma_{\Delta tr}$ (included in σ_{vig}) in order to always have the red curve above the blue one.

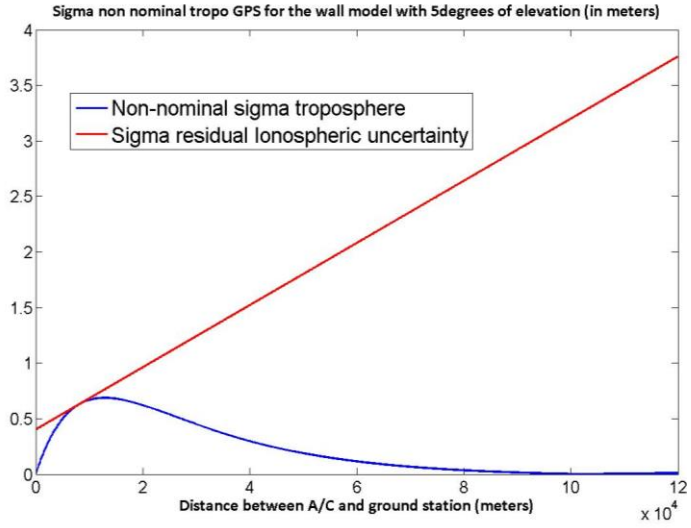

Figure 55-Determination of σ_vig for 5° Elevation

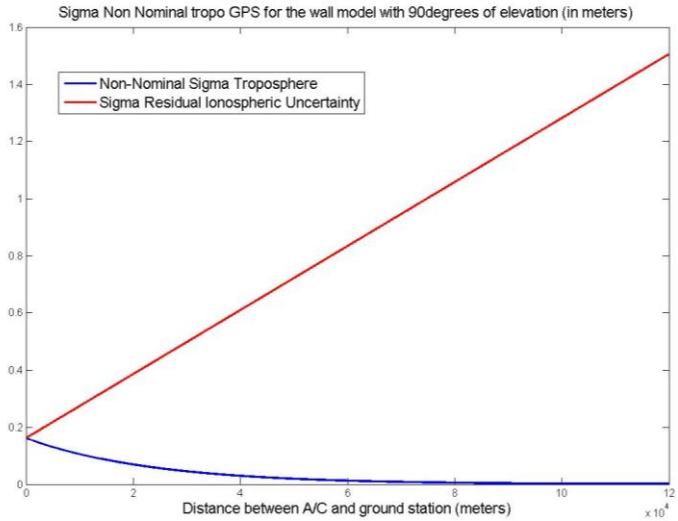

Figure 56-Determination of σ_vig for 90° Elevation

As seeing in these figures, it is the case but for the 5° elevation case, $\sigma_{\Delta tr}$ is found to be 9.2mm/km and for 90° $\sigma_{\Delta tr}$ is found to be 11.2mm/km. So, the worst case elevation angle was chosen to be 90°.

In this study, It was decided to select this optimal parameterization with the 90° as the worst case.

Unfortunately, due to the undersampling mentioned above, using GNSS measurements from a permanent tracking network does not capture the entire troposphere and a potential worst case gradient could be missed. This was the motivation for the use of Numerical Weather Models (NWMs) to provide the necessary surface and atmospheric data for computing the range tropospheric delays along the entire path without resorting the useful yet simple wall model. These models are detailed in the following sections.

5.2.2 Numerical Weather Model

5.2.2.1 Introduction

NMWs are three dimensional layered models of the atmospheric conditions from the surface of the Earth up to an altitude of about 30 km. The models contain meteorological and geographical parameters such as temperature, pressure, relative humidity and geopotential height. The primary use of NWMs is in the domain of weather prediction when paired with a dynamical model but in this study the interest is purely in the current meteorological state. Indeed, data extracted from these model are combined over 3 hours, assuming all observations occur at the midpoint [118] (therefore temporal variations are not captured over these 3 hours) and radars have an horizontal resolution of 15km but augmented with a wide variety of sensors (as shown in Figure 57) [119] that enables a higher resolution of the final NWM format. Accuracy of some atmospherical parameters are shown for Arome with vertical profiles in 5.2.2.2 in Figure 65, Figure 66 and Figure 67.

Two NWMs are used in this study: Harmonie [120] provided by KNMI (Royal Netherland Meteorological Institute) and Arome [121] provided by Meteo France. Both models are essentially the same (few physical parameterization differences exist and are neglected in this study).

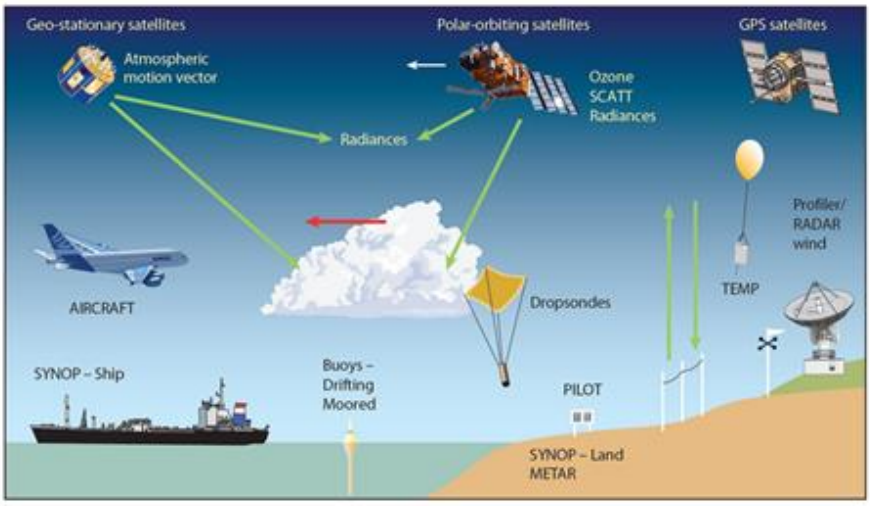

Figure 57-Sensors for NWM [119]

5.2.2.2 Arome

One year (01/2014 - 12/2014) of Arome data with a resolution of 3 hours have been processed. The geographic limits shown in Figure 58 are defined by latitudes 44°19'49,5"N and 46°43'24,8"N and longitudes 5°11'57,4"E and 11°47'27,8"E with a horizontal grid resolution of 2.5km.

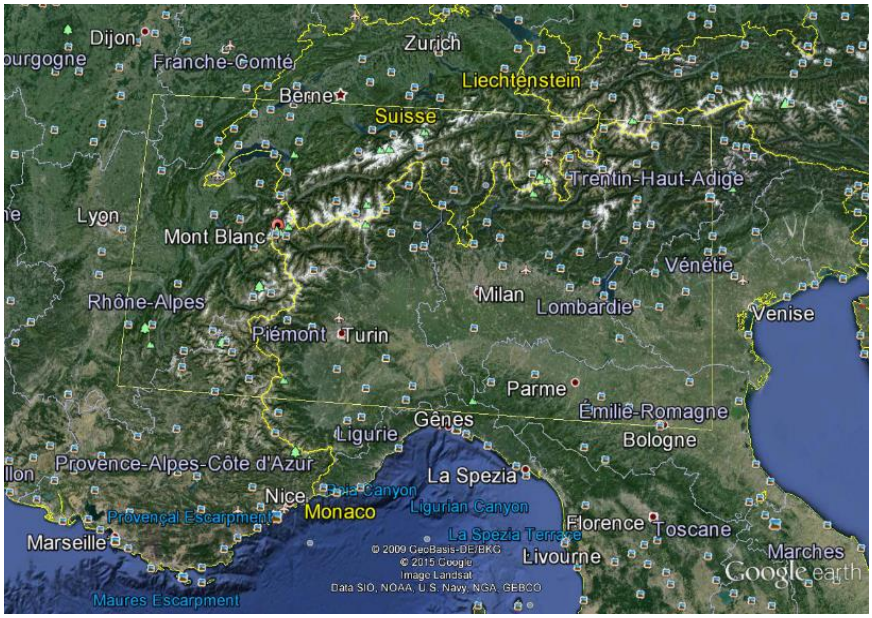

Figure 58-Area of study with Arome – Source : Google Earth V7.1.5.1557- 10/04/2013

Parameters available from this NWM are Pressure, Temperature and Relative Humidity for 12 height levels represented in Figure 60 (from 20 to 3000meters) and 15 Isobar levels (100hPa, 150hPa, 200hPa, 250hPa,

300hPa, 400hPa, 500hPa, 600hPa, 700hPa, 800hPa, 850hPa, 900hPa, 925hPa, 950hPa, 1000hPa). The surface heights of these data over the region are represented in the following Figure 59.

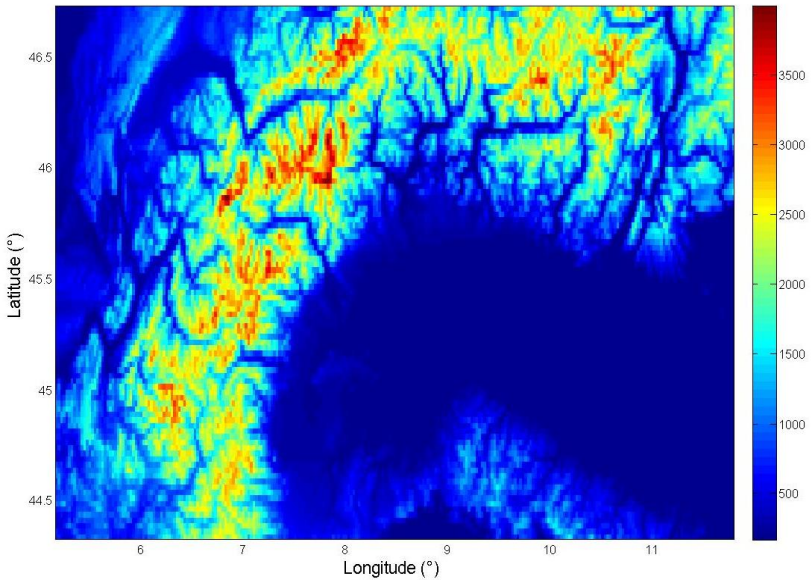

Figure 59-Surface height of Arome domain

The 12 Height levels Arome data represented in the Figure 60 (where 2 levels are below 200ft) can be used to validate the Tropospheric Correction as defined in standards [16] [84] and to assess the duct issue (vertical abnormal behavior below the Aircraft).

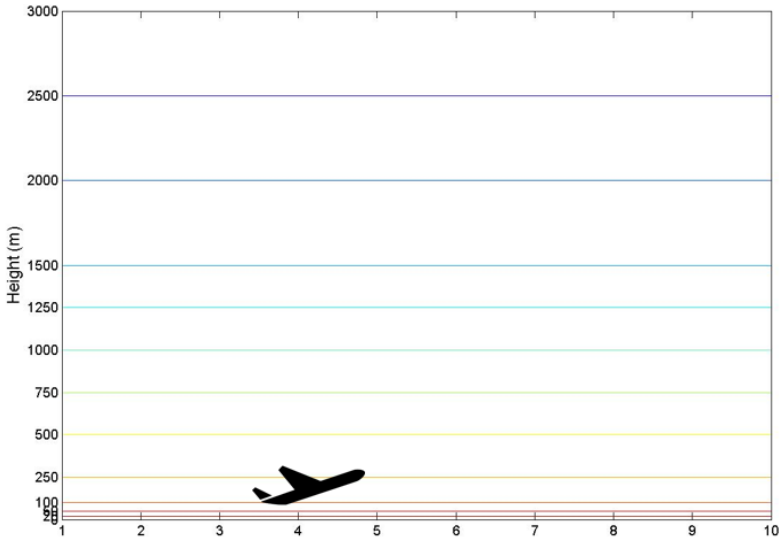

Figure 60-12 Height levels

The Isobar levels could be used for computing the total range tropospheric delay along the path from ground to satellites because these levels will be defined for higher heights than for the 12 heights levels.

These data, extracted from these isobar levels can be represented in the vertical plane as a function of longitude with a constant latitude (or as a function of latitude with a constant longitude). Parameters are represented through the following figures: heights on Figure 61, pressures on Figure 62, temperatures on Figure 63 and finally relative humidities on Figure 64 . In each figure, the black lines represent values given for the surface level then levels increase until the top of the grid (16km) starting from lines in the “warmest” colors (red) to the lines in “coldest” colors (blue).

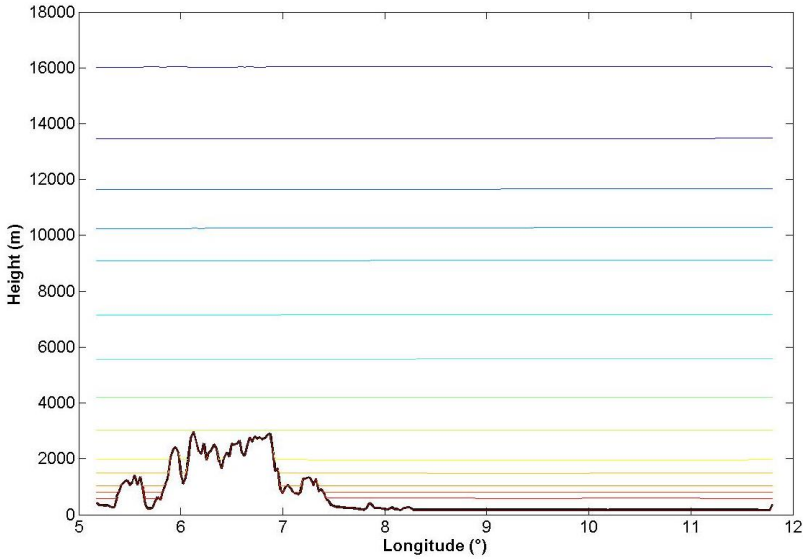

Figure 61-Height levels of NWM

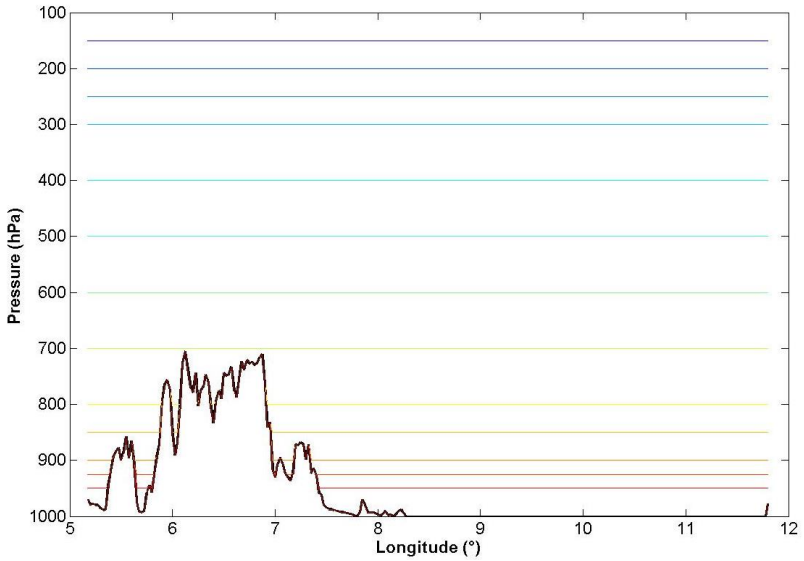

Figure 62-Pressure levels of NWM

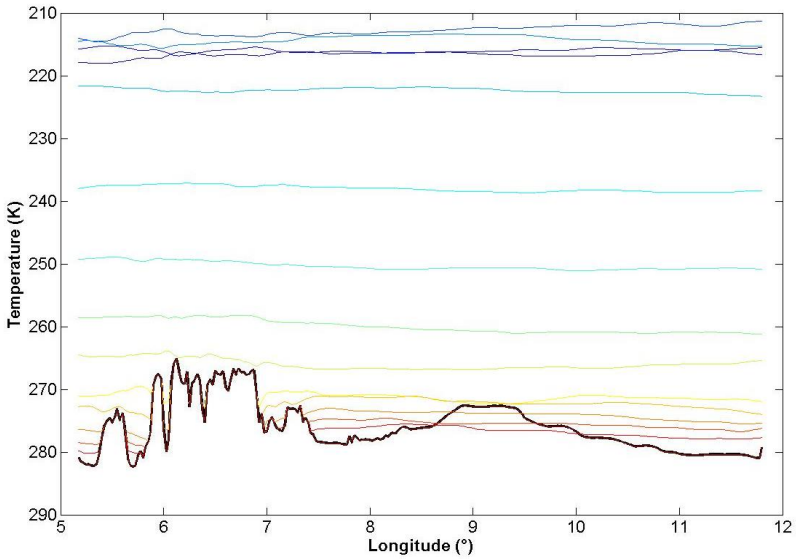

Figure 63-Temperature levels of NWM

In this last Figure 63 where each level of temperatures are represented, it is noted that it could appear that for some longitudes (as 9° for instance), it exists temperature levels whose values are superior to the temperature at the surface height (represented by the black line). This could be seen as temperature inversion which is a potential cause of atmospherical phenomena such as ducts (introduced in 4.2.2.1.2).

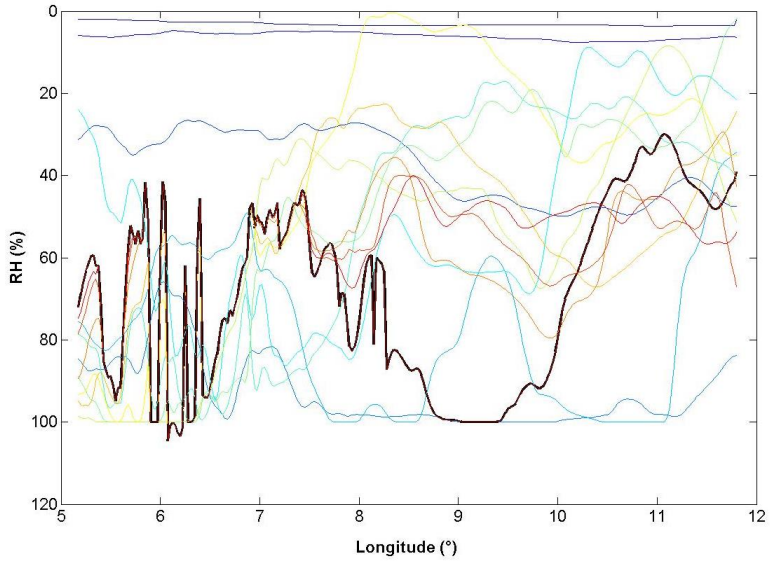

Figure 64-RH levels for NWM

This Figure 64 representing the relative humidity levels is difficult to analyze but it could be noted that for levels closed to the surface (black and warmest color lines) RH values vary significantly with longitude whilst for the highest levels (in dark blue), these values seem more stable (smoothed). This could be explained by the fact that effectively the humidity is more stable at higher altitudes than close to the surface where clouds and weather instabilities are frequently present.

In order to judge the accuracy of parameters extracted from such Numerical Weather Model, Meteo France [118] provided vertical profiles (in Pressure coordinates (hPa)) of the average errors of atmospherical parameters over the 2014 year, computed by comparing the extracted analyzed data with radio-sonde observations. Heights, Temperature and Relative Humidity profiles are represented in the figures below. Error biases are represented by the dashed lines and Mean Square Errors (MSE) in solid lines.

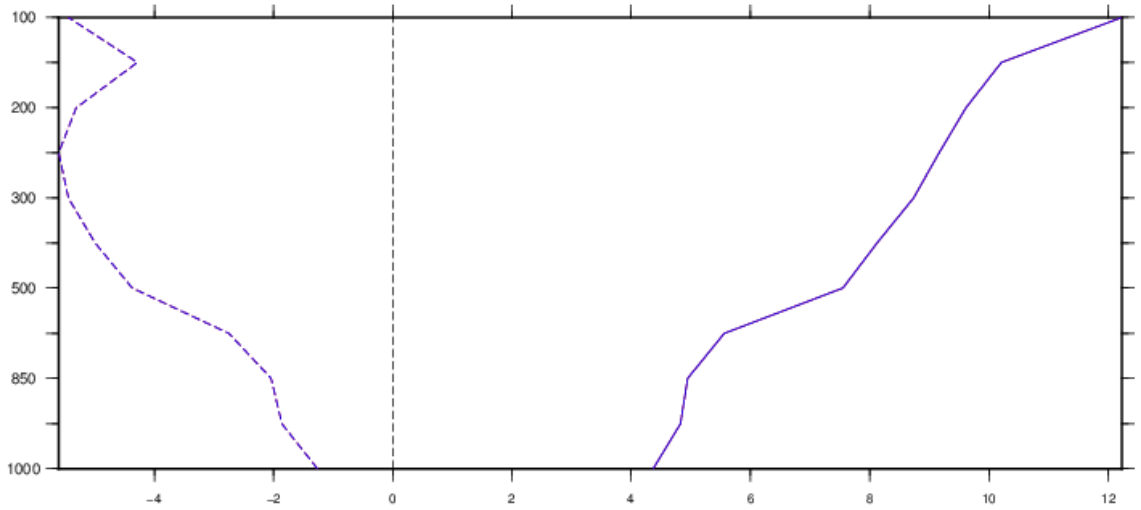

Figure 65-Vertical Profiles (over pressure coordinates in hPa) for Height Parameter in meters

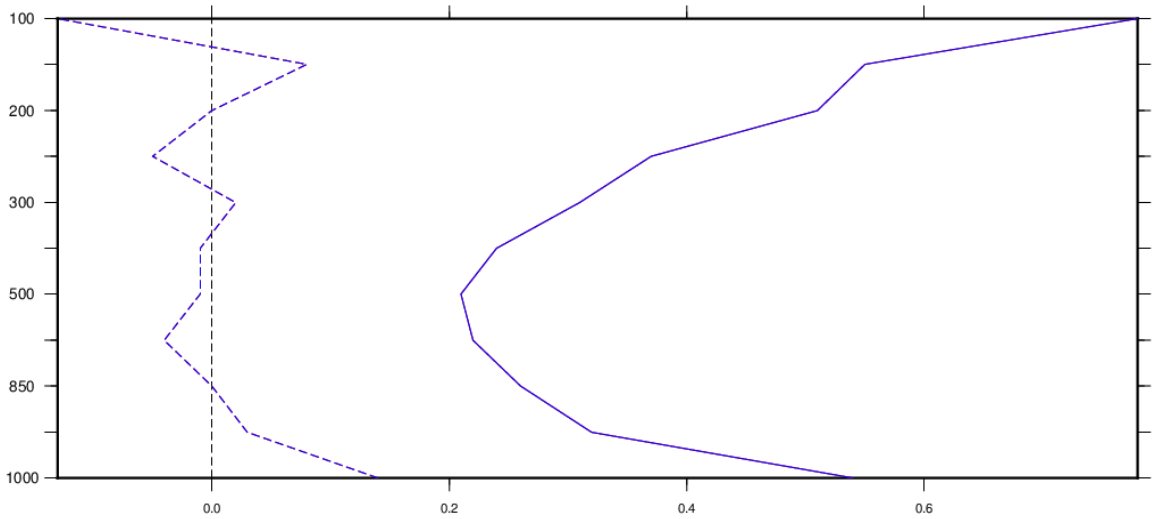

Figure 66-Vertical Profiles (over pressure coordinates in hPa) for Temperature Parameter in K

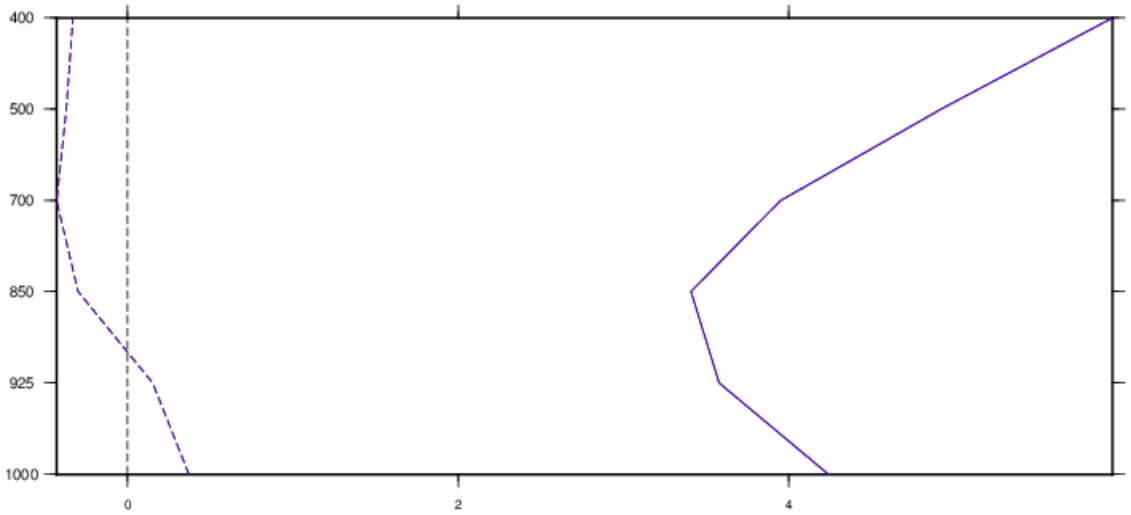

Figure 67-Vertical Profiles (over pressure coordinates in hPa) for RH Parameter in %

It could be relevant to add that according the discussion with Meteo France scientist [118], horizontal correlation between parameters in among 15km (i.e 50% of correlation is observed for higher distances than 15km). That means that in this PhD study context, by considering that the highest distance between the ground station and the aircraft at 200ft (Cat I decision height) with regards to the Ground Facility siting of D_{TH}=5km (as defined in standards [117]) is about 6.5km, the correlation between errors will be about 74%.

5.2.2.3 Harmonie

Two years (09/2012 - 09/2014) of Harmonie data with a resolution of 3 hours have been processed. The geographic limits shown in Figure 68 are defined by latitudes from 49.00 to 55.88 degrees and longitudes from 0.00 to 9.99 degrees with a horizontal grid resolution of 2.5km.

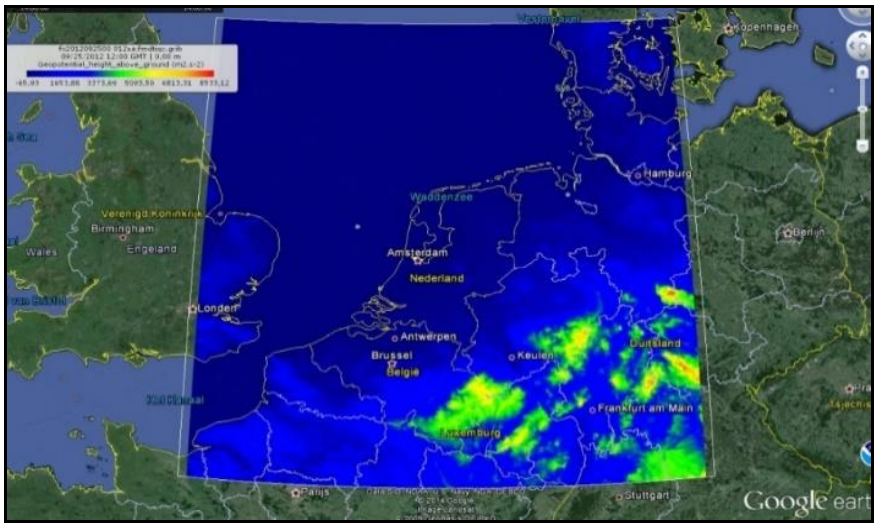

Figure 68-Harmonie domain –Source: Google Earth V7.1.5.1557- 10/04/2013

Parameters available from this NWM are: Surface Geopotential Height, Surface Pressure as surface parameters and also Temperature, Specific Humidity for 60 levels in the vertical, with the top level at 0.1 hPa. These parameters could be also represented as for Arome data for each levels as a function of longitudes or latitudes in a plane (Figure 61, Figure 62, Figure 63, Figure 64) but they won't be shown in this report.

The Height of the surface over the Harmonie domain extracted from the data is represented on the Figure 69

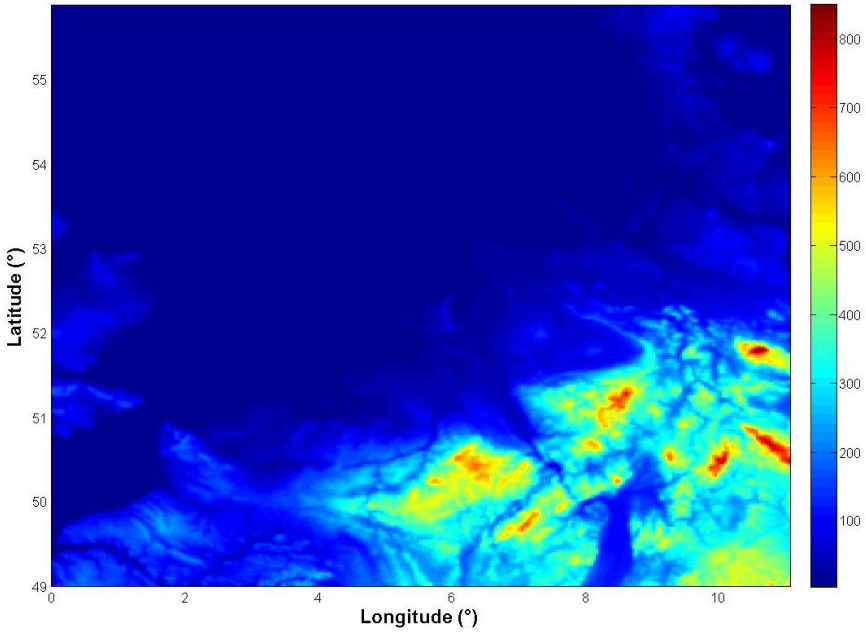

Figure 69-Surface height of Harmonie domain

Once these atmospheric parameters obtained, the range tropospheric delay can be modelled and computed with different approaches. They are explained in the following sections 5.3.1, 5.3.2 and 5.3.3 of this report.

5.3 Tropospheric Delay Modelling and Computation

As introduced above in sections 4 and 3.2.2.3, after having obtained the relevant atmospheric parameters Pressure, Temperature and Relative Humidity, the tropospheric delay may be determined. This section details the modelling and the computation of the tropospheric delay for both the Slant Tropospheric Delay (STD) and the Zenith Tropospheric Delay (ZTD) (presented in 4.2.1.1.4) in the absolute case (not differential). First, some notions about tropospheric delays will be introduced, then two methodologies used in this study will be presented: one by taking into account the surface atmospheric data which is described in 5.3.2 and the other by using layered NWM data presented in 5.3.3.

5.3.1 Total Refractive Index

The tropospheric delay may be decomposed into two components: the dry (or hydrostatic) delay and the wet (or non-hydrostatic) delay. The dry component usually consists of 90% of the total delay and varies with the local temperature and atmospheric pressure [122] whereas the wet component is generally smaller (from a few millimeters in arctic regions to forty centimeters in tropical regions) but more variable.

The Slant Tropospheric Delay (STD) for a satellite signal received at any elevation angle can be computed by using following equation defined in [61] and [62]:

$$STD = 10^{-6} \int N ds$$

Equation 147-STD

Where N defines the refractive index and ds is the differential form of path length over which the integration is performed. The integration is over the entire signal path length, although the tropospheric delay is understood to be zero for the path outside the troposphere. Equation 147 can be decomposed into 2 components the dry part Slant Hydrostatic (or dry) Delay denoted SHD and Slant Wet Delay denoted SWD as:

$$STD = SHD + SWD = 10^{-6} \int N_d ds + 10^{-6} \int N_w ds$$

Equation 148 - Decomposition of STD

Where N_d and N_w are respectively the dry and the wet refractivities defined by the following equations [123]:

$$N_w = \left(\frac{k_2 e}{T} + \frac{k_3 e}{T^2}\right) \times {Z_w}^{-1}$$

Equation 149 - Wet refractivity

$$N_d = \frac{k_1 P}{T} \times {Z_d}^{-1}$$

Equation 150 - Dry refractivity

Where k_1, $k_2$and $k_3$are constants, P is the partial pressure of the dry air, T is the temperature and e is the partial pressure of water vapor, Z_d and Z_w are the compressibility factors for dry air and water vapor respectively.

Figure 70 considers a troposphere split into layers (as defined in NWMs for example).

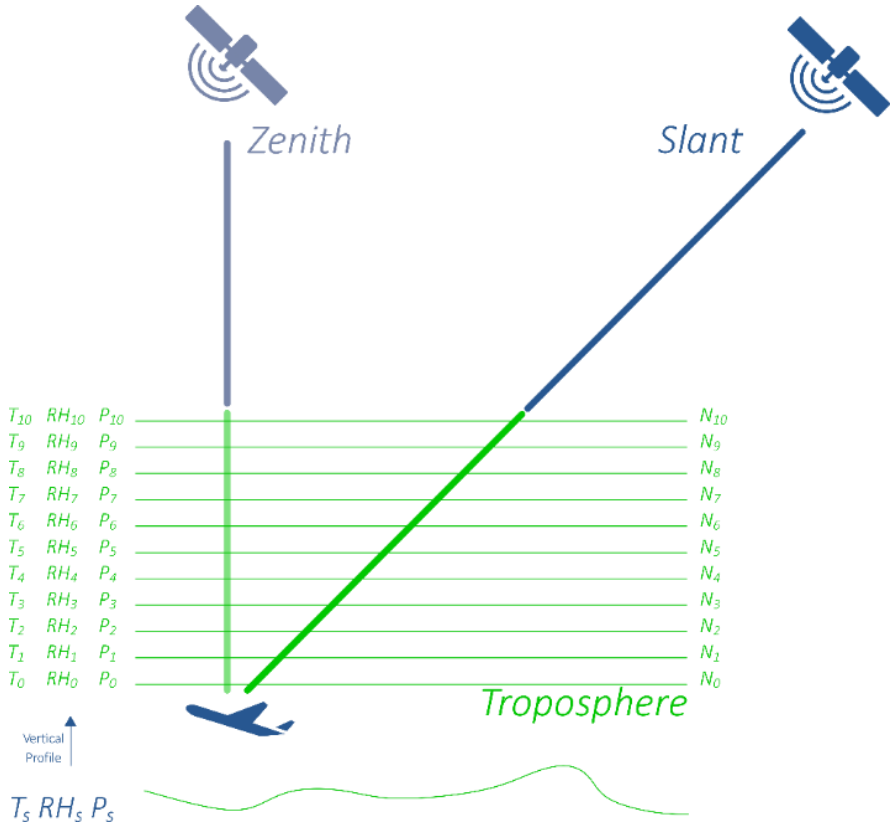

Figure 70-Illustration of a troposphere split into layers

Therefore, by applying this previous decomposition, an approximation of the STD may then be formed from a summation of the refractive indices at these L levels (e.g. 10 levels shown in Figure 58).

$$STD \approx 10^{-6} O(\theta) d \sum_{i=0}^{L} N_i$$

Equation 151 - STD over layers

Where the refractivity index N_i is a function of the atmospheric conditions at that level T_i, RH_i and P_i, $O(\theta)$ is the obliquity factor as a function of the elevation θ (as defined in Equation 13) and d is the height between layers. In the event of perfect horizontal spatial correlation such that the atmospheric parameters T_i, RH_i and P_i and thus the refractive indices N_i are independent of θ, then the Zenith Tropospheric Delay (ZTD) is given as.

$$ZTD \approx 10^{-6} d \sum_{i=0}^{L} N_i$$

Equation 152 –ZTD over layers

The relationship between the surface parameters T_s, RH_s and P_s and the atmospheric parameters throughout the troposphere can be approximated through the use of vertical profile which enables to get for example T_i from T_s. Alternatively the total refractivity along the path can be approximated using an empirical model in terms of the atmospheric parameters at the receiver (often at the surface).

$$ZTD \approx f(T_0, RH_0, P_0)$$

Equation 153 -Empirical Model for ZTD

Based on these notions, the following subsections outline different methodologies for determining the STD which have been used during this research, firstly taking into account the surface atmospheric data and then NWM data over layers.

5.3.2 2D Empirical Model

This methodology is the simplest for computing STD. It consists at first of estimating the Zenith Tropospheric Delay (ZTD) before applying the mapping function, for example as found in [16]:

$$STD = O(\theta) \times ZTD$$

Equation 154 - Relation between STD and ZTD

The ZTD is obtained by using surface atmospheric parameters of Pressure, Relative Humidity, and Temperature. Vertical profiles introduced in 5.3.1 are assumed for deriving these three parameters. Different empirical models have been derived [68] [62] [122] [61] [124] [125] [115], also based on splitting the delay into the Zenith Wet Delay (ZWD) and Zenith Hydrostatic (dry) Delay (ZHD) components. ZHD can be computed through one such model, the Saastamoinen model [66]:

$$ZTD_{saas} = 0.002277 \times \left[P + \left(\frac{1255}{T} + 0.05\right) \times e\right]$$

Equation 155 - Saastmoinen

Where P is the Pressure, T is the Temperature and e is the partial pressure of water vapor related to the relative humidity by the Clausius-Clapeyron equation [61]:

$$e = e_s \times \frac{RH}{100}$$

Equation 156 - Clausius-Clapeyron Equation

where e_s is the saturation water vapor pressure. These parameters are often taken at the surface, for a receiver located at or close to the surface.

The methodology for computing accurately ZWD by using surface data and a novel vertical profile approximation is detailed in [68].

Of the tropospheric delay models referenced above, the Modified Hopfield Model [125] is a practical choice for computations at the lower part of the atmosphere including both hydrostatic (dry) and wet components [7] [61] whilst the Saastamoinen model provides a good estimate for the upper dry atmosphere. These two models are thus used where appropriate, in particular, the MHM for the weather wall model approximation explained in section5.2.1 by Figure 54.

In this section, tropospheric delays were derived using only surface atmospheric data. When the atmospheric parameters are available at both the surface and at multiple layer it should be possible to use another model to more accurately estimate this tropospheric delay. The following section describes such a methodology.

5.3.3 3D layered Model

As already mentioned, in the previous section 5.3.2 only surface atmospheric data was used, whilst in NWMs the atmospheric parameters are available at both the surface and at multiple layers. It is therefore possible to use this 3D data model to more accurately determine the total tropospheric delay. An integration of the refractive index as suggested in subsection 5.3.1 is then possible (Figure 70), either directly in the slant domain (through ray tracing) or in the zenith before application of the mapping function. The Saastamoinen model [66] (Equation 8) is used for the near-negligible component above the highest NWM layer.

The numerical integration process uses a variable path increment length as the variation of the atmospheric parameters at higher altitudes is smoother and more predictable [126]. In fact, the NMW layers are also more tightly spaced near the ground to capture this greater variability. Interpolation is used to obtain the values of the atmospheric parameters at points along the signal path. Interpolation in the vertical domain is linear in the case of temperature and relative humidity and exponential for the pressure. Interpolation in the horizontal domain is performed through a spherical distance weighted averaged. Figure 71(a) shows vertical interpolation of atmospheric parameter A between layers i and i+1 for a NWM grid point which does not require horizontal interpolation. Figure 71(b) illustrates the additional horizontal interpolation required to obtain the atmospheric parameters between NMW layers at an arbitrary point.

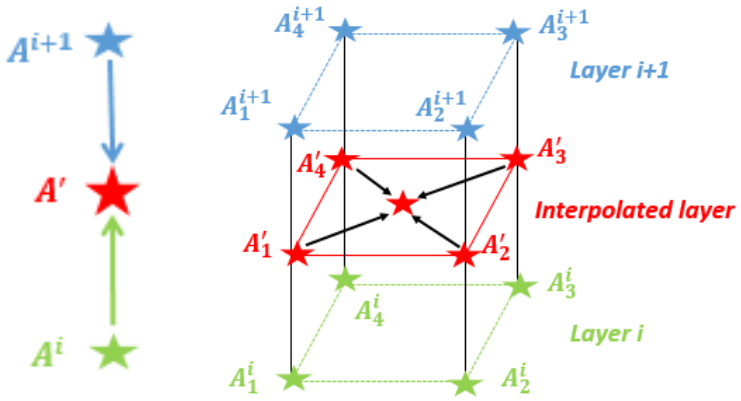

Figure 71-(a) -Vertical Interpolation - (b) Additional Horizontal Interpolation

The numerical integration process differs slightly between the ZTD and STD cases [61] .The path increment is scaled according to the elevation so to have approximately the same number of integration points per layer and avoid excessive computation time. Another methodology is to find ZTD numerically by integration and then apply the mapping function as per Equation 154.

By using the Arome NWM data, each of these parameters (Height on Figure 72, Pressure on Figure 73, Temperature on Figure 74 and RH on Figure 75) are represented for illustration purpose in a plane format as a function of longitude (for a fixed latitude) over the path length for a satellite elevation angle of 5°:

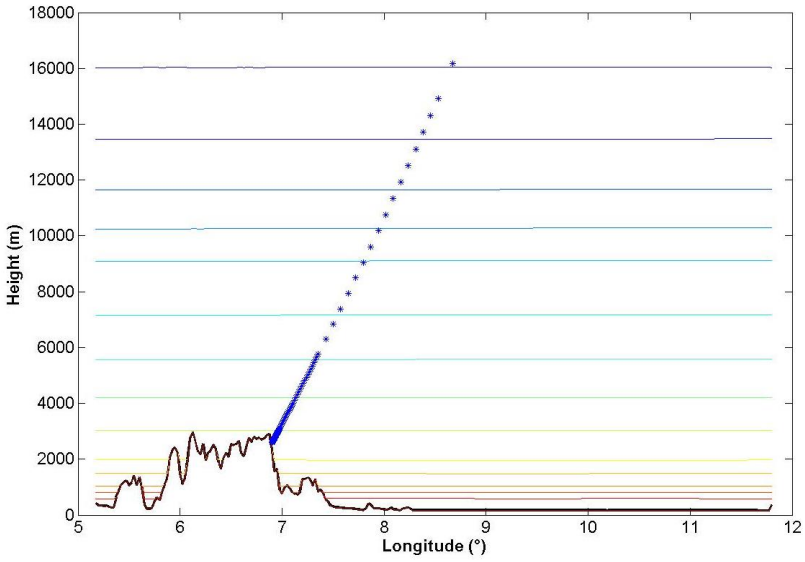

Figure 72-Interpolation of Heights

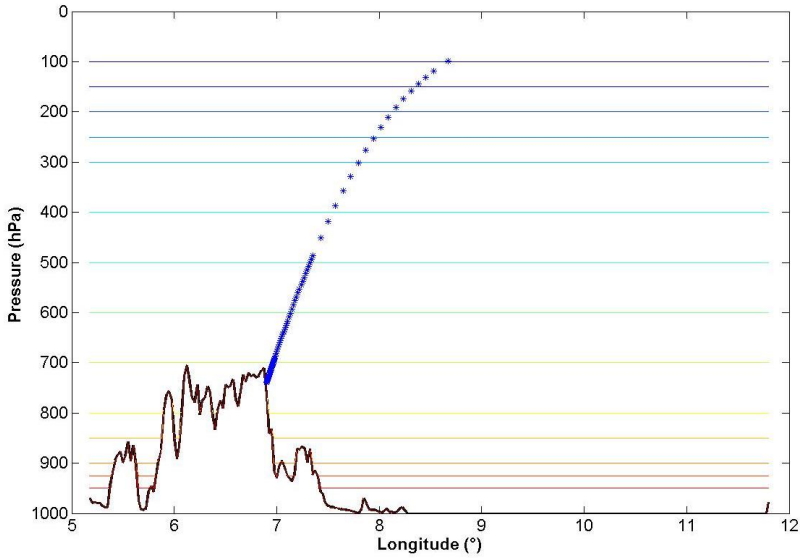

Figure 73-Interpolation of Pressures

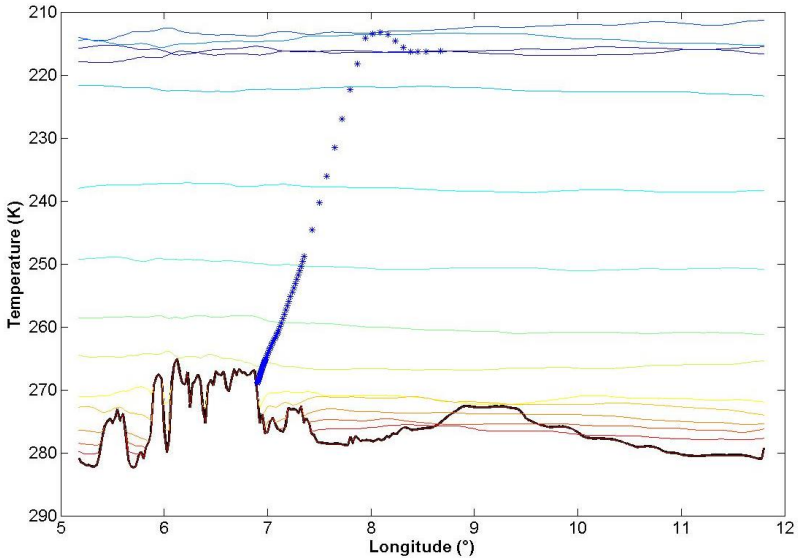

Figure 74-Interpolation of Temperatures

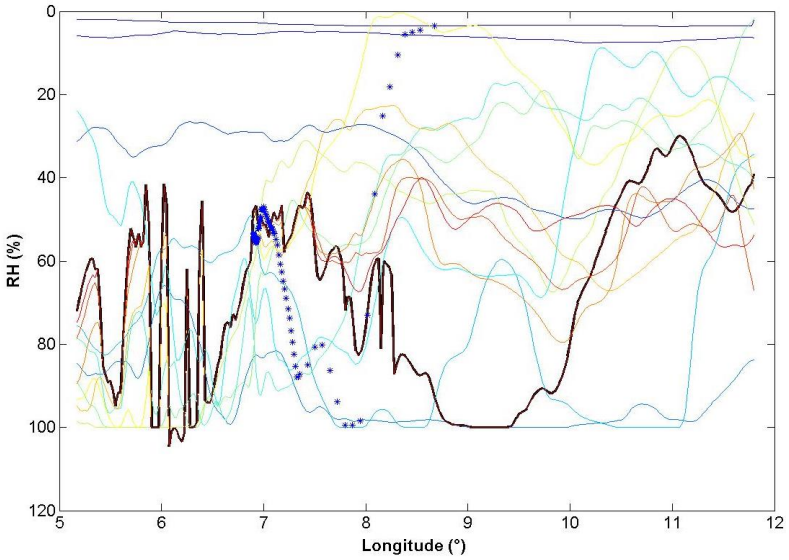

Figure 75-Interpolation of RH

Observing these figures, note that the number of integration points is greater at the beginning of the "ray-tracing" algorithm since the path increment length varies. Also, as it could be expected, Height parameters in Figure 72 and Pressure parameters in Figure seems to "linearly" increase and decrease respectively during the ray-tracing algorithm. Furthermore, the exponential vertical profile of the Pressure can also be remarked through this Figure 73. The temperature in Figure 74 decrease until a highest level, decrease a little bit and seems constant at the end of the interpolation. This observation is in accordance with the behavior of the Height level temperatures (linear vertical profile of the temperature). By seeing at the Figure 75, it can be noted that this relative humidity parameters appear to be the less predictable and stable parameters during the ray tracing algorithm. Therefore by viewing the Equation 149, the dependency of the wet component of the troposphere to the relative humidity, explains the fact that this wet component is also the more difficult part of the tropospheric delay to model.

Once each parameter is obtained, wet and dry refractivities can be computed over the path length as explained in 5.3.1 through Equation 149 and Equation 150. These values are represented in the following figure.

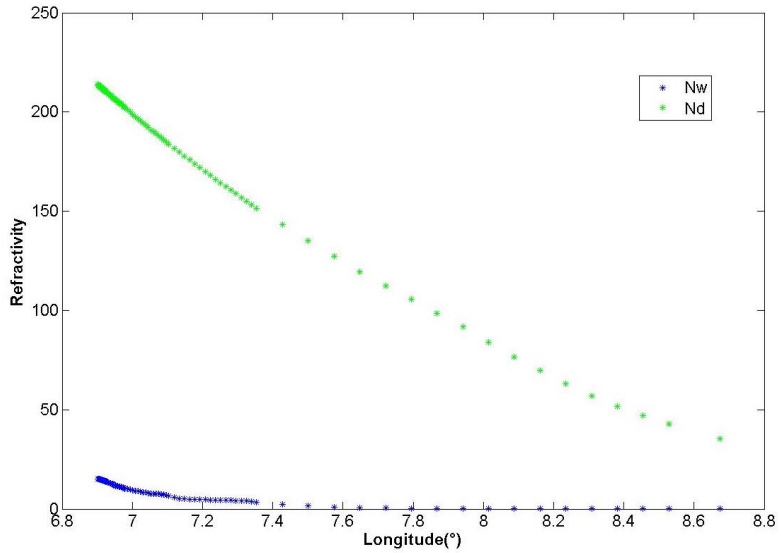

Figure 76-Interpolation of Refractivities

These refractivities parameters are used to compute the tropospheric delays as explained through the Equation 148. These single delays can then be combined to estimate the differential range tropospheric delays over paths 2 and 3 as presented in Figure 1. Also because in this Chapter 5, the focus is made on the worst case conditions, the following section details the research and the methodology to obtain the worst differential range Tropospheric Delay.

5.4 Horizontal Differential Tropospheric Delay

The previous part of this report outlined the means to compute a single tropospheric delay for a receiver at an arbitrary location using either a simple empirical model or through a more sophisticated 3D NWM. This section addresses the differential range error resulting from the range tropospheric delay over paths 2 and 3 as presented in Figure 1. It is important to recall that the focus of this work is in worst case anomalous conditions.

Two approaches have been used in this study to determine this differential range delay. The first follows the Wall model approach of [7] utilizing the Modified Hopfield Model [115] [125] and shown schematically in Figure 54. The second approach uses the NWMs summarized in section 5.2.2 by performing a search for the worst case differential error. The methodology of this search in addition to further details regarding the derivation using the Wall model is given below in5.2.1.

The simplest logic for the search would be a brute force approach considering all GBAS installation locations within the region of interest (φ,λ) where φ denotes the longitude and λ the latitude of the GBAS installation locations, all approach trajectory directions α and distances D, all satellite azimuths ζ and elevations θ and all time points t of the NWM data. However, a seven-dimensional search over $(\varphi, \lambda, \alpha, D, \zeta, \theta, t)$ is not feasible

within the time constraints and computational capabilities of the project. Therefore an alternative methodology was used where for each epoch t the following steps were taken:

- **A.** Compute the ZTD over the NWM grid (over φ, λ) using 5.3.3
- **B.** Compute the differential ZTD between nearby grid points (low resolution of D and ζ) correcting for height variations for different distances r and select the worst cases $(\varphi, \lambda, \zeta)$ for each r
- **C.** Refine the search over ζ for the worst cases selected (fixes worst case ζ and α)
- **D.** For each θ vary the φ, λ in the direction perpendicular to the gradient in order to find the worst differential range tropospheric delay

Steps A to C are performed with the ZTD whilst during step D, the elevation dependency ensures the STD must be computed (as described in section 5.3.3). This relies on the strong correlation between ZTD and STD [127].The following subsections outline each of the steps above.

5.4.1 Zenith Tropospheric Delay (Step A)

The ZTD is determined using the integration procedure outlined in 5.3.1 and 5.3.3. the following Figure 77 shows the ZTD for the 18th of September 2012 at 00h00 over the Netherlands and North Sea region using the Harmonie (5.2.2.3) data. A total of two years of Harmonie data were processed in total.

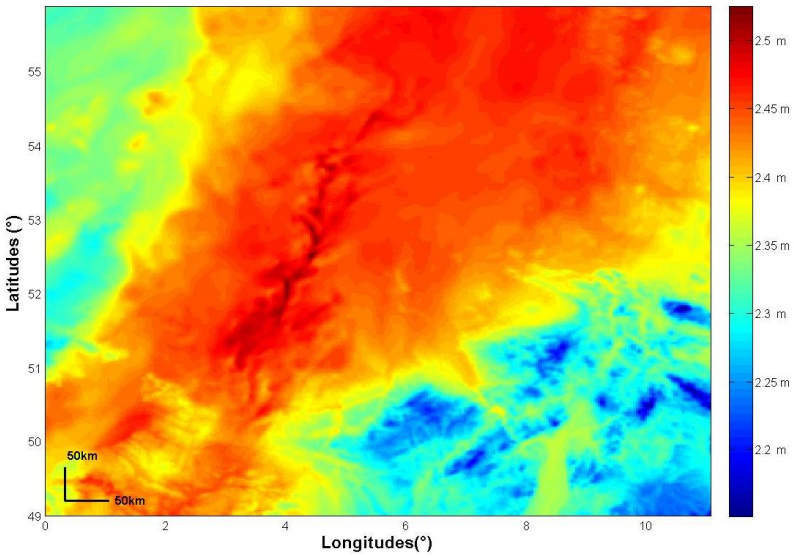

Figure 77-ZTD computed with Harmonie data

For this particular epoch, as shown in the Figure 77, variations of 30cm are observed over the whole NWM with greater variations in the north west region. Variations over the remaining parts do not exceed 10cm even over distances greater than 100km. Obtaining a ZTD map is the first step in the algorithm as well as gaining an understanding of the data and tropospheric behavior.

5.4.2 Differential Zenith Tropospheric Delay (Step B)

Once the absolute ZTDs determined with the methodology explained in 5.3.3, this second step B computes the differential ZTD, denoted ΔZTD, between nearby points. The nearby points are defined using ten segment types with lengths (r) ranging from 2.5km to 10.61km (7.5×√2) as shown for single quadrant in the following Figure 78. Each segment type may have multiple orientations in all directions, some of which are shown for illustration in grey in Figure 78.

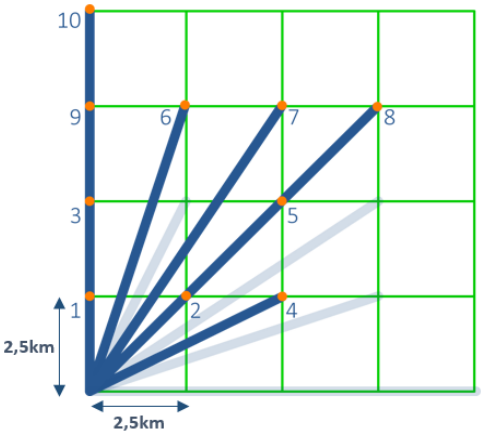

Figure 78-Definition of the 10 segments of study

Therefore this $\Delta ZTD$is determined over the entire grid for each type of segment and its variations. For this computation it is important to notice that whilst, in step A, a single ZTD is computed for each point, here in step B, due to height variations it is necessary to correct the ZTDs to a normalized common height, otherwise horizontal spatial gradients would include the effects of these height variations.

The worst case differential error observed over the entire grid (pairs) for each of the ten types is then selected for processing by the following steps C-D.

5.4.3 Worst Direction for Differential Zenith Tropospheric Delay (Step C)

The definition of the ten segment types in step B limits the search over azimuth direction to these fixed angles. In this step, for each of the ten worst case candidates relating to the segment types, a refinement is performed to obtain the worst case azimuthal direction. This is achieved by keeping the segment length constant and considering a fan of azimuthal angles 45 degrees either side of the original segment as shown in Figure 79. A fine resolution of one degree is used for this search and the ZTD is obtained by horizontal interpolation.

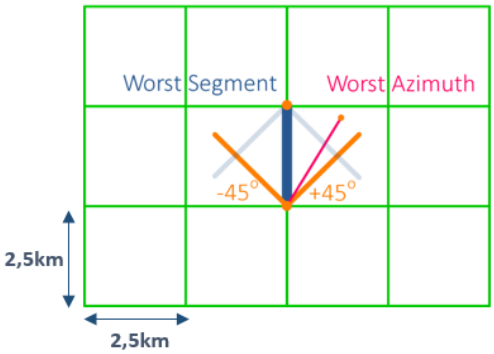

Figure 79-Searching for worst azimuthal direction

Following this refinement, worst case differential range zenith tropospheric delays are obtained for each time point. In the next section, the search is extended to account for elevation dependency of the STD.

5.4.4 Worst Differential Tropospheric Delay (Step D)

In this fourth step of the methodology, the ray-tracing algorithm used for numerical integration is applied as described in section 5.3.3. As well as introducing the elevation dependency, the distance between ground station and aircraft is also extended beyond the fixed distances of the predefined ten segments. Finally, its unknown along which portion of the path is the tropospheric delay decorrelated between the segment end points. For this reason, when using elevations lower than 90 degrees, an additional search parameter is introduced, by translating the ground-to-aircraft plane by a series of distances $D_{w.}$ as shown in the following figure. Indeed, without translation the worst condition (represented by the cloud) could be missed, therefore it is needed to move the segment for finding the worst differential range tropospheric delay.

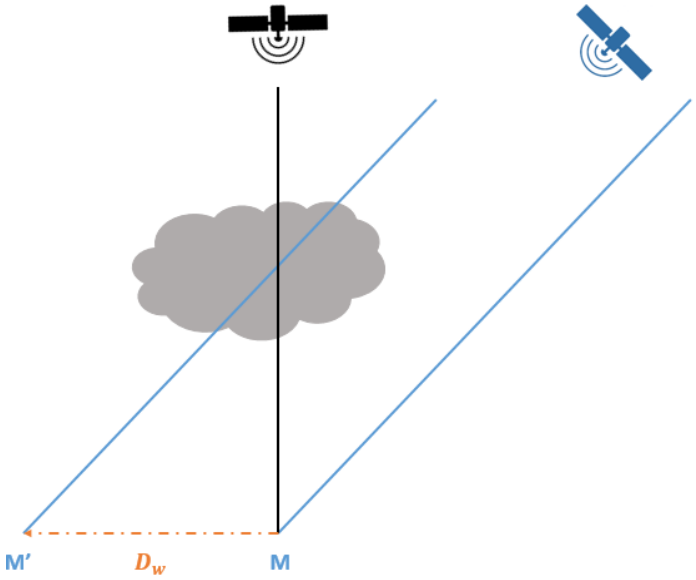

Figure 80-Segment translation

At the end of the loop, the worst case over D_w is used. Figure 81 shows how the perpendicular translation is performed, shifting the midpoint M to a new midpoint M'.

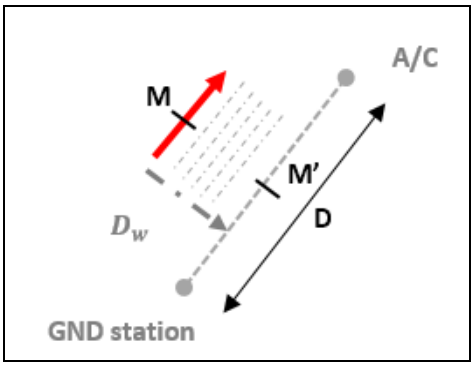

Figure 81-Finding the worst case for Differential Range Tropospheric Delay

It is important to remind here in this report that, the differential range tropospheric delay varies with distance between aircraft and ground as shown in the following figure obtained by using the MHM described in 5.3.2 for a satellite at 5° of elevation:

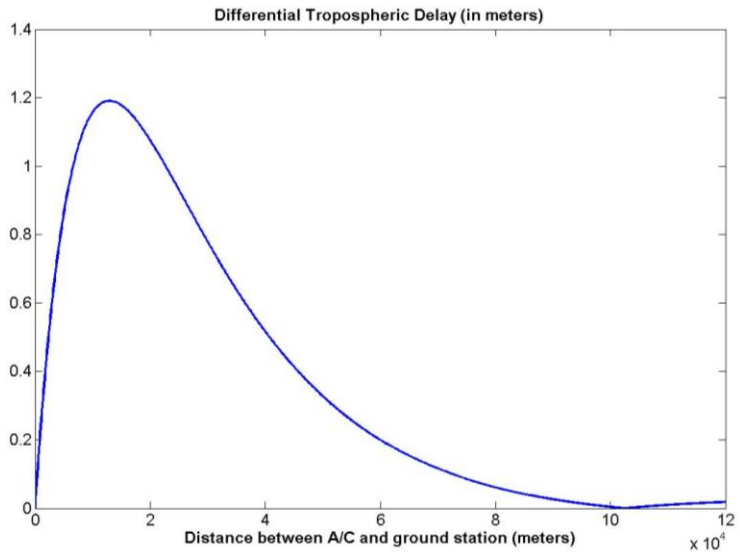

Figure 82-Differential range Tropospheric Delay

Therefore, in this section the distance D was fixed as the sum of the ground distance of the aircraft to the runway threshold (LTP, Landing Threshold Point) at the 200ft Cat I decision height which is considered as the furthest point where Cat II/III performance requirements are applicable and a nominal D_{TH} of 5km between the LTP and ground station according SARPs [117]. In the previous Figure 82, it is interesting to remark that the first part of the curve grows up with distance and then the second part decreases with distance. This could be explained by the fact that the first part shows the spatial decorrelation between aircraft and ground station. Then, this study assumes a glide path angle at 2.5° with an "infinite" approach therefore the second part decreases because the horizontal variation of the troposphere decrease with the height of aircraft. This approach is not realistic but is ok as the critical part is the closest to the ground station and therefore the first part of the curve.

A fitting curve has been derived using the Wall model parameters defined in [7] with the Modified Hopfield Model (MHM) explained in 5.3.1 to compute the differential range tropospheric delay and plotted in blue denoted by the Curve A in Figure 83. Then in order to compare this "Ohio" parameterization 5.2.1.2 with the "European" parameterization, the same approach as explained in 5.2.1 was derived by using the "Harmonie" data and "Arome" data. Indeed, by examining these data (5.2.2.3), worst case weather conditions appear for "Harmonie" to be T_w at 37.01°C, Pw set at 1003.2hPa, RH_w set at 100% and for "Arome" to be T_w at 36.9°C, Pw set at 1009.8hPa, RH_w set at 100%. Then, the red dashed Curve represents the Wall model derived with Harmonie data and the green dashed Curve represents the Wall model derived with Arome data.

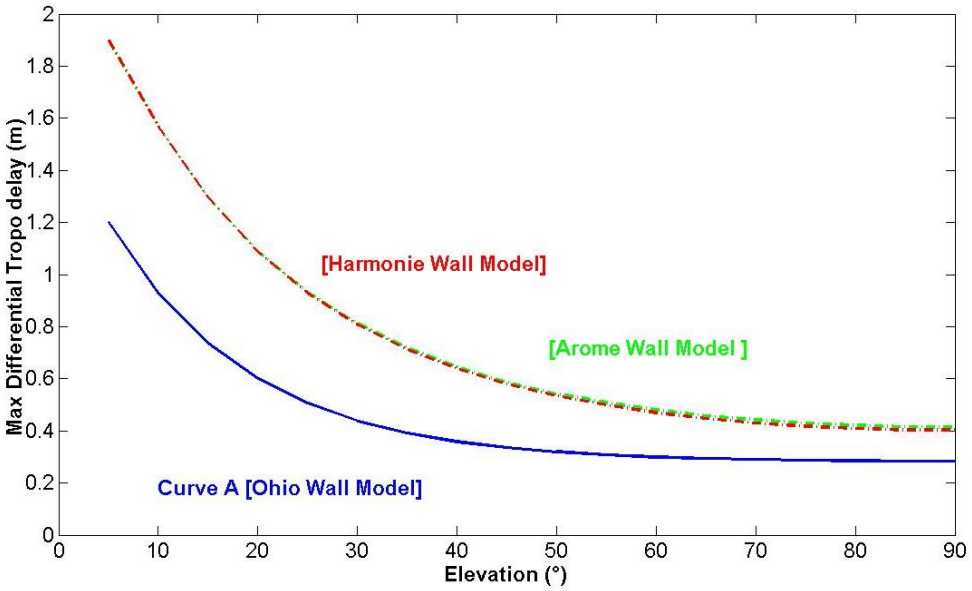

Figure 83-Wall model with different parameterizations

Differences in the curves can be explained due to the means the parameters were derived and ways the worst conditions were found and the environment of the region of data employed. Indeed, for analyzing the environment impact, it is possible to compare the "Wall Model" curves in Figure 83 , then it can be noticed an important difference between the blue curve representing the Ohio parameterization derived from a restricted set of data (GPS data only at one location) and the dashed curves which represent the "European" parameterization derived from a large amount of data (Arome and Harmonie). Therefore, this figure suggests that gradients in Europe could be more important than for this set of data examined at Ohio because differences on maximum differential range tropospheric delay appear to be about 0.75m at 5° of elevation and 0.15m at 90°. But it should be added that theses differences could be also explained by the fact that worst conditions in Harmonie and Arome data were found by using a conservative methodology. Indeed the search was realized for the worst conditions on all data and compared to standard values even if in the same set of data standard conditions and worst conditions are not present at the same time and at "approach" distance (up to 12km).

Then, Figure 84 plots the worst cases found with the methodology explained in this section 5.4 for each of the 4945 sample points of Harmonie NWM over 2 years. A red curve denoted Curve B was fitted to worst case over time for each five degrees of elevation.

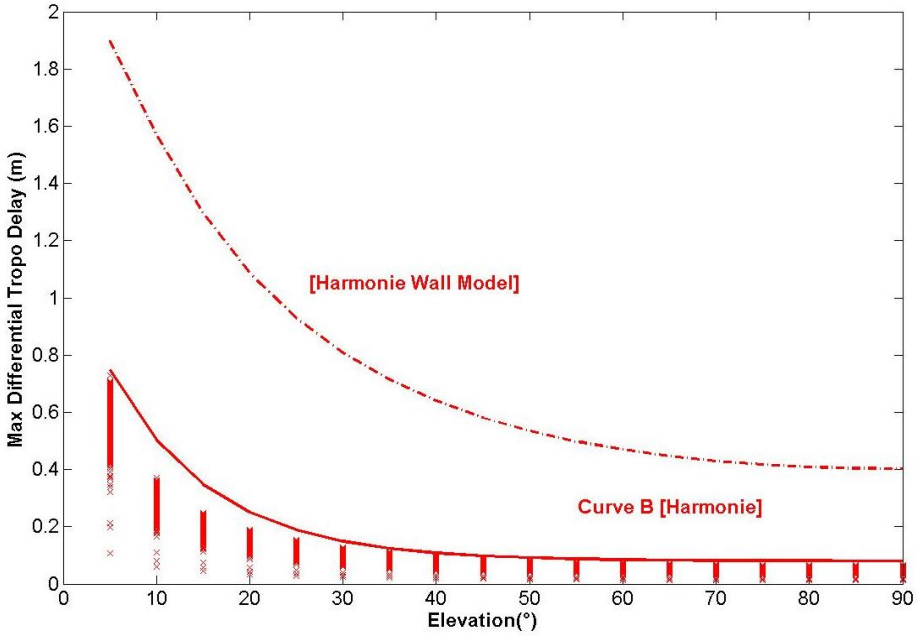

Figure 84-Max differential range tropo delay for Harmonie

Also the Figure 85 plots these worst cases found with the methodology explained in this section 5.4 for each of 2920 sample points of Arome NWM over 1 year, then a green curve denoted Curve C was fitted to worst case over time for each five degrees of elevation.

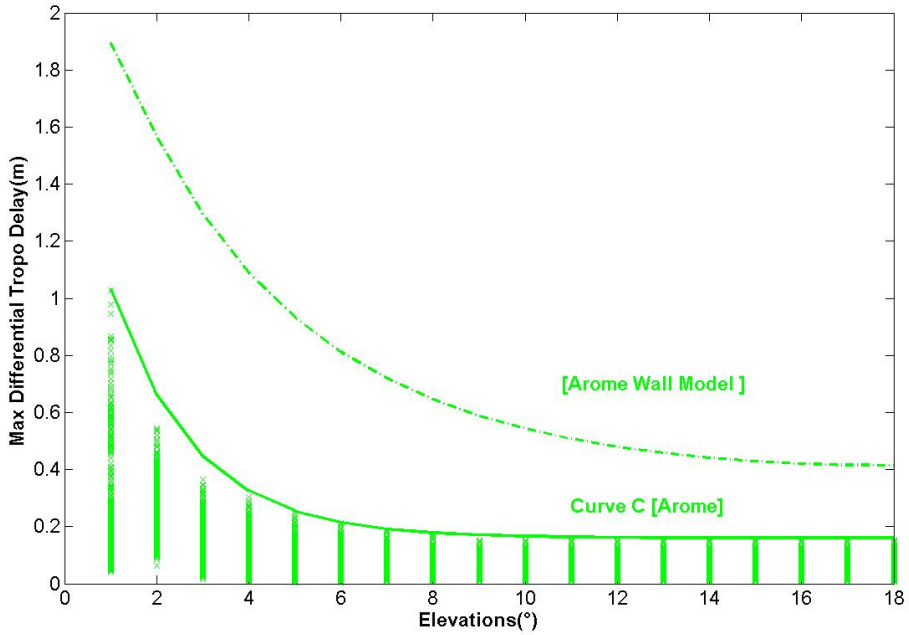

Figure 85-Max differential range tropo delay for Arome

It is relevant to notice the sharped shape of the Curve C at low elevations of 5°. This phenomena can be explain by the fact that in this Alpines area, gradients in atmospherical parameters are higher and they change more frequently as in Netherlands area particularly closer to the surface (which is the case for low elevations case in

this research). Also, it is important to notice that for this Arome Case, the dash line is below the green line for elevations angle smaller than 6°,therefore the Wall Model methodology appear conservative only for angle superior to 6° of elevation. Furthermore, for Alpines data realy conservative assumptions about the way to find the worst case were taken (as possible approaches closed to the mountain) which are no realistic these can explain the highest values obtained for low elevation angles. Then it could be interesting to only plot results just for elevation angle from 10° to 90° as presented in the following figure and to fit them by the Curve D.

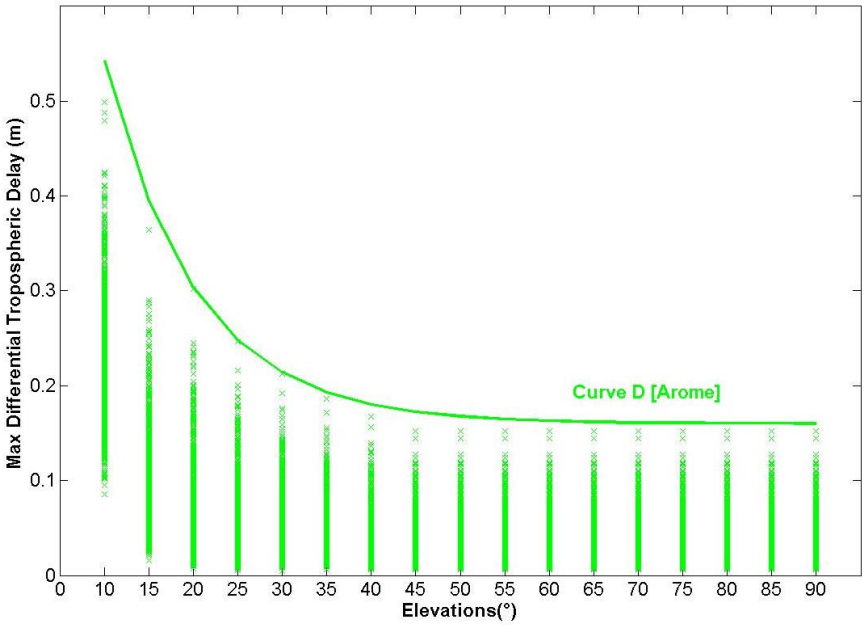

Figure 86-Max differential range tropo delay for Arome from 10°

Finally, the bounding/fitting curves obtained with each model and data (Ohio, Arome and Harmonie) is represented starting at 5° elevations angle (Curve A,B and C) in Figure 87 and at 10° elevation angle (Curve A,B and D) in Figure 88.

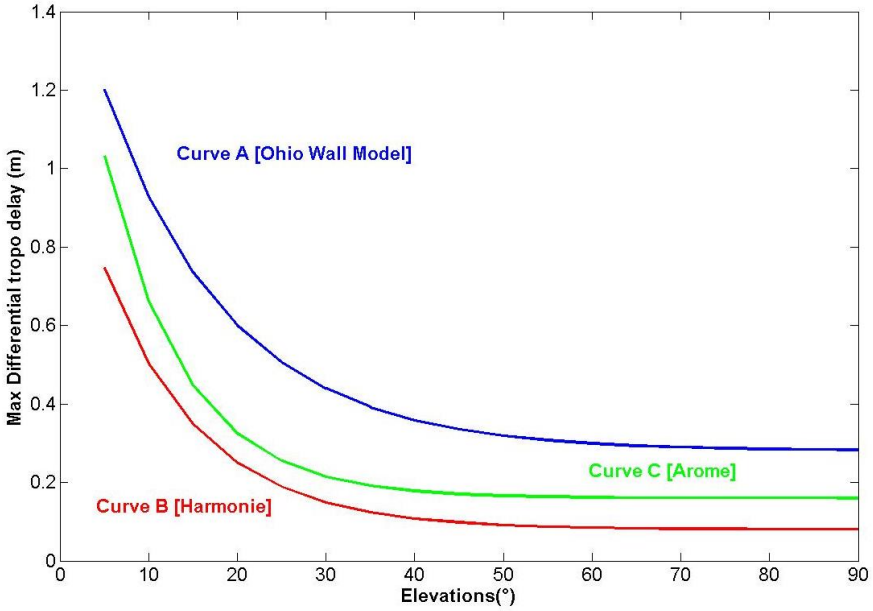

Figure 87-Bounding Curves for each model stating at 5°

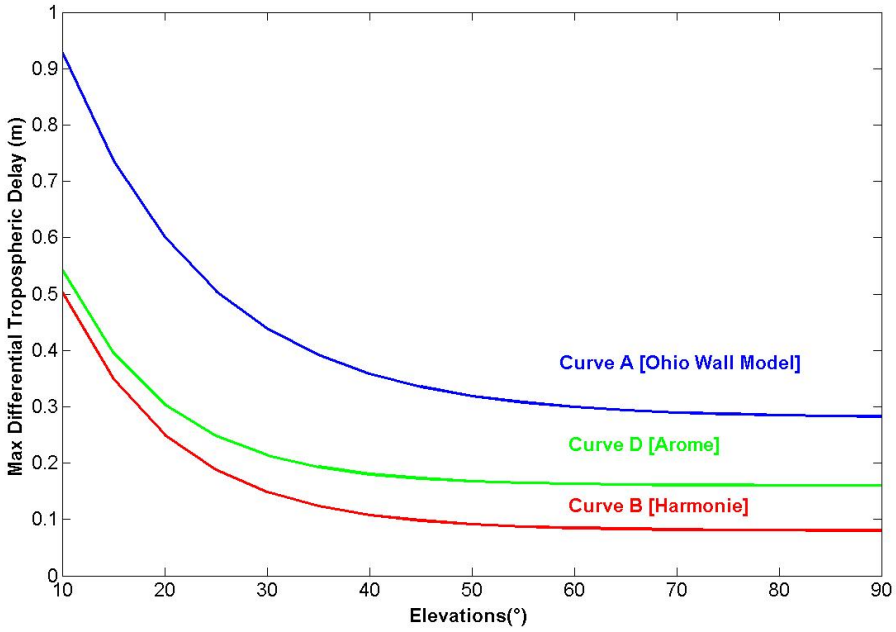

Figure 88-Bounding Curves for each model stating at 10°

The differential range tropospheric delay follows an expected trend with respect to elevation. Equations of these curves A, B, C and D are detailed in section 6.3.1.2. Also according to some previous analysis [7] [128], differential range tropospheric delays appeared as large as 0.4m in Ohio for a particular set obtained with GPS data, in the Figure 87, maximum differential range tropospheric delay appear to be about 0.8m by seeing the red Curve B and about 1.1m regarding the Curve C at 5° of Elevation (0.55m at 10° regarding the Curve D) so gradient in Europe seems again (as thought by seeing Figure 83) more important than in the data set examined by Ohio

particularly in Alpines area at low elevation. This could be explained by the fact that abnormal changings in atmospherical parameters should happen more frequently and should be more localized close to the surface (i.e at low elevation) in Alpines area.

Also, it is relevant to notice that the dashed red/green lines (representing the Wall Model curves)are really above the red/green lines that means that using the "Wall model" as a methodology for finding the maximum differential range tropospheric delay is a too conservative methodology therefore the Wall Model methodology appear really conservative.

5.4.5 Accuracy of this methodology with NWM

In order to validate the methodology introduced above in 5.4, the accuracy of it as to be examined. Indeed, by using the curves representing the vertical profiles of atmospherical parameters in Figure 65, Figure 66 and Figure 67, it is possible to evaluate the impact of errors on parameters on differential range tropospheric delay estimation with this methodology. First, analysis was realized by assuming that horizontal correlation between errors on parameters over the grid is about 74% as explained in 5.2.2.2. Then, the worst differential range tropospheric delay was computed as presented in 5.4 for different cases at +/- 2σ for Temperature and Relative Humidity parameters and some elevations such as 90°, 45°, 15°. Therefore, impacts on wet and dry refractivities were compared and are represented in the figure below for an elevation of 45° for both A/C and Ground sides.

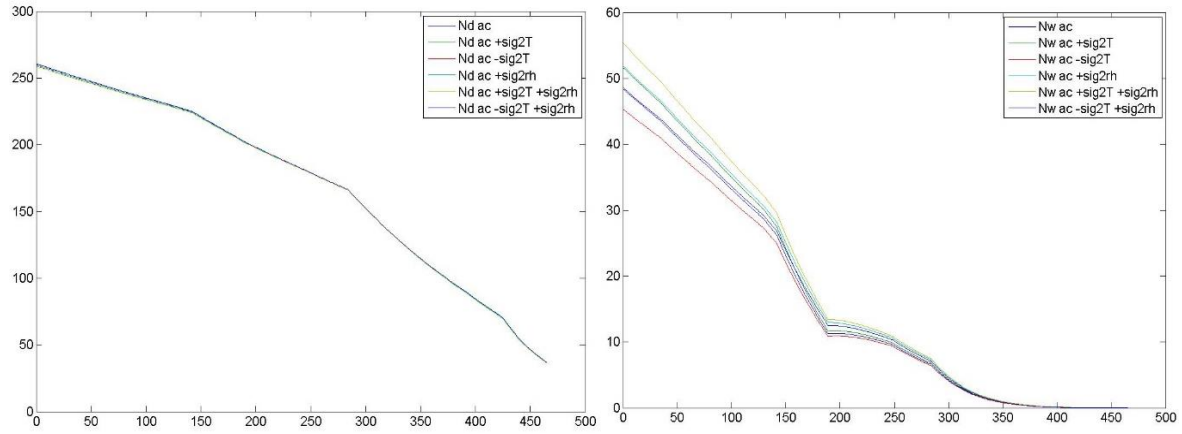

Figure 89-Nd/Nw for A/C

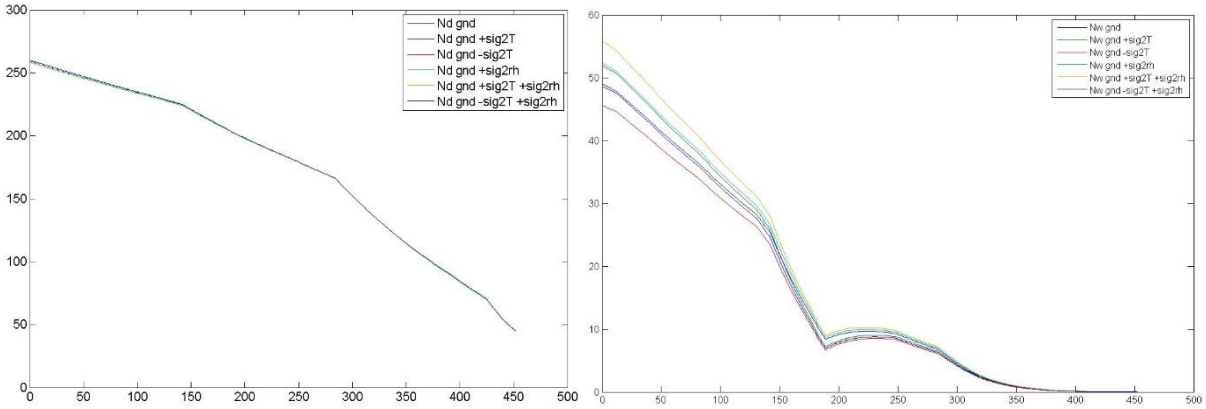

Figure 90-Nd/Nw for Gnd

These refractivity curves in Figure 89 and Figure 90 show and confirm (3.2.2.3) that the wet component is less accurate and difficult to predict as the space between curves in the right figures is more important than in the left figures. Therefore the accuracy of the differential range tropospheric delay computations is mainly lead by this wet part of the troposphere.

Then, range tropospheric delays were computed as explained in 5.3 and plotted for these all cases for both A/C and Ground sides.

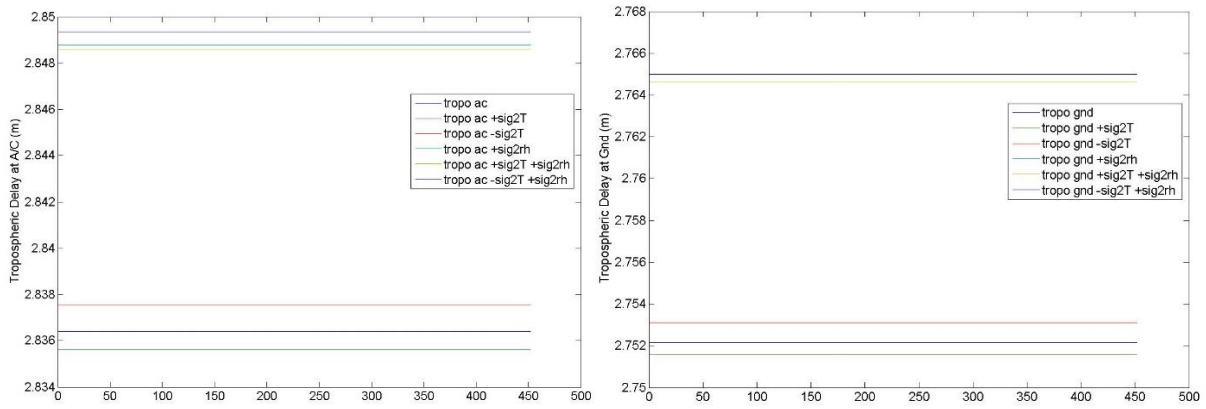

Figure 91-Tropospheric Delay for A/C (left) and Ground (right)

Finally, impact on differential range tropospheric delays between A/C and Ground was analyzed and curves are represented in the following figure.

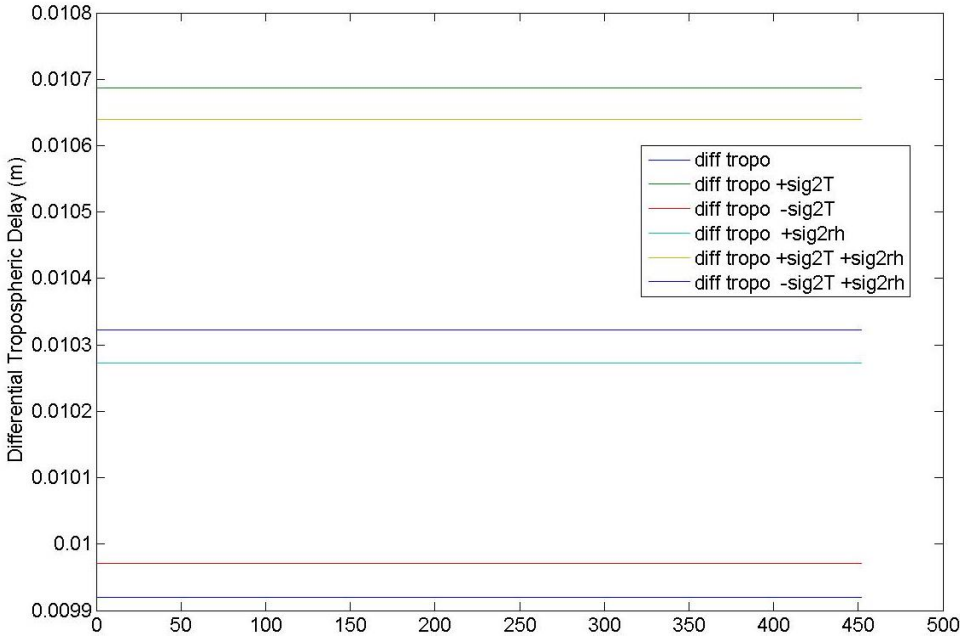

As showing in this last figure, the worst case (i.e highest differences compared to differential range tropospheric delay without error) appears here to be for the case at +2σ for Temperature.

In this case, to evaluate the accuracy of this differential range tropospheric delay computation, the following computation was realized by taking into account that the correlation between errors is about 74% (5.2.2.2):

$$\varepsilon_{gnd} = \frac{\left|STD_{gnd}(T) - STD_{gnd}(T + 2\sigma_T)\right|}{\left|STD_{gnd}(T) - STD_{ac}(T)\right|} \times (1 - 0.74)$$

$$\varepsilon_{ac} = \frac{\left|STD_{ac}(T) - STD_{ac}(T + 2\sigma_T)\right|}{\left|STD_{gnd}(T) - STD_{ac}(T)\right|} \times (1 - 0.74)$$

Equation 157 – Accuracy errors of the differential range tropospheric delay computation using NWMs

Then, by taking into

Worst Values obtained in this case were:

$$\varepsilon_{gnd} \approx \varepsilon_{ac} \approx 21\%$$

Following table summarizes results obtained for different elevation angles:

Elevations	Aircraft Side	Ground Side
90°	6%	7%
45°	21%	21%
15°	25%	20%
5°	45%	39%

Table 22 – Percentage of errors done by using NWMs for computing differential range tropospheric delays

In view of this results, it appears that errors at the 95th percentile result in a differential range tropospheric delay computation error at zenith of 7% up to 25% at 15°. Therefore, using NWMs for assessing the troposphere threat seems to be an efficient methodology.

Furthermore, a similar analysis was realized to estimate the accuracy of the NWMs for heights up to 200ft.The following table summarizes results found for different elevation angles:

Elevations	Aircraft Side	Ground Side
90°	17%	22%
45°	25%	29%
15°	18%	19%
5°	31%	33%

Table 23-Percentage of errors done by using NWMs for computing differential range tropospheric delays up to 200ft

5.5 Vertical Component Modelling

The previous subsection has addresses the worst differential range error resulting from the range tropospheric delay over paths 2 and 3 as presented in Figure 1 As mentioned in 4.2.2.1.2, it could be possible that large differences between path 1 and the TC value (shown in Figure 1) occur which are not appropriately bounded by the Gaussian model established in standards [84] [16] .Therefore in order to assess these possible vertical gradients (also called Ducts) at first the standardized GAST C/D tropospheric correction model is presented based on standards followed by its representation based on NWM data before the tropospheric corrections are statistically analyzed.

5.5.1 GAST C/D Tropospheric Correction

5.5.1.1 Literature Results

As already presented in 3.2.3.3.2 and 0, a Tropospheric Correction (TC) is applied by the GBAS avionics. Indeed, TC is only based on vertical height difference between aircraft and GBAS ground station for satellite i as reminded from 3.2.3.3.2:

$$TC(\theta_i) = N_R h_0 \frac{10^{-6}}{\sqrt{0.002 + sin^2(\theta_i)}} \left(1 - e^{-\frac{\Delta h}{h_0}}\right)$$

Where N_R is the Refractivity Index, h_0 defines the tropospheric Scale height, θ_i is the elevation for the satellite i and Δh is the height of the aircraft above the GBAS reference location (in meters).

Then recalling 3.2.3.3.3, the residual tropospheric uncertainty is defined [42] for both GAST C and GAST D by:

$$\sigma_{tropo}(\theta_i) = \sigma_N h_0 \frac{10^{-6}}{\sqrt{0.002 + sin^2(\theta_i)}} \left(1 - e^{-\frac{\Delta h}{h_0}}\right)$$

Where σ_N is the refractivity uncertainty transmitted by ground subsystem which is in fact the standard deviation of N_R over 1 year period, h_0 defines the tropospheric scale height, θ_i is the elevation for the satellite i and Δh is the height of the aircraft above the GBAS reference location (in meters).

As already noticed in 3.2.3.3.3 and by seeing at the Figure 19, parameters such as σ_N, N_R and h_0 are determined by using the local yearly mean value (normally measured by the GBAS meteo station) for exchange with the aircraft during approach operations.

5.5.1.2 Harmonie

TC computed for Schiphol Airport shown in Table 11 in the section 3.2.3.3.2.1 was compared to the zenith tropospheric delay computed as described in section 5.3.3 for an aircraft height of 200ft above the surface (i.e difference between ZTD at surface and ZTD at 200ft). The ZTDs were computed by using all the Harmonie grid for the set of data of the 18th of September 2012 at 00h00 and are represented in Figure 92. Then in Figure 93 the differences between ZTDs and TC are plotted in the following Figure 93 :

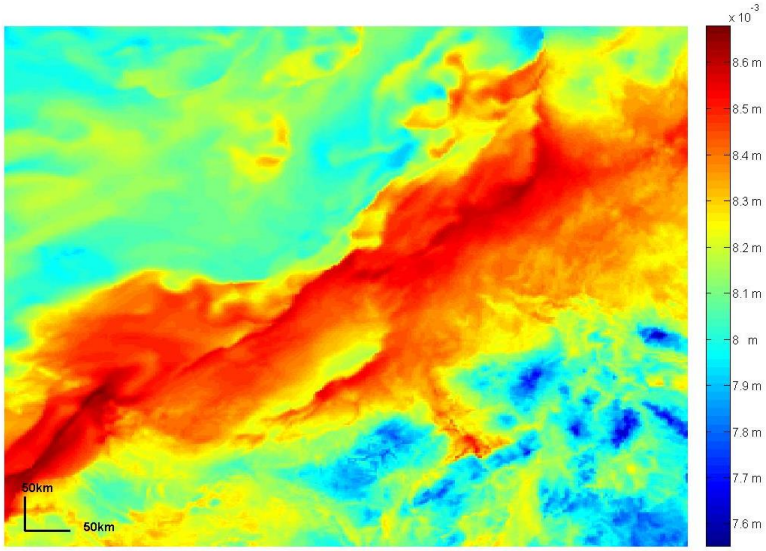

Figure 92-ZTD for Harmonie data at 200ft

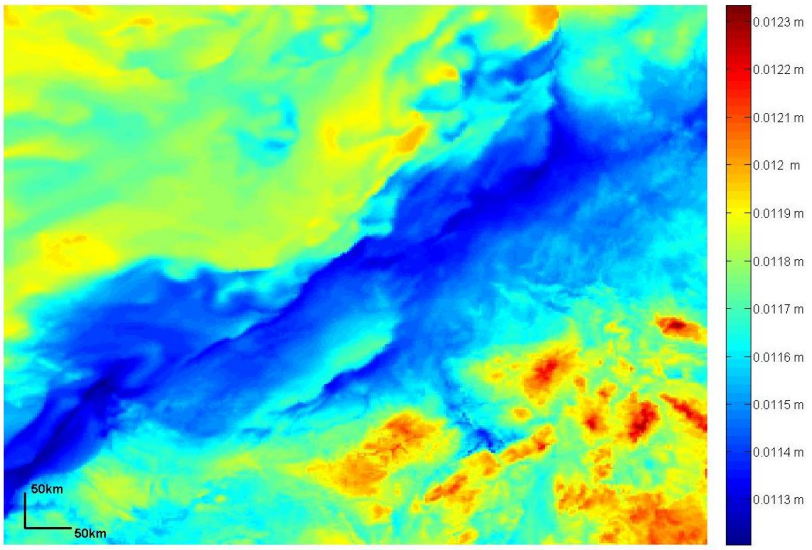

Figure 93-Difference between TC and ZTD for Harmonie data

At first sight of ZTD over the Harmonie area in Figure 92, it should be remarked by comparison with the Figure 69 that there is a clear dependency on height for ZTD. Then when the difference with the constant TC computed at Schiphol, the dependency remains therefore that explain the pcolor Figure 93.

By analyzing this result of differences between TC and ZTD from the Ground to an altitude of Aircraft defined at 200ft., it appears that values varies from 11 to 12mm which can be considered relatively small if compared to TC values (about 2cm at 90° of elevation as described in Table 25)) . Moreover, the variation of these differences over the grid is up to 1mm which seems to be on the same order as the standard deviation of the residual tropospheric error Table 25 . Nevertheless, more analysis are needed to conclude about the validation of the standardized model TC and to assess the vertical anomalies which can be due to duct phenomena. This analysis is realized in section 5.5.2.

5.5.1.3 Arome

The same process as for Harmonie data in section 5.5.1.2 was also undertaken for Arome.

The TC was computed at Turin Airport and compared with ZTD computed between ground station and an aircraft at 200ft for the set of data of the 1st January 2014 at 00h00 for the complete Arome grid and is represented in Figure 94. The difference between these values of ZTD and TC was made and results are plotted in the following Figure 95.

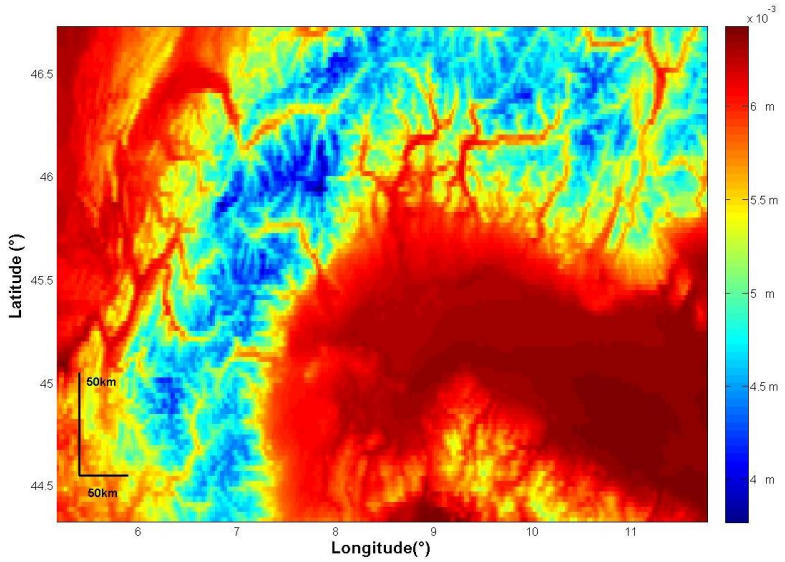

Figure 94-ZTD for Arome data at 200ft

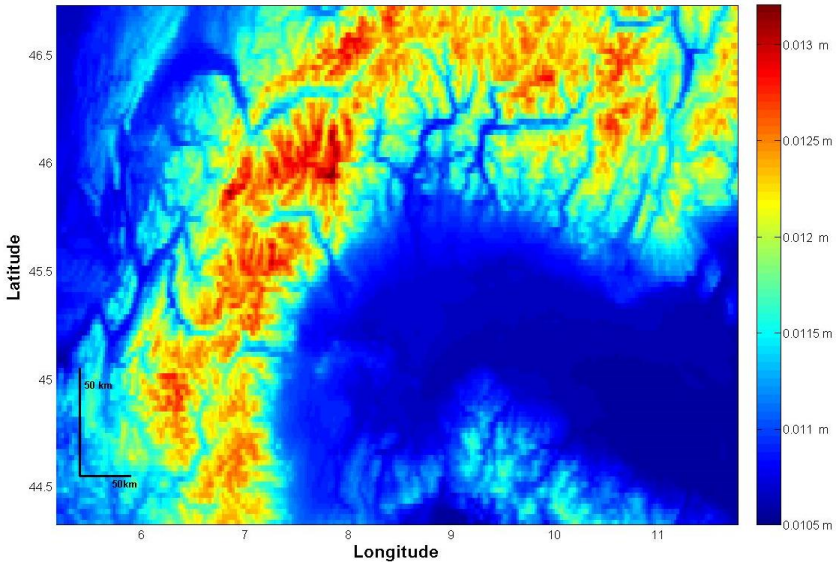

Figure 95-Difference between TC and ZTD for Arome data

As for Harmonie model, at first sight of ZTD over the grid on Figure 94, it should be remarked by comparison with the Figure 59 that there is a clear dependency on height for ZTD. Then when the difference with the constant TC computed at Turin, the dependency remains therefore that explain the pcolor Figure 95.

By viewing these results of differences between TC and ZTD from the Ground to an altitude of Aircraft defined at 200ft., it appears that values varies from 12 to 15mm which can be considered relatively small if compared to TC values (about 2cm at 90° of elevation as described in Table 25) . Furthermore, the variation of these differences over the grid is up to 2.5mm which is in the same order as the standard deviation of the residual tropospheric error Table 25. Therefore, more investigations are needed especially a statistical analysis is essential to validate

properly these results about the standardized model TC and to assess the vertical anomalies which can be caused by duct phenomena. The following section 5.5.2 focuses on this statistical analysis.

5.5.2 Tropospheric Correction Analysis

This part of the report assesses the tropospheric correction and the vertical anomalies which can be caused by tropospheric ducts. First some results found in literature are presented, then a real data analysis is performed and results found by using NWM data are given.

5.5.2.1 Literature Results

Previous investigations have analyzed the presence of tropospheric ducts. Particularly in [129] , a description of tropospheric ducts is given and some results are presented. Indeed, it appears that these vertical anomalies can cause errors of up to 7cm with a high likelihood of occurrence. Then, a threat model is derived for establishing a duct threat model in the form of ranging measurement error probability distribution. The corresponding histogram shows that the maximum error observed at 200m is 6mm in zenith (5cm for a 7°elevation satellite signal) and that the duct error distribution is non Gaussian and is non-zero mean. These literature [129] suggests that these duct errors cannot simply be accounted for by inflating the measurement standard deviation and methods such as bounding ranging biases approach and inflation approach (as detailed in Chapter Chapter 6) are proposed.

5.5.2.2 Numerical Weather Model Based Results

In this section, Arome (5.2.2.2) data and Harmonie (5.2.2.3) data are analyzed and compared to assess the tropospheric correction and the possible ducts. Indeed, according literature [129] and some discussions with specialists [130], ducts tend to form when some abnormal behavior and sudden change concerning temperature (increasing with height) or/and relative humidity appear. Therefore ducts should be more important and should occur more frequently in mountain area such in Arome area (Alpines data) but for comparison purpose, results obtained in Alpines data are compared to those of Harmonie.

Furthermore, some studies about vertical gradients within the Harmonie data were already undertaken by NLR [105]during the SESAR project investigations dealing with the WP15.3.7.

Then three locations were investigated: Turin Airport, Milan with the Arome data and Schiphol with the Harmonie data.

	Longitude(°)	Latitude(°)	Height(m)
Turin	7.382185	45.005447	316.6
Milan	9.1881714	45.463681	103
Schiphol	4.7642	52.3080	-3

Table 24-Turin, Milan, Schiphol coordinates

In the Zenith Direction, the tropospheric correction and the standard deviation of the residual tropospheric error computed as explained in 3.2.3.3.2.1 and 3.2.3.3.2.2 are summarized in the Table 25:

	TC(m)	σ_{tropo}(m)
Turin	0.0178	0.0023
Milan	0.0129	0.0016
Schiphol	0.0195	0.00057

Table 25-TC and sigma tropo for Turin, Milan and Schiphol locations

In order to evaluate how the user is protected during an approach (20NM (37km) for the farthest point along the approach path), for each of these three locations a "squared-subgrid" with a 80km length horizontally and vertically was selected in order to cover both sides of each location approach. Then statistical analysis is performed over 1year of data (from the 1st January 2014 at 00h00) for each locations over its corresponding subgrid.

First for each location, difference between the zenith tropospheric delay and the zenith TC over these subgrids were computed and plotted in the following figures respectively for Turin, Milan and Schiphol:

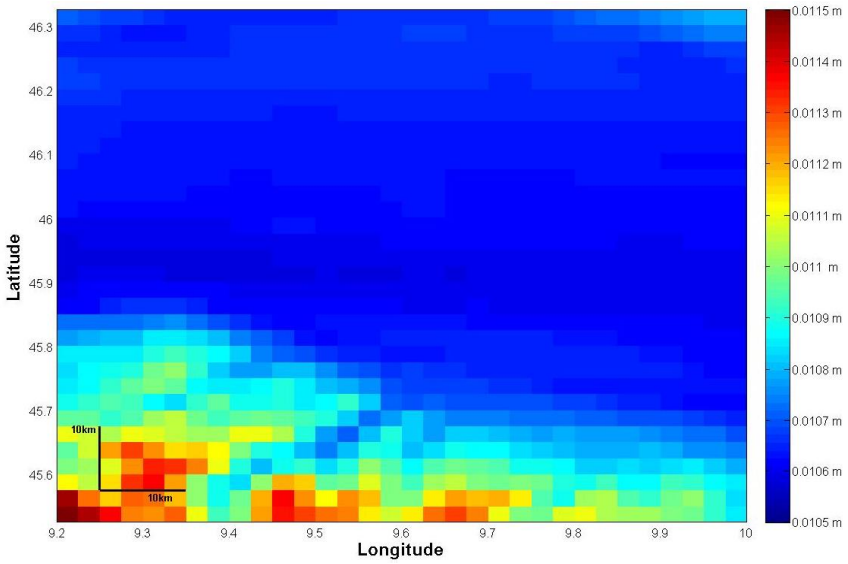

Figure 96-Difference between TC and ZTD for Turin

By analyzing this Turin case in the Figure 96, errors between TC and ZTD are at one centimeter level and the variation within this grid is up to 1mm.

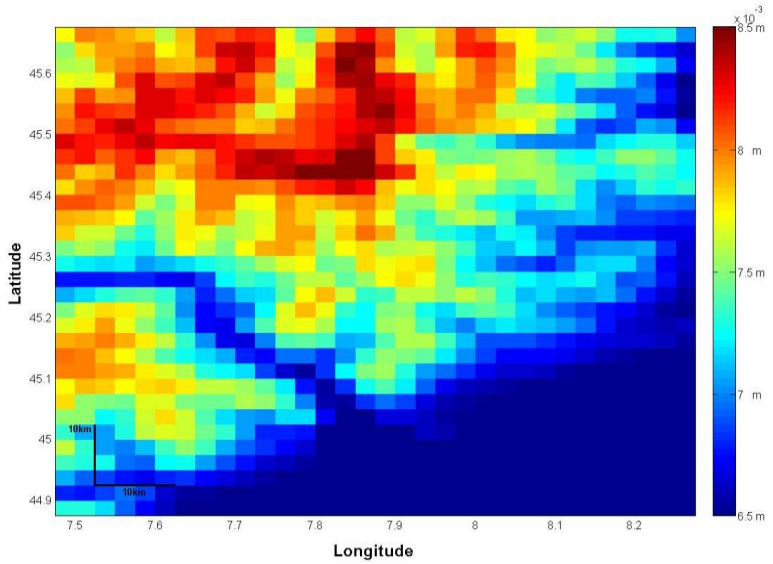

Figure 97-Difference between TC and ZTD for Milan

Concerning the Milan location case in the Figure 97, errors between TC and ZTD are up to 8.5millimeters and the variation within this grid is up to 2mm. Therefore with this 2mm level, error variations appear more important at this location compared to Turin location where 1mm level variation was observed.

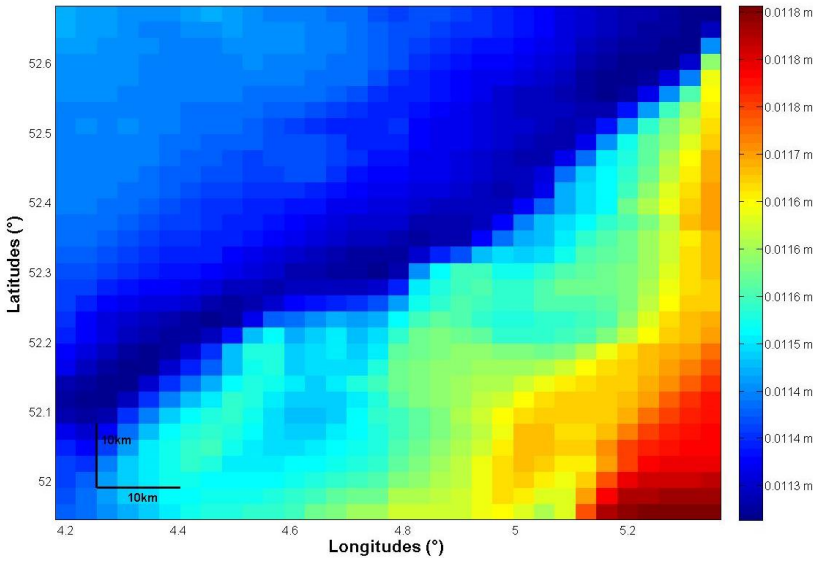

Figure 98-Difference between TC and ZTD for Schiphol

For the Schiphol location case in the Figure 98, errors between TC and ZTD are up to 1.2centimeters and the variation within this grid is up to 0.5mm. By comparing this variation level with other cases above, error variations appear less important at this location compared to Milan and Turin location where 2mm and 1mm level variations were observed respectively. This conclusion could be expected by guessing that in Alpines area, weather variations should be more important than in a flat domain such as Netherlands.

Then the mean errors between the zenith tropospheric delay and the zenith tropospheric correction over these subgrids were computed and it appears that the standards deviations for these errors over the grid is really small compared to the σ_{tropo}given in the previous Table 25 as the following figures show:

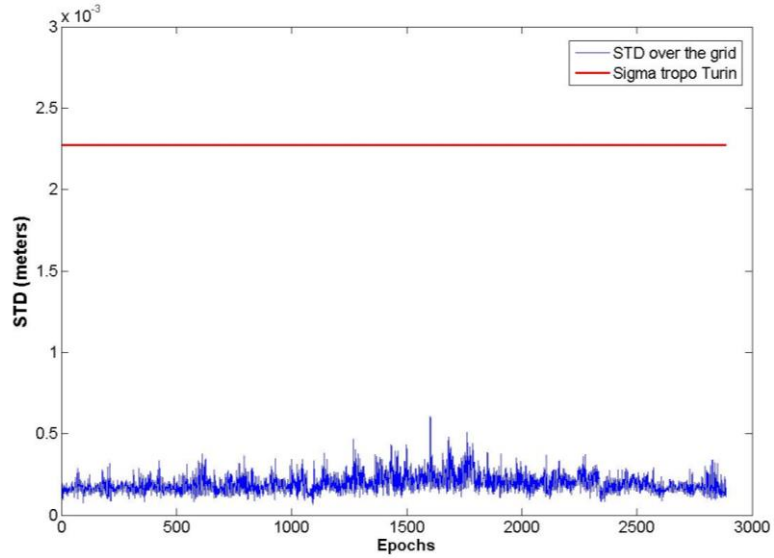

Figure 99-STD of (TC-ZTD) over the grid compared to sigma tropo at Turin

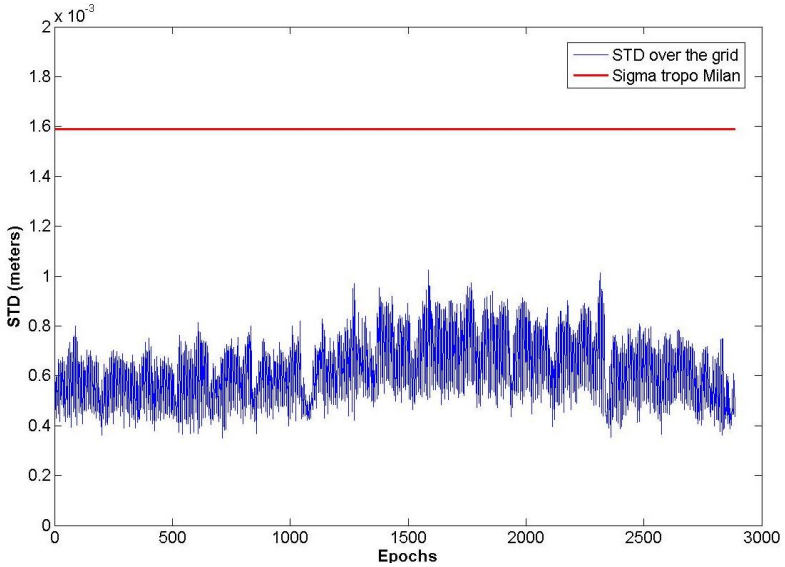

Figure 100-STD of (TC-ZTD) over the grid compared to sigma tropo at Milan

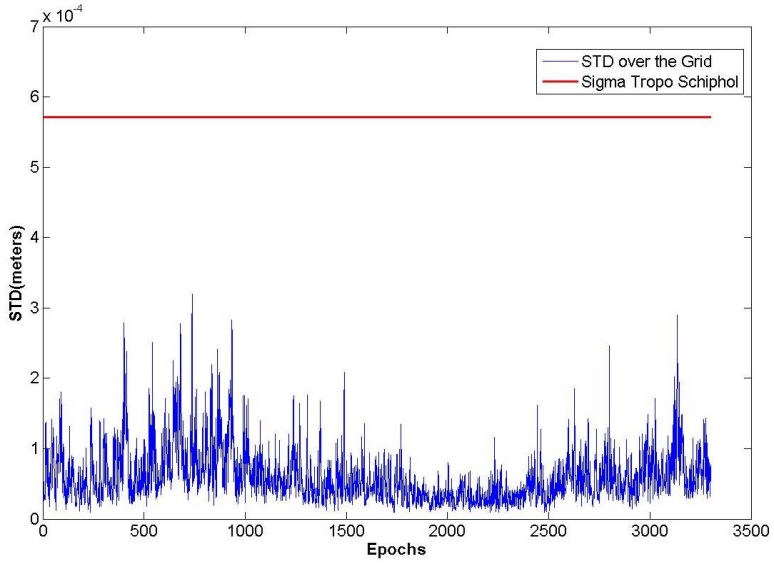

Figure 101-STD of (TC-ZTD) over the grid compared to sigma tropo at Schiphol

By analyzing these figures, because the standard deviation of the error between ZTD and TC all over the grid can be considered as small compared to the σ_{tropo} for each location, it could be concluded that the spatial variation is not important for this statistical study and the analysis realized at one location can lead to same conclusions as for all the grid without a huge impact. That is why for the following work of this statistical analysis, only Turin, Milan and Schiphol locations are investigated.

Therefore, differences between TC and ZTD were computed over all epoch for each NWM (1 year for Arome, 2 years for Harmonie) at Turin, Milan and Schiphol. Then histograms were realized in order to analyze the errors distribution at these locations and they are represented below:

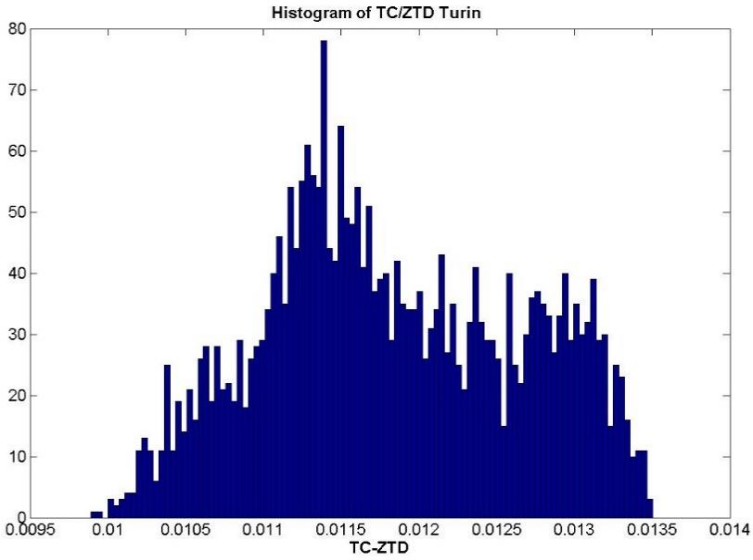

Figure 102-Histogram of TC-ZTD over 1 year at Turin

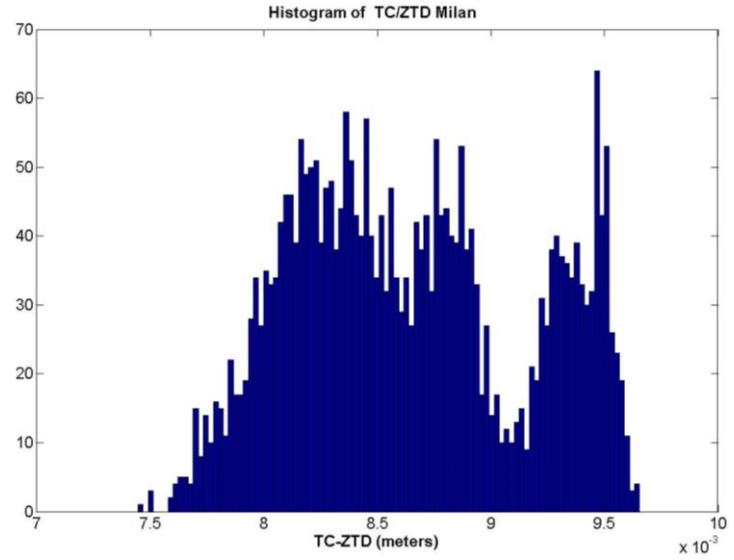

Figure 103-Histogram of TC-ZTD over 1 year at Milan

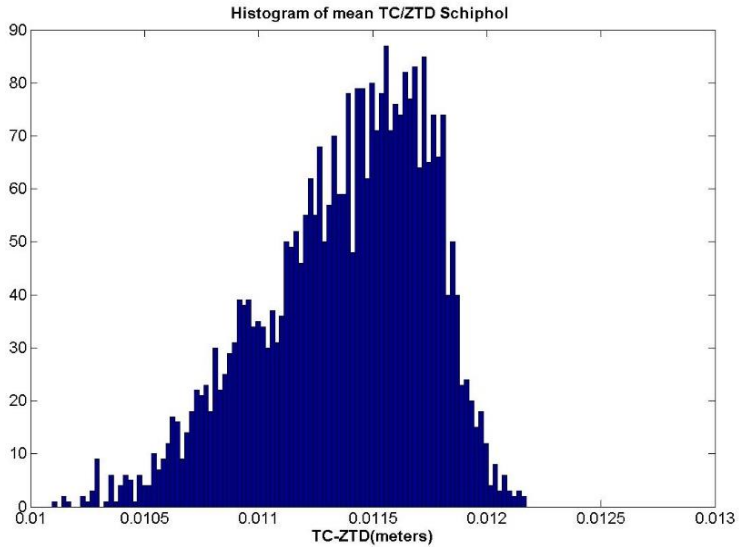

Figure 104-Histogram of TC-ZTD over 2 years at Schiphol

By viewing these distributions of the errors between TC and ZTD, it can be remark that they are not centered and biases appear which are not covered by the actual TC computation. (Note that these histograms of Turin, Milan and Schiphol have respectively a resolution of 0.04mm, 0.022mm and 0.02mm).

Indeed, the following table represents these ranging biases named μ_{TC} for each location. They were obtained by taking the mean of the distributions illustrated by previous histogram. It could be considered as an approximation of the bias because they could not have enough samples in the study to represent this non-stationary processus.

	μ_{TC}(m)

Turin	0.0118
Milan	0.0086
Schiphol	0.0114

Table 26-Bias between TC and ZTD

By analyzing the previous table, ranging biases are not negligible and have to be treated. Indeed, in the slant domain they can lead to higher values (up to 12cm) than those presented in zenith direction by this previous table as represented in the following figure:

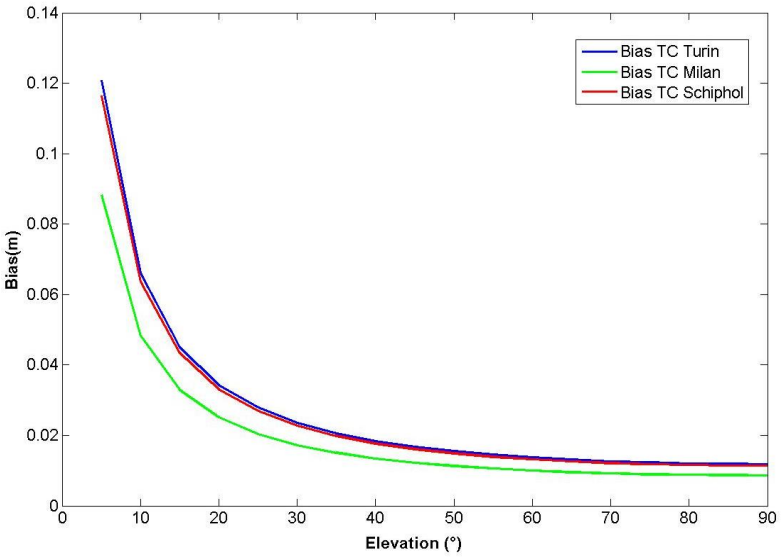

Figure 105-TC bias

Two possibilities can be applied for dealing with them. Either, the TC computation have to be modified. These methodology was already suggested and studied by NLR into the SESAR project [105]. Or these ranging biases have to be bound as the same way as for non-nominal troposphere explained and illustrated in Chapter 6 and included in the VPL computation.

Also, the amplitude of deviation from the mean values μ_{TC} of these histograms Figure 102, Figure 103 and Figure 104 can reach 2mm in zenith. Therefore, because the errors due to mismodelling are included in the bias term μ_{TC}, this deviation can be the effect of duct phenomena as observed in literature and shown in 5.5.1.1. Further work needs to be done for assessing properly the presence of these vertical anomalies as mentioned in 7.2.

Indeed, as presented in 5.5.2.1, ducts tend to form when some abnormal behavior and sudden changes of temperature variation with height (increasing with height) or/and relative humidity appear. Therefore, refractivity will not follow the typical nominal curve (as shown in Figure 76 and in literature [129]), that is why it is possible to compare the results obtained through the tropospheric correction analysis (5.5.2) with the behavior of the refractivities.

The same methodology as explained in [129] was applied for the worst set of data found in the statistical analysis in 5.5.2.2. Therefore refractivities where computed and plotted during the assumed duct phenomena and compared to the nominal trend of refractivities. Indeed, it was assumed that refractivity gradient under nominal conditions is about -40/km. The following figure was obtained.

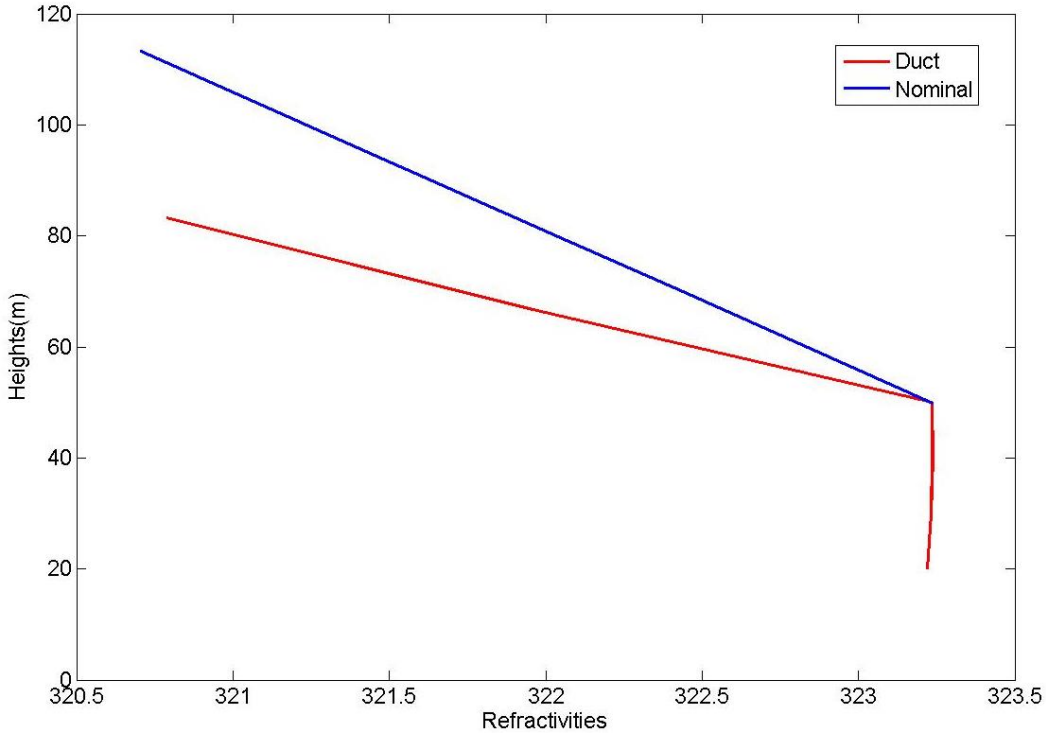

Then for computing the differential tropospheric delay, the area between the two curves was determined and value obtained was about 0.033mm which is really small compared to value found during ducting phenomena in [129]. Therefore, it could be concluded that this deviation observed in 5.5.2.2. seems to be not due to duct

5.5.3 Conclusions

In this subsection dealing with vertical component of the differential range tropospheric delay, the overbounding Gaussian model for the TC error which had been previously validated for nominal and rare conditions [84] [16] was presented. Then the NWMs data was used to compute to derive values of TC and σ_{tropo} for different locations.

To complete this study some investigations and statistical analysis with Arome (5.2.2.2) data and Harmonie (5.2.2.3) data were realized for analyzing the tropospheric correction. By seeing that the spatial variation of the error between ZTD and TC is not important for this statistical study, only locations such as Turin, Milan and Schiphol were investigated. Then after having analyzed distributions of their errors between TC and ZTD, it was remarked that they were not centered and ranging biases μ_{TC} appeared which are not covered by the actual TC computation. These biases, in the slant domain, can lead to high values up to 12cm so they are not negligible and have to be treated. Therefore either, the TC computation have to be modified as it was already suggested and studied by NLR into the SESAR project [108]. Or these ranging biases have to be bound as the same way as for non-nominal troposphere explained in Chapter 6 and included in the VPL computation. Then, further work needs to be done for assessing properly the presence of vertical anomalies known as ducts as mentioned in 7.2. Preliminary analysis shown in 5.5.2.2 showed that this deviation is not due to ducts.

This section explained how to model the range troposphere delay within GBAS and how to estimate the worst differential range troposphere delay in order to model the anomalous troposphere. Then the following chapter Chapter 6 will presents some methodologies to bound this anomalous troposphere in order to protect the aircraft against these gradients.

Chapter 6 : Anomalous Troposphere Bounding

6.1 Introduction

As already presented in section 4.2.2.1 and in Chapter 5, there are then two possible threats related to the troposphere. Firstly, significantly different range delays over paths 2 and 3 shown in Figure 1, could occur due to horizontal gradients. Secondly, as presented above, vertical gradients could occur and were assessed in the previous section 5.5.

Therefore, this section mainly focus on the horizontal gradients impacting the differential error.

Then, a detailed analysis will deal with the means to protect an aircraft from ranging biases due to horizontal gradients. This is achieved firstly using an existing methodology [112] [113] [6] [7] [131] followed by a novel approach using each of the differential bias models determined in the previous section 5.4 as input.

6.2 Existing GAST C/D Methodology

As previously introduced, both horizontal and vertical gradients could be a threat for GBAS. A study about the vertical component was realized in 5.5, therefore this section deeply analyses the horizontal component of the differential tropospheric range error.

6.2.1 Introduction

In section 5.4, worst case differential horizontal range tropospheric delays as a function of elevation were obtained for an aircraft passing the Cat I to Cat II/III transition (the Cat I Decision Height of 200ft). This provides a basis for bouding the impact of differential tropospheric ranging biases on GBAS. In this section, the means to protect an aircraft from these biases is addressed. This is achieved firstly using an existing methodology [112] [113] [6] [7] [131] followed by an innovative approach using each of the differential bias models determined in section 5.4 as input.

The derivation of the worst case horizontal differential range tropospheric delays or biases in section 5.4 represents a threat model for GBAS. As already said in the integrity section (3.3.2.2.3), for each threat identified for GBAS, either a monitor must be defined with the necessary missed detection performance [1] or the threat may be incorporated into the nominal model and overbounded by the protection levels.

A differential range troposphere delay monitor is difficult to develop since the tropospheric error is difficult to separate from other error sources, particularly in the single frequency case when nominally dwarfed by the ionospheric error. Also the tropospheric gradient can be smaller than the distance between aircraft and ground station therefore, monitoring could not work properly in this case leading to some fault missed detections. Finally, whilst independent monitors may be used on a per satellite basis for payload faults and under certain assumptions for ionospheric anomalies, the possibility of multiple satellites being subject to differential tropospheric ranging biases cannot be discounted.

It is therefore the second approach of overbounding the effect of tropospheric ranging biases which has been suggested in previous work ([112] [113] [6] [7] [131]) and which is followed in this section of the report. As presented in 3.3.2.2.3, protection levels are the means by which errors are overbounded in GBAS and other augmentation systems [16] [132]. Currently, the differentially corrected range errors are assumed to follow a zero-mean Gaussian distribution and be free of any ranging source failures (ground subsystem receiver failures are protected by additional protection levels). The fault free vertical protection level ($VPL_{Apr_{H0}}$defined in 3.3.2.2.3.1.1) is considered as the requirements are generally more difficult to satisfy than the lateral. Therefore the fault-free VPL is defined as the *noisy* VPL (which contains only the noise component of each error sources) denoted VPL_n:

$$VPL_n = K_{ffmd} \sqrt{\sum_{i=1}^{N} {S_{v,i}}^2 {\sigma_{n,i}}^2}$$

Equation 158 – Fault-free VPL – VPL_n

Where N is the number of satellite ranges included in the position solution, $S_{v,i}$ is the projection factor of range biases onto the vertical position domain (also accounting for longitudinal position component as per [84]), K_{ffmd} is the fault-free missed detection multiplier and $\sigma_{n,i}$ is the standard deviation of the differentially corrected ranges from satellite i in the absence of the considered biases and assuming a valid Gaussian overbounding ([113] [7] [131])

Consider the relationship between the current fault-free VPL as defined in Equation 158 and a composite VPL which bounds the combination of the fault-free nominal errors and additional tropospheric ranging biases obtained in section 5.4 ([112] [113] [6] [7] [131]). The composite VPL_c may be expressed as the sum of the existing VPL_n and a bias term VPL_b as [84] [16] :

$$VPL_c = VPL_n + VPL_b$$

Equation 159 - VPL composite decomposition – VPL_c

Where

$$VPL_b = \sum_{i=1}^{N} VPL_{b,i} = \sum_{i=1}^{N} \left| S_{v,i} \mu_i \right|$$

Equation 160 - VPL bias – VPL-b

With μ_i is defined as the differential ranging bias for satellite i, the previous Equation 160 is conservative since the absolute values of the biases are taken, thus assuming the ranging biases conspire in the worst possible way.

It is relevant here to remind that for the moment, the standards make no allowance for the threat of tropospheric differential ranging biases. In order to protect aircraft from biases such as those seen in Figure 105 (section 5.4)two options are available, either the differential range standard deviation terms must be modified or the actual form of the VPL equation changed as the remaining parameters are governed by the system design and satellite geometry. The possible modification of the VPL equation by introducing additional parameters provides greater flexibility but would require an evolution of the protection levels concept within the standards. At this late stage of GAST D standardization such modifications are unfeasible but standardization of a future MC/MF GBAS concept (known as GAST F) could allow for such a provision. In this first subsection an existing methodology from the literature [113] [7]is assessed which assumes no modification to the current VDB message structure before subsection 6.3 takes the latter approach of providing additional data to the aircraft and changing of protection levels concept.

6.2.2 Overbounding and Sigma Inflation Concepts

As introduced above, in order to bound the combination of nominal errors and tropospheric biases one solution is to inflate the contributors to ranging standard deviations from $\sigma_{n,i}$ to $\sigma_{inf,i}$. The inflated VPL then follows:

$$VPL_{inf} \approx K_{ffmd} \sqrt{\sum_{i=1}^{N} {S_{v,i}}^2 {\sigma_{inf,i}}^2}$$

Equation 161 - VPL Inflated - VPL_inf

Figure 106 shows the VPL relations in the position domain considering the inflation of a single ranging source only.

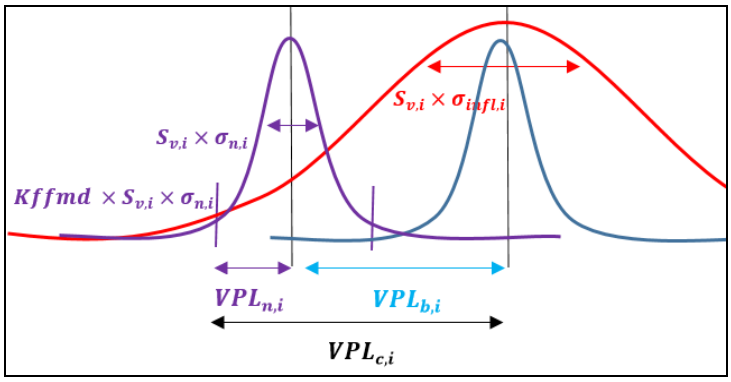

Figure 106-Inflated VPL

The VPL_c can be seen as the ideal VPL (although taking the absolute values in Equation 160 introduces some conservatism) and the VPL_{inf} as the feasible VPL given the current constraints (without modification to the current VDB message structure or avionics standards). Integrity is then ensured by the inequality:

$$VPL_c \leq VPL_{inf}$$

Equation 162 - Inequality between VPL_c and VPL_inf

By applying the same approach as outlined in [113] [7] to maintain conservatism, the VPL_b is computed using the conspiring ranging biases assumption ([6]) which relies on applying the same maximum differential bias μ_{max} to all satellites.

$$VPL_{b\,max} = \sum_{i=1}^{N} \left| S_{v,i} \mu_{max} \right|$$

Equation 163 - Maximum VPL-b

According to [6] [114] a bound for $VPL_{b\,max}$ exists and can be defined through the following inequality:

$$VPL_{b\,max} \leq \mu_{max} \sqrt{N}\, VDOP$$

Equation 164 - Bound of the VPL-b

Where $VDOP$ is the vertical dilution of precision as defined in [115].

In order to ensure that the sigma inflation maintains integrity, Equation 162 must be satisfied. This can be achieved by using Equation 164 to derive $VPL_{b\,max} \approx Kffmd \times VDOP \times \sigma_{\Delta tr}$ as shown in [114] [6] where the standard deviation of the differential range tropospheric delay , $\sigma_{\Delta tr}$ is defined as:

$$\sigma_{\Delta tr} = \frac{\mu_{max}\sqrt{N}}{K_{ffmd}}$$

Equation 165 - Sigma non nominal troposphere

Rather than broadcasting $\sigma_{\Delta tr}$ to the aircraft it is possible to inflate [113] the existing sigmas, such as σ_{vig}, which characterizes the vertical ionospheric gradient, in order to ensure inequality in Equation 162 is met. Then the following equation is defined :

$$\sigma_{vig\ inf} = \sqrt{\sigma_{vig}^2 + {\sigma_{\Delta tr}}^2}$$

Equation 166 - Sigma inflated

By reminding that the results presented in section 5.4 were shown at the Cat I decision point, it is also possible to derive the differential bias as a function of elevation and baseline distance between aircraft and GBAS ground facility, x_{air}. Therefore, firstly the differential tropospheric bias μ_{max} and secondly the sigma $\sigma_{\Delta tr}$ may be derived and expressed as shown by Equation 165 and Equation 166. The inflation must therefore respect the way standard dependency on x_{air} (previously introduced in 3.2.3.3 and in section 5.4 with the Figure 82) and an inflated σ_{iono} is derived as :

$$\sigma_{iono} = F_{pp}\sigma_{vig\ inf}(x_{air} + 2\tau v_{air})$$

Equation 167 - Sigma ionosphere

Where σ_{iono} is the standard deviation of the nominal slant differential ionospheric error, F_{pp} is the vertical to slant obliquity factor [16], x_{air} is the horizontal distance between GBAS ground facility and user , τ is the smoothing constant (set at 100s in the study regarding the GAST D VPL computation in 3.3.2.2.3.2) and v_{air} is the ground speed of the aircraft.

As clear from Equation 167 and the result given in section 5.4 with the Figure 82, there is a linear dependency on x_{air}. Figure 55 plots in blue the "Wall" non-nominal troposphere standard deviation from Equation 165 assuming a Wall model for computing the differential tropospheric μ_{max} as a function of distance of the aircraft to the GBAS ground station (shown in Figure 82), with the methodology explained in 6.2 and Figure 54 with the MHM and "optimal" parameters given in 5.2.1.2 . The red upper curve represents a bound on the blue curve through inflation of the vertical ionospheric gradient standard deviation which is found numerically. Indeed, after having computed $\frac{\mu_{max}\sqrt{N}}{K_{ffmd}}$ with K_{ffmd} set at 6 as mentioned in 5.2.1.2, $\sigma_{\Delta tr}$ is dertermined in order to always have $F_{pp}\sigma_{\Delta tr}\ (x_{air} + 2\tau v_{air}) > \frac{\mu_{max}\sqrt{N}}{K_{ffmd}}$ (for always having the red curve above the blue one).

Table 27 presents standard deviations determined by using the Equation 166 with the nominal value of of $\sigma_{vig} = 4mm/km$ and the methodology explained above in this section.

	D_{TH} = 5km	D_{TH} = 10km
N=6	$\sigma_{\Delta tr} = 8.0\text{mm/km}$ $\sigma_{vig\ inf} = 8.94mm/km$	$\sigma_{\Delta tr} = 9.9\text{mm/km}$ $\sigma_{vig\ inf} = 10.68mm/km$

N=12	$\sigma_{\Delta tr} = 11.2\text{mm/km}$ $\sigma_{vig\ inf} = 11.89mm/km$	$\sigma_{\Delta tr} = 13.8\text{mm/km}$ $\sigma_{vig\ inf} = 14.37mm/km$
N=24	$\sigma_{\Delta tr} = 15.9\text{mm/km}$ $\sigma_{vig\ inf} = 16.40mm/km$	$\sigma_{\Delta tr} = 19.5\text{mm/km}$ $\sigma_{vig\ inf} = 19.91mm/km$

Table 27- $\sigma_{\Delta tr}$ and $\sigma_{vig\ inf}$ for different cases

Then the previous work outlined in this part is assessed by comparing VPL_n ([16]) VPL_c (Equation 159) and VPL_{inf} (using Equation 161) and the inflation methodology outlined). The goal of the following subsection is to ascertain the extent to which the VPL increases.

6.2.3 Protection Levels

Once the results of the previous subsection are obtained ($\sigma_{vig\ inf}$ and therefore the corresponding σ_{iono} with Equation 167), it is possible to check the impact of non-nominal troposphere on VPL for the different scenarios. Indeed, some simulations were realized over 24 hours for the case of GPS constellation [133] and 10 days for the case of GPS/GALILEO [134], with a time resolution of 10 seconds. Ideally, the more airport locations were tested, the more accurate conclusions should be but by lacking of time only few were selected which are at least at high, mid and low attitudes : Seattle Airport, Anchorage Airport, Miami Airport and an Airport located at a Latitude 0. Their coordinates are given in the following table:

	Latitude(°)	**Longitude(°)**	**Altitude(m)**
Seattle	47.4498889	-122.311778	132.00
Anchorage	64.174361	-149.996361	46.33
Miami	25.793250	-80.290556	2.44
LAT 0	0.000000	-122.311778	20.00

Table 28-Airports Coordinates

Distance from Ground Station to Runway threshold(D_{TH}) was set at both 5km and 10km and also five key points along the approach were defined either by the distance from A/C to Runway Threshold (D) of 20NM and 10NM or by the Altitude of A/C (h) of 200ft, 100ft and 0ft.

In this report, the results for Seattle Airport and for an altitude of Aircraft (h) at 200ft (reminding that the Cat I Decision Height is 200ft), are presented. Results obtained for other airports are shown in the Appendix B.

On the Figure 107, Figure 108, Figure 109 and Figure 110 different results are represented:

- VPL_{inf} with non-nominal troposphere computed with the inflation methodology (presented in 6.2.2) is represented in **red**
- VPL_c computed by adding the exact value of VPL_n and VPL_b (presented in6.2.1) is represented in **black**
- VPL_n representing VPL without non-nominal troposphere (presented in6.2.1) is represented in **purple**

At this stage of the report it is relevant to note that if the tropospheric threat is considered significant enough to be bounded separately, the intention is to derive a means to bound the resulting error whilst keeping the data transmission load low. Indeed, in view of the Chapter 4, it is important to minimally modify the VDB message structure.

On Figure 107, the different VPLs presented above are represented for the GPS constellation and for the GPS/Galileo constellations on the Figure 108 with a distance from ground station to runway threshold (D_{TH})of 5km (as defined in standards [16]).

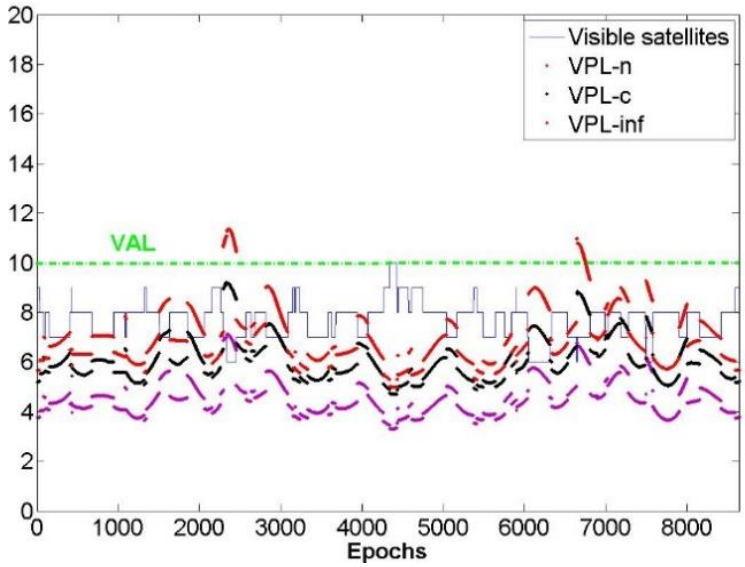

Figure 107-VPLs with D_TH=5km for GPS constellation

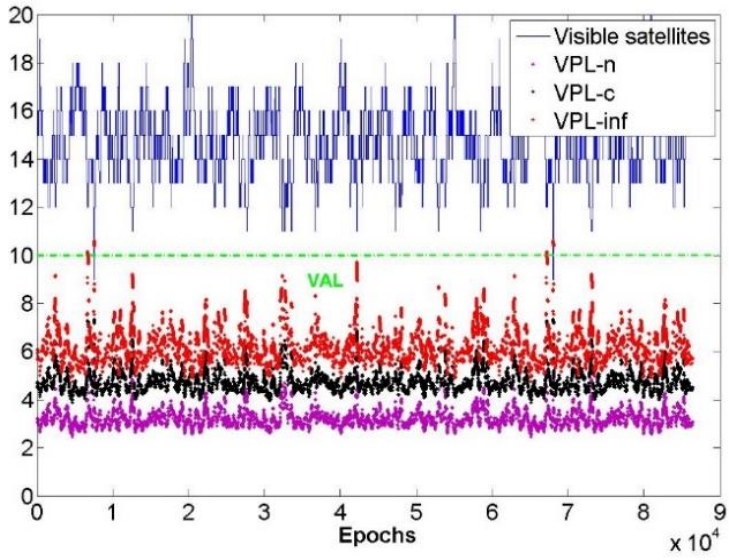

Figure 108-VPLs with D_TH=5km for GPS+GAL

In Figure 109 and Figure 110, the same results as above are presented but for (D_{TH}) of 10km (in view of constraints relaxation with the GAST-D/F development [45]).

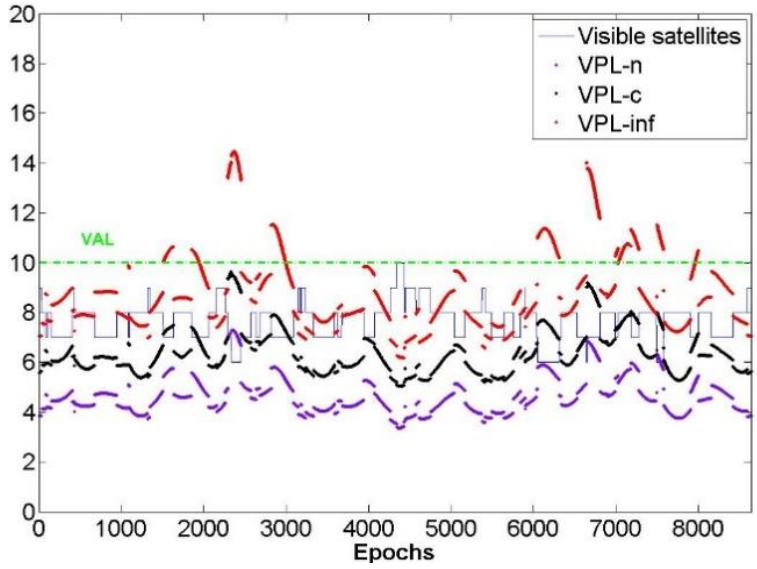

Figure 109-VPLs with D_TH=10km for GPS constellation

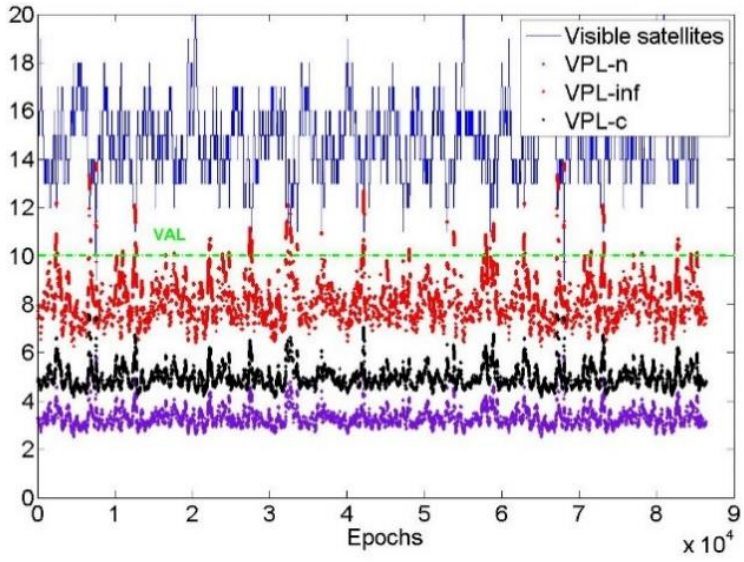

Figure 110-VPLs with D_TH=10km for GPS+GAL

By analyzing these Figure 107, Figure 108, Figure 109 and Figure 110, in both GPS and GPS/GAL constellations cases, the following inequality is verified:

$$VPL_{inf} > VPL_c > VPL_n$$

Equation 168- Inequality for existing methodology

Furthermore, the VPLs are significantly larger for the case of D_{TH} =10km than for D_{TH}=5km with differences up to 3meters between curves. This could be explained by seeing the residual uncertainty of the ionosphere (Equation 167) has a dependency on the distance from the GBAS ground facility. Therefore the farther the aircraft is ($highest\ D_{TH}$) the bigger the VPL will be.

Also by seeing the Vertical Alert Limit (VAL) (set to 10m as defined in standards [42] [135]), the remark that for some epochs VPL_{inf} is above to VAL thus reducing availability. These epochs appear more numerous if a larger D_{TH} is chosen and consequently the availability is impacted further.

In the Dual Constellation (GPS/Galileo) case in Figure 108 and Figure 110, the difference between the VPL inflated (in red) and the VPL composite (in black) is greater due to the impact of assuming conspiring ranging biases across many more satellites.

Conclusions about this methodology are given in the following subsection.

6.2.4 Conclusions

By analyzing Figure 107, Figure 108, Figure 109 and Figure 110, there is an important difference between VPL inflated (defined as the existing methodology) and the VPL composite (defined as the “ideal” VPL) .These jumps in VPL (between the red and black curves) suggest the model is overly conservative and finding a closer bound should be sought. Furthermore, in the case of the Dual-Frequency (DF) I-free smoothing which may be used for

GAST F, an alternative approach is needed because the ionosphere component will be removed and the σ_{iono} and therefore the equivalent $\sigma_{vig\ inf}$ will not exist anymore. An innovative methodology is therefore needed whilst maintaining a minimum data transmission load. That is why, the following section describes this innovation in both SF and DF cases through the I-free smoothing technique.

6.3 Innovative Methodology

In section 6.2, an existing methodology which assumes no modification to the current VDB message structure was assessed but in this section the approach of providing additional data to the aircraft and changing of protection levels concept is taken.

The proposed methodologies for computing differential range tropospheric delays which can be called Bias-Parameter Transmission methodologies, relies on the Modified Hopfield Model (MHM) [115] explained above in 5.2.1, on the fact that that they depends on satellite elevations and distances from Ground Station to Aircraft and on the idea that additional data (parameters) can be send to the aircraft. In this part of the work, the assumption that D_{TH} is defined at 5km according SARPs [117] is made. This value defines the largest distance between Ground Station and runway threshold.

In this subsection, these Bias-Parameter Transmission methodologies are presented firstly by describing and analyzing an initial proposal for both SF and DF cases (with I-free smoothing). Then some improvements are introduced in order to develop a less conservative model whilst reducing the data transmission load.

6.3.1 Bias-Parameter Transmission Methodologies

At first an initial proposal is made and called as Look-Up table Transmission (LUT) methodology then an improvement of it is realized through the new Low Data Transmission (LDT) methodology and finally another proposal is made to improve the availability by developing a less conservative methodology under a new satellite geometry called Worst Satellites Subset (WSS) methodology.

6.3.1.1 Look-Up Table Transmission (LUT)

6.3.1.1.1 Presentation

In the first phase of the study, the idea was to compute a table representing differential range tropospheric delays obtained by applying the Modified Hopfield Model (MHM) [110] (explained above in 5.2.1) for sets of satellite elevations bin with a width of 5°, from 0° to 90° and for distances between the ground station (GND) and aircraft (A/C) varying from 300m up to 30km with different steps according to how far aircraft is. Indeed this choice was made in view of the differential range tropospheric delay dependency to satellite elevations and distances from Ground Station to Aircraft. Therefore, differential range tropospheric delays are computed with a variant step according the following table because these delays are not covered by model presented in:

Distances GND-A/C	300m→ 1km	1km→ 8km	8km→ 30km
Steps	100m	500m	1km

Table 29-Steps according Distances GND-A/C

The second phase was to take, for each elevation bin of 5°, the maximum value of these differential range tropospheric delays over distances. Then, 18 values of μ_{max} are obtained as in the look-up table presented below. It differs from the existing methodology presented in 6.2 because there is not only one value of μ_{max} applicable for all elevation angles.

Elevations (°)	5	10	15	20	25	30	35	40	45
μ_{max} (m)	1.19	0.86	0.67	0.56	0.48	0.43	0.38	0.33	0.31
Elevations (°)	**50**	**55**	**60**	**65**	**70**	**75**	**80**	**85**	**90**
μ_{max} (m)	0.30	0.29	0.28	0.27	0.27	0.27	0.27	0.27	0.27

Table 30-Look-up table of μ_{max}

Then, the associated protection level VPL_{LUT} is computed the same way as the previous VPL_c as explained by the Equation 159.

Finally, several VPL curves are plotted in order to compare this methodology with others as done in the previous section. Results are presented in the section below.

6.3.1.1.2 Protection Levels

According to this LUT, the associated protection level VPL_{LUT} is computed the same way as the previous VPL_c as explained by the Equation 159. Simulations were processed over 24 hours in the case of GPS and 10 days in the case of GPS /GALILEO, with a time resolution of 10 seconds. This analysis was undertaken for the five key approach points, as presented in 6.2 . Then, in order to compare with previous results presented on Figure 107, Figure 108, Figure 109 and Figure 110, results for Seattle Airport and for an altitude of Aircraft (h) at 200ft, are presented. Results obtained for other key points along the approach are shown in the Appendix A.

Figure 111 and Figure 112 present the following quantities:

- VPL_{inf} with non-nominal troposphere computed with the inflation methodology (presented in 6.2.1) is represented in **red**
- VPL_c computed by adding the exact value of VPL_n and VPL_b (presented in 6.2.1) is represented in **black**
- VPL_n representing VPL without non-nominal troposphere (presented in 6.2.2) is represented in **purple**
- VPL_{LUT} computed with the new proposed methodology (presented in 6.3.1.1.1) is represented in **green**

In Figure 111, the different VPLs presented above are represented for the GPS constellation with a distance from ground station to runway threshold D_{TH} of 5km.

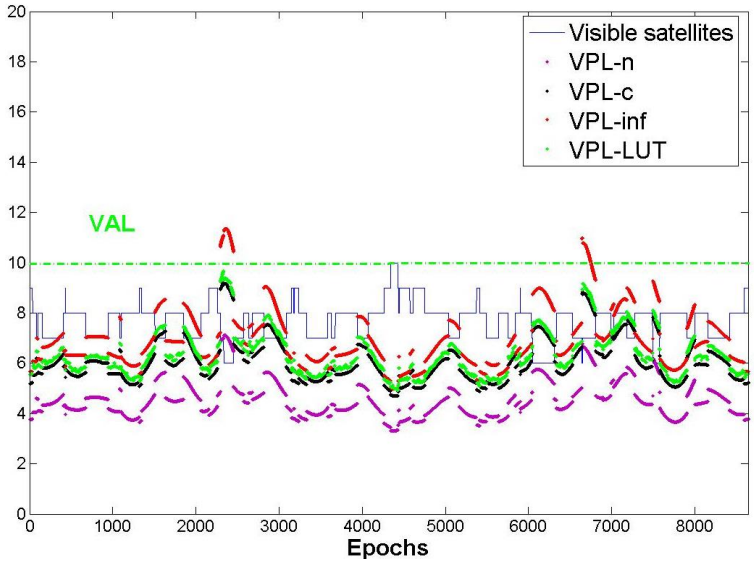

Figure 111-VPLs with D_TH =5km for GPS constellation only

In Figure 111, integrity is ensured since the following inequality is verified:

$$VPL_c \leq VPL_{LUT}$$

Equation 169 - Inequality between VPL-c and VPL LUT

Furthermore, the availability is improved compared to the existing inflation methodology. Indeed the following inequality is obtained:

$$VPL_{LUT} \leq VPL_{inf}$$

Equation 170 – Inequality between VPL_inf and VPL LUT

The level of VPL with this new methodology represented by the green line is closer to the VPL_c (black line) which is seen as the "ideal" VPL than with the inflation methodology (red line). The mean reduction of VPL is about 0.7m which represents almost 10% of improvement, and 100% of availability during this period is obtained with the LUT methodology compared to 99.2% with the inflation methodology where VPL_{inf} is superior to VAL 702 times over 86401 epochs. Therefore, for the GPS constellation case, the LUT approach of providing the 18 parameters in a look up table (Table 30) to the Aircraft improves performances in term of availability by keeping the integrity insured.

In the Figure 112, the different VPLs presented above are represented for the GPS and Galileo constellations with a distance from ground station to runway threshold (D_{TH}) of 5km.

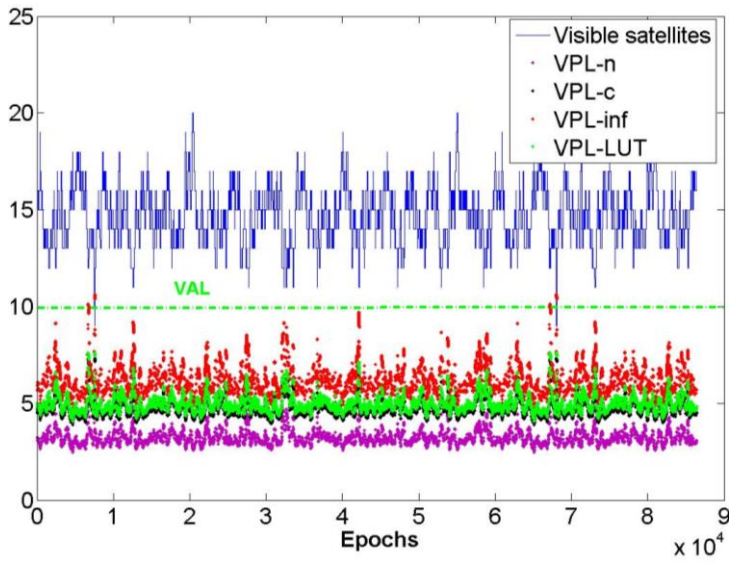

Figure 112-VPLs with D_TH =5km for GPS + GAL constellations

In this GPS and Galileo constellations case, the same conclusions can be made as in the GPS case presented before and inequalities Equation 169 and Equation 170 are still verified. Moreover, the difference between VPL_{inf} (red line) and VPL_{LUT} (green line) is larger and the VPL_{LUT} is closer to VPL_c (black line) compared to the GPS case presented in Figure 111. In this case availability is also improved compared to the reduced GPS constellation because the mean reduction in VPL is about 1.2m which represents almost 19% of improvement, and 100% of availability during this period is obtained with the LUT methodology compared to 99.9% with the inflation methodology where VPL_{inf} is superior to VAL 124 times over 86401 epochs.

By analyzing these results and because the VPLs were found to be closer to the black line representing VPL_c it may be concluded that this LUT methodology relying on sending 18 parameters in a look up table (Table 30) to the Aircraft to bound non-nominal troposphere provides a better availability than the existing methodology (described in 6.2) and keeps the integrity ensured is made. An alternative approach was to set a variable width for each satellite elevations bin with a width of 1°, from 5° to 15° and a larger width of 5° from 10° to 50° and 40° until 90° in the LUT methodology. The new table found in this case is given below:

Elevations (°)	**5**	**6**	**7**	**8**	**9**	**10**	**11**	**12**	**13**
μ_{max} **(m)**	1,19	1,11	1,03	0,97	0,91	0,86	0,81	0,77	0,74
Elevations (°)	**14**	**15**	**20**	**25**	**30**	**35**	**40**	**45**	**50-90**
μ_{max} **(m)**	0,71	0,67	0,56	0,48	0,43	0,38	0,35	0,33	0,31

Table 31-Look up table with a variable width of bin

In Figure 113 and Figure 114, the different VPLs obtained with this new configuration are represented for the GPS constellation and GPS and Galileo constallations with a distance from ground station to runway threshold D_{TH} of 5km.

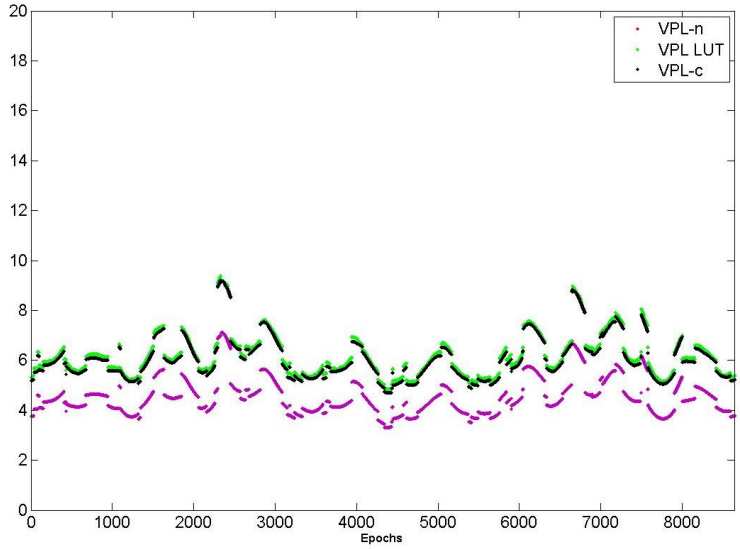

Figure 113-VPLs with D_TH =5km for GPS constellation only

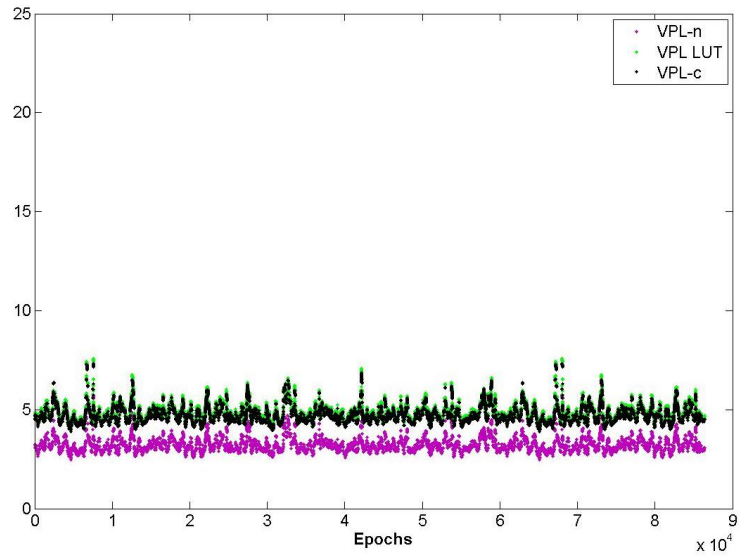

Figure 114-VPLs with D_TH =5km for GPS and Gal constellations

By comparing these Figure 113 and Figure 114 to the Figure 111 and Figure 112, some improvement can be seen. Indeed levels of VPL with the methodology using a variable width of bin is reduced about 2.3% with GPS consteallation and 2.6% with the GPS and Galileo constellations. Therefore this methodology improve also the performance and provides a better availability than the existing methodology (described in 6.2) and keeps the integrity ensured.

However, this methodology requires to transmit a large amount of data to the aircraft (18 parameters μ_{max} in Table 30). By considering that these μ_{max} values vary between 0 and 2m with an accuracy of 0.01m, 8bits will be necessary for coding each μ_{max}therefore an empty place of 144bits (18 Bytes) is needed in a message type to apply this methodology. The message type 2 (MT2 presented in 3.2.3.4.3) where GBAS related data and local information are included is chosen to be modified for including these local tropospheric values. Indeed, in order

to send these parameters, the MT2 could be modified as the same way and same format as it was proposed in the SESAR project [92] with new MC/MF considerations by defining a new Additional Data Block (ADB) number 6 (the number is supposed to be the one proposed in [92]) as described by the following table:

Data Content	Bits	Range of Values	Resolution
ADB Length (=20)	8	20	1 Byte
ADB Number (=6)	8	6	1
$\mu_{max,1}$	8	0-2m	0.01m
…	8	0-2m	0.01m
$\mu_{max,18}$	8	0-2m	0.01m

18 values

Table 32-Proposed ADB 6 for MT2 with LUT

In the ADB 3 defined in 3.2.3.4.3 and in ADB 5 proposed in [92], the ADB length is 6 and the total number of bits is therefore 48 bits. In view of this Table 32, the ADB length is 20 with a total number of bits of 160 bits. In order to keep a similar ADB format and a similar amount of data sent. This ADB 6 could be sent only every 3 MT2 ($160/3{\sim}54\ bits$). Indeed, by considering that the duration of a typical approach is 5minutes and that the MT2 transmission rate is 0.1Hz then 30 MT2 are sent during this operation. With the conservative consideration that only half of MT2 are properly transmitted, 15 MT2 are received at the aircraft side. If ADB 6 is sent every 3 MT2, then 5 ADB 6 will be received at the aircraft even if only one is necessary during the approach.

Therefore by keeping in mind that low data transmission methodology is required, an improvement is realized and explained in the following part.

6.3.1.2 Low Data Transmission (LDT)

As introduced before, the LUT methodology (detailed in 6.3.1.1) requires to send 18 parameters μ_{max} at the aircraft. A reduction of the data transmitted load is realized by developing the methodology below.

6.3.1.2.1.1 Presentation

In order to reduce the number of parameters, this methodology was modified by fitting the curve representing the μ_{max} over elevations by a "bounding" curve always above μ_{max}. The following equation was found and verified this condition:

$$\mu_{max}(i) = A \times \exp\left(-\frac{\theta(i)}{B}\right) + C$$

Equation 171 - Bounding curve equation for Wall Model

Where A, B and C are parameters defined through the following Table 33, $\theta(i)$ is the elevation angle of the satellite i (in degrees) and $\mu_{max}(i)$ is the maximum differential range tropospheric delay for the satellite i .

	A	*B*	*C*
The Wall	*1.31*	*14.21*	*0.28*

Table 33-Fitted curves parameters for Wall Model

The Figure 115 represents μ_{max}over elevations for both new methodologies: with the 18 parameters sent (LUT) and with the Equation 171 (LDT).

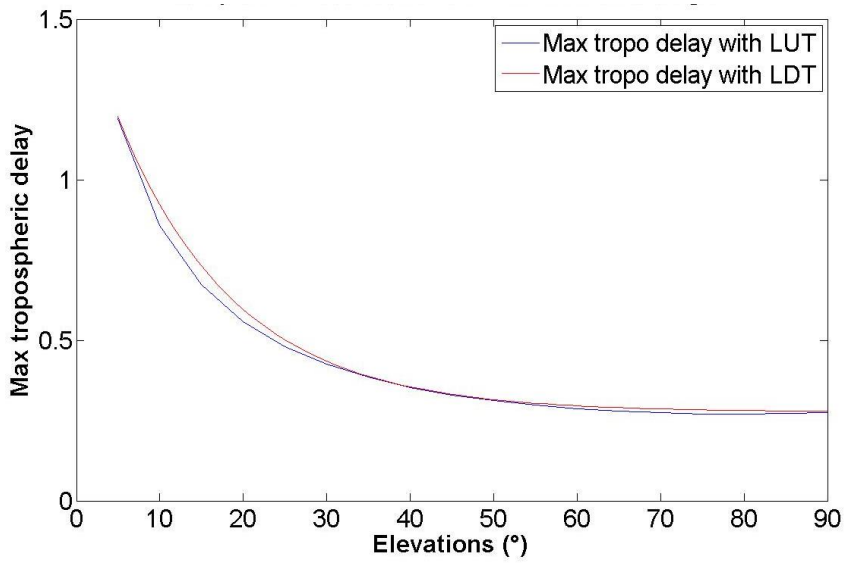

Figure 115-$\mu_{max}$with the 2 new methodologies

It can be seen that 3 parameters A, B and C are required to compute the μ_{max}. So in order to protect the user against non-nominal troposphere, they have to be transmitted to the aircraft (with other local information in the message type 2 (3.2.3.4.3) with a transmission rate of 0.1Hz) . Several options exists, either these parameters are standardized but that will relying on the capability of generating a global model, or these 3 parameters should be set by NSP at each ground station or if more simulations are processed, different model parameters could be defined (per location -regional settings) and a single index is sent to the Aircraft to select the model as it is made for other GBAS Designator (3.2.3.4.1 and 3.2.3.4.3). The issue with this last approach is to determine the appropriate levels for all regions (even unmodelled regions).

Then, a new VPL named VPL_{LDT} based on this Low Data Transmission (LDT) calculation of μ_{max}according to Equation 171 is computed in order to compare performance results obtained with other methodologies previously analyzed. The following part describes these results.

6.3.1.2.1.2 Protection Levels

The same considerations and assumptions are made in this part as in the section 6.3.1.1.2 by processing simulations over 24 hours in the case of GPS and 10 days in the case of GPS /GALILEO, with a time resolution of 10 seconds and only results for Seattle Airport and for an altitude of Aircraft (h) at 200ft, are presented in this section (more airports in Appendix B). Figure 116 shows results for the GPS constellation and Figure 117 results for the GPS/Galileo constellations with a D_{th} set at 5km:

- VPL_{inf} with non-nominal troposphere computed with the inflation methodology is represented in **red**
- VPL_c computed by adding the exact value of VPL_n and VPL_b is represented in **black**
- VPL_n representing VPL without non-nominal troposphere is represented in **purple**
- VPL_{LUT} computed with the LUT methodology with a fixed width bin over elevations (presented in 6.3.1.1.1) is represented in **green**
- VPL_{LDT} computed with the LDT methodology is represented in **yellow**

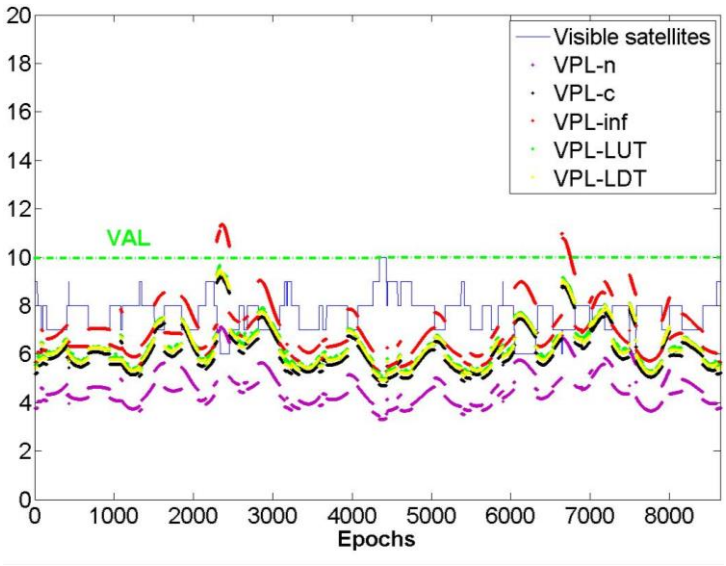

Figure 116-VPLs with D_TH =5km for GPS constellation

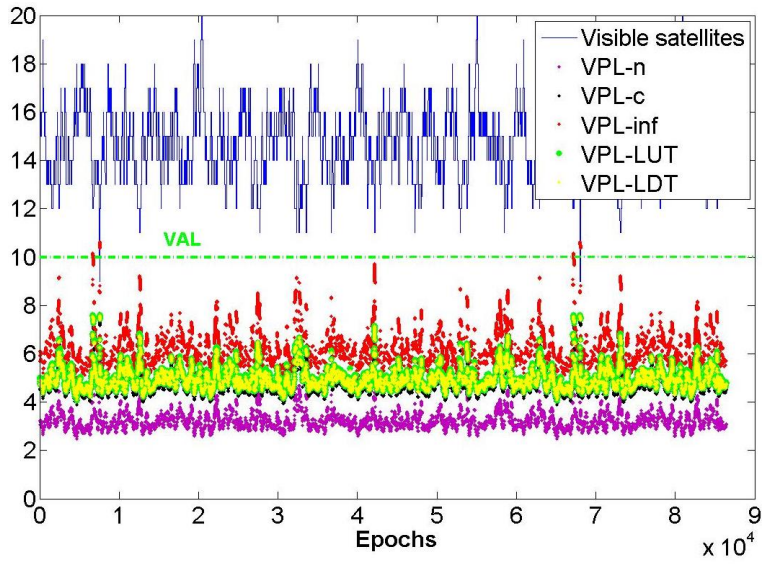

Figure 117-VPLs with D_TH=5km for GPS+GAL

In the previous Figure 116 and Figure 117, integrity is ensured because the following inequality is verified:

$$VPL_c \leq VPL_{LDT}$$

Furthermore, the availability is improved compared to the existing inflation methodology and the LUT methodology. Indeed, the following inequality between the VPL_{LUT} represented by the green line, the VPL_{LDT} represented by the yellow line and the VPL_{inf} represented by the red line is verified:

$$VPL_{LDT} \leq VPL_{LUT} \leq VPL_{inf}$$

The level of VPL with this new LDT methodology represented by the yellow line is closer to the VPL_c (black line) than with the inflation methodology (red line) and the LUT methodology (green line). That is why in all cases, an performance improvement in term of availability is made.

As a matter of fact it should be added that the mean reduction in VPL by using LDT instead of LUT is around 5cm which represent almost 1% of improvement and the mean reduction by using this LDT compared to the inflation methodology is about 1.24m which represents almost 20% of improvement.

That means that availability is improved compared to the existing methodology (100% of availability compared to 99.2% in the inflation methodology for GPS constellation and 99.9% for the GPS/GAL constellation) and the first proposed LUT methodology presented in 6.3.1.1 although the difference between both data for VPL_{LUT} and VPL_{LDT} is quite small (1%).

Note that in the GPS and Galileo case, the difference between the VPL_{inf} (red line) and the VPL_{LDT} (yellow line) is larger than the GPS case whilst the VPL_{LDT} is closer to the VPL_c (black line).

Availability, for all airports where these methodologies were applied, are summarized in the following table by considering the percentage of epochs when the protection levels are below the alert limit VAL set at 10 for the 200ft point along the approach as written in standards [16].

	Seattle		Miami		Anchorage		Lat 0	
Methodology	**Inflation**	**LDT**	**Inflation**	**LDT**	**Inflation**	**LDT**	**Inflation**	**LDT**
GPS constellation	99.2%	100%	95.3%	99.4%	96.1%	96.6%	100%	100%
GPS/GAL constellation	99.9%	100%	99.8%	100%	100%	100%	100%	100%

Table 34-SF Availabilities

The LDT approach with the bias curve-fitting is preferred because it improves performances at each location (Table 34) and requires less data to be transmitted. Indeed, the Equation 171 can be directly applied at the aircraft by setting parameters at the ground station as explained above in the conclusion of the section 6.3.1.2.1.1.

This LDT methodology was also compared to the LUT methodology obtained with a variable width of bin over elevations.VPls obtained in this case are represented below:

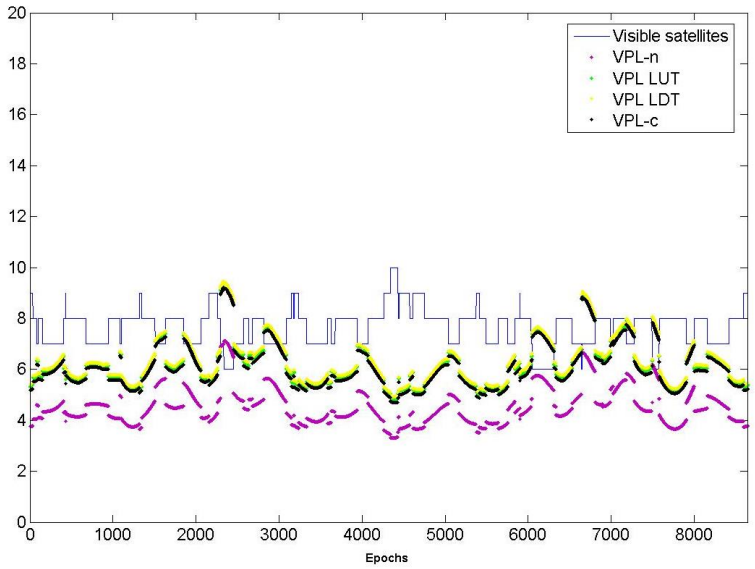

Figure 118-VPLs with D_TH=5km for GPS

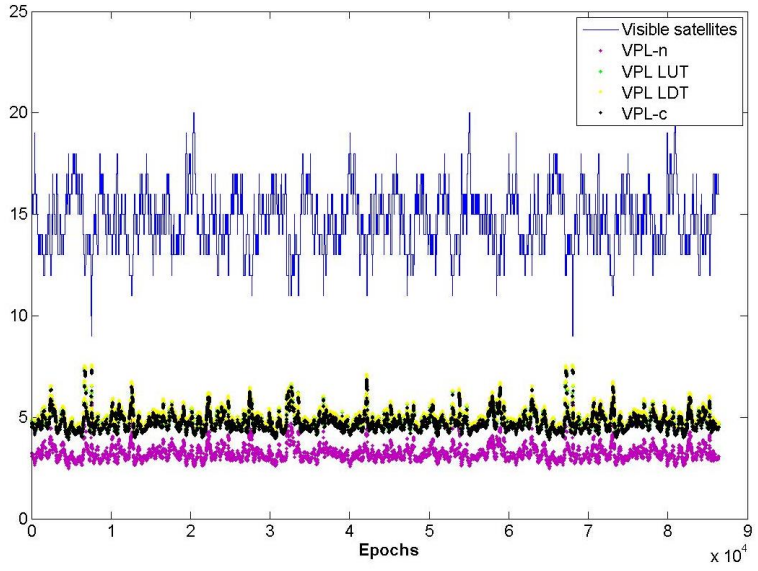

Figure 119-VPLs with D_TH=5km for GPS+GAL

By analyzing these figures, it appears that VPL_{LUT} with a variable width improves performance compared to VPL_{LDT} as a reduction of 1.4% in the mean VPL is visible for GPS and 1.78% for GPS and Galileo.

In order to complete this analysis and for being less conservative another advancement could be realized and is explained in the following part.

6.3.1.3 Worst Satellites Subset (WSS)

6.3.1.3.1 Presentation

In the techniques presented thus far, the conspiring ranging biases assumption has been taken. In this section an attempt to relax this assumption is made by considering that the worst case tropospheric conditions do not impact all satellites. Instead a wall is assumed (though differing from the wall model applied in section 6.2) whose worst case azimuthal orientation is found and which separates the satellites between those impacted by anomalous troposphere and those in entirely nominal conditions. The search is performed over the subset Q which varies with wall azimuth where the value sought is the minimum of $\sum_Q |S_{vert} \times \mu_{max}|$ (referring to the VPL computation in Equation 163). Q is defined as the set of satellites on one side of the wall.

This subset is represented and explained in the following Figure 120 and Figure 121 :

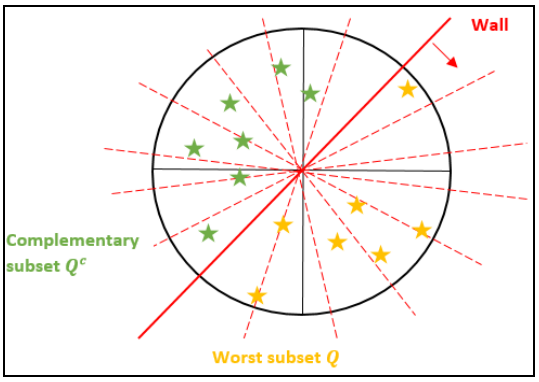

Figure 120-Representation of the Worst subset Q

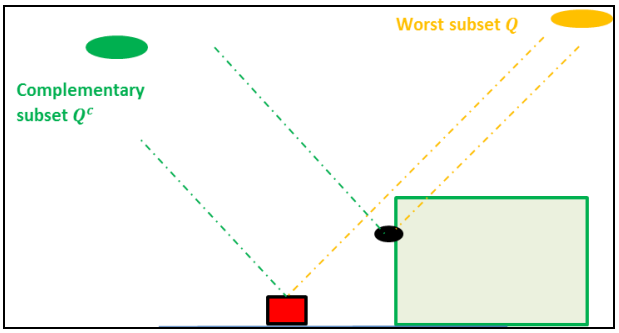

Figure 121-Representation of the Subset Q and the wall model

This methodology is so called Worst Satellite Subset (WSS) methodology and then, protection levels are computed as described in the previous sections 6.3.1.1.2 and 6.3.1.2.1.2.

6.3.1.3.2 Protection Levels

The corresponding new VPLs named VPL_{c-wss}, $VPL_{LUT-wss}$ and $VPL_{LDT-wss}$ are computed in the same way as VPL_c, VPL_{LUT} and VPL_{LDT} respectively but based on subset Q defining the new WSS methodology.

In the following figures, the different VPLs presented above are represented for the GPS constellation (in Figure 122) and for GPS and Galileo constellations (in Figure 123) with a distance from ground station to runway threshold (D_{TH}) of 5km for Seattle Airport (other Airport Results are presented in Appendix B). The new VPL_{c-wss}, $VPL_{LUT-wss}$ and $VPL_{LDT-wss}$ are represented in **black**, green and yellow respectively.

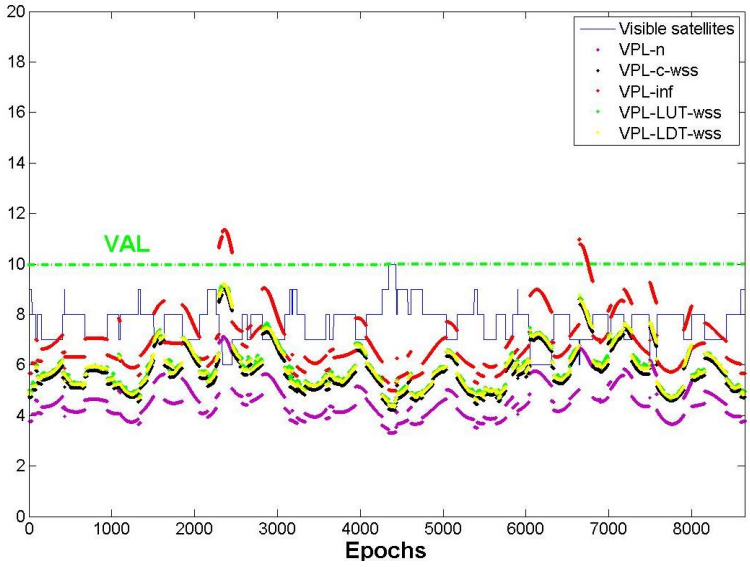

Figure 122-VPLs with D_TH=5km for GPS constellation

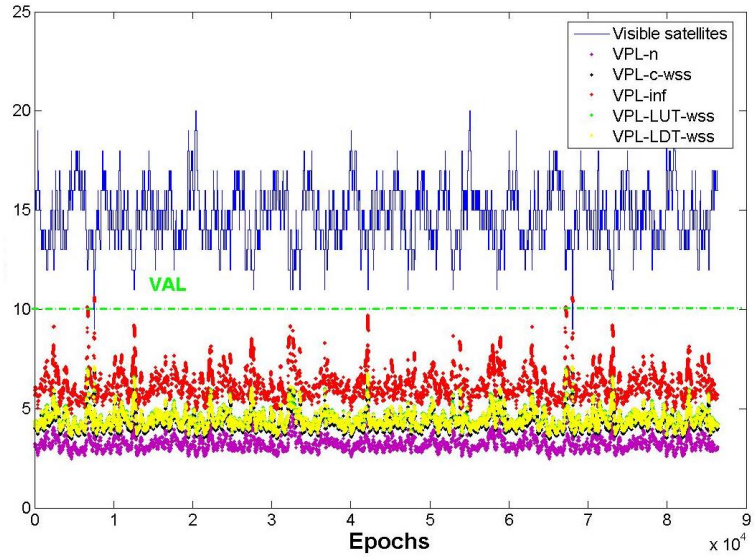

Figure 123-VPLs with D_TH=5km for GPS+GAL

By analyzing the previous Figure 122, Figure 123 and by comparing with previous case represented in Figure 116 and Figure 117, this new WSS methodology implies a translation to the bottom of VPLs curves but in fact VPLs are not reduced much through this methodology except for VPL_{inf} and VPL_n where this WSS methodology has no impact. Indeed, by using this innovative approach when using the preferred LDT methodology, the mean reduction of VPL is almost 40cm in this scenario which represents 6% of VPL level reduction.

Then with less conservative assumptions, performance improvements in term of availability are not important and therefore the LDT methodology detailed in 6.3.1.2 should be preferred by assuming that ranging biases conspire in the worst possible way. Therefore, following sections only focus on this LDT methodology.

6.3.2 Ionosphere-Free case

In case of Dual Frequency GBAS known as GAST F, I-free smoothing may be used to eliminate the ionospheric delay term from the pseudorange observables and corrections. But as it is already mentioned above this thesis (3.2.3.4 and 4.2.1), the differential residual range error due to the range tropospheric delays has the same form as for single frequency case. It is expressed through the Equation 140.

To complete this study, the same simulations were performed as for single frequency case with Dual Frequency case as I-Free smoothing technique. Several analyses with different smoothing constants were realized but in this section of this report only results for 100s smoothing constant are presented (other analysis are given in Appendix C). To clarify figures, only results for the preferred LDT methodology (described in 6.3.1.2) are analyzed in this section.

In the Figure 124 and Figure 125, VPL_c, VPL_n and VPL_{LDT} are represented in **black**, **green** and **yellow** respectively, for the GPS constellation (in the) and for GPS and Galileo constellations (in the) with a distance from ground station to runway threshold (D_{TH}) of 5km at the Seattle Airport (other Airports are presented in Appendix C).

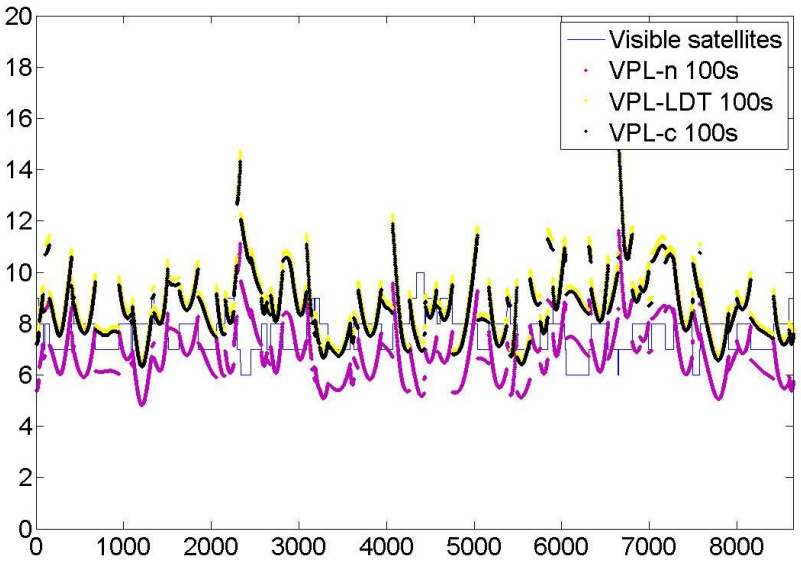

Figure 124-VPLs for I-free case with 100s smoothing constant with D_TH =5km for GPS constellation

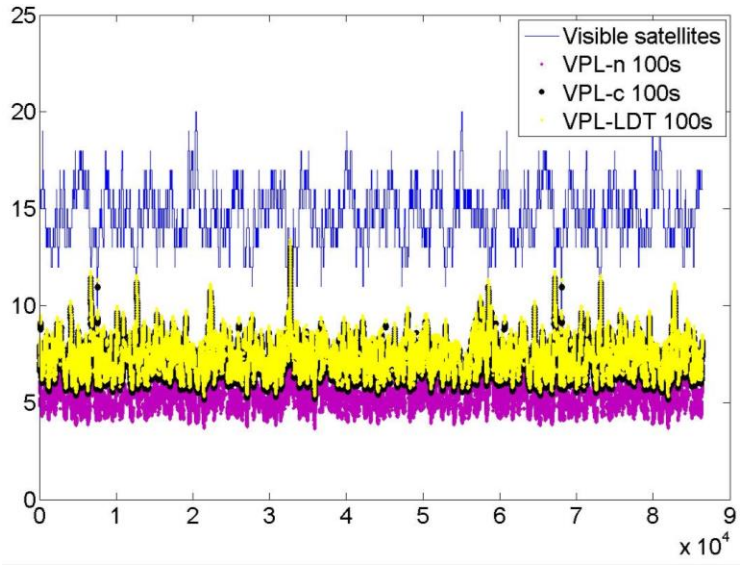

Figure 125-VPLs for I-free case with 100s smoothing constant with D_TH =5km for GPS/GAL constellations

By analyzing the previous Figure 124 and Figure 125, integrity seems to be ensured because the following inequality is still verified:

$$VPL_c \leq VPL_{LDT}$$

Equation 172 - Inequality for the I-free case

These results show that this new 6.3.1.2 LDT methodology are still applicable in the Dual Frequency case by applying the I-Free smoothing technique.

Availabilities, for all airports where the preferred LDT methodology was applied, are summarized in the following table for different smoothing constants, by considering the percentage of epochs when the protection levels are below the alert limit VAL set at 10 for the 200ft point along the approach as written in standards [16].

	Seattle			Miami			Anchorage			Lat 0		
Methodology	**LDT**			**LDT**			**LDT**			**LDT**		
Smoothing Constant	100s	300s	1000s	100s	300s	1000s	100s	300s	1000s	100s	300s	1000s
GPS constellation	85.5%	88.8%	100%	74.9%	99.4%	100%	54.4%	97.2%	100%	66%	100%	100%
GPS/GAL constellation	99.6%	100%	100%	98.1%	100%	100%	95.6%	99.99%	100%	98.8%	100%	100%

Table 35-I-free Availabilities

As it shown by this table, the impact of smoothing constant on availabilities is important. Indeed, the higher the smoothing constant is, the better the availability is.

So, in this section of the report, innovative methodologies were presented which seem to reduce the level of protection levels and therefore improving performances by having a better availability (up to 0.8% of availability improvement in the SF case with LDT methodology) than with the existing methodology described in section 6.2 (see Table 34 for more availability values) and this by keeping integrity ensured. These new LDT methodology which can be also used in the Dual Frequency case with I-free smoothing technique, can be seen as a "low data transmitted". Also by comparing performance for both cases: with (in Figure 122 and Figure 123) and without (in Figure 116 and Figure 117) the geometry improvement, it should be noticed that only few gain is visible in term of performance but the processing of selection the subsets of satellites is more onerous in computation. That is why the LDT methodology explained in 6.3.1.2 is preferred and the following analysis with only focus on this method.

In this section only surface atmospheric data following the simple empirical wall model described in section5.2.1, whilst in a NWM the atmospheric parameters are available at both the surface and at multiple layers. As explained in5.3.3, it is therefore possible to use this 3D data model to more accurately determine the total range tropospheric delay and to find the worst horizontal differential range tropospheric delay (Figure 82 in section 5.4 and details in section). Then the innovative methodologies such as LDT (6.3.1.2) could be applied. This computation and the corresponding analysis is explained in the following part of this report.

6.4 Numerical Weather Model Based Methodology

The previous section outlined the means to protect an aircraft from ranging biases due to horizontal gradients by computing the worst differential range tropospheric delay with a simple empirical model. Here, a more sophisticated 3D NWM is used for deriving the new preferred LDT methodology presented in 6.3.1.2.

At first, the impact of horizontal differential tropospheric ranging biases is analyzed and then, the impact of the potential presence of vertical differential ranging biases as those found in the section 5.5.2 is studied. This section finishes with the use of NWMs for validating one of the most important assumption made in the PhD project dealing with the conspiring ranging biases.

6.4.1 Worst Horizontal Differential Tropospheric Delay

As introduced above, with the data obtained with NWM Arome and Harmonie, the maximum horizontal differential range tropospheric delay over elevations was obtained (Figure 84, Figure 85, Figure 86 in section 5.4). Then, for each elevation from 5° to 90° the worst value was selected as explained in 5.4.4 (represented by the red curve B in the Figure 84 and the green curve C in the Figure 85) and the LDT (6.3.1.2) was applied. Another

case was examined when the cut off angle is set at 10° (should be possible in DC) regarding the sharped shape of the Curve C obtained with Arome data (Figure 85 in 5.4.4), therefore another Curve D (in Figure 86) was derived starting at 10° of elevation and was named Curve D for this particular case.

By similitude with standards' curves equations for other error sources (as described in Chapter 4 and [16]), the following formula was derived in this case (curves previously explained in 5.4.4 and 6.3.1.2) with other parameters than in the study with the Wall Model (in 6.3.1.2)

$$\mu_{max}(i) = A \times \exp\left(-\frac{\theta(i)}{B}\right) + C$$

Where A, B and C are parameters defined through the following Table 36, $\theta(i)$ is the elevation angle of the satellite i and $\mu_{max}(i)$ is the maximum differential range tropospheric delay for the satellite i.

	A	*B*	*C*
The Wall (Curve A - Figure 83)	*1.31*	*14.21*	*0.28*
Harmonie NWM (Curve B - Figure 84)	*1.05*	*11*	*0.08*
Arome NWM (Curve C - Figure 85)	*1.52*	*9*	*0.16*
Arome NWM (Curve D - Figure 86)	*1.02*	*10.2*	*0.16*

Table 36-Fitted curves parameters for Ohio/ Harmonie / Arome

Once this equation obtained the protection levels are computed as for the Wall Model in 6.3.1.2.1.2 and impact on VPL_{LDT}performances was computed and analyzed in the following section for the Single Frequency case and Dual Frequency case.

6.4.1.1 Single Frequency Case

In this subsection, impact on VPL_{LDT} performances (6.3.1.2) is computed in the Single Frequency case.

In order to compare with previous analysis, results are presented for the GPS constellation and for GPS and Galileo constellations with a distance from ground station to runway threshold D_{th})of 5km and a height of A/C at 200ft at Seattle Airport with NWM Harmonie (cyan line) and Arome (pink line) data and the results obtained with "Ohio" data (yellow line) by considering the Wall Model as presented in previous section5.2.1.

Firstly, results are presented for GPS constellation in Figure 126 and for GPS and Galileo constellations in Figure 127 where the cut-off angle is set at 5° for the GPS constellation (10° for Galileo) therefore, the Curve A, B and C equations (Table 36) are used to derive the LDT methodology (explained in 6.3.1.2 and 6.4.1 for NWMs) and to compute protection levels.

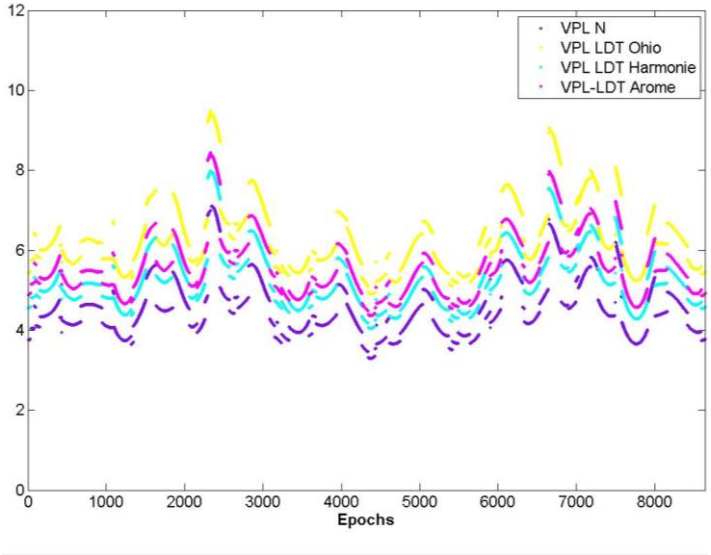

Figure 126-VPLs for GPS constellation

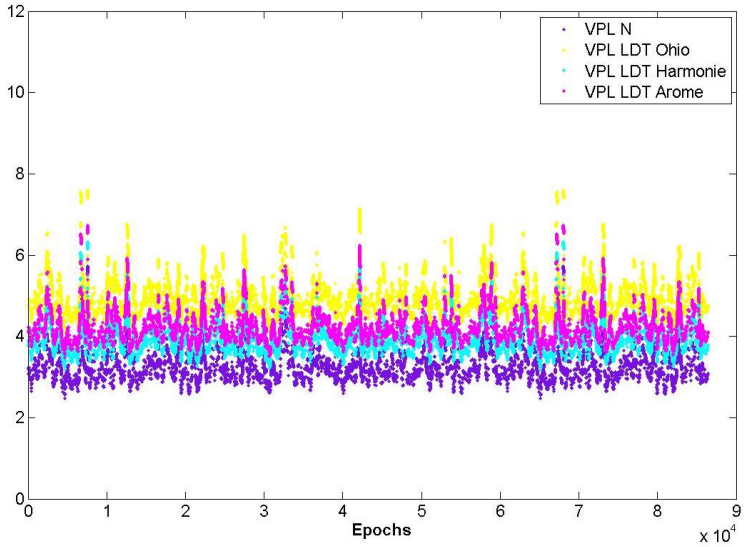

Figure 127-VPLs for GPS and GAL constellations

By viewing these results on Figure 126 and Figure 127, it can be conclude that either gradients in Ohio are larger than in Netherlands or the "Wall Model" methodology is too conservative. Reminding the results presented in 5.4, gradients in Europe seemed to be more important than for the data set examined at Ohio therefore, the "Wall Model" Methodology appear really conservative compared to the results found in view of European data. Also, it appears that VPLs are 15.87% higher for Arome than for Harmonie(Table 37) therefore gradients seems

more important in Alpines area than in Netherlands. This could be explained by the fact that abnormal changings in atmopherical parameters and therefore in tropospheric delays should appear more frequently in Alpines area than in Netherlands.

Then results are presented for the case where the cut-off angle is set at 10° therefore, the Curve A, B and D equations (Table 36) are used to derive the LDT methodology (explained in 6.3.1.2 and 6.4.1 for NWMs) and to compute protection levels.

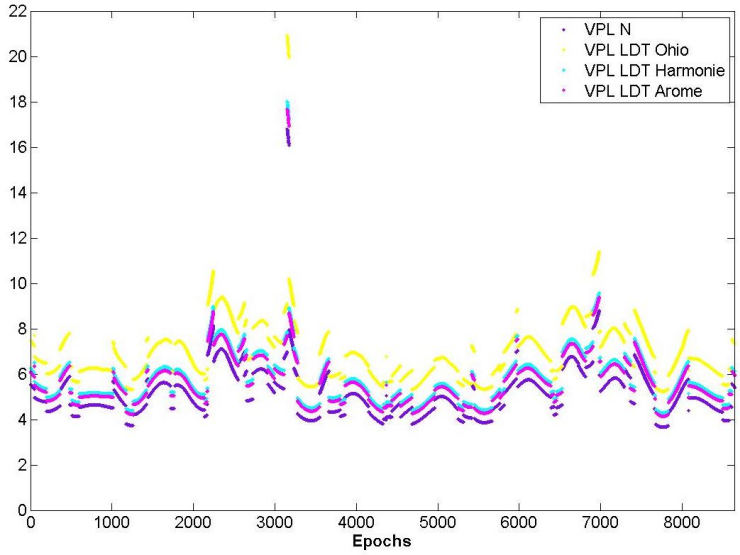

Figure 128-VPLs for GPS with a cut-off angle of 10°

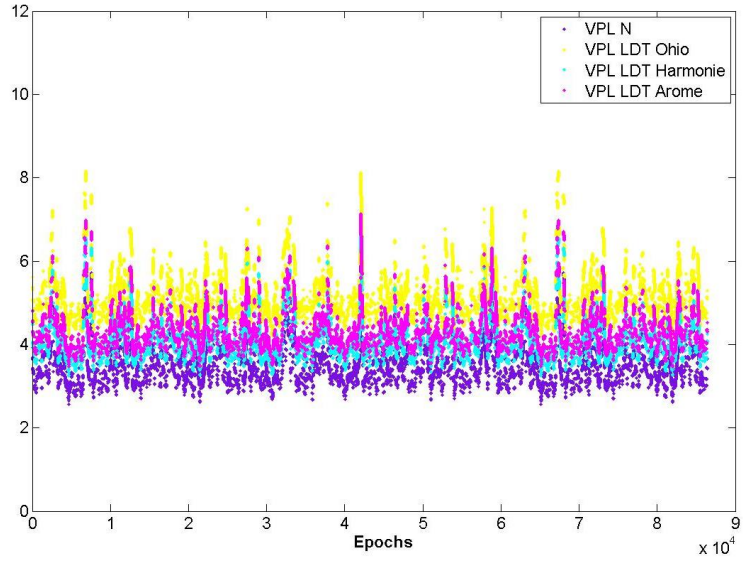

Figure 129-VPLs for GPS and GAL constellations with a cut off angle of 10°

By analysing these results on Figure 128 and Figure 129 and Figure 126, it can be concluded that reminding the section 5.4, gradients in Europe seemed to be more important than for the data set examined at Ohio therefore, the "Wall Model" appear again really conservative in view of the results obtained with European data. (Yellow

line up to 26.5% above the others (Table 37)). Also, a pic in the VPL on Figure 128 can be noticed which is due to the fact that number of satellites (represented by the blue curve) is very low. Therefore having only GPS constellation with the cut-off angle of 10° seems not feasible, then focus is made on DC case (GPS and Galileo) for following studies (6.4.1.2 and 6.4.2)

Results comparing Arome and Harmonie protection levels on Figure 129 are not so different than with the 5° cut off angle (Figure 127). Indeed it appears that VPLs are up 6.21% higher for Harmonie than for Arome(Table 37)(that should be guessed by seeing the shape of curves B and D in Figure 88) therefore also in this case, gradients seems more important in Alpines area than in Netherlands.

In order to conclude about the impact on performances, the percentages of the mean differences in VPLs for each of data are summarized in the following table according the constellations (GPS/GPS and Galileo with cut-off angle at 5°/GPS and Galileo with cut-off angle at 10°):

	GPS	**GPS and Galileo (5°)**	**GPS and Galileo (10°)**
Arome-Harmonie	6.42%	8.3%	6.21%
Arome-Ohio	-11.3%	-14.44%	-18.52%
Harmonie-Ohio	-20.0%	-26.5%	-26.4%

Table 37-Percentage of the mean difference between VPLs

Moreover, in DC case it should be possible to set the cut-off angle at 10°, in this case either the parameters corresponding to the Curve C or the parameters corresponding to the Curve D have to be sent to the aircraft. The accurate method is guess to be the one using the Curve D parameters but the loss of performance realized by using the Curve C parameters need to be investigated. Therefore, the following figure represents VPLs computed in the DC case with a cut-off angle at 10° using either the Curve C or the Curve D parameters.

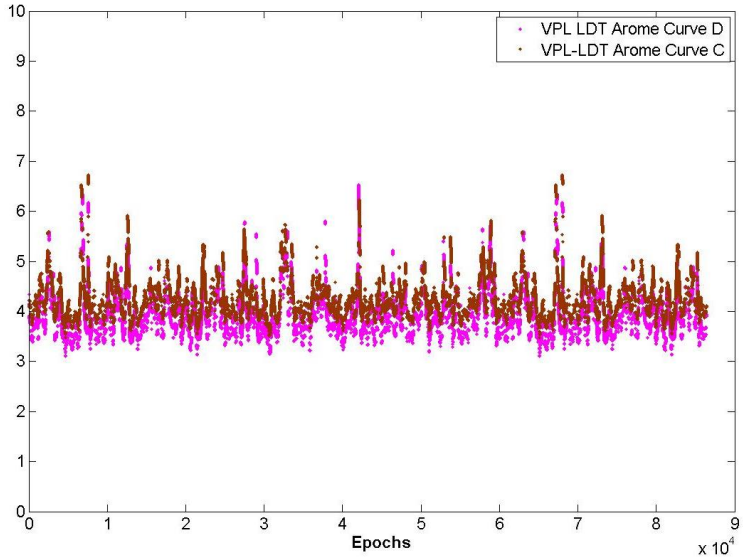

Figure 130-VPL LDP for Arome with GPS/GAL and cut off angle at 10° with Curves C and D

By analyzing this Figure 130, it could be noticed that using the Curve C obtained for the cut-off angle at 5° in the case of a cut-off angle set at 10° will increase the protection level of 2.1% therefore this loss of performance appear not negligible even if the availability will not be so impacted. So it could be recommended to use the Curve D if the cut-off angle in the case of DC is set at 10° and in next sections, analysis will be also done for this special case.

Also, by viewing the differences between the two Curve C and D in 5.4.4 and the impact on performances explained in this section, it should be relevant to develop a more accurate model than the one presented with this LDT methodology. Indeed, main differences between these curves appears at low elevations between 5° and 10° and the worst differential range tropospheric delay appears less elevation dependent (as shown curves in5.4.4 and by the look-up Table 30). With the aim of defining a more accurate model, the LUT methodology could be improved by setting a variable width for each satellite elevations bin with a width of 1°, from 5° to 15° and a larger width of 5° from 15° to 50° and 40° until 90° (μ_{max} is considered constant from 50° to 90°) . Therefore in this settings example ,18 values of μ_{max} should be obtained and the format of the proposed ADB 6 (defined in Table 32) will not change but if other widths and parameterization are chosen that could have an impact in the ADB 6 format proposed in Table 32 . This methodology is intended to be more accurate than the LUT methodology presented in 6.3.1.1 and could be a good alternative to the LDT methodology without constraint about the angle mask in the DC case. That is why, data were reprocessing and the following look-up table was found for the Arome data.

Elevations (°)	**5**	**6**	**7**	**8**	**9**	**10**	**11**	**12**	**13**
μ_{max} **(m)**	1.03	0.82	0.71	0.64	0.44	0.42	0.42	0.41	0.41
Elevations (°)	**14**	**15**	**20**	**25**	**30**	**35**	**40**	**45**	**50-90**

μ_{max} (m)	0,38	0,36	0,30	0,25	0,21	0,19	0,17	0,15	0,15

Table 38-Look up table for AROME data with a variable width of bin

Then VPLs were plotted and compared to those obtained in the LDT methodology. Results are represented in the figures below:

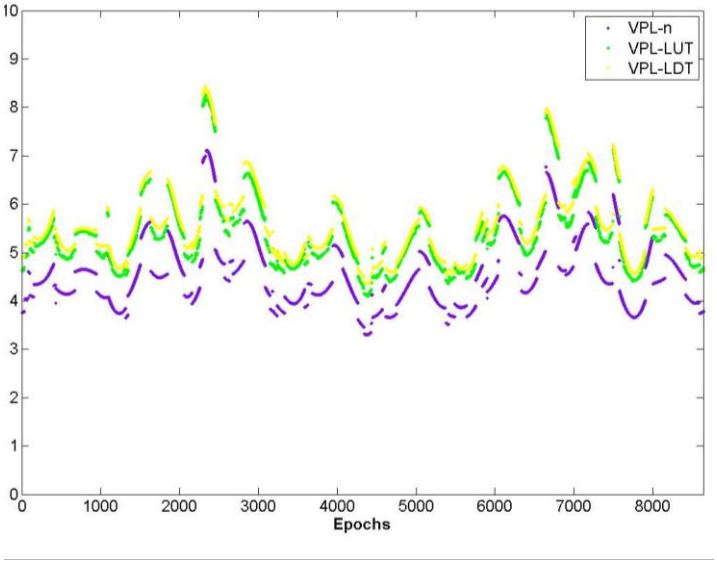

Figure 131-VPLs for GPS constellation

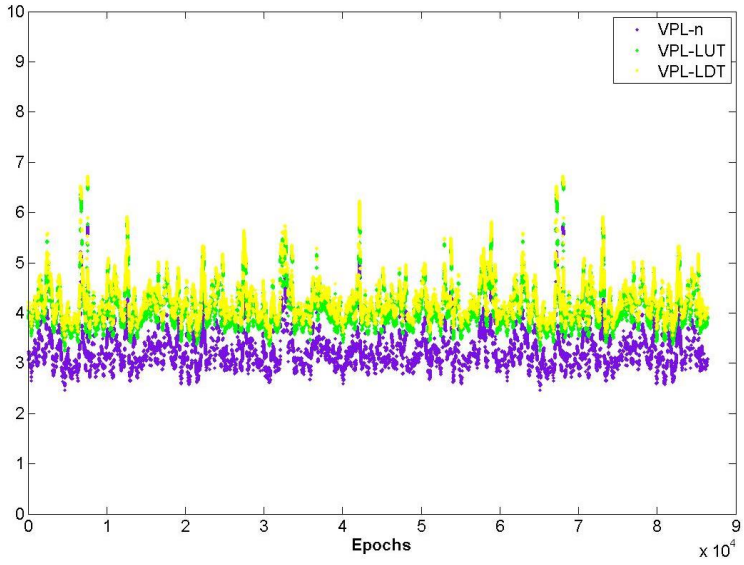

Figure 132-VPLs for GPS and GAL constellations

By analyzing these figures, as expected an improvement of performance is visible as the mean VPL obtained with the LUT methodology is 3.3% lower than with the LDT for GPS constellation and 3.9% for the GPS and Galileo constellations.

6.4.1.2 Ionosphere-Free Case

In this subsection, impact on VPL_{LDT} performances (6.3.1.2) was computed in the I-free case.

In order to compare with previous analysis, results are presented for the GPS constellation on the Figure 133 and for GPS and Galileo constellations on the Figure 134 with a distance from ground station to runway threshold (D_{TH}) of 5km and a height of A/C at 200ft at Seattle Airport with NWM data from Harmonie (cyan line) and Arome (pink line) and the results obtained with "Ohio" data (yellow line) by considering the Wall Model as presented in previous section.

First results are presented for GPS constellation in Figure 133 and for GPS and Galileo constellations in Figure 134 where the cut-off angle is set at 5° for the GPS constellation (10° for Galileo) therefore, the Curve A, B and C equations (Table 36) are used to derive the LDT methodology (explained in 6.3.1.2 and 6.4.1 for NWMs) and to compute protection levels.

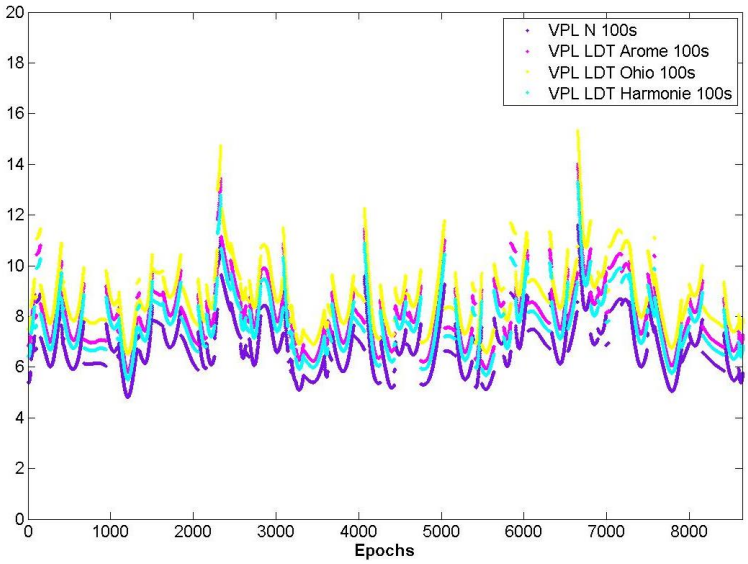

Figure 133-VPLs I-free for GPS constellation

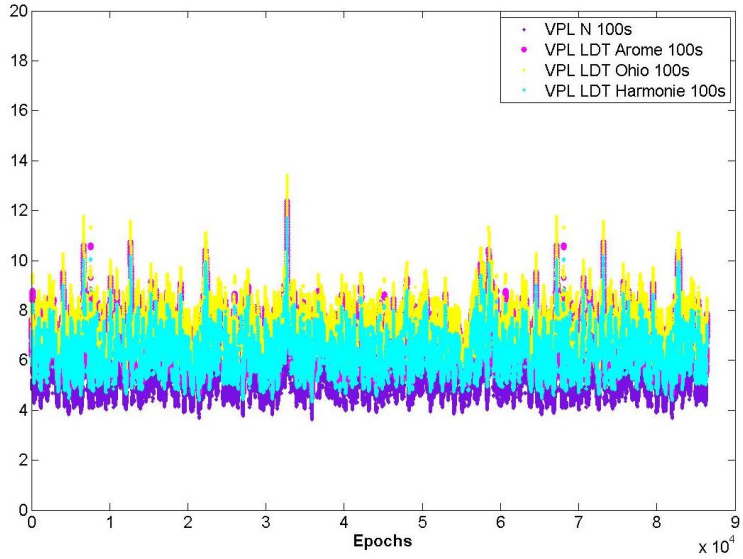

Figure 134-VPLs I-free for GPS and GAL constellation

Then, in the figure below, results are presented for the case where the cut-off angle is set at 10° for the GPS and Galileo constellations case, therefore, the Curve A, B and D equations (Table 36) are used to derive the LDT methodology (explained in 6.3.1.2 and 6.4.1 for NWMs) and to compute protection levels.

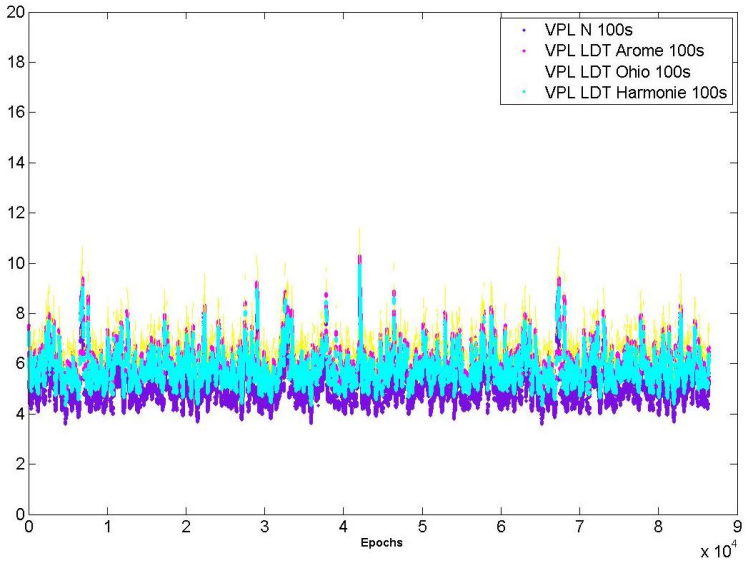

Figure 135-VPLs I-free for GPS and GAL constellation with cut off angle at 10°

By analyzing these Figure 133, Figure 134 and Figure 135, same conclusions as for single frequency case (described in 6.4.1.1) can be done. Indeed, gradients in Europe seemed to be more important than in the data set examined at Ohio (reminding results found in 5.4), therefore, even in the IF case the "Wall Model" methodology appear really conservative in view of the result found within the European data. Also, it appears for a cut off angle of 5° and 10° that VPLs are higher for Arome than for Harmonie therefore gradients seem larger in the Alpine area than in the Netherlands.

6.4.2 Vertical Ranging Biases

As presented in the section 5.5, by analyzing the distributions of the errors between TC and ZTD for the three locations Turin, Milan and Schiphol, it has been remarked that ranging biases which are not covered by the actual TC computation exist.

Indeed, the Figure 105 represents these ranging biases named μ_{TC} over the elevation angle for each location. In view of their magnitudes up to 12mm, they cannot be negligible and have to be treated. Therefore these biases were included into the innovative VPL computation with the LDT methodology (explained in 6.3.1.2 and 6.4.1for NWMs) and results are presented below.

In order to compare with previous analysis, results are presented for the GPS constellation on the Figure 136 and for GPS and Galileo constellations on the Figure 137 with a distance from ground station to runway threshold(D_{th}) of 5km and a height of A/C at 200ft at Seattle Airport. Then for comparison purpose, the results for Milan and Turin are compared with those obtained with Arome data without the bias insertion and the results obtained for Schiphol are compared with those obtained with Harmonie. Also the impact of these ranging biases on VPLs is really small that is why a zoom was made to notice differences between curves.

First, results for Harmonie and Schiphol are shown for the GPS constellation on the Figure 136 and for GPS and Galileo constellations on the Figure 137 :

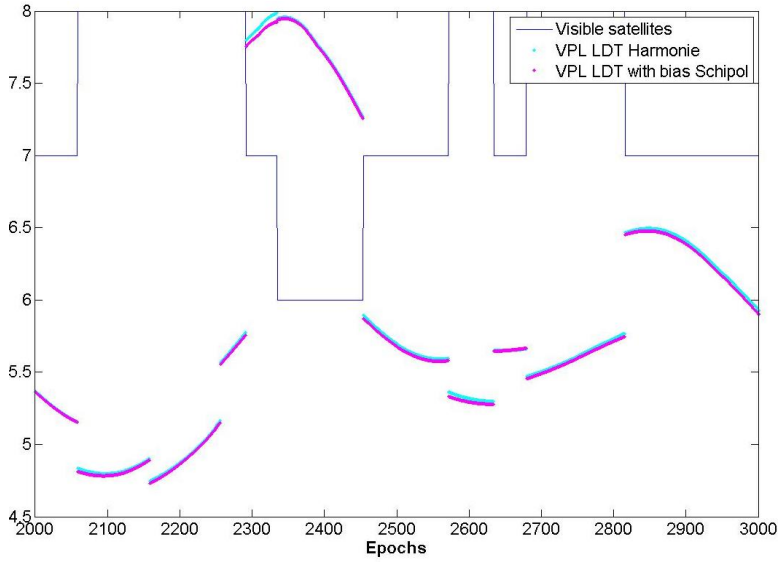

Figure 136-VPLs at Schiphol for GPS constellation

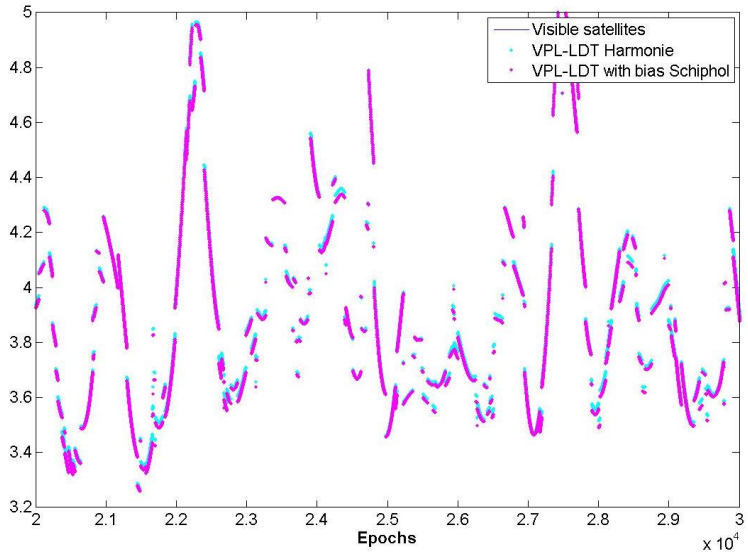

Figure 137-VPLs at Schiphol for GPS+GAL

Regarding the Figure 138, Figure 139 and Figure 140, only few differences are visible between the VPL computed without the vertical ranging biases ("VPL Harmonie") and the VPLs computed at Turin and Milan by taking into account vertical ranging biases. Therefore, it appears that impact of the vertical bias in Schiphol is not important in the derivation of the protection level and will not have an impact on performances.

Then in following Figure 138 and Figure 139 same results as above for Harmonie are presented but for Arome with Turin and Milan Locations. First results are presented for GPS constellation in Figure 138 and for GPS and Galileo constellations in Figure 139 where the cut-off angle is set at 5° for the GPS constellation (10° for Galileo) therefore, the Curve A and C equations (Table 36) are used to derive the LDT methodology (explained in 6.3.1.2 and 6.4.1 for NWMs)and to compute protection levels.

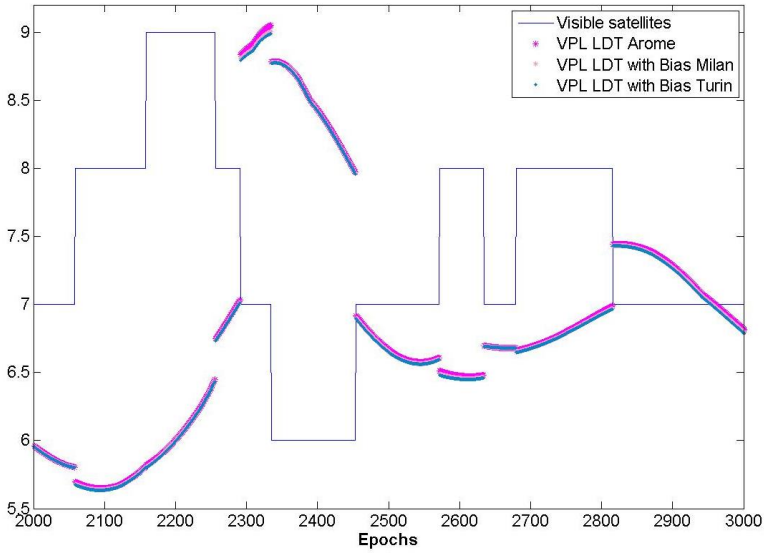

Figure 138-VPLs at Turin and Milan for GPS constellation

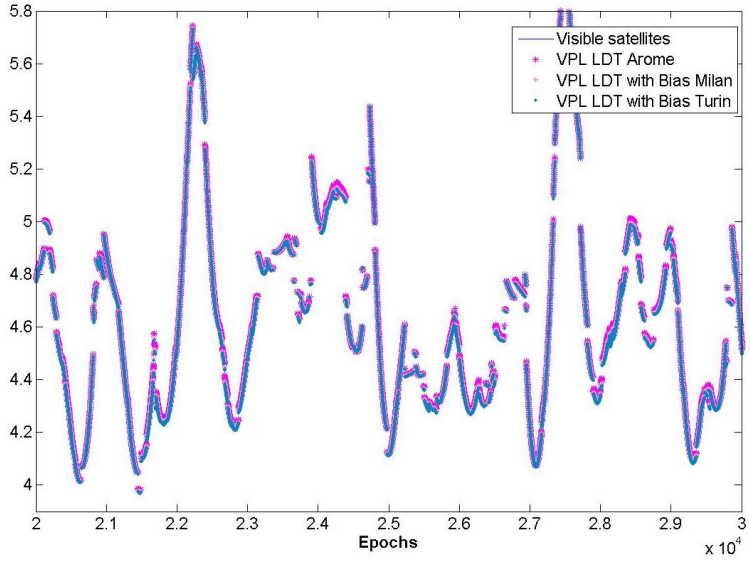

Figure 139-VPLs at Turin and Milan for GPS+GAL

Then results are presented for the case where the cut-off angle is set at 10° therefore, the Curve A and D equations (Table 36) are used to derive the LDT methodology (explained in 6.3.1.2 and 6.4.1 for NWMs) and to compute protection levels.

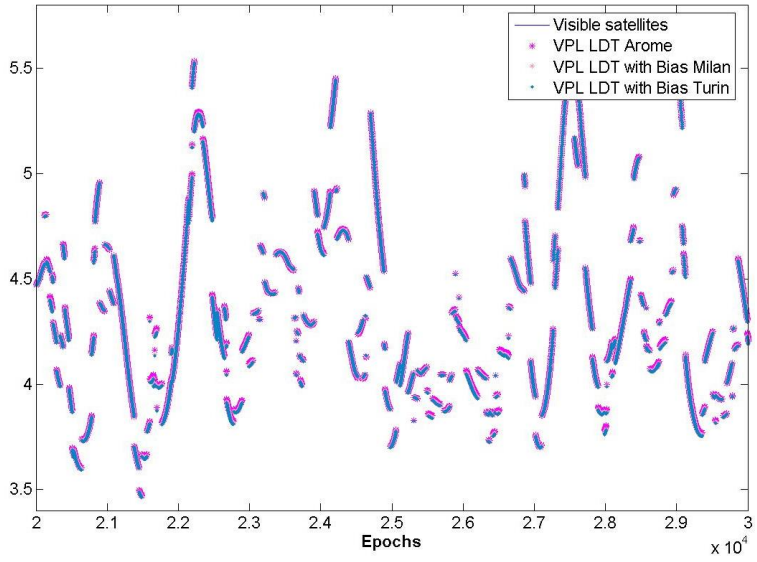

Figure 140-VPLs at Turin and Milan for GPS+GAL with a cut-off angle at 10°

In these Figure 138, Figure 139 and Figure 140, only few differences are visible between the VPL computed without the vertical ranging biases ("VPL Arome") and the VPLs computed at Turin and Milan by taking into account vertical ranging biases (Table 39). Therefore, it appears that impact of the vertical biases are not important in the derivation of the protection levels and will not have an impact on performances.

In order to conclude this subsection on vertical ranging biases, mean differences on VPLs with (VPLs Turin, Milan, Schiphol) or without (VPLs Arome and Harmonie) taking into account the vertical ranging biases are summarized

in the following table according the constellations (GPS/GPS and Galileo with cut-off angle at 5°/GPS and Galileo with cut-off angle at 10°):

	GPS	GPS and Galileo (5°)	GPS and Galileo (10°)
Turin – Arome	-0.26%	-0.22%	-0.14%
Milan – Arome	-0.19%	-0.16%	-0.10%
Schiphol - Harmonie	-0.29%	-0.26%	

Table 39 – Percentage of differences between VPLs with and without vertical biases.

6.4.3 Conspiring Ranging Biases Assumption Validation

NWMs can also be used to validate important assumptions made in previous analysis. Indeed, all analysis realized in this PhD project assumed that ranging biases conspired. Therefore, in order to check if the conspiring biases assumption made for LUT (6.3.1.1) and LDT (6.3.1.2) methodologies was correct, it was decided to fix an A/C and a GND station at the 10 worst case segments found with the methodology explained in previous section 5.4, then to run the ray tracing process for the corresponding nominal GPS and GALILEO constellations every 5min over 10 days for finding the maximum differential range tropospheric delay for each satellites and finally to compute VPL_c (named VPL-Validation in this part) as described by the Equation 159 which can be considered as the "ideal" VPL.

After, having computing the Maximum differential range tropospheric delay obtained for all satellites, VPL was computed with LDT methodology for single frequency case (assuming that conspiring ranging biases impact should be the same for SF than I-free case) with Harmonie parameters (5.2.2.3). Also the VPL_{inf} was computed for N=24 satellites in view as well as the VPL Validation. Results are presented in the following Figure 141.

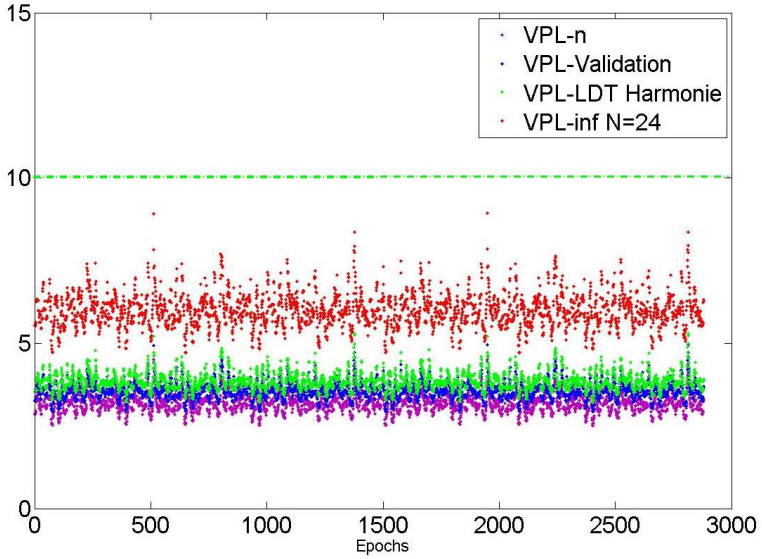

Figure 141-VPLs for validating conspiring biases assumptions

By analysing these curves, it is possible to see that VPL-validation in blue is always below the VPL_{LDT}in green. But the difference between them is not so noticeable. Indeed the mean difference is equal to 0.081meters which represent about 2.3% of the VPL-Validation mean value. Therefore, by viewing these curves, it seems correct to assume that considering conspiring ranging biases on all satellites in view is not so conservative and the lack of performance realized by making this assumption is really small.

6.5 Conclusions and Recommendations

The results presented with the existing methodology proposed by Ohio University show a significant inflation of the VPLs in order to bound the non-nominal troposphere. However, this is the simplest solution to implement given the GAST C/D message definition. It appears excessively conservative to apply this bound. Furthermore, in the case of the I-free smoothing which may be used for GAST F, an alternative approach is needed because the ionosphere component will be removed and the σ_{iono} and therefore the equivalent $\sigma_{vig\ inf}$ will not exist anymore. An innovative methodology is therefore needed whilst maintaining a minimum data transmission load.

By considering the possibility of providing additional data to the aircraft and changing of protection levels computation, an initial proposal was made known as Look-Up table Transmission (LUT) methodology then an improvement of it is realized through the new Low Data Transmission (LDT) methodology with the aim of reducing the data transmission load and finally another proposal is developed to improve the availability by developing a less conservative methodology under a new satellite geometry called Worst Satellites Subset (WSS) methodology.

Therefore by keeping in mind that low data transmission methodology is required and by comparing performance improvements realized through all proposed techniques, the LDT detailed in 6.3.1.2 should be preferred by assuming that ranging biases conspire in the worst possible way. Through this methodology, in order to protect the user against non-nominal troposphere, 3 parameters A, B and C have to be transmitted to the aircraft (in the message type 2 (MT 2 introduced in 3.2.3.4.3) as for other GBAS related data and local information at the rate of 0.1Hz). As mentioned above, several options exists, either these parameters are standardized but that will relying on the capability of generating a global model, or these 3 parameters should be set by NSP at each ground station. By seeing the Table 36, the “A” parameter takes value from 0 to 3.5, the “B” parameter from 0 to 14.5 and the “C” parameter from 0 to 0.28 with an accuracy of 0.01. Therefore they will need respectively 9, 10 and 5 bits to be send to aircraft. With this methodology, 24 bits (5Bytes) are necessary in the MT 2 to apply this methodology. In order to send these parameters, the MT 2 could be modified as the same way as it was proposed in the SESAR project [92] with new MC/MF considerations by defining a new Additional Data Block (ADB) number 6 (the number is supposed to be the one proposed in [92]) as described by the following table:

Data Content	Bits	Range of Values	Resolution
ADB Length (=5)	8	5	1 Byte
ADB Number (=6)	8	6	1
A	9	0-3.5	0.01
B	10	0-14.5	0.01
C	5	0-0.28	0.01

Table 40-Proposed ADB 6 for MT2 with LDT

In the ADB 3 defined in 3.2.3.4.3 and in ADB 5 proposed in [92], the ADB length is 6 and the total number of bits is therefore 48 bits. In view of this Table 40, the ADB length is 5 with a total number of bits of 40 bits. In order to keep a similar ADB format and a similar amount of data sent. This ADB 6 could be sent at the same rate of 0.1Hz of MT2.

Or if more simulations are processed, different model parameters could be defined (per location -regional settings) and a single index is sent to the Aircraft to select the model as it is made for other GBAS Designator (3.2.3.4.1 and Chapter 4). The main issue with this last approach is to determine the appropriate levels for all regions (even unmodelled regions) but the great advantage is that only 2bits should be needed for sending the designator to the A/C without much modification of the MT 2. Indeed there is spare bits with 8 bits available within the existing ADB 3 therefore the new designator could be applied at this field by re-defining spare bits only.

Moreover, in the scope of MC/MF GBAS development and in view of results obtained with Arome (6.4) with a cut off angle at 10°, two possibilities exist. The first one is to send parameters corresponding to 2 curve equations to the A/C (6 parameters) where 3 parameters will be used in the case of SC with a cut off angle set at 5° and the others used in the case of DC with a cut off angle at 10°. The second is to consider only the 3 parameters obtained with the cut off angle at 5° in both SC and DC cases. Using this last solution will increase the VPL about 9% (Figure 130) but will require less data to transmit. This percentage is not negligible therefore in case of DC if the cut off angle is defined at 10° the ADB 6 will have this kind of format by taking into account Single or Dual constellations (SC/DC):

Data Content	Bits	Range of Values	Resolution
ADB Length (=8)	8	8	1 Byte
ADB Number (=6)	8	6	1
A_{SC}	9	0-3.5	0.01
B_{SC}	10	0-14.5	0.01
C_{SC}	5	0-0.28	0.01

A_{DC}	9	0-3.5	0.01
B_{DC}	10	0-14.5	0.01
C_{DC}	5	0-0.28	0.01

Table 41-Proposed ADB 6 for MT2 with LDT if DC with a cut off angle at 10°

In view of this Table 41, the ADB length is 8 with a total number of bits of 64 bits. In order to keep a similar ADB format and a similar amount of data sent as the ADB 3 defined in 3.2.3.4.3 and in ADB 5 proposed in [92] (48 bits). This ADB 6 could be sent every 2 MT2). As already mentioned in 6.3.1.1, by considering that the duration of a typical approach is 5minutes (300seconds) and that the MT2 transmission rate is 0.1Hz then 30 MT2 are sent during this operation. With the conservative consideration that only half of MT2 are properly transmitted, 15 MT2 are received at the aircraft side. If ADB 6 is sent every 2 MT2, then about 7 ADB 6 will be received at the aircraft even if only one is needed during the approach.

As presented in 6.3.1.2, by remarking the differences between the two Curve C and D in 5.4 at low elevations and their impact on performances, in order to define a more accurate model than those presented with the LUT and LDT methodologies, an improvement could be made by setting a variable width for each satellite elevations bin with a width of 1°, from 5° to 15° and a larger width of 5° from 15° to 50° and 40° until 90° in the LUT methodology as sown in 6.3.1.1 and 6.4. Therefore, also 18 values of μ_{max} should be obtained. This methodology is more accurate than the LUT methodology presented in 6.3.1.1 and could be a good alternative to the LDT methodology without constraint about the angle mask in the DC case.

In this section, more sophisticated 3D NWMs were used for deriving the preferred LDT methodology (6.3.1.2) and the corresponding parameters for threating the horizontal component of the troposphere. Furthermore, in view of the vertical results found in previous section, the vertical ranging biases μ_{TC} were included into the innovative VPL computation with the LDT methodology (explained in 6.3.1.2 and Chapter 4 for NWMs). Their impact on performance appeared really small that could suggest they can be omitted.

Finally, NWMs was also be used to validate important assumptions made in this PhD project such as the fact that ranging biases conspired. Results showed that within this consideration only an increase of 2% is seen on PL value therefore, assuming this conspiring ranging biases is not so conservative and the lack of performance realized by making this assumption is really small

Chapter 7 : Conclusions and Future Work

This chapter presents the conclusions from the results obtained in the previous chapters and draws some perspectives for future work.

7.1 Conclusions

In this PhD work, key issues relating to GBAS were investigated to define an optimal MC/MF GBAS solution. Indeed, issues concerning the available space for message transmission from the GBAS VHF Data Broadcast (VDB) unit [4] were examined. One of the proposals described in this PhD work for an updated GBAS VDB message structure is to transmit corrections and integrity status of each corrections into separated messages and to send them at different transmission rates. As a matter of fact, the possibility of transmitting one message type containing corrections properly at a lower rate than the existing 2Hz and one message type containing integrity flags at the existing rate was discussed.

Also, in order to meet the most stringent requirements of Cat II/III precision approach operations, key issues must be solved relating to atmospheric modelling, therefore this PhD work contains also a specific analysis to the tropospheric modelling for both nominal and non-nominal cases. Then, a focus was made on how to compute the range troposphere delay within GBAS and on how to estimate the worst differential range troposphere delay in order to characterize the tropospheric threat model.

Previous work done by Ohio University to assess the anomalous troposphere, due to the horizontal decorrelation between aircraft and ground, uses a GPS data collection which is undersampling the possible geometries. Also, the proposed methodology appeared conservative and was constrained by the already defined data message format of the SF GPS GBAS. In the scope of MC/MF GBAS development, an alternative approach to assess fully the worst case horizontal component of the differential range tropospheric error was needed whilst maintaining a minimum data transmission load. That is why in this PhD project, by considering the possibility of providing additional data to the aircraft and changing of protection levels computation, an initial proposal was made known as Look-Up table Transmission (LUT) methodology which reduces the protection level (obtained with the existing methodology) of 10% with single constellation and 19% within dual constellation case. Then an improvement is obtained through the new Low Data Transmission (LDT) methodology with the aim of reducing the data

transmission load and finally another proposal is developed to improve the availability by developing a less conservative methodology under a new satellite geometry called Worst Satellites Subset (WSS) methodology.

Therefore by keeping in mind that low data transmission methodology is required and by comparing performance improvements obtained through all proposed techniques, the LDT methodology detailed in 6.3.1.2 should be preferred by assuming that ranging biases conspire in the worst possible way. Through this approach, in order to protect the user against non-nominal troposphere, a minimum of 3 parameters A, B and C has to be transmitted to the aircraft in the MT 2 at the rate of 0.1Hz (6 parameters if the cut-off angle is set at 10° in the DC case). Several options exist (presented and detailed in 6.5), either these parameters are standardized but that will rely on the capability of generating a global model, or these parameters should be set by NSP at each ground station. Also, if more simulations are processed, different model parameters could be defined (per location - regional settings) and a single index could be sent to the aircraft to select the model as it is made for other GBAS Designator (3.2.3.4.1 and Chapter 4). The issue with this last approach is to determine the appropriate levels for all regions (even unmodelled regions).

3D NWMs (Arome and Harmonie) were used firstly for deriving the preferred LDT methodology (6.3.1.2) and the corresponding parameters in Europe for treating the horizontal component of the differential range tropospheric delay but also for modelling its vertical component. Indeed, NWMs data were used to derive values of TC and $\sigma_{tropo}$for different locations and to conduct a statistical analysis for assessing the tropospheric correction. Then it was remarked that vertical differential ranging biases named μ_{TC} appeared which are not covered by the actual TC computation. These biases, in the slant domain, can reach high values up to 12cm so they seemed to be not negligible and have to be treated. Therefore, either the TC computation has to be modified as it was already suggested and studied by NLR into the SESAR project [108] or these ranging biases have to be bound as the same way as for non-nominal troposphere and included in the innovative VPL computation with the LDT methodology (explained in 6.3.1.2 and 6.4 for NWMs). This last option was chosen and analyzed in this PhD project. Impact of these ranging biases on performance appeared really small and could suggest that they can be omitted.

Moreover, the important differences between the two Curves C and D in 5.4.4 at low elevations and impact of these differences on performances in 6.4.1 have been remarked. Therefore, it is thought that a more accurate model than those presented with the LUT and LDT methodologies could be defined. Indeed it is possible to modify the LUT approach with a variable width for each satellite elevations bin in the look-up table, for example a width of 1°, from 5° to 15° then a larger width of 5° from 15° to 50° and finally a width of 40° until 90° could be chosen as shown in 6.3.1.1 and 6.4. This methodology is more accurate than the LUT methodology presented in 6.3.1.1 and could be a good alternative to the LDT methodology without constraint on the angle mask in the DC case.

Finally, NWMs was also used to validate an important assumption made in this PhD work such as the fact that ranging biases conspired. Under this hypothesis, results showed an increase on PL values up to 2%, then, the

approach of assuming these conspiring ranging biases is not so conservative and the lack of performance realized by making this assumption is really small.

So, this PhD work has initiated the process of assessing the troposphere threat by determining the optimal Dual Constellation (DC)/ Dual Frequency (DF) GBAS processing.

7.2 Perspectives for future work

In the scope of generating a global model or characterizing a region's model, more simulations should be processed in other areas. Therefore, a single index could be sent to the aircraft to select the model as it is made for other GBAS Designator (3.2.3.4.1 and Chapter 4) by considering the appropriate levels for all regions.

A validation step should be conducted to validate the methodology developed in this thesis for finding the worst case horizontal differential range tropospheric delay. A solution could be to process a full user grid search for all satellites in view for some specific epochs. This approach may take a long time to process and run but could validate properly the results found within this PhD work. Because of time constraints, this validation step has not been done yet.

Other validations tasks should be conducted as a mean of validating the LDT methodology. Therefore, other tools using for example GPS data could be used such as RTKLIB [136] for estimating the range tropospheric delay. Indeed, within the next years, this open source software should be able to process efficiency a Precise Point Positioning with an ambiguity resolution but for the moment, it is only at an experimental stage of development and it does not work fine. Therefore an accurate estimation of the range tropospheric delay should be possible, and this could help validating the LDT methodology developed in this PhD work.

Further analysis should be done regarding the improvement which could be made within the LUT methodology by setting a variable width for each satellite elevations bin with a width of 1°, from 0° to 10° and a larger width of 5° from 10° to 30° and 20° until 90° in the LUT methodology.

References

[1] ICAO, International Standards and Recommended Practices, Annex 10 to Convention on International Civil Aviation, Volume I, Radio Navigation Aids, Sixth edition (including Amendment 85 Dated July 12, 2010), July 2006.

[2] FANS Commitee, *Report of the fourth meeting of the Special Commitee for the monitoring and Co-ordination of Development and Transition Planning for the FANS Phase II, Doc 9623.*

[3] ICAO, Annex 10 to the Convention on the Internation Civil Aviation Volume I (Radio Navigation Aids), 5th Edition, Amendment 83, 2007.

[4] F. Beck, O. Glaser and B. Vauvy, "Standards – Draft Standards for Retained Galileo GBAS Configurations".

[5] D. W. Diggle, "An investigation into the use of Satellite Based positioning systems for flight reference/autoland operations," Ohio, 1994.

[6] F. Van Graas, V. Krishnan, R. Suddapalli and T. Skidmore, "Conspiring Biases in the LAAS," in *ION 60th Annual Meeting/U.S Air force institute os Technology & the U.S Air force Research Laboratory*, Dayton,OH, 2004.

[7] F. Van Graas and Z. Zhu, "Tropospheric Delay Threats for the GBAS," in *ITM of the ION*, San Diego, CA, 2011.

[8] M. Roelandt, "PBN fleet equipage according to FPL content," in *RAiSG/PBN TF meeting*, 2014.

[9] J. Burns, ICAO NSP - Conceptual Framework for the proposal for the Proposal for GBAS to Support CAT III Operations, draft version 6.5, ICAO NSP WGW, November 2009.

[10] ICAO NSP WGW WP 16, "Observed Nominal Atmospheric Behavior Using Honeywell's GAST D Ionosphere Gradient Monitor," Montreal, 2014.

[11] SESAR, "sesarju," 2009. [Online]. Available: http://www.sesarju.eu.

[12] "Fly GLS, GBAS Approach and landing systems, the future of precision approach," [Online]. Available: http://flygls.net/.

[13] Thales, "GBAS CAT II/III L1 Approach, CAT II-III L1 as a step to multiconstellation GBAS,D05," 2006.

[14] A. Van Dierendonck, "Benefits and limitations of new gnss signal designs," Toulouse, 2014.

[15] FAA, "faa.gov," [Online]. Available: http://www.faa.gov/about/office_org/headquarters_offices/ato/service_units/techops/navservices/gnss/laas.

[16] RTCA Inc., Minimum Operational Performance Standards (MOPS) for GPS Local Area Augmentation System (LAAS) Airborne Equipment - RTCA DO-253C, Washington DC, 2008.

[17] ICAO, Performance-based Navigation (PBN) Manual, Third Edition, 2008.

[18] RTCA Inc. , " http://www.rtca.org," October 2010. [Online].

[19] EUROCAE, " http://www.eurocae.net," Oct 2010. [Online].

[20] EASA, CS AWO 1, Joint Aviation Requirements – All Weather Operations, Subpart 1, Automatic Landing Systems, 2003.

[21] CICTT, Phases of flight definitions and usage notes,Commercial Aviation Safety Team/International Civil Aviation Organization,Common Taxonomy Team, Feb. 2006.

[22] Macabiau, Analysis of the Feasibility of Using GPS Carrier Phase Ambiguity Resolution Techniques for Precision Approaches, PhD thesis, Institut National Polytechnique de Toulouse, Sep. 1997.

[23] ICAO, International Standards and Recommended Practices, Annex 6 to Convention on International Civil aviation, Operation of aircraft, Eight edition, Jul. 2001.

[24] L. Montloin, Impact of GNSS singular events on the integrity of airport navigation systems, Toulouse, 2014.

[25] B. D. H. Cabler, " LPV : New, Improved WAAS Instrument Approach," *Proceedings of ION GPS 2002,* 2002.

[26] P. Neri, PhD thesis : Use of GNSS signals and their augmentations for Civil Aviation navigation during Approaches with Vertical Guidance and Precision Approaches.

[27] RTCA Inc., MASPS for LAAS - RTCA DO-245A, Washington DC, 2004.

[28] W. Schuster and W. Ochieng, "Harmonisation of Category-III Precision Approach Navigation System Performance Requirements," *THE JOURNAL OF NAVIGATION,* 2010.

[29] O. Julien, Advanced Concepts of GNSS-IENAC 3rd year, 2011/2012.

[30] GPS Directorate, "Global Positioning System Directorate Systems engineering ans integration interface specification, IS-GPS-200," 2011.

[31] US Air Force Departement, "GPS.GOV," 2016. [Online]. Available: http://www.gps.gov/systems/gps/space/.

[32] A. Martineau, Perfomance of Receiver Autonomous Integrity Monitoring (RAIM) for Vertically Guided Approaches, PhD thesis, Institut National Polytechnique de Toulouse, Nov. 2008.

[33] Department of Defense USA, GPS NAVSTAR, GPS SPS PS, 2008.

[34] Federal Space Agency - IAC, "IAC official Website," 2016. [Online]. Available: https://www.glonass-iac.ru/en/.

[35] ESA.int, "The Future - GALILEO," 2015. [Online]. Available: http://www.esa.int/Our_Activities/Navigation/The_future_-_Galileo/What_is_Galileo.

[36] BeiDou.gov, "BeiDou Navigation Satellite System," [Online]. Available: http://en.beidou.gov.cn/.

[37] A.-C. Escher, GNSS integrity course notes, 2011.

[38] C. Macabiau and C. Milner, GNSS integrity monitoring, ENAC, Prague, 2014.

[39] J. Celada, D. Pérez, J. Perocacho, J. Lera, M. Fernandez, J. Barrios, J. Ostolaza and J. Caro, "Multi-Constellation, Dual-frequency SBAS," in *ION GNSS 2015*, Tampa (FL), 2015.

[40] F. Belloir, *Airbus status on SBAS, EGNOS Service Provision Worshop,* Copenhagen, 2015.

[41] RTCA.Inc, RTCA DO-246D - GNSS-Based Precision Approach Local Area Augmentation System (LAAS) Signal-in-Space Interface Control Document (ICD), 2008.

[42] RTCA, "Minimum Operational Performance standards for GPS Local Area Augmentation System Airborne Equipment, DO-253C, RTCA SC-159," 2008.

[43] C. Milner, "GNSS for Civil Aviation, course notes".

[44] Thales, "SESAR JU - GBAS cat II/III L1 approach- D07 - 15.03.06".

[45] FAA/NAVTAC, "Extended Service Volume Operational Requirements, IGWG SG4," 2013.

[46] A. Lipp, "Ground Based Augmentation Systems (GBAS) Introduction,Technical and Operational Overview,," in *GBAS Implementation Workshop, ICAO EUR/NAT Paris,* , Paris, 18 March 2010.

[47] SESAR JU, "D3.6.1 Measurement Processing ST3.6 Initial Processing Options, Project 15.3.7," 2014.

[48] Anon., Navstar GPS Space Segment/Navigation User L1C interfaces (IS-GPS-800C),U.S Air force, Global Positioning System Directorate, El segundo,CA, 2012.

[49] A. Tetewsky, J. Ross, A. Soltz, N. Vaughn, J. Anszperger, C. O'Brien, D. Graham, D. Craig and J. Lozow, "Making sense of Inter-Signal Corrections," *Inside GNSS,* pp. 37-48a, 2009.

[50] ICAO, Beidou ICD NSP WGW IP8, Montreal, 2013.

[51] IGS, "IGS," [Online]. Available: IGS.org.

[52] SESAR(JU), "Satellite constellations and Signals - Int ST3.3-WP15.03.07 Multi GNASS CAT II/III GBAS," 2014.

[53] W. Gurtner and L. Estey, RINEX: The Receiver Independent Exchange Format Version 2.11, 2007.

[54] A. LEICK, "GPS Satellite Surveying," in *Wiley-Interscience, 2nd edition*, 1995.

[55] ESA.int, "Ionospheric Delay," [Online]. Available: http://www.navipedia.net/index.php/Ionospheric_Delay.

[56] J. KLOBUCHAR, "Ionospheric time-delay algorithm for single-frequency GPS users," *IEEE transactions on Aerospace and Electronic Systems,* 1987.

[57] ARINC Engineering Services, Navstar GPS Space Segment/Navigation User Interfaces, IS-GPS-200 Revision D, 2004.

[58] B. Arbesser-Ratsburg, "The GALILEO Single Frequency Ionospheric Corection Algorithm," in *Third European Space Weather Week*, November, 2006.

[59] GJU-GALILEO Joint Undertaking, European GNSS (GALILEO) Open Service, Signal In Space Interface Control Document (OS SIS ICD), Issue 1.1, Sept. 2010.

[60] Egis avia, EUROCONTROL'S FUNDED STUDY,STUDY ON THE IMPACT OF SOLAR ACTIVITIES ON AVIATION APPLICATIONS BASED ON GNSS OVER ECAC, D2.2 final work plan, 2010.

[61] T. Schuler, PhD Thesis, On ground based GPS tropospheric delay estimation, 2001.

[62] C. Andrei and C. Ruizhi, Tropospheric Delay estimation based on NWM, 2007.

[63] RTCA, "Minimum Operational Performance Standards for Global Positioning System/Wide Area Augmentation System Airborne Equipment, DO229-D,RTCA SC-159," 2006.

[64] EUROCAE WG-62, "Interim Minimum Operational Performance Specification for Airborne GALILEO Satellite Receiving Equipment, version 0.26," 2007.

[65] H. S. Hopfield, Two-quartic Tropospheric refractivity profile for correcting satellite data, 1969.

[66] J. Saastamoinen, Contributions to the theory of atmospheric refraction, 1973.

[67] I. Ifadis, The atmospheric delay of radio waves.Modeling the elevation dependence on a global scale, Goteborg, 1986.

[68] J. Dousa and M. ELias, "An improved model for calculating tropospheric wet delay," *AGU publication/Geophysical Research letters,* pp. 4389-4397, 2014.

[69] C. Macabiau, M. Raimondi, L. Moriella, C. Dupouy, A. Steingass and A. Lehner, "GNSS Airborne Multipath Errors Distribution Using the High Resolution Aeronautical Channel Model and Comparison to SARPS Error Curve," in *Proceedings of ION NTM*, 2006.

[70] J. Booth, T. Murphy, B. Clark and F. Liu, "“Validation of the Airframe Multipath Error Allocation for Local Area Differential GPS”," in *Proceedings of the IAIN/ION Meeting*, June 2000.

[71] T. Murphy and J. Booth, ""GBAS SARPs Review and Validation of Airborne Multipath Requirements"," in *GNSSP WG B*, Canberra, Jan. 2000.

[72] A. Steingass, A. Lenher, F. Perez-Fontan, E. Kubista, M. J. Martin and B. Arbesser-Rastburg, ""The High Resolution Aeronautical Multipath Navigation Channel"," in *Proceedings of ION GPS*, 2004.

[73] RTCA.Inc., "Minimum Operational Performance Standards for GNSS Airborne Active Antenna Equipment for the L1 frequency Band - DO-301," 2006.

[74] A. Raghuvanshi and F. Van Graas, "Characterization of Airborne Antenna Group Delay Biases as a Function of Arrival Angle for Aricraft Precision Approach Operations," 2015.

[75] J. Spilker, GPS: Theory and Application, Volume 1, 1996.

[76] R. R. Hatch, "The Synergism of GPS Code and Carrier measurements," *Proceedings of the Third International Geodetic Symposium on Satellite Doppler Positioning, New Mexico, II,* pp. 1213-1232, 1982.

[77] P. Y. Hwang, G. A. McGraw and J. R. Bader, "Enhanced Differential GPS Carrier-Smoothed Code Processing Using Dual-Frequency Measurements," *Journal of The Institute of Navigation,* vol. 46, no. 2, 1999.

[78] RTCA,Inc., DO-246D,GNSS based precision approach LAAS Signal-in-Space ICD, 2008.

[79] EUROCAE, "MOPS for Global Naviagation Satellite Ground Based Augmentation System ground equipment tp support Category I operations, ED 114," 2012.

[80] A. Van Dierendonck, "What is h_0," 1998.

[81] S.-M. Circiu, M. Felux, P. Remi, Yi Lai, B. Belabbas and Pullen Sam, "Evaluation of DF GBAS Performance using Flight Data".

[82] T. Murphy, M. Harris and S. Beauchamp, "Implications of 30-Second Smoothing for GBAS Approach Service Type D," in *ION 2010 International Technical Meeting*, San Diego, CA, 2010.

[83] B. Belabbas, P. Remi and M. Meurer, "Performance Assessment of GBAS Cat III using GPS and Galileo," in *ION GNSS 08*, Savannah,CA, 2008.

[84] RTCA Inc., MASPS for LAAS - RTCA DO-245A, Washington DC, 2004.

[85] A. Zappavigna, "Galileo Phase B2C UERE Budget Results," 2002.

[86] G. A. McGraw, T. Murphy, M. Brenner, S. Pullen and A. Van Dierendonck, "Development of LAAS accuracy Models," in *ION GPS 2000*, Salt Lake City (UT), 2000.

[87] SESAR JU, D03 , SESAR 15.3.6 - High Performance Allocation and Split of Responsibilities between Air and Ground.

[88] ICAO, "NSP, Proposed amendments to Annex 10 GBAS provisions," Montreal, 2015.

[89] H. Konno, S. Pullen, J. Rife and P. En, "Evaluation of Two Types of Dual-Frequency Differential GPS Techniques underAnomalous Ionosphere Conditions," in *ION NTM 06*, 2006.

[90] P. Y. HWANG, G. A. MCGRAW and J. R. BADE, "Enhanced Differential GPS Carrier-Smoothed Code Processing Using Dual-Frequency Measurements," *Journal of The Institute of Navigation,* p. Vol 46 numero 2, 1999.

[91] B. Vauvy and O. Glaser, "STANDARDS-Company-2600-D-2610-PU-V1., GSA/OP/07/07 - Analysis of GBAS standardisation options," 2010.

[92] SESAR JU, "VDB Transmission Intermediate Status," 2015.

[93] A.-C. Escher, GNSS Integrity,IENAC 09L, 2011.

[94] D. Salos, PhD, Integrity monitoring applied to the reception of GNSS signals in urban environments, toulouse, 2012.

[95] P. Ladoux, The GBAS , course document ENAC CNS Master, Toulouse, 2011.

[96] S. Pullen and P. Enge, "An overview of GBAS integrity monitoring with a focus on ionospheric spatial anomalies," *Indian Journal of Radio and Space Physics,* vol. 36, pp. 249-260, 2007.

[97] A. Martineau, SiS integrity concept, course document for ENAC CNS Master, 2011.

[98] L. Azoulai, F. Souchon, C. Brunet, A. Lipp and D. Duchet, "GBAS GAST D Parametric Study and Availability Simulations to support Category III operations," in *ION 2012*, Nashville,TN, 2012.

[99] M. Stanisak, R. Schork, M. Kujawska, T. Feuerle and P. Hecker, "Conception, Implementation and Validation of a GAST-D Capable Airborne Receiver Simulation," in *ION GNSS 2012*, NAshville, Tennessee, 2012.

[100] C. A. Shively and T. T. Hsiao, "Availability of GAST D GBAS considering continuity of airbrone monitors," Center for advanced aviation system development, the MITRE corporation, McLean VA, 2009.

[101] SESAR JU, "15.3.6 D03High Level Performance Allocation and Split of responsabilities between Air and Ground," 2012.

[102] M. Felux, M.-S. Circiu, B. Belabbas, M. Meurer, M. Stanisak, C. Milner, Y. Jiang, A. Guilbert and A. Lipp, "Concept for a Dual Frequency Dual Constellation GBAS," in *ION GNSS+*, Tampa (FL), 2015.

[103] T. Walter, J. Blanch and P. Enge, “Implementation of the L5 SBAS MOPS,” in *ION GNSS 2013*, 2013.

[104] A. F. Ken, J. Mcdonald and B. Johnson, "ICAO/NSP/WGW WP16, Observed Nominal Atmospheric Behavior using honeywell's GAST D Ionosphere Gradient Monitor, CSG meeting," Montreal, 2014.

[105] C. Milner, A. Guilbert and C. Macabiau, "Evolution of Corrections Processing for MC/MF GBAS," in *ION ITM 2015*, Dana Point (CA), 2015.

[106] M.-S. Circiu, M. Felux, P. Remi, L. Yi, B. Belabbas and S. Pullen, "Evaluation of Dual Frequency GBAS Performance using flight Data," *ITM 2014.*

[107] A. Guilbert, C. Milner and C. Macabiau, "Optimal Processing Scheme for meeting CAT II/III with MC/MF GBAS," in *NAVITEC 2014*, ESA/ESTEC - Noordwijk - The Netehrlands, 2014.

[108] SESAR JU, "ST 3.6.4.2, Nominal and Anomalous Tropospheric modelling for GBAS GAST-F," 2015.

[109] RTCA.Inc, RTCA DO-246D - GNSS-Based Precision Approach Local Area Augmentation System (LAAS) Signal-in-Space Interface Control Document (ICD), 2008.

[110] ICAO, "NSP- Review and Validation of GBAS GAST-D SARPs," Montreal, 2015.

[111] ICAO, "NSP-Sesar GAST-D verification strategy and status of ground verification results," Montreal, 2014.

[112] B. Pervan, S. Pullen and I. Sayim, "Sigma etimation, Inflation and Monitoring in the LAAS Ground System," in *ION GPS 2000*, Salt lake city, 2000.

[113] J. Rife and S. Pullen, "The Impact of Measurement Biases on Availability for CAT III LAAS," in *ION*, 2005.

[114] T. Skidmore and F. Van Graas, "An Investigation of Tropospheric Errors on Differential GNSS accuracy and Integrity," in *Ion GNSS* , Long Beach (CA), 2004.

[115] G. Xu, GPS Theory, Algorithms and Applications, Springer, 2007.

[116] R. Suddapalli, Aircraft Position Integrity for Differential Satellite Based Navigation in presence of both biases and noise errors, Ohio, 2004.

[117] NSP working group, GBAS CAT II/III Development Baseline SARPs, 2010.

[118] Mr.Brousseau, *Personnal Correspondance,* Toulouse, 2016.

[119] ECMWF, "ECMWF," [Online]. Available: www.ecmwf.int/.

[120] "HIRLAM," [Online]. Available: http://hirlam.org/index.php/hirlam-programme-53/general-model-description/mesoscale-harmonie.

[121] Y. Seity, P. Brousseau, S. Malardel, G. Hello, P. Benard, F. Bouttier, C. Lac and V. Masson, The AROME-France Convective-Scale Operational Model, toulouse, 2010.

[122] J. Spilker, Tropospheric Effects on GPS (GPS Theory and Applications Vol.1), 1996.

[123] R. Langley, The GPS observables,GPS world, 1993.

[124] T. Schuler, On Ground Based GPS Tropospheric Estimation, Munchen, 2001.

[125] H. Hopfield, Tropospheric Range Error parameters : Further studies, 1972.

[126] Rocken, S. Sokolovskiy, J. Johnson and D. Hunt, "Improved mapping of tropospheric delays," *Journal of Atmospheric and Oceanic technology,* vol. 18, no. 7, pp. 1205-1213, 2001.

[127] SESAR JU, "ST3.6.4.2 - Nominal and anomalous tropospheric modelling for GBAS GAST-F," 2015.

[128] J. Huang, F. Van Graas and C. Cohenour, "Characterization of Tropospheric Spatial Decorrelatin Errors over 5km baseline," *Navigation: Journal of Navigation ,* vol. 55, no. 1, 2008.

[129] S. Khanafseh, M. Joerger, B. Pervan and A. Von Engeln, "Accounting for Tropospheric Anomalies in High Integrity and high Accuracy Positionning Applications," in *24th ITM*, Portland(OR), 2011.

[130] *Private discussions with F. Van Graas,* 2015.

[131] J. Seo, J. Lee, S. Pullen, P. Enge and S. Close, "Targeted Parameter Inflation within GBAS to minimize anomalous Ionospheric Impact," *Journal of aircraft,* vol. 49, no. 2, p. 587, 2012.

[132] RTCA,Inc., DO-229D, Mininum Operational Performance Standards for Global Positioning System/Wide Area augmentation System Airborne Equipment, Washington, 2006.

[133] PosiTim, "High Accuracy GNSS Solutions and Services, GNSS overview," october 2009. [Online]. Available: http://www.positim.com/navsys_overview.html.

[134] ESA, "esa.int/Galileo System," 17 Aout 2007. [Online]. Available: http://www.esa.int/Our_Activities/Navigation/The_future_-_Galileo/Galileo_system/%28print%29.

[135] RTCA,Inc., Minimum Aviation system performance, standards for LAAS,DO-245A, December 2004.

[136] T. TAKASU, "RTKLIB:An Open Source Program Package for GNSS Positioning," 2007. [Online]. Available: http://www.rtklib.com/rtklib.htm.

[137] FAA, FAA Advisory Circular 120-28D, “Criteria for Approval of Category III Weather Minima for Takeoff, Landing and Rollout, Jul. 13, 1999.

[138] Cabinet Office, Government of Japan, "QZSS," 2016. [Online]. Available: http://qzss.go.jp/en/.

[139] Indian Space Research Organisation, "IRNSS Programme," 2016. [Online]. Available: http://www.isro.gov.in/irnss-programme.

[140] N. Klenshe, "ainonline," 18 may 2014. [Online]. Available: wwww.ainonline.com. [Accessed May 2016].

[141] W. B. III, "aviationtoday," 04 02 2016. [Online]. Available: http://www.aviationtoday.com/av/commercial/Australia-ADS-B-Mandate-Now-in-Operation-at-Perth_87102.html#.VycFHXonZ08.

Appendix A : Other scenarios for computing Anomalous Tropospheric delays

A.1 Ohio Assumption for Number of Visible Satellites

Same considerations and assumptions are made in this part as in the section 6.3.1.1.2 except for the number of visible satellites. Indeed, in this section the assumption of N is equal to 6 satellites for GPS constellation and equal to 12 for GPS and Galileo constellations is made (as mentioned in 5.2.1.1.)

On the following figures different results are represented in different colors for both the GPS constellation (on the figure above) and the GPS and Galileo constellations (on the figure below) with a $(\mathrm{D_{TH}})$ of 5km in the first part and for $(\mathrm{D_{TH}})$ of 10km :

- VPL_{inf} with non-nominal troposphere computed with the inflation methodology is represented in **red**
- VPL_c computed by adding the exact value of VPL_n and VPL_b is represented in **black**
- VPL_n representing VPL without non-nominal troposphere is represented in **purple**
- VPL_{LUT} computed with the LUT methodology (presented in 6.3.1.1.1) is represented in **green**
- VPL_{LDT} computed with the LDT methodology is represented in **yellow**

A.1.1 D_{th}= 5km

Results for GPS constellation with N set at 6 visible satellites are represented in the figure below:

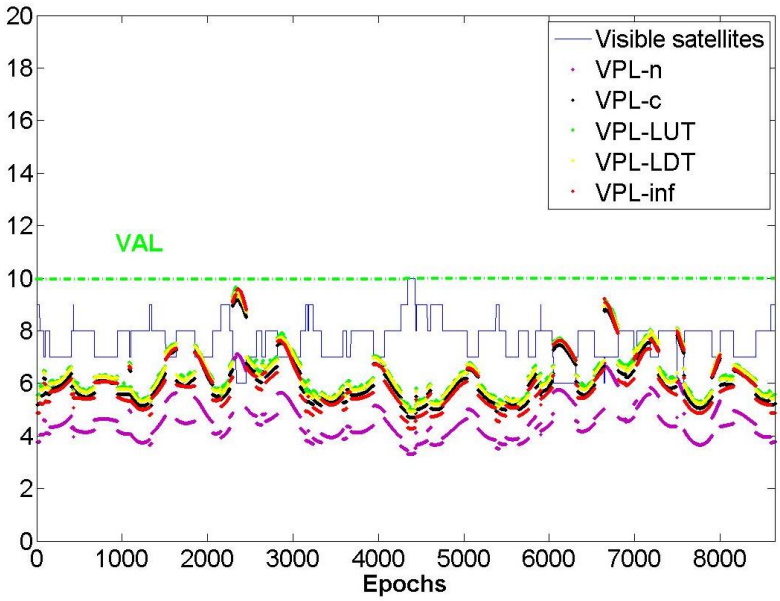

Figure 142-VPLs Seattle Dth=5km, GPS N=6

Results for GPS and Galileo constellations with N set at 12 visible satellites are represented in the following figure:

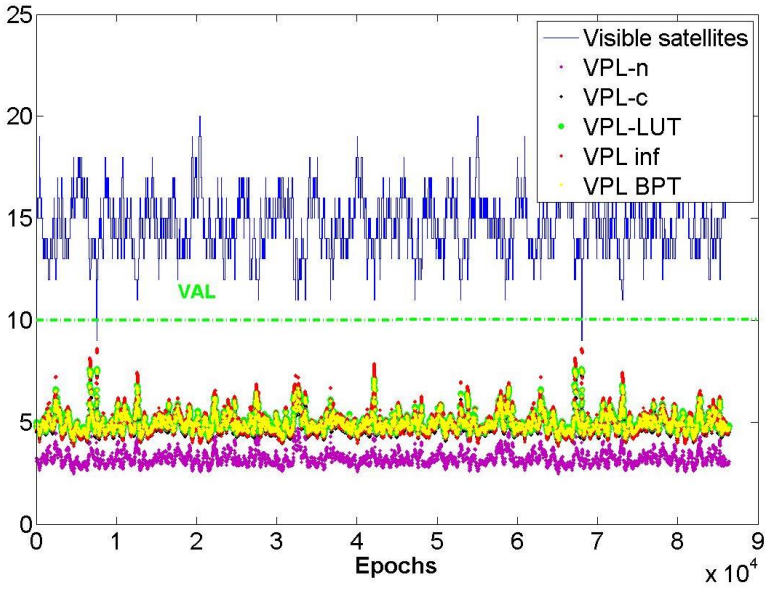

Figure 143-VPLs Seattle Dth=5km, GPSand GAL N=12

A.1.2 D_{th} = 10km

Results for GPS constellation with N set at 6 visible satellites are represented in the figure below:

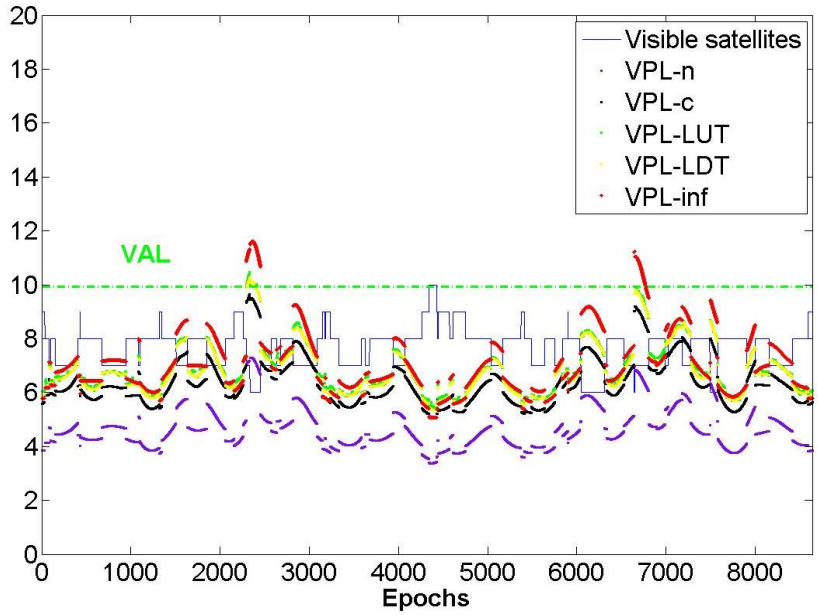

Figure 144-VPLs Seattle Dth=10km, GPS N=6

Results for GPS and Galileo constellations with N set at 12 visible satellites are represented in the following figure:

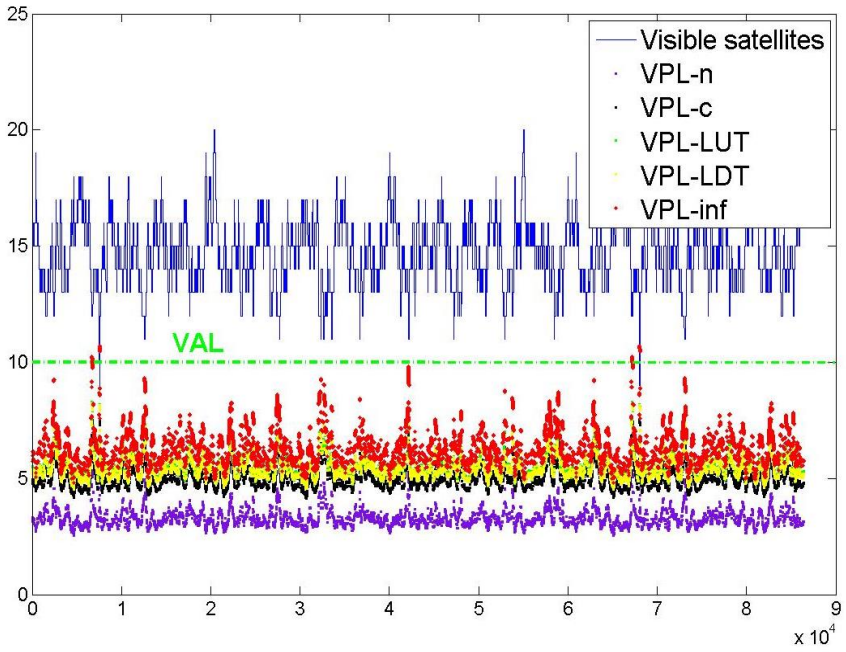

Figure 145-VPLs Seattle Dth=10km, GPS and GAL N=12

A.2 Other points along the Approach for Seattle Airport with D_{th}=5 km

Same considerations and assumptions are made in this part as in the section 6.3.1.1.2 except for the distance from runway threshold to the aircraft. Indeed, five key points along the approach defined either by the distance from A/C to Runway Threshold (D) of 20NM and 10NM or by the Altitude of A/C (h) of 200ft, 100ft and 0ft.

In this section results are presented for D equal to 20NM and 10NM or for the Altitude of A/C (h) of 100ft and 0ft.

On the following figures different results are represented in different colors for both the GPS constellation (on the figure above) and the GPS and Galileo constellations (on the figure below)

- VPL_{inf} with non-nominal troposphere computed with the inflation methodology is represented in **red**
- VPL_c computed by adding the exact value of VPL_n and VPL_b is represented in **black**
- VPL_n representing VPL without non-nominal troposphere is represented in **purple**
- VPL_{LUT} computed with the LUT methodology (presented in 6.3.1.1.1) is represented in **green**
- VPL_{LDT} computed with the LDT methodology is represented in **yellow**

A.2.1 D=20NM

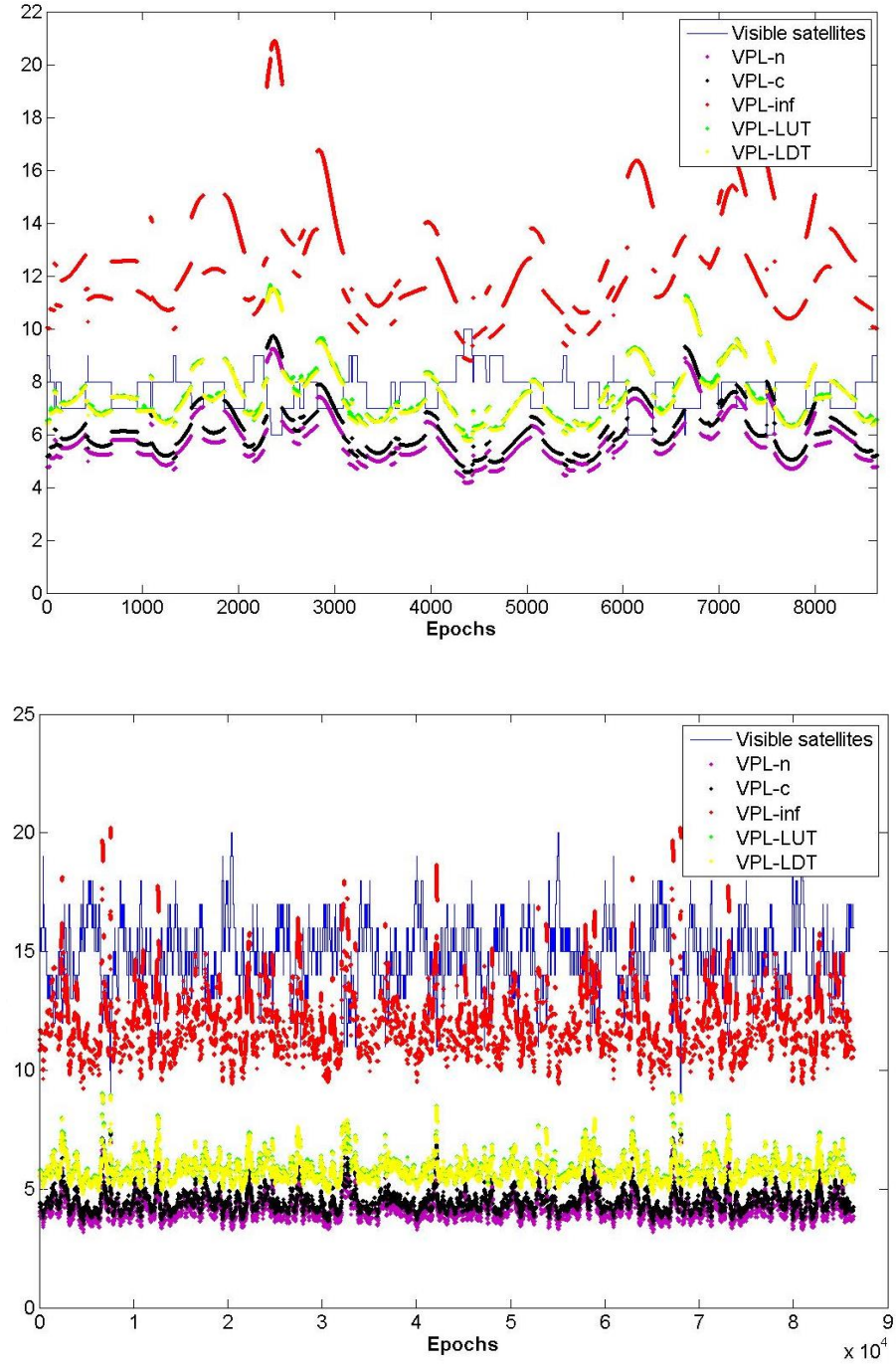

Figure 146-VPLs Seattle, D=20NM, Dth=5km, GPS (figure above) and GPS and GAL(figure below)

A.2.2 D=10NM

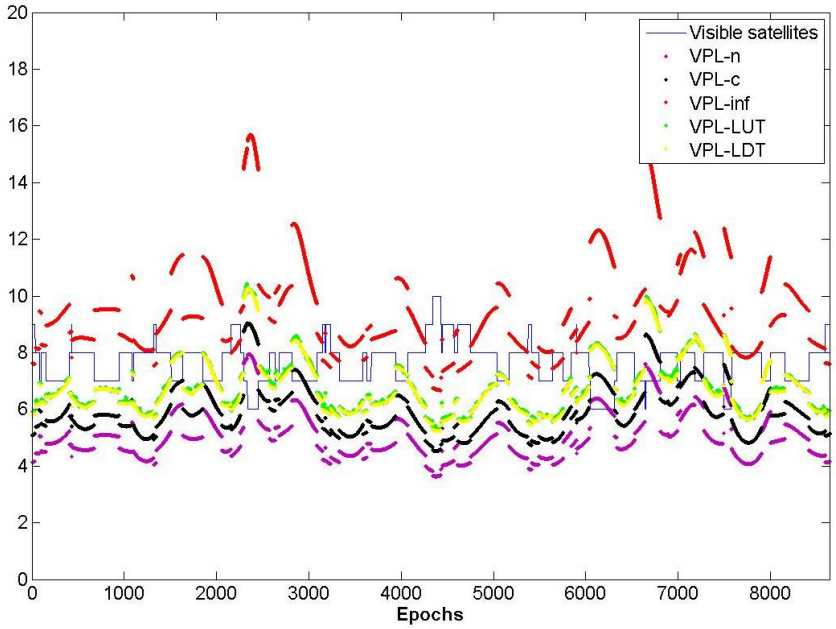

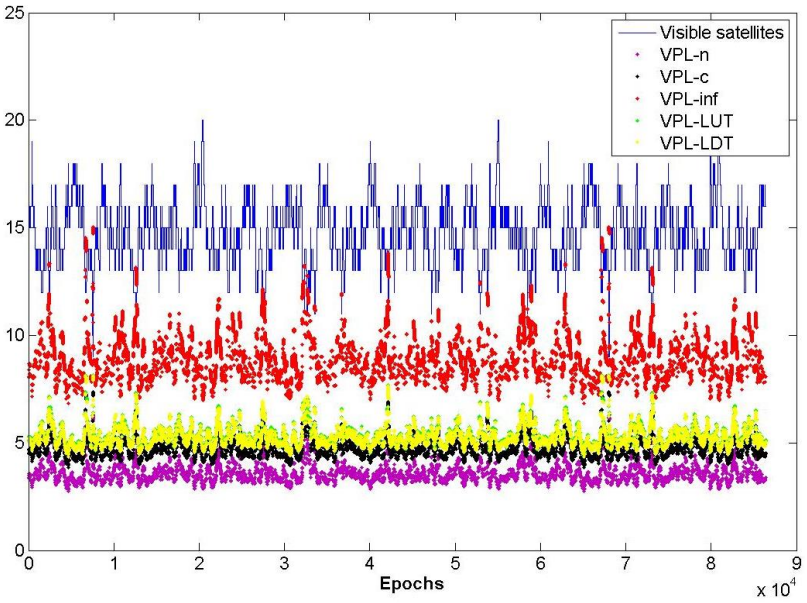

Figure 147-VPLs Seattle, D=10NM, Dth=5km, GPS (figure above) and GPS and GAL(figure below)

A.2.3 H=100ft

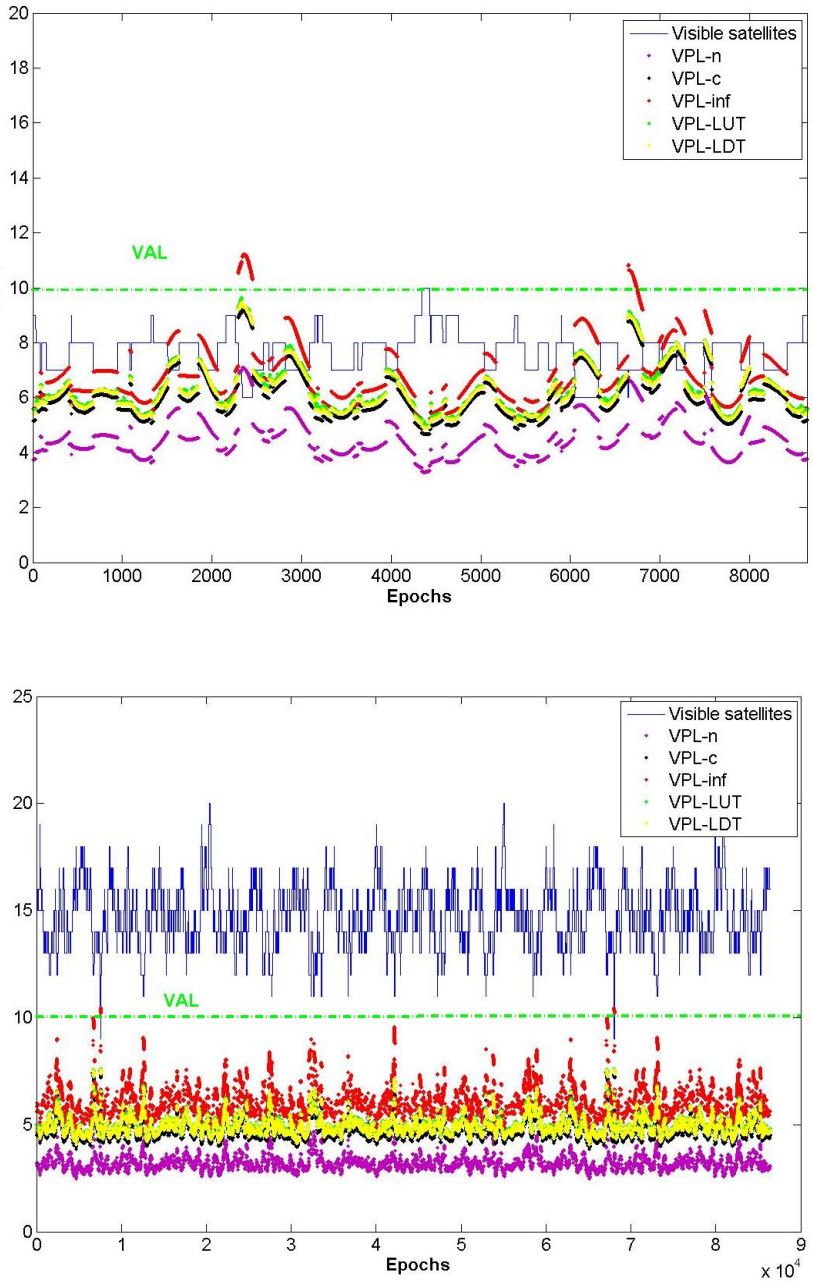

Figure 148-VPLs Seattle, h=100ft, Dth=5km, GPS (figure above) and GPS and GAL(figure below)

A.2.4 H=0ft

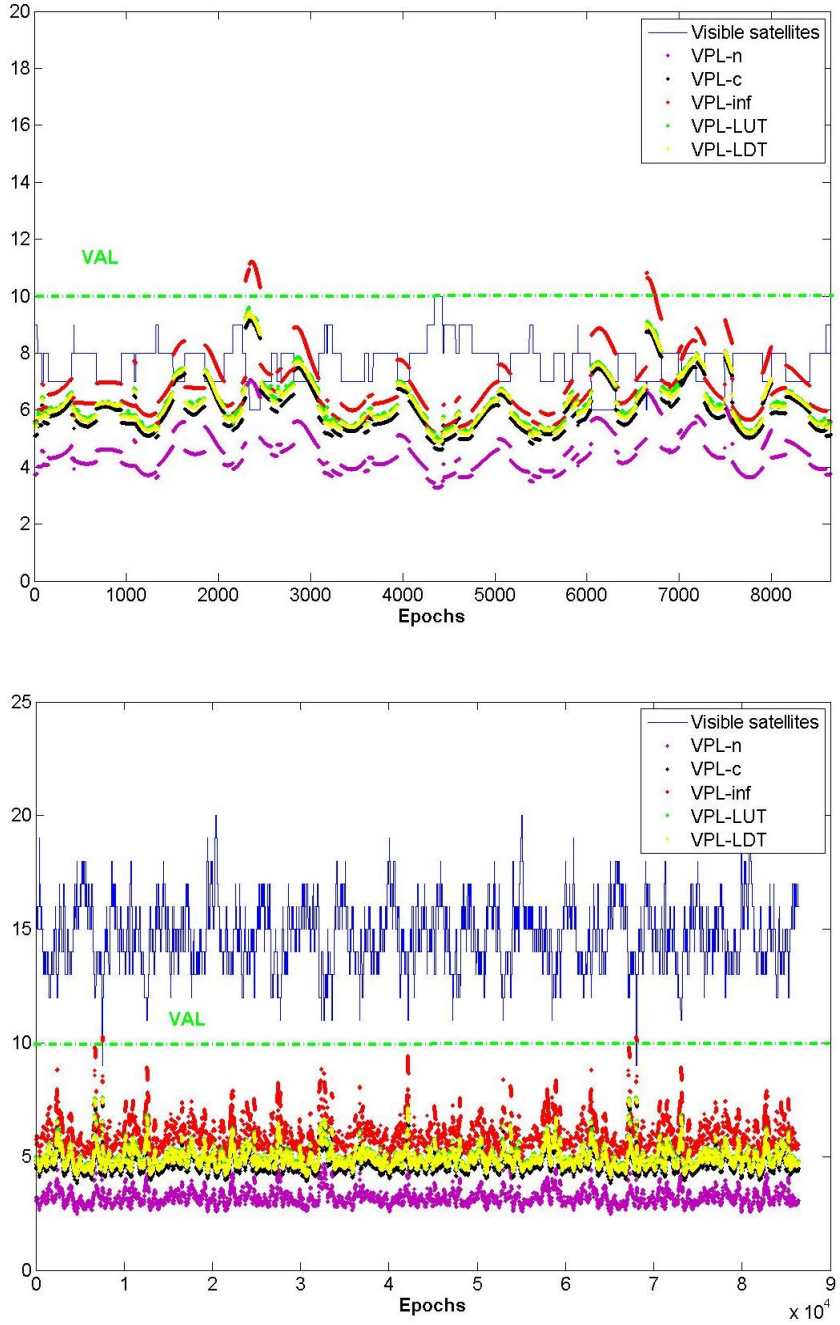

Figure 149-VPLs Seattle, h=0ft, Dth=5km, GPS (figure above) and GPS and GAL(figure below)

A.3 Seattle airport with D_{th} =10 km

Same considerations and assumptions are made in this part as in the section 6.3.1.1.2 except for the distance from ground station to runway threshold. Indeed, in this section the assumption for D_{TH} equal to 10km is made

On the following figures different results are represented in different colors for both the GPS constellation (on the figure above) and the GPS and Galileo constellations (on the figure below)

- VPL_{inf} with non-nominal troposphere computed with the inflation methodology is represented in **red**
- VPL_c computed by adding the exact value of VPL_n and VPL_b is represented in **black**
- VPL_n representing VPL without non-nominal troposphere is represented in **purple**
- VPL_{LUT} computed with the new proposed methodology (presented in 6.3.1.1.1) is represented in **green**
- VPL_{LDT} computed with the BPT methodology is represented in **yellow**

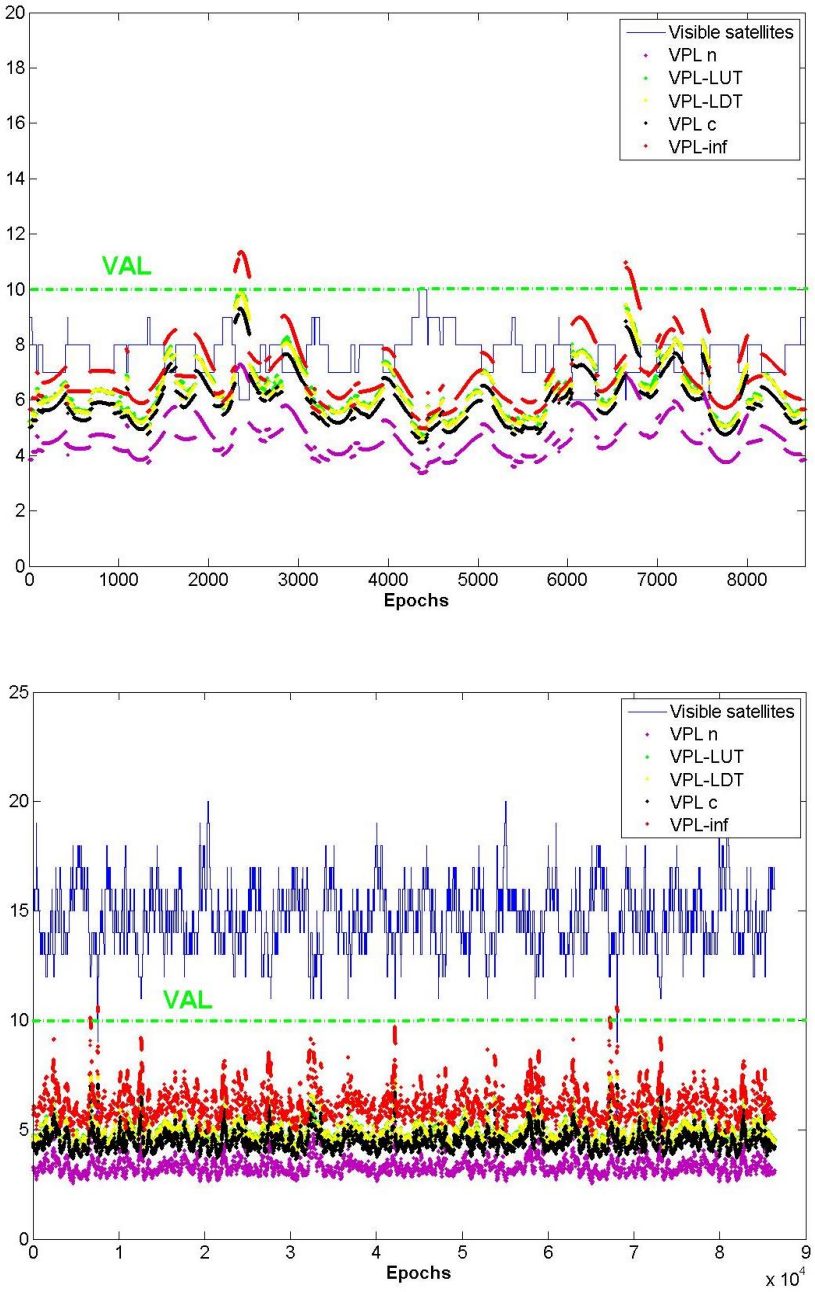

Figure 150-VPLs Seattle, GPS (left) and the GPS and GAL (right), Dth=10km

Then VPLs computed with the WSS methodology are computed as shown in 6.3.1.3, VPLs named VPL_{c-wss}, $VPL_{LUT-wss}$ and $VPL_{LDT-wss}$ are computed in the same way as VPL_c, VPL_{LUT} and VPL_{LDT} respectively but based on subset Q defining a new geometry-improved methodology.

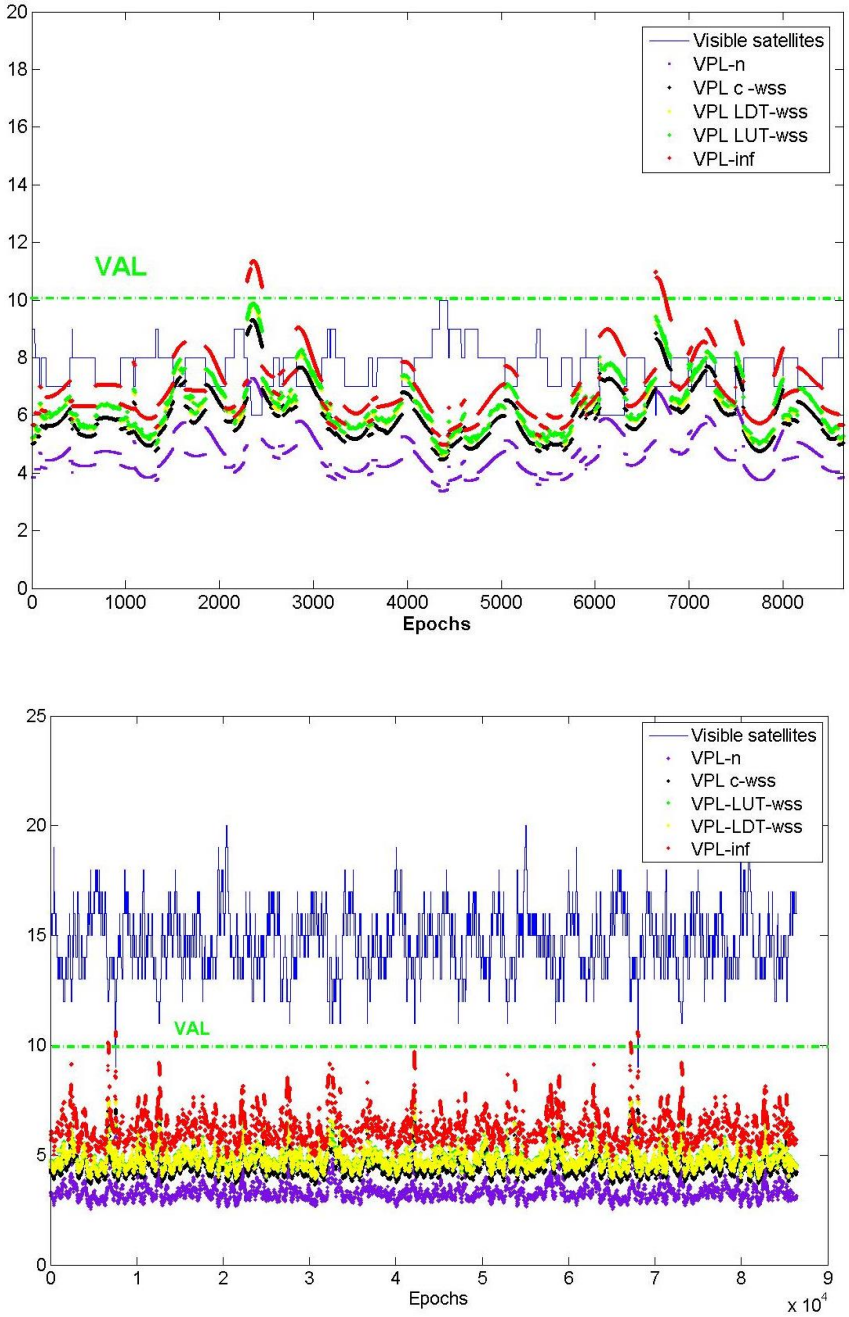

Figure 151-VPLs with WSS methodology for Seattle, GPS (left) and the GPS and GAL (right), Dth=10km

Appendix B : Different Airport Locations

Same considerations and assumptions are made in this part as in the section 6.3.1.1.2 except for the location. Indeed, in this section computations are made for Lat 0 airport, Miami airport and Anchorage Airport (as mentioned in 5.2.1.1.)

On the following figures different results are represented in different colors for both the GPS constellation (on the figure above) and the GPS and Galileo constellations (on the figure below) with a D_{TH} set at 5km and 10km:

- VPL_{inf} with non-nominal troposphere computed with the inflation methodology is represented in **red**
- VPL_c computed by adding the exact value of VPL_n and VPL_b is represented in **black**
- VPL_n representing VPL without non-nominal troposphere is represented in **purple**
- VPL_{LUT} computed with the LUT (presented in 6.3.1.1.1) is represented in **green**
- VPL_{LDT} computed with the LDT methodology is represented in **yellow**

B.1 LAT 0

B.1.1 Dth=5km

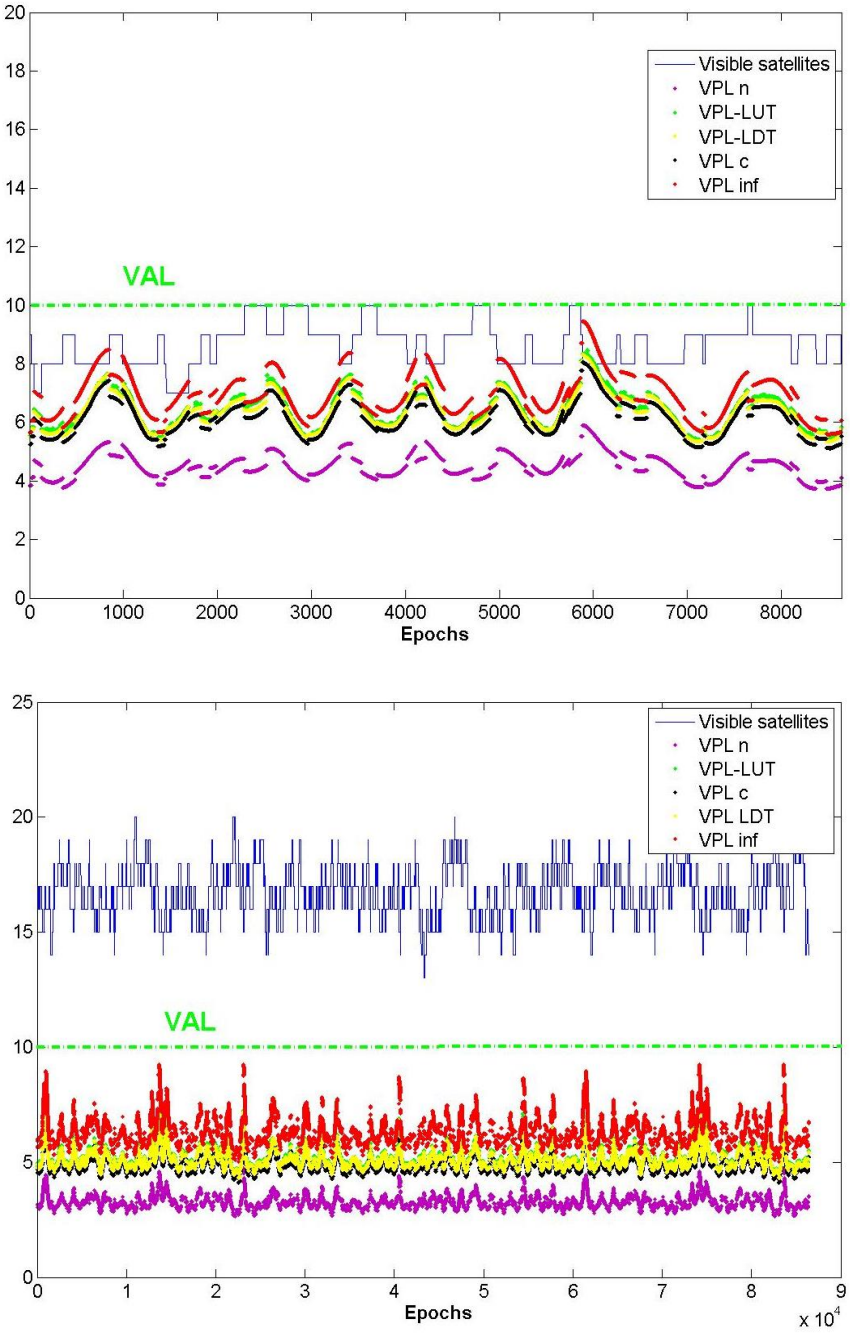

Figure 152-VPLs Lat0 GPS (left) and the GPS and GAL (right), Dth=5km

Then VPLs computed with the WSS methodology are computed as shown in 6.3.1.3, VPLs named VPL_{c-wss}, $VPL_{LUT-wss}$ and $VPL_{LDT-wss}$ are computed in the same way as VPL_c, VPL_{LUT} and VPL_{LDT} respectively but based on subset Q defining the WSS methodology.

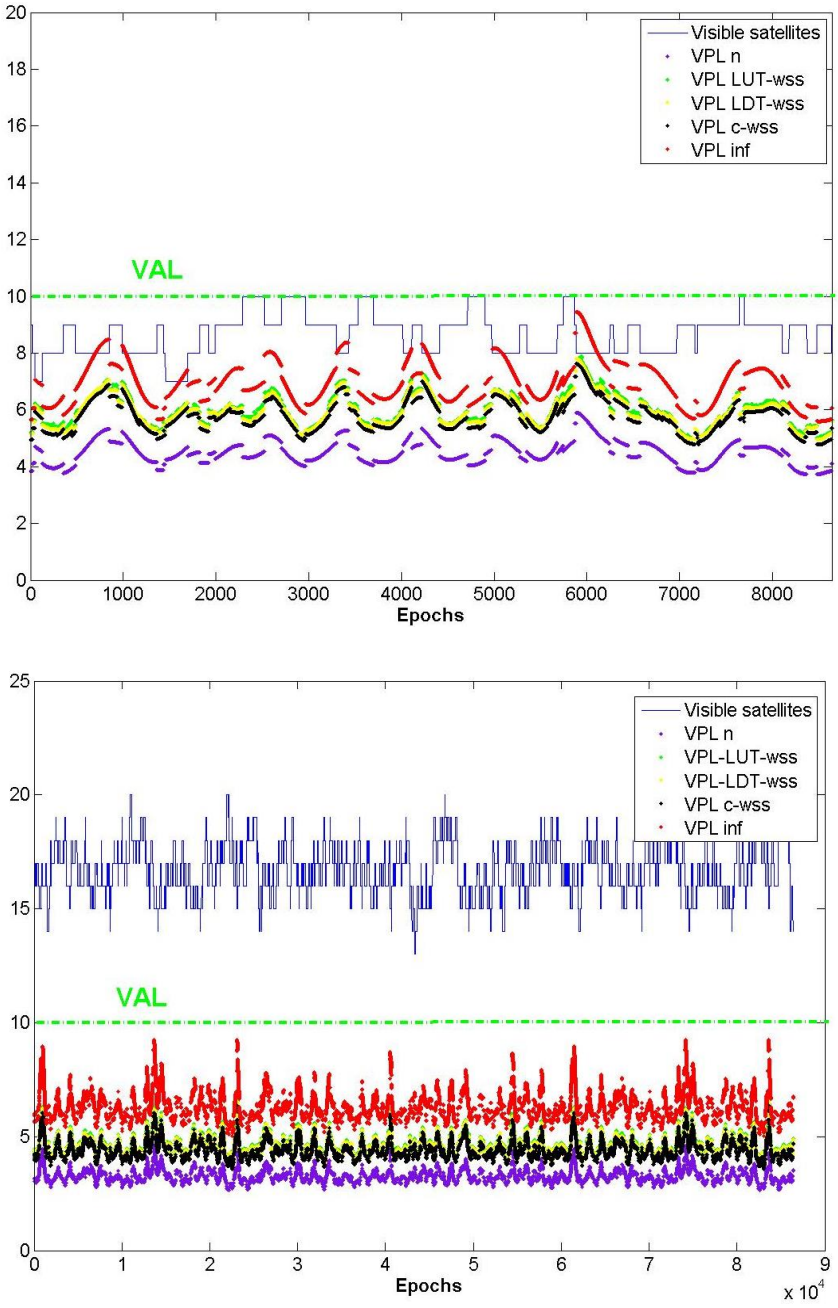

Figure 153-VPLs geometry improved Lat0 GPS (left) and the GPS and GAL (right), Dth=5km

B.1.2 Dth=10km

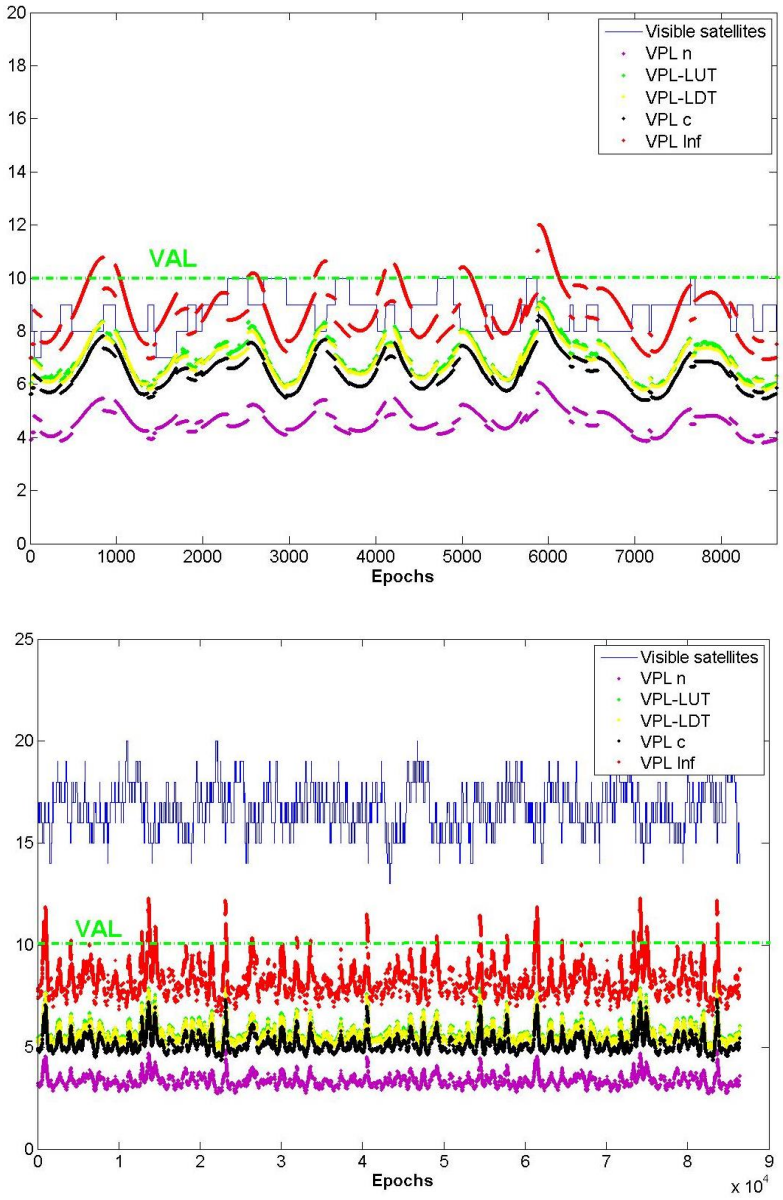

Figure 154-VPLs Lat0 GPS (left) and the GPS and GAL (right), Dth=10km

Then VPLs computed with the WSS are computed as shown in 6.3.1.3, VPLs named VPL_{c-wss}, $VPL_{LUT-wss}$ and $VPL_{BDT-wss}$ are computed in the same way as VPL_c, VPL_{LUT} and VPL_{LDT} respectively but based on subset Q defining the WSS methodology.

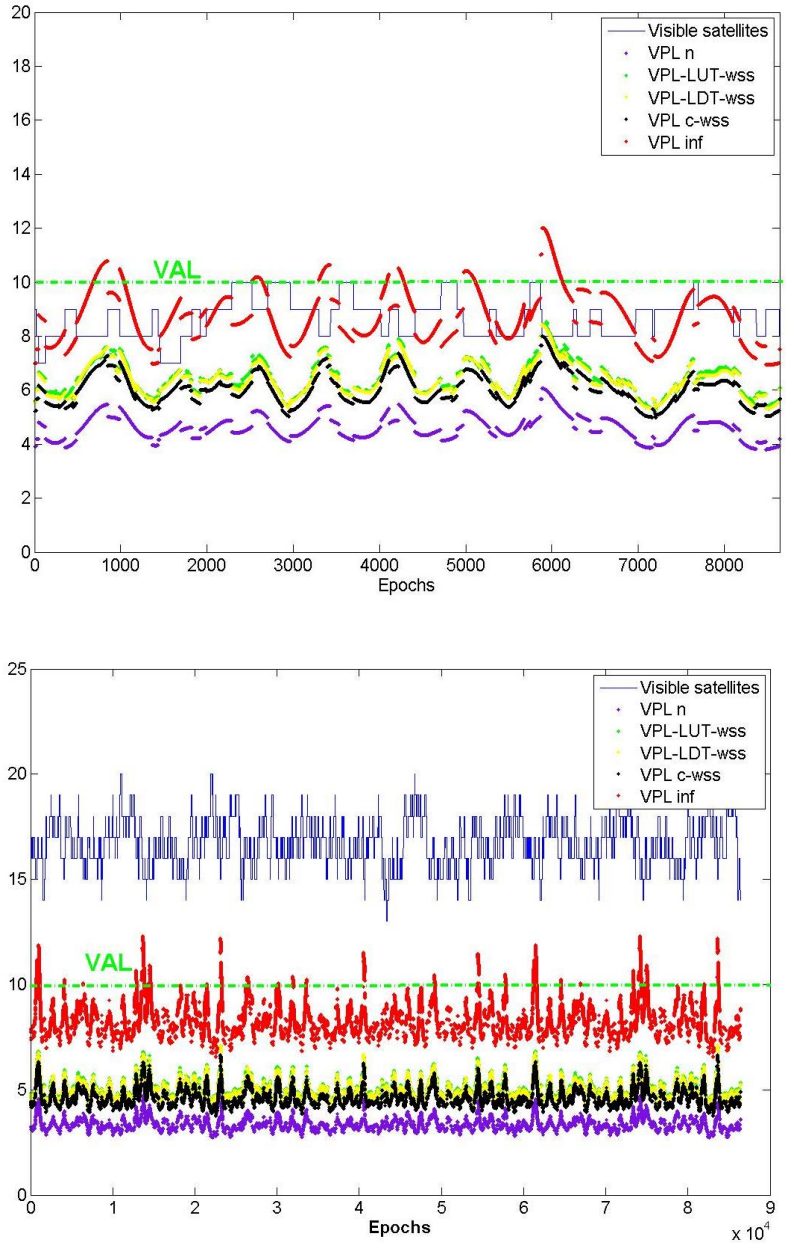

Figure 155-VPLs geometry improved, Lat0 GPS (left) and the GPS and GAL (right), Dth=10km

B.2 Miami

B.2.1 Dth=5km

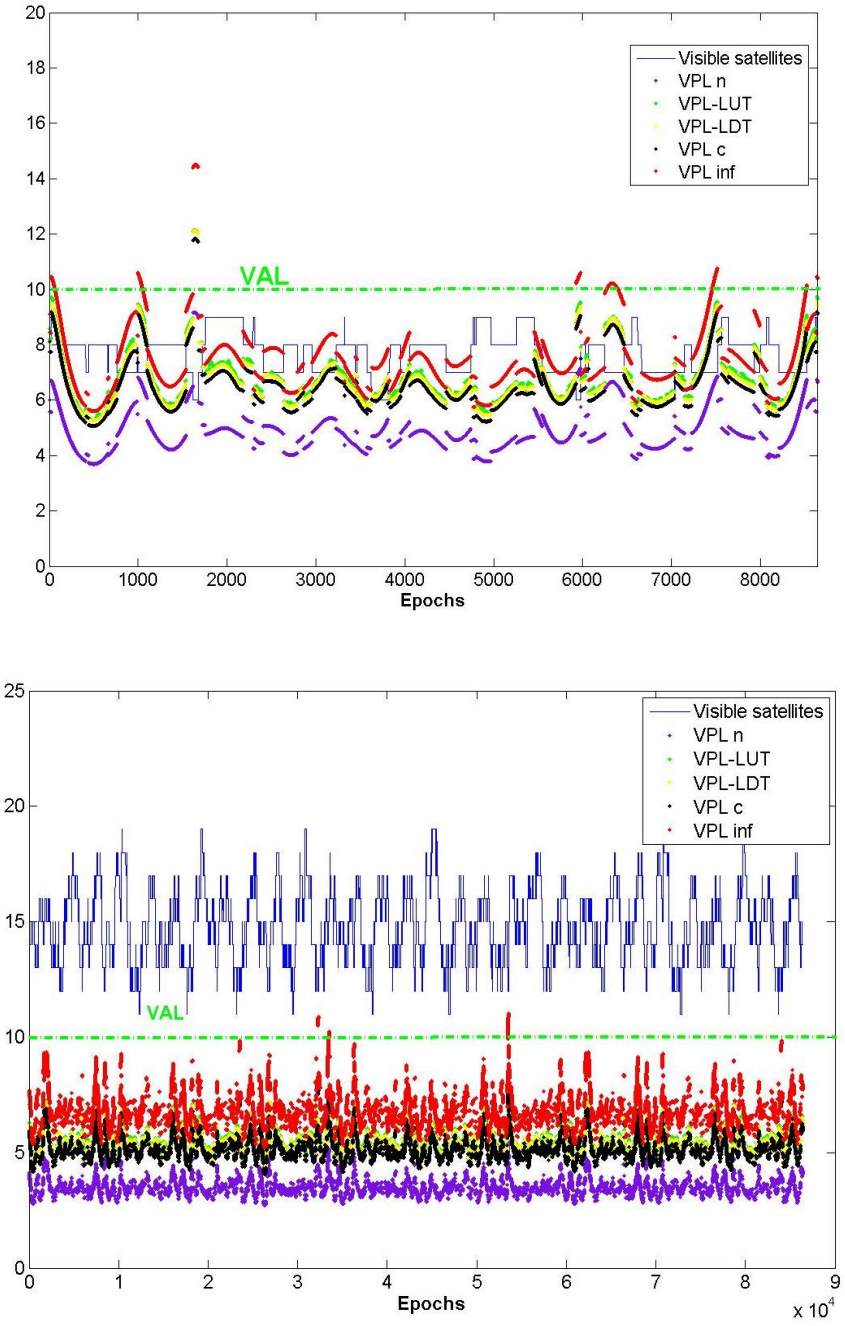

Figure 156-VPLs Miami GPS (left) and the GPS and GAL (right), Dth=5km

Then VPLs computed with the WSS are computed as shown in 6.3.1.3, VPLs named VPL_{c-wss}, $VPL_{LUT-wss}$ and $VPL_{LDT-wss}$ are computed in the same way as VPL_c, VPL_{LUT} and VPL_{LDT} respectively but based on subset Q defining the WSS methodology.

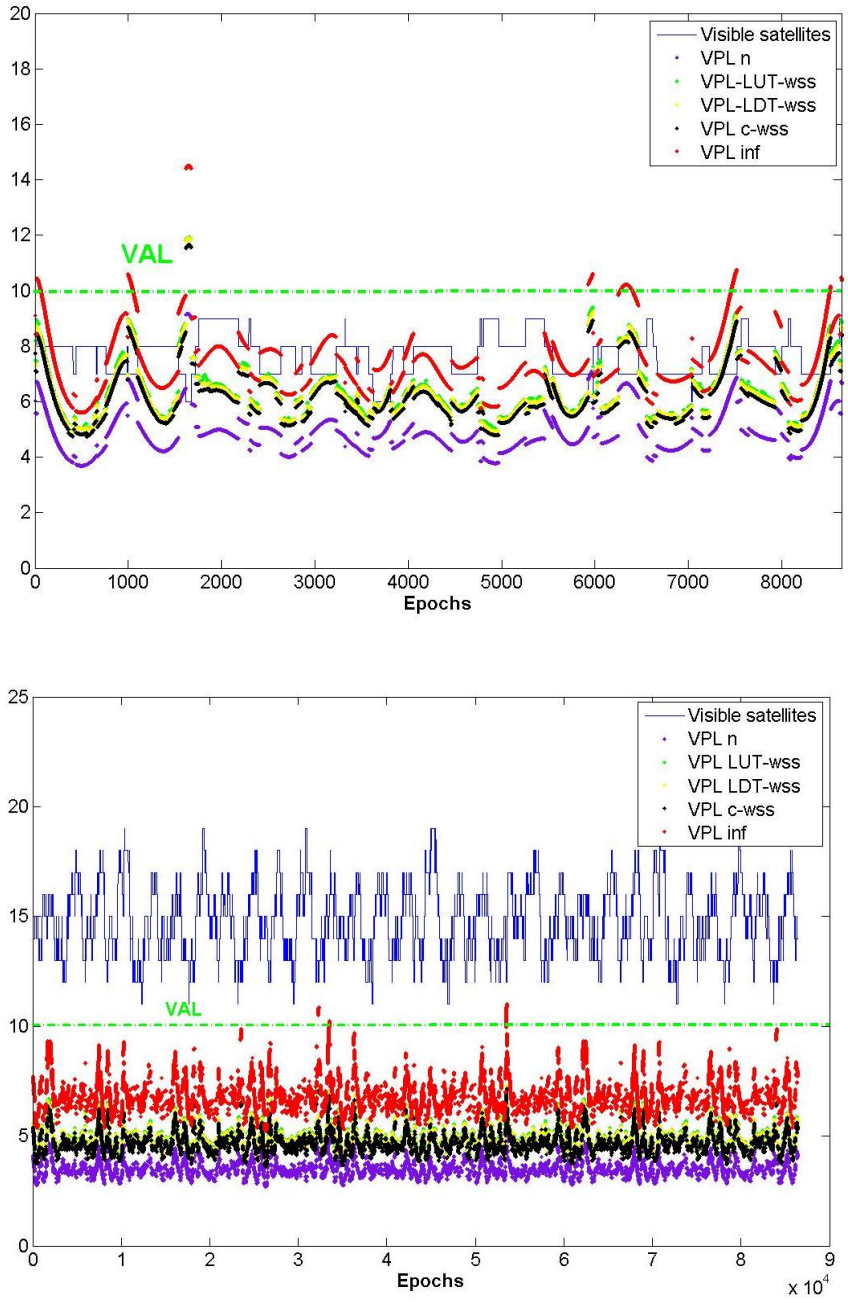

Figure 157-VPLs Miami geometry improved, GPS (left) and the GPS and GAL (right), Dth=5km

B.2.2 Dth=10km

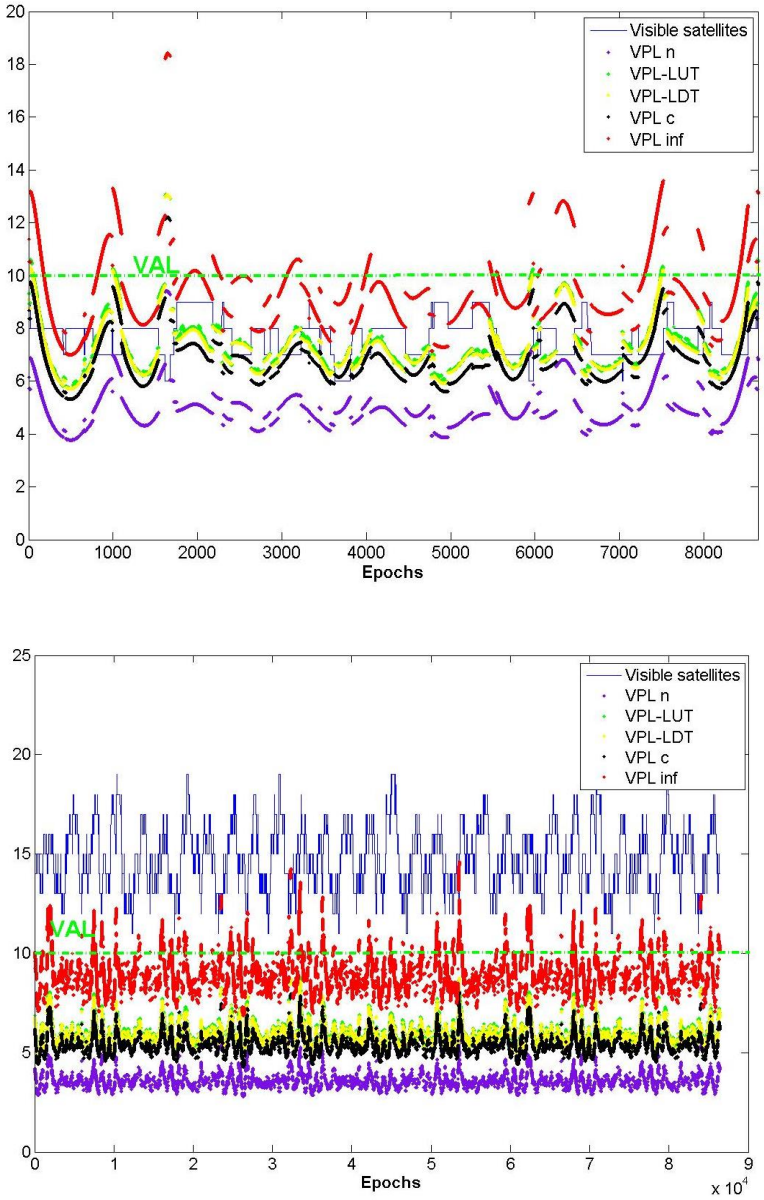

Figure 158-VPLs Miami GPS (left) and the GPS and GAL (right), Dth=10km

Then VPLs computed with the WSS methodology are computed as shown in 6.3.1.3, VPLs named VPL_{c-wss}, $VPL_{LUT-wss}$ and $VPL_{LDT-wss}$ are computed in the same way as VPL_c, VPL_{LUT} and VPL_{LDT} respectively but based on subset Q defining the WSS methodology.

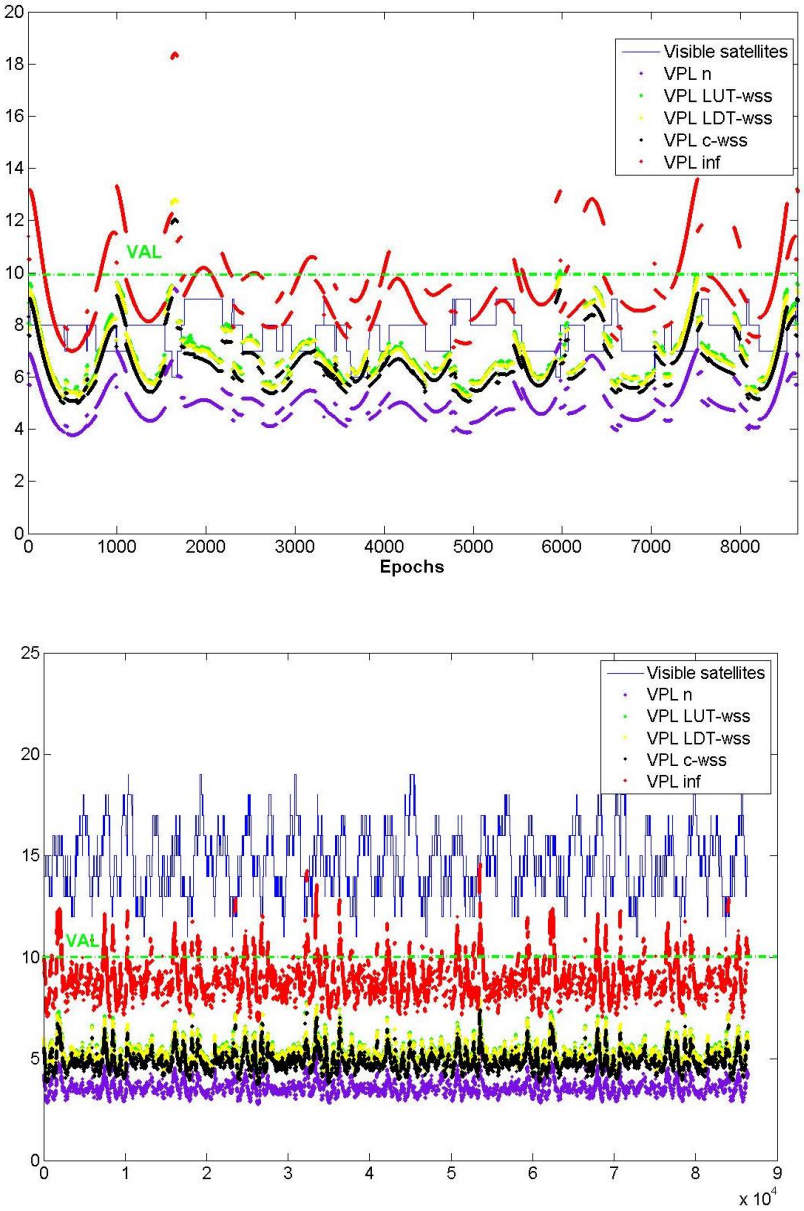

Figure 159-VPLs Miami geometry improved, GPS (left) and the GPS and GAL (right), Dth=10km

B.3 Anchorage

B.3.1 Dth=5km

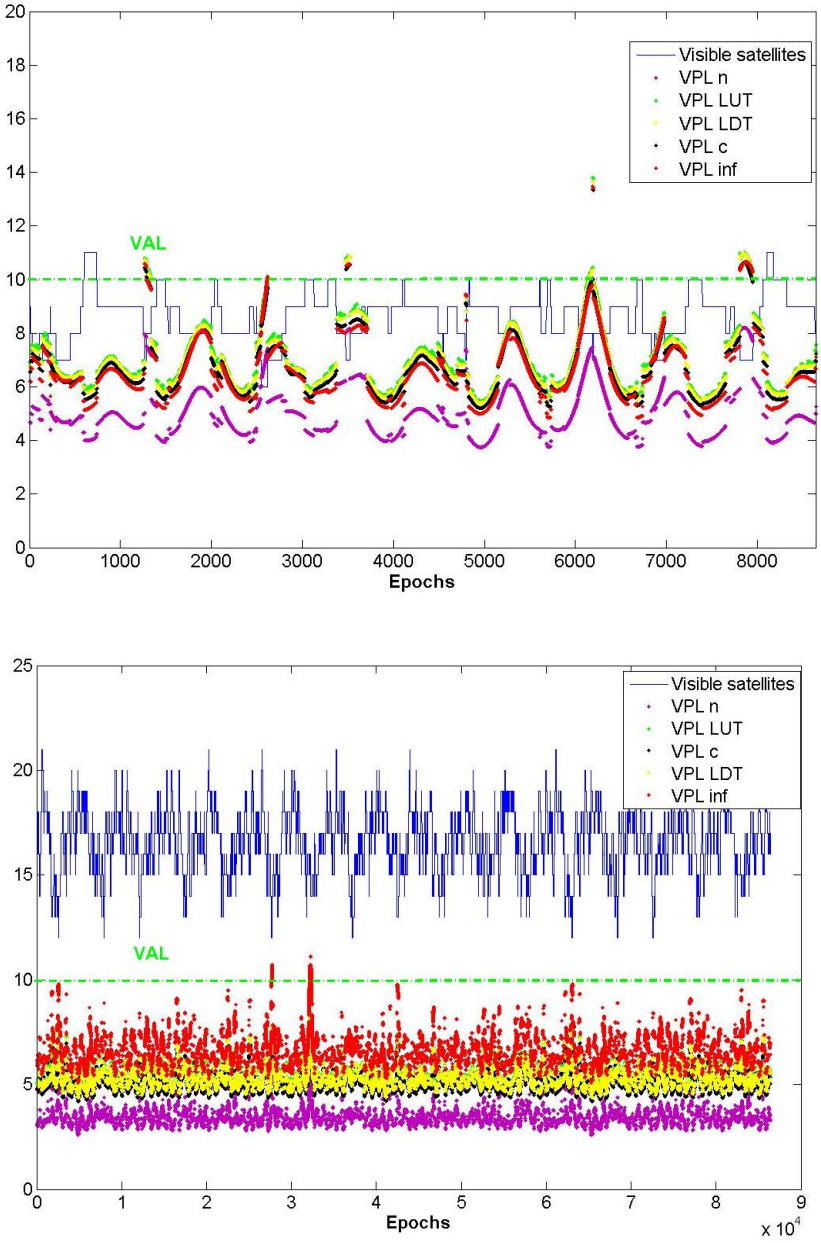

Figure 160-VPLs Anchorage GPS (left) and the GPS and GAL (right), Dth=5km

Then VPLs computed with the WSS are computed as shown in 6.3.1.3, VPLs named VPL_{c-wss}, $VPL_{LUT-wss}$ and $VPL_{LDT-wss}$ are computed in the same way as VPL_c, VPL_{LUT} and VPL_{LDT} respectively but based on subset Q defining the WSS methodology.

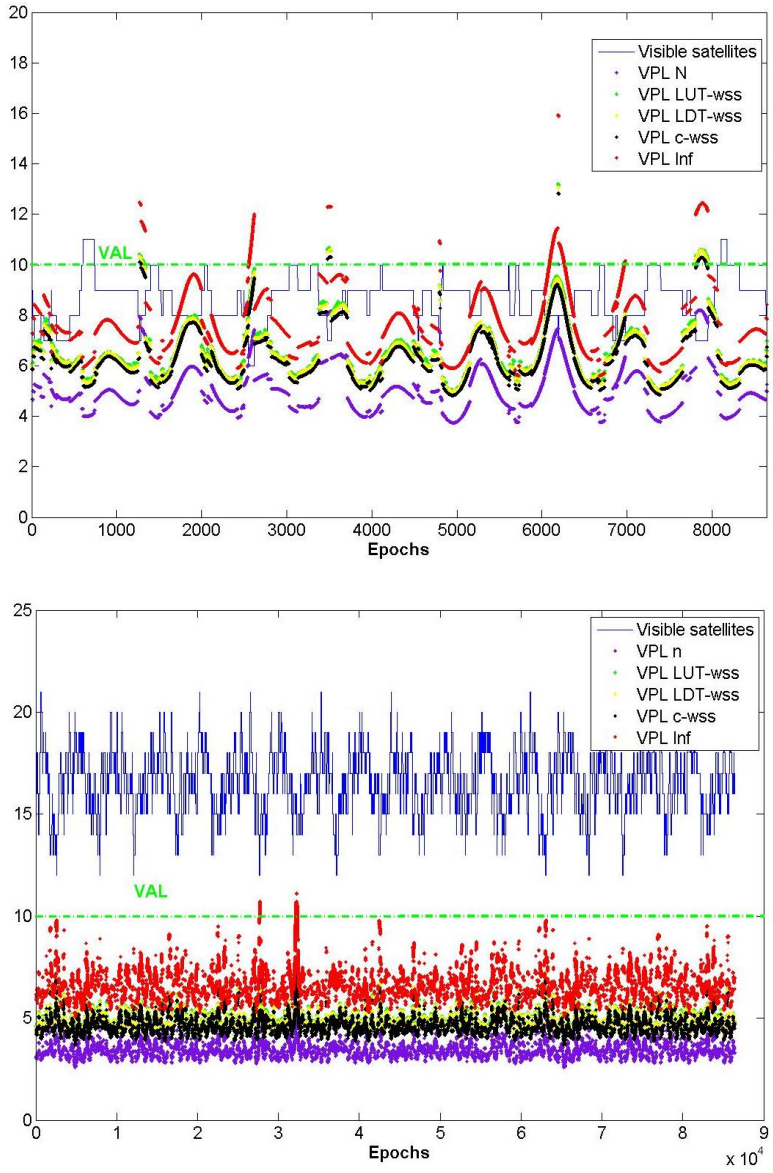

Figure 161-VPLs Anchorage geometry improved GPS (left) and the GPS and GAL (right), Dth=5km

B.3.2 Dth=10km

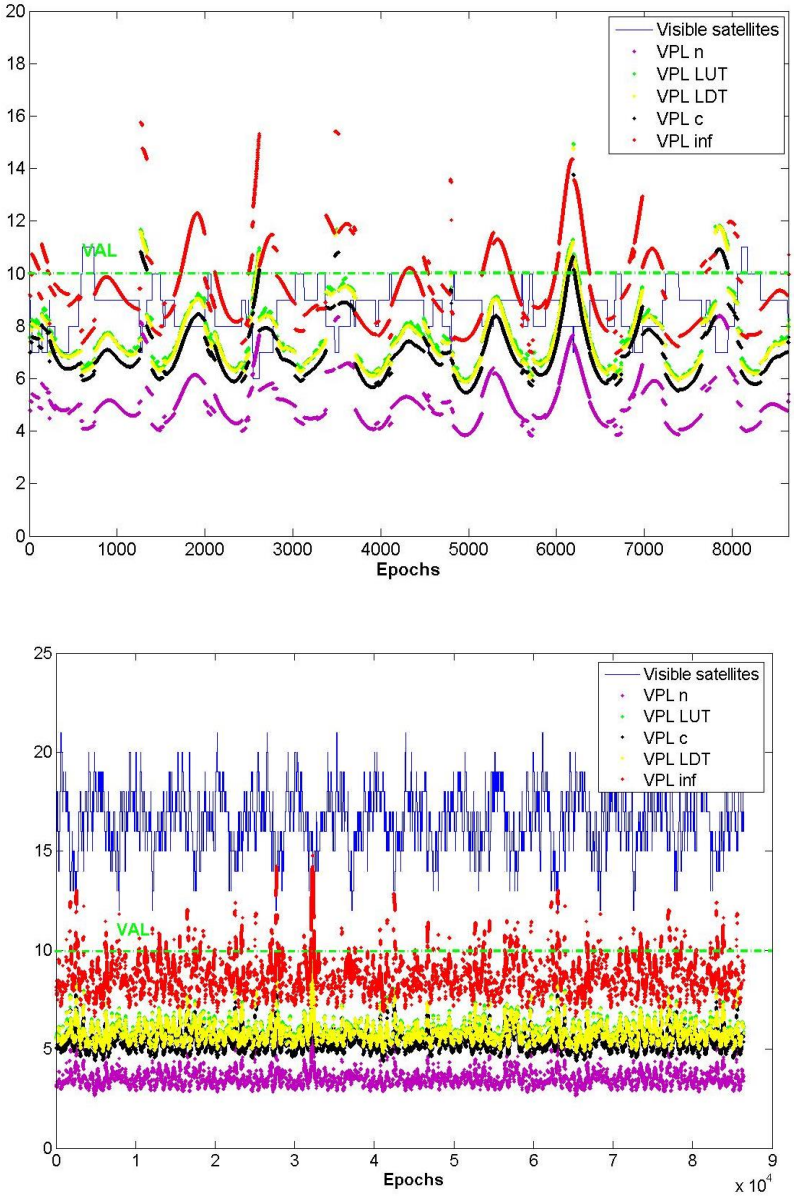

Figure 162-VPLs Anchorage GPS (left) and the GPS and GAL (right), Dth=10km

Then VPLs computed with the WSS methodology are computed as shown in 6.3.1.3, VPLs named VPL_{c-wss}, $VPL_{LUT-wss}$ and $VPL_{LDT-wss}$ are computed in the same way as VPL_c, VPL_{LUT} and VPL_{LDT} respectively but based on subset Q defining the WSS methodology.

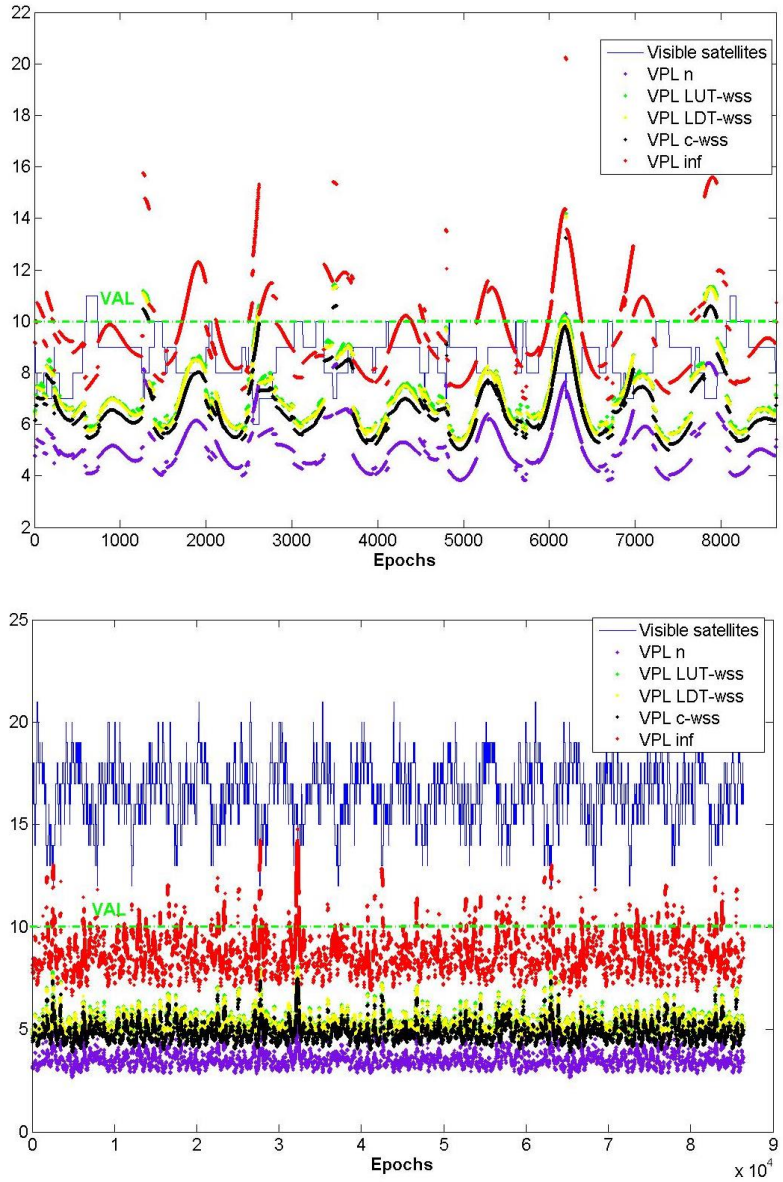

Figure 163-VPLs Anchorage geometry improved GPS (left) and the GPS and GAL (right), Dth=10km

Appendix C : Other I-free scenarios

C.1 Seattle

C.1.1 Dth=5km

Results for GPS constellation (figure above) and for GPS and Galileo Constellations (figure below) with τ set at 300s are represented below:

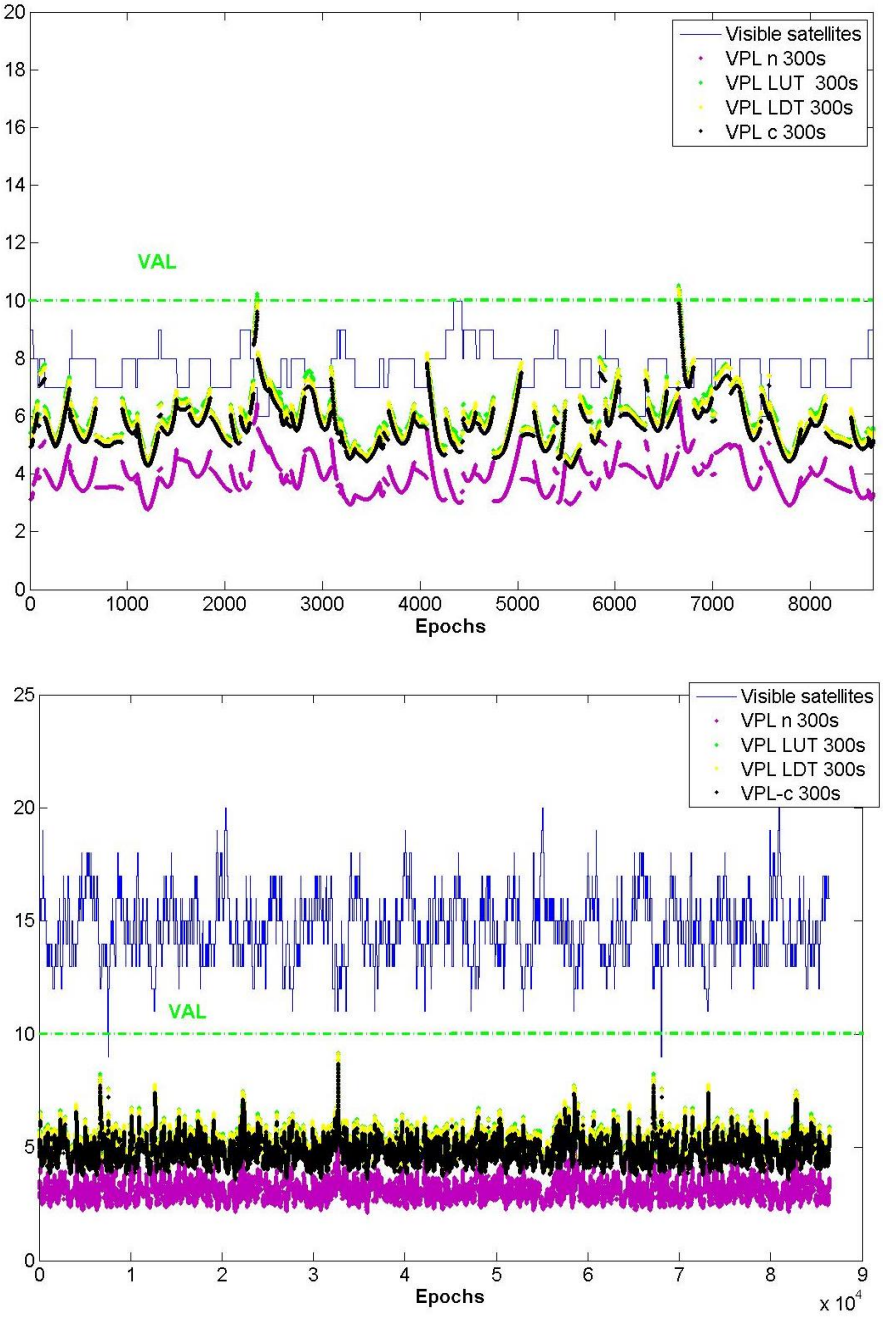

Figure 164-VPLs IF 300s Seattle, GPS (left) and GPS and GAL (right), Dth5km

Results for GPS constellation (figure above) and for GPS and Galileo Constellations (figure below) with τ set at 1000s are represented below:

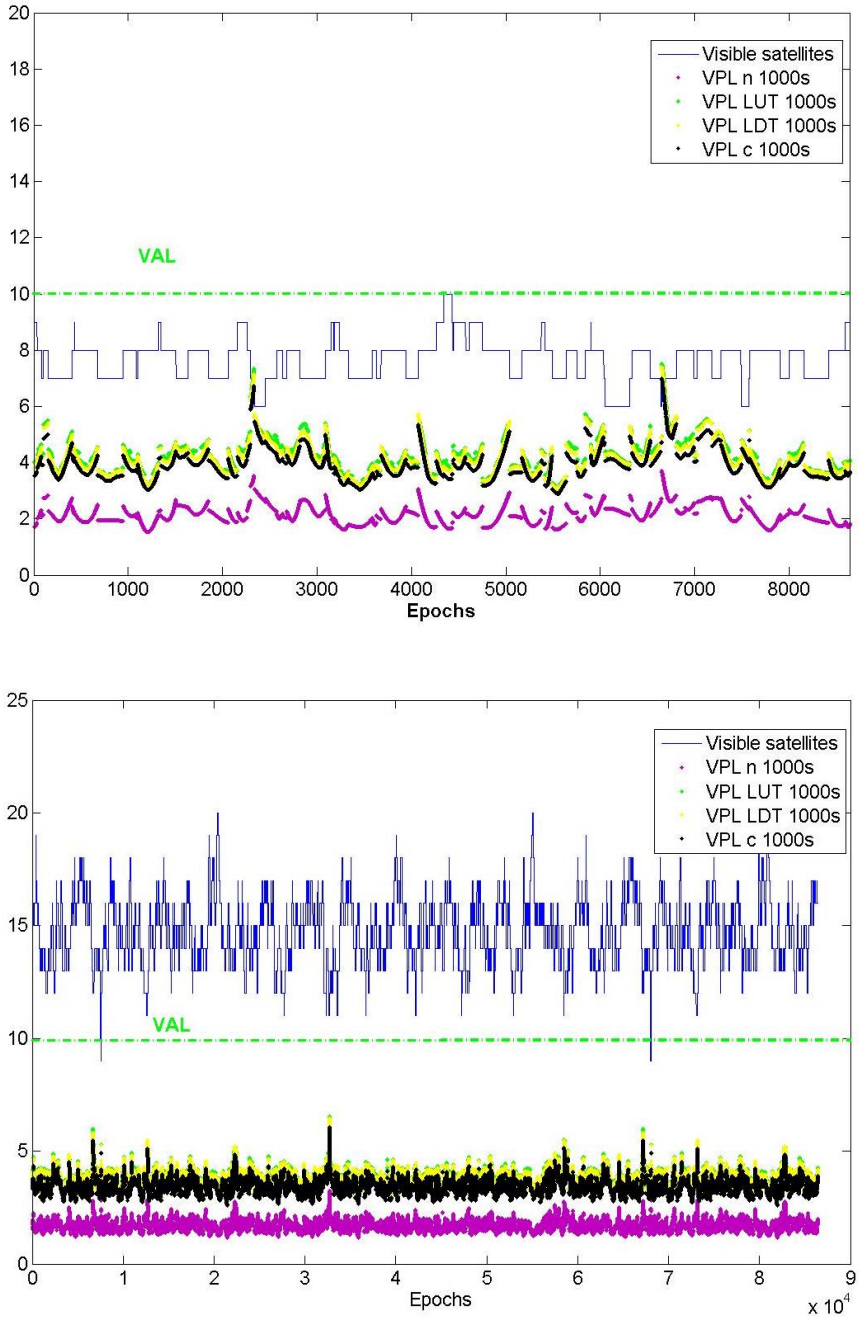

Figure 165-VPLs IF 1000s Seattle, GPS (left) and GPS and GAL (right), Dth5km

C.1.2 Dth=10km

Results for GPS constellation (figure above) and for GPS and Galileo Constellations (figure below) with τ set at 100s are represented below:

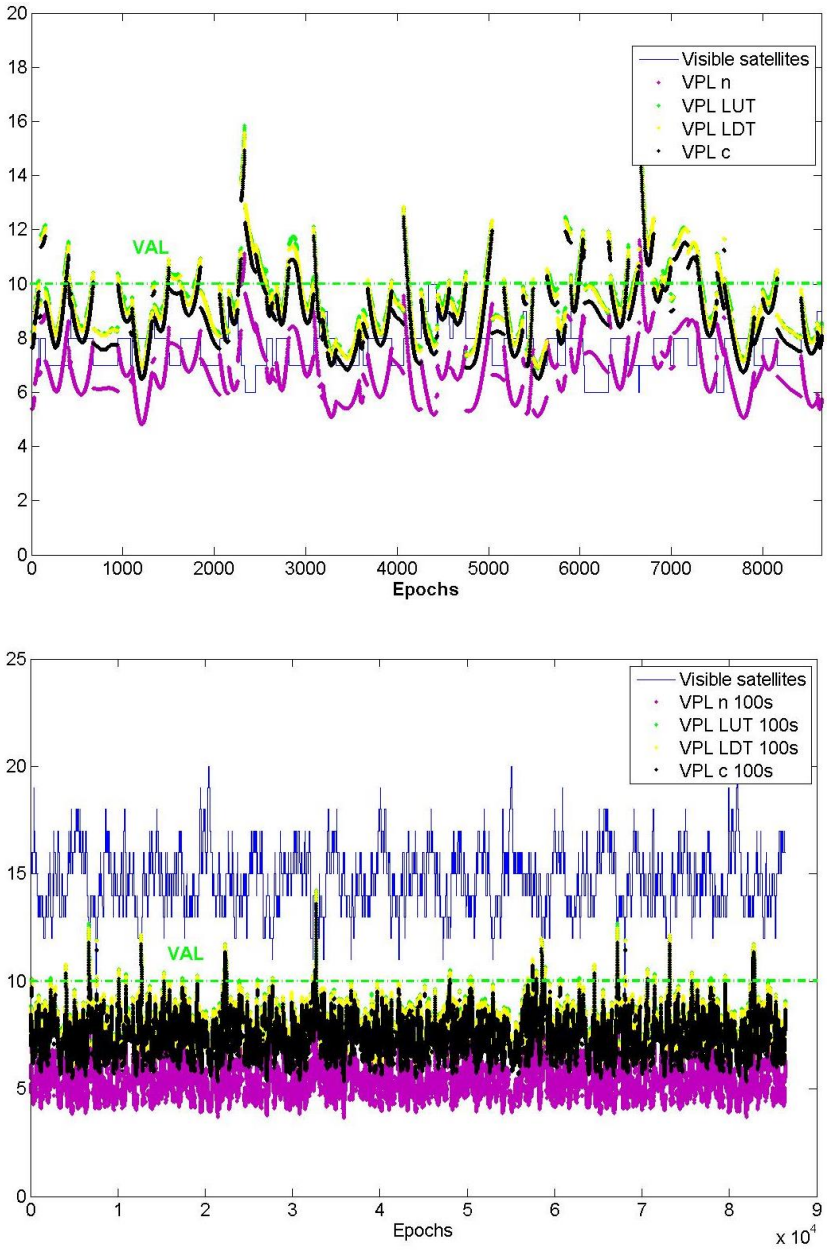

Figure 166-VPLs IF 100s Seattle, GPS (left) and GPS and GAL (right), Dth10km

Results for GPS constellation (figure above) and for GPS and Galileo Constellations (figure below) with τ set at 300s are represented below:

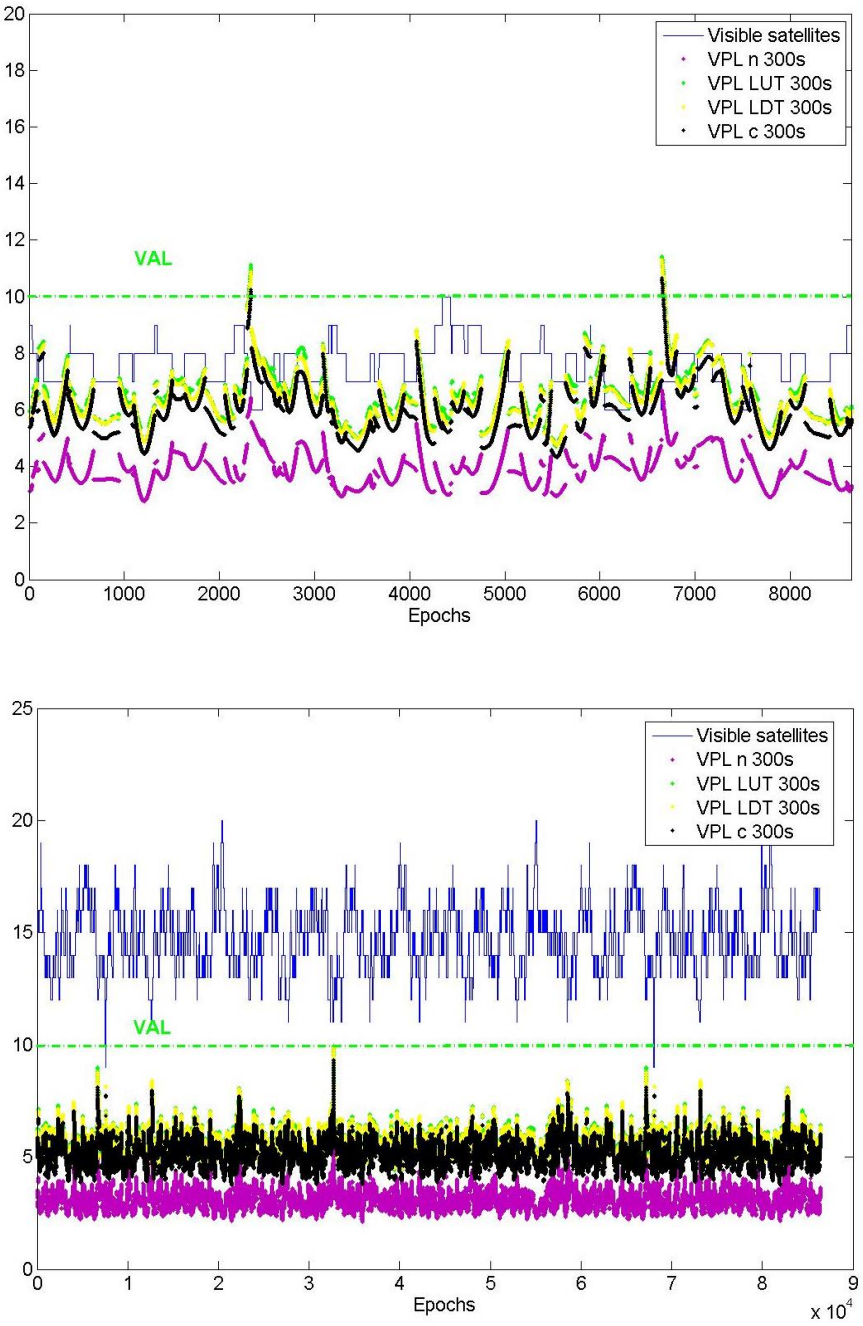

Figure 167-VPLs IF 300s Seattle, GPS (left) and GPS and GAL (right), Dth10km

Results for GPS constellation (figure above) and for GPS and Galileo Constellations (figure below) with τ set at 1000s are represented below:

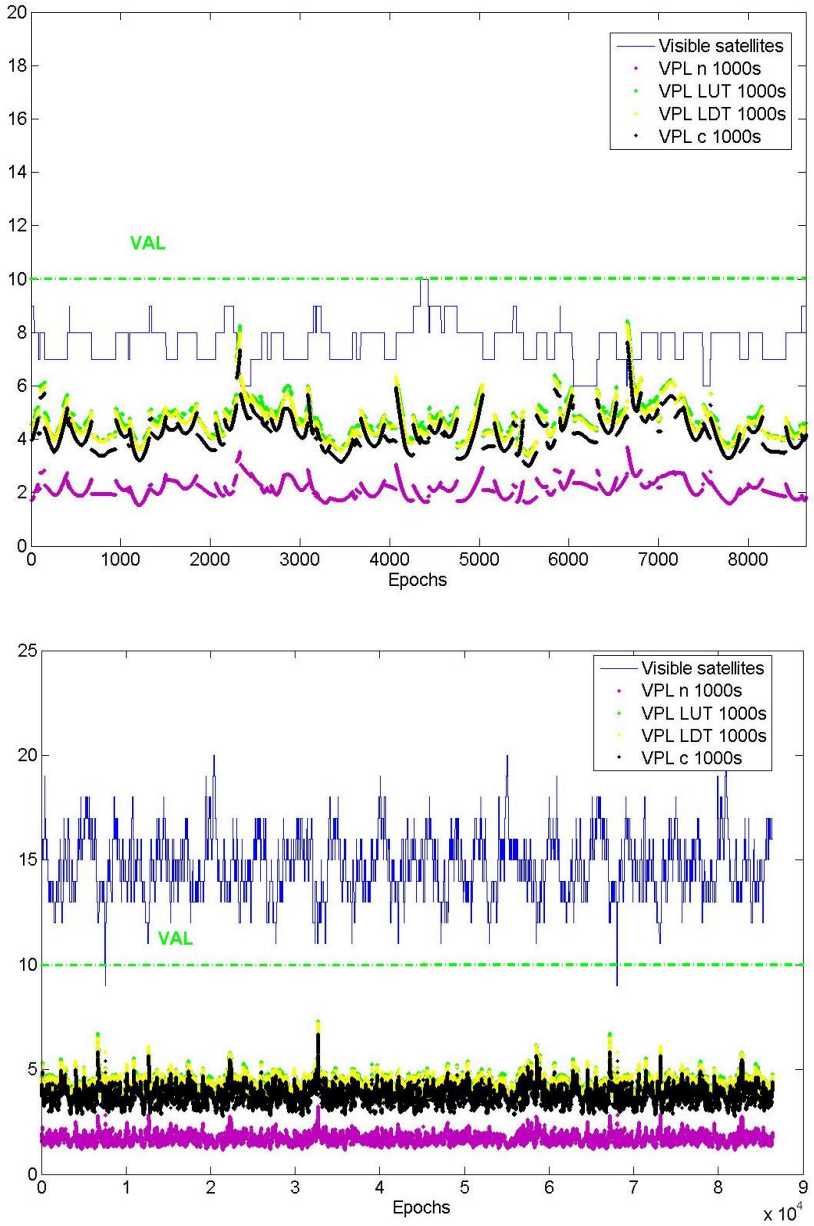

Figure 168-VPLs IF 1000s Seattle, GPS (left) and GPS and GAL (right), Dth10km

In order to conclude about performances evaluation as a function of smoothing constant and Distance from ground station to runway threshold D_{th}, figures were plotted to summarize VPL computed for all D_{th} and smoothing constants for the LDT methodology for GPS and GPS and Galileo constellations. Results are presented below :

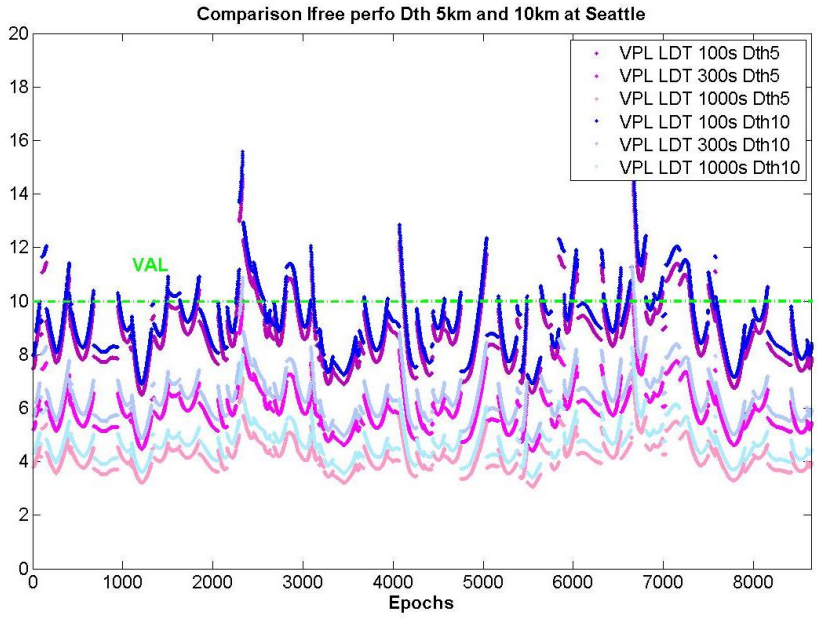

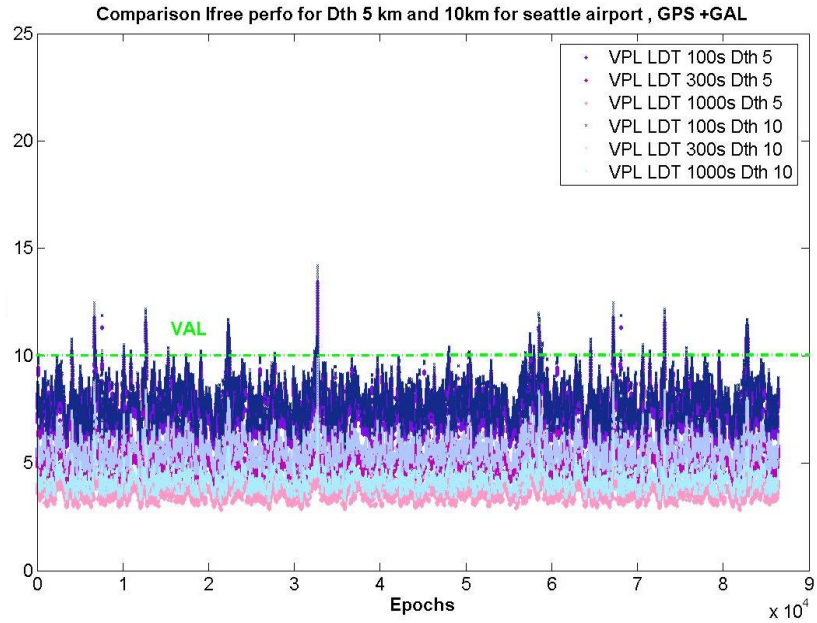

Figure 169-Comparison VPLs IF performance for Seattle

C.2 LAT 0

C.2.1 Dth=5km

Results for GPS constellation (figure above) and for GPS and Galileo Constellations (figure below) with τ set at 100s are represented below:

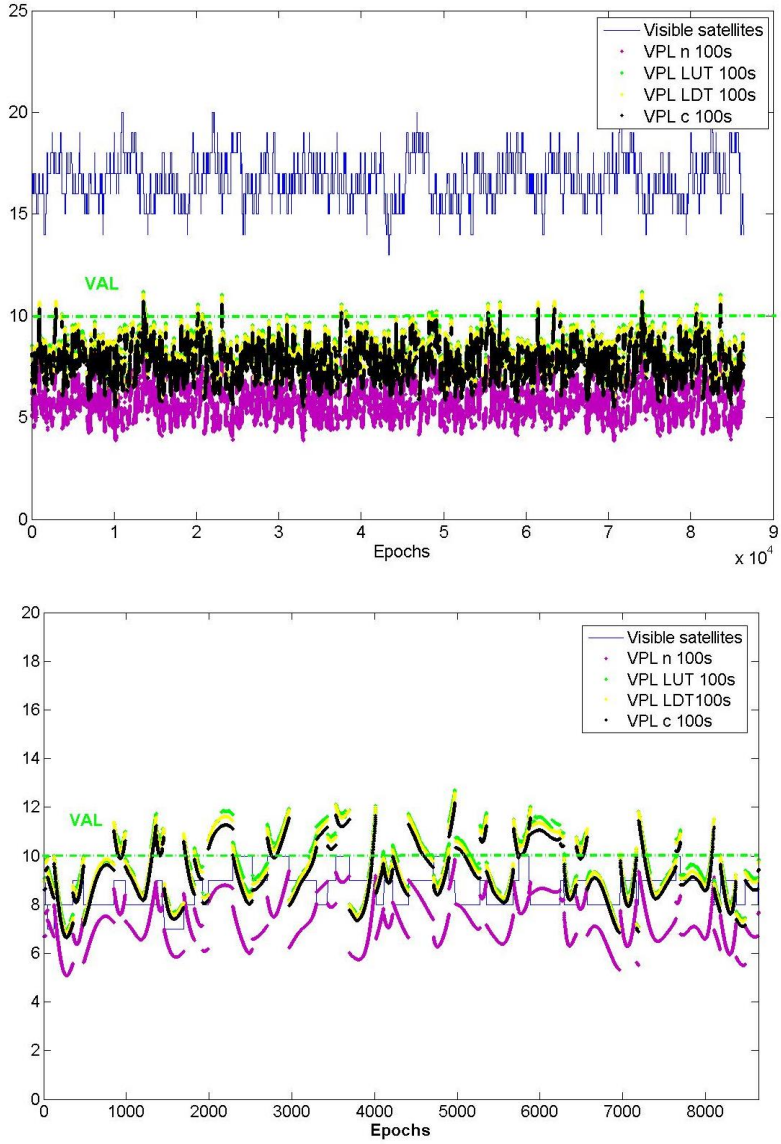

Figure 170-VPLs IF 100s LAT0, GPS (left) and GPS and GAL (right), Dth5km

Results for GPS constellation (figure above) and for GPS and Galileo Constellations (figure below) with τ set at300s are represented below:

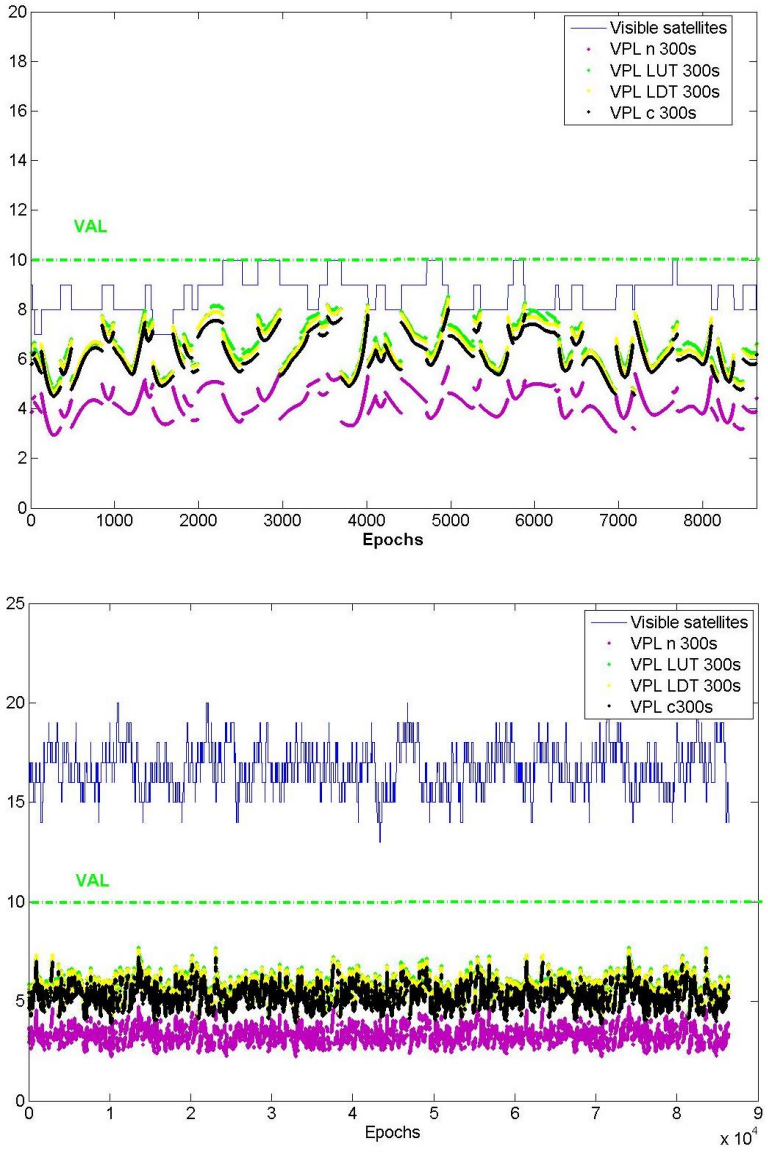

Figure 171-VPLs IF 300s LAT0, GPS (left) and GPS and GAL (right), Dth5km

Results for GPS constellation (figure above) and for GPS and Galileo Constellations (figure below) with τ set at 1000s are represented below:

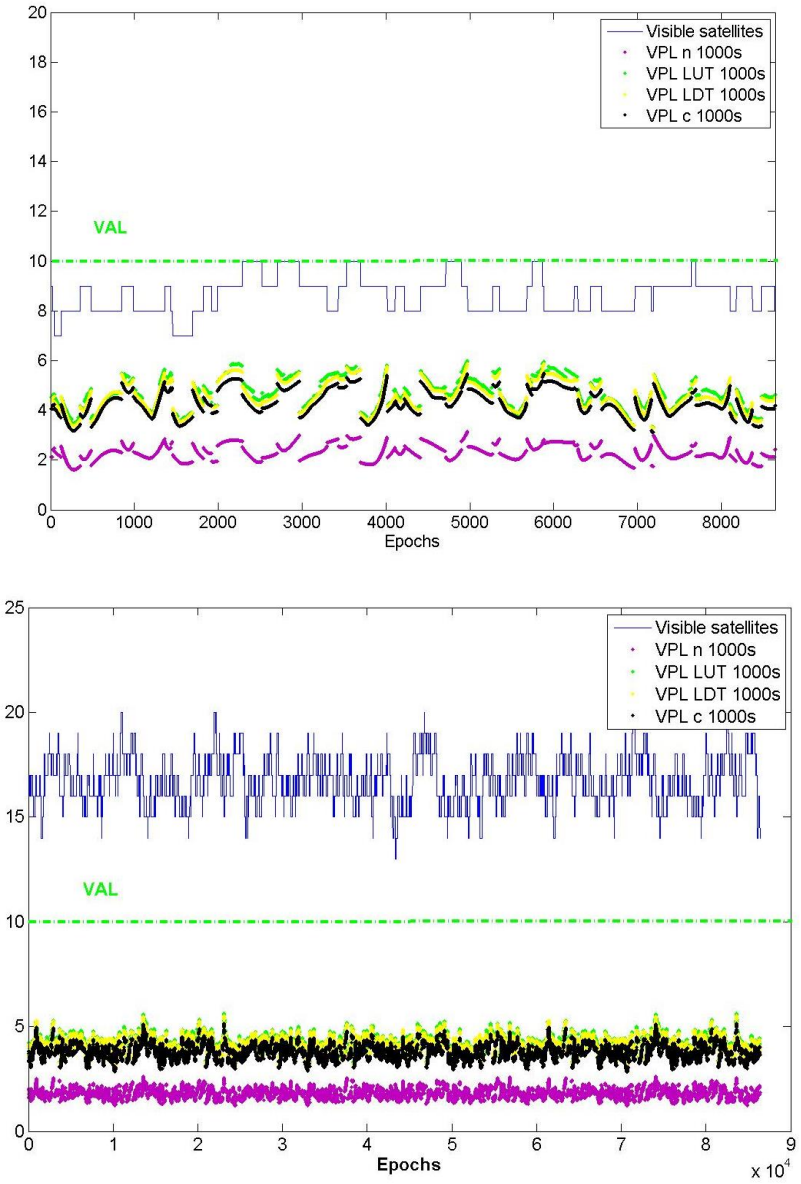

Figure 172-VPLs IF 1000s LAT0, GPS (left) and GPS and GAL (right), Dth5km

C.2.2 Dth=10km

Results for GPS constellation (figure above) and for GPS and Galileo Constellations (figure below) with τ set at 100s are represented below:

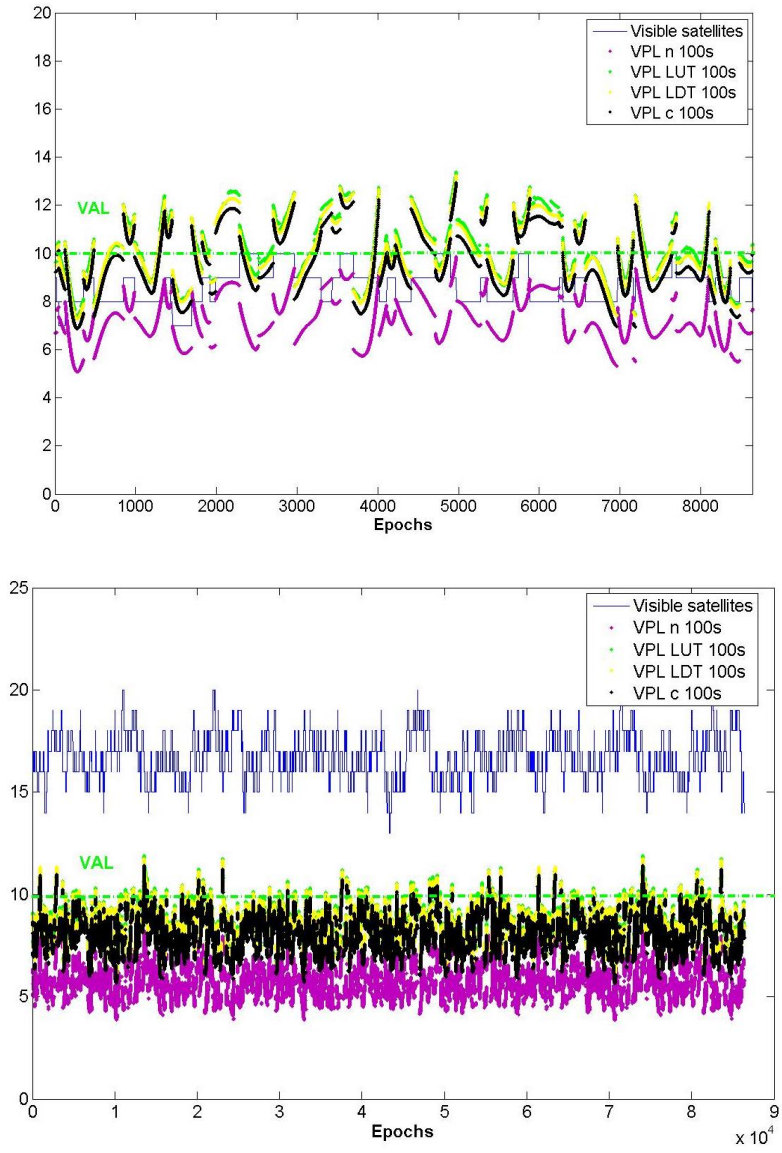

Figure 173-VPLs IF 100s LAT0, GPS (left) and GPS and GAL (right), Dth10km

Results for GPS constellation (figure above) and for GPS and Galileo Constellations (figure below) with τ set at 300s are represented below:

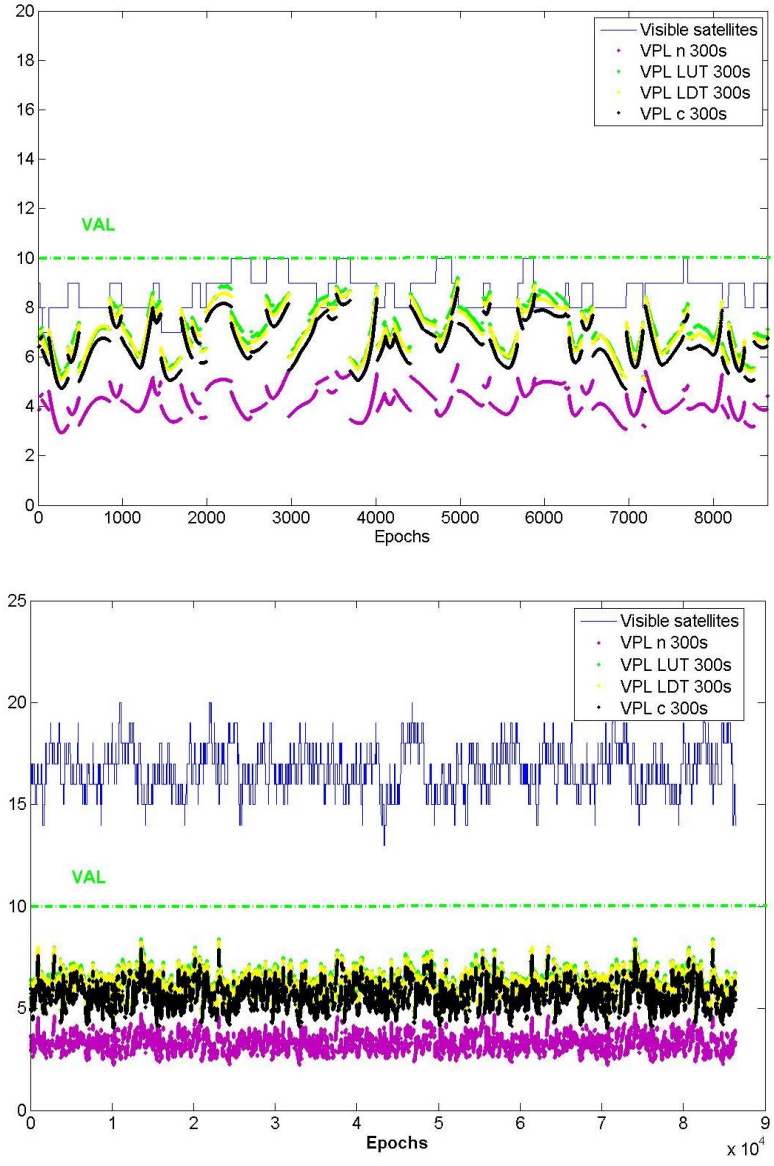

Figure 174-VPLs IF 300s LAT0, GPS (left) and GPS and GAL (right), Dth10km

Results for GPS constellation (figure above) and for GPS and Galileo Constellations (figure below) with τ set at 1000s are represented below:

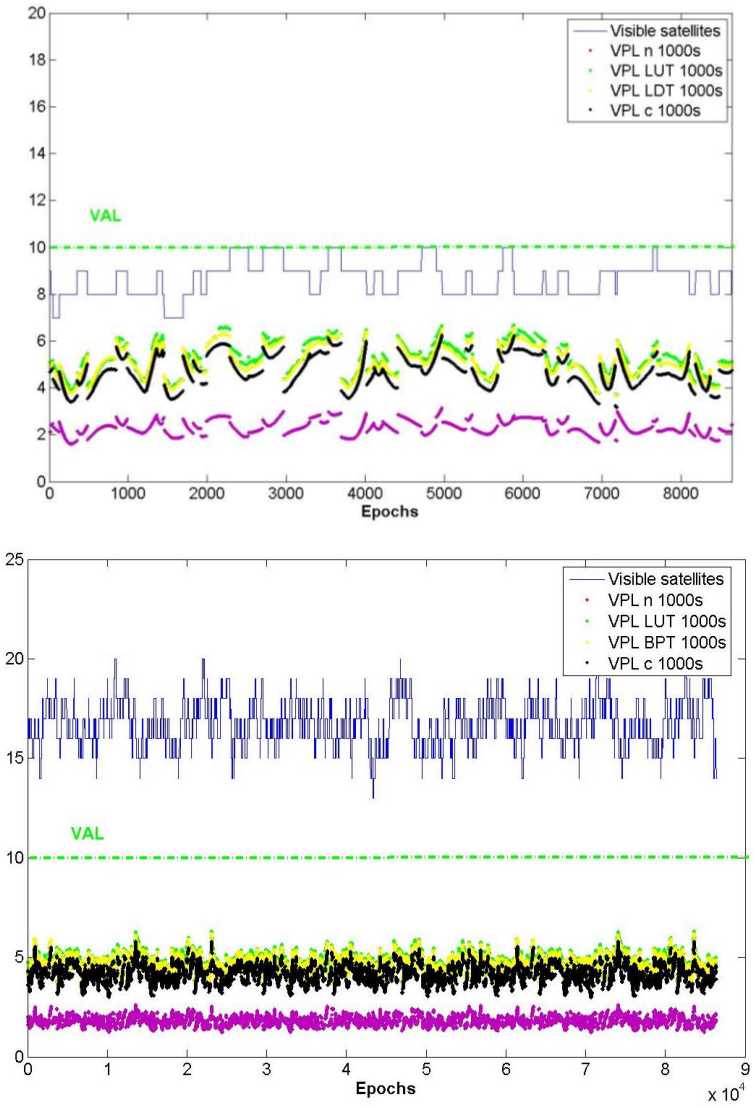

Figure 175-VPLs IF 1000s LAT0, GPS (left) and GPS and GAL (right), Dth10km

C.3 Miami

C.3.1 Dth=5km

Results for GPS constellation (figure above) and for GPS and Galileo Constellations (figure below) with τ set at 100s are represented below:

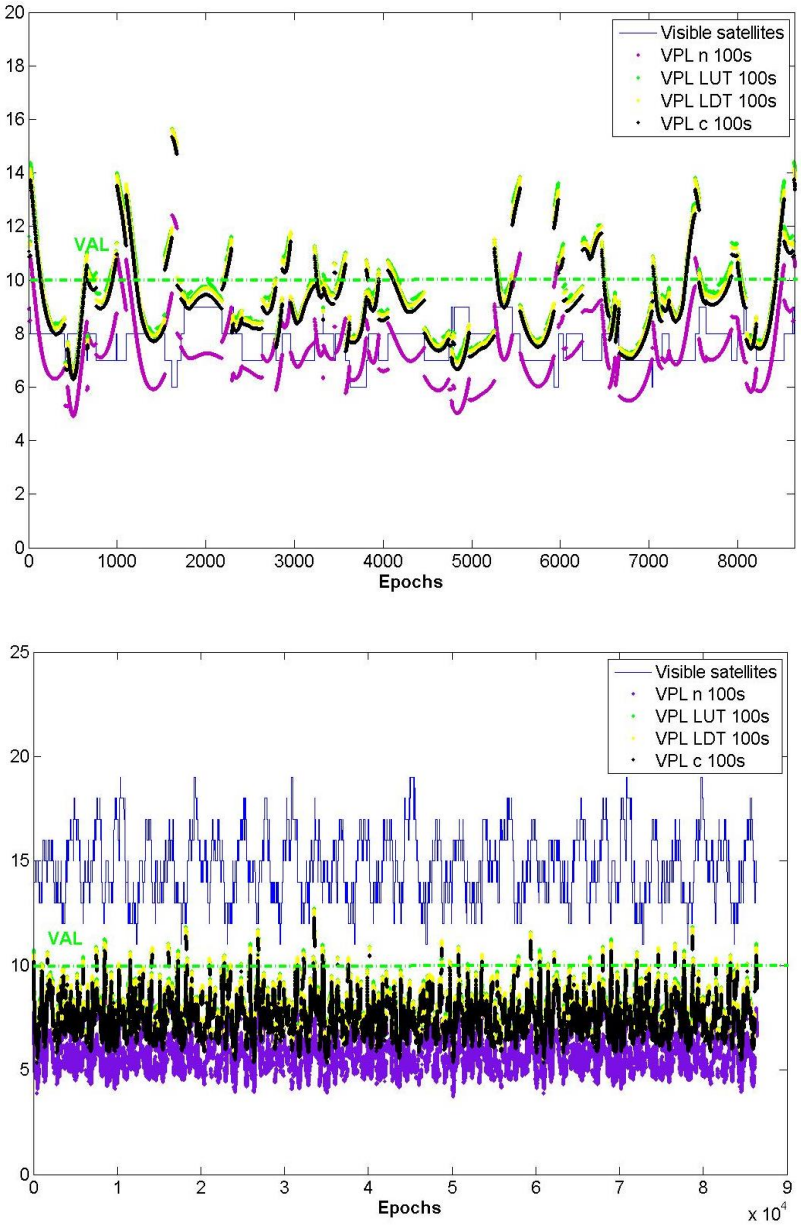

Figure 176-VPLs IF 100s Miami, GPS (left) and GPS and GAL (right), Dth5km

Results for GPS constellation (figure above) and for GPS and Galileo Constellations (figure below) with τ set at 300s are represented below:

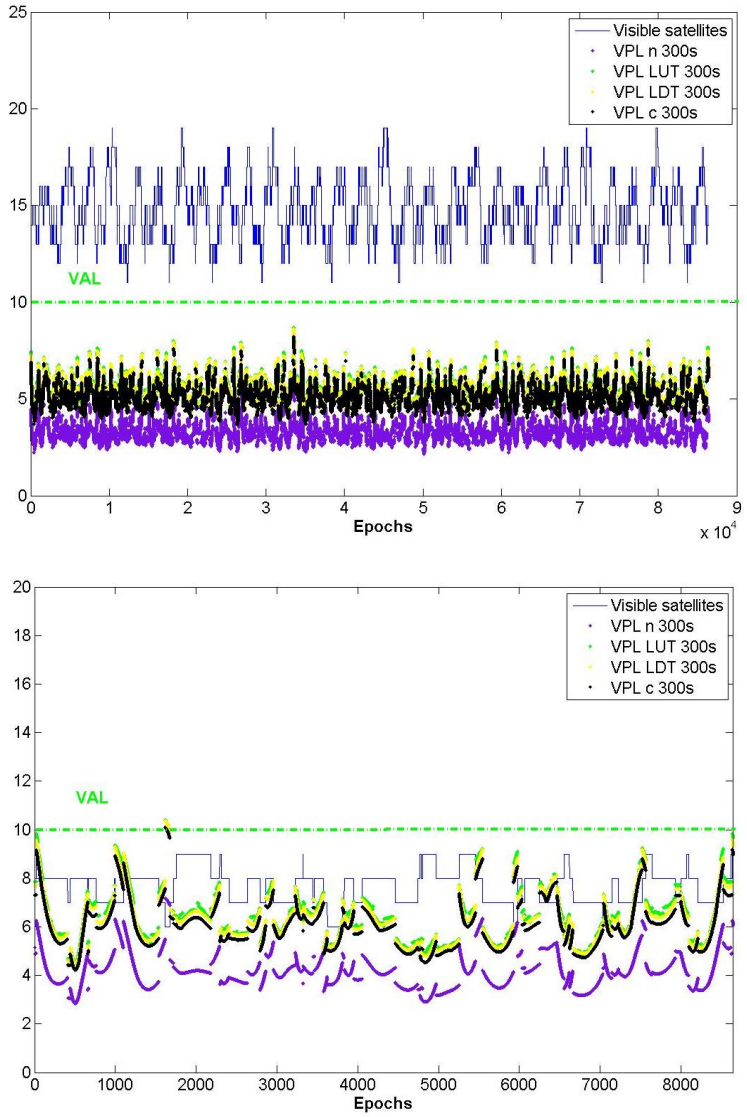

Figure 177-VPLs IF 300s Miami, GPS (left) and GPS and GAL (right), Dth5km

Results for GPS constellation (figure above) and for GPS and Galileo Constellations (figure below) with τ set at 1000s are represented below:

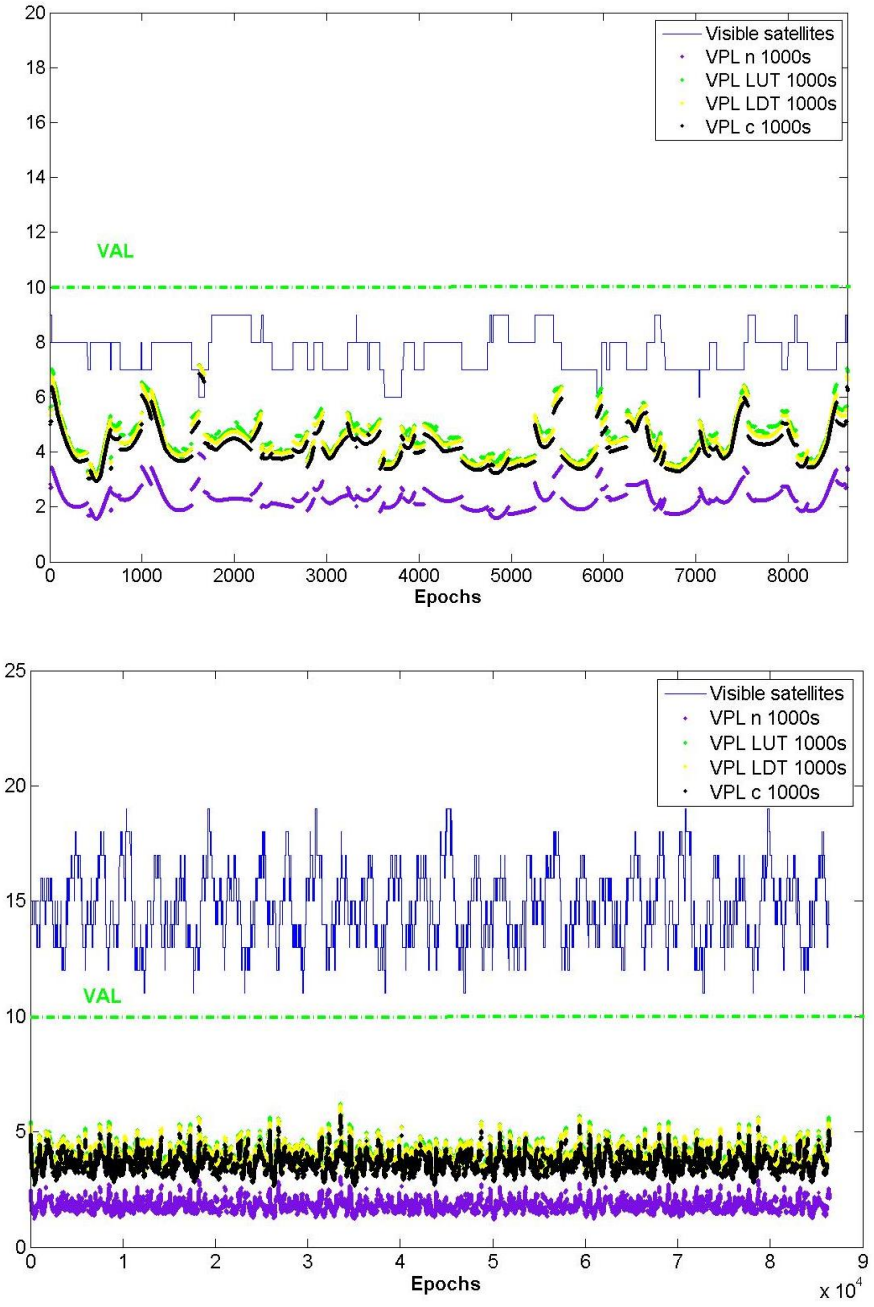

Figure 178-VPLs IF 1000s Miami, GPS (left) and GPS and GAL (right), Dth5km

C.3.2 Dth=10km

Results for GPS constellation (figure above) and for GPS and Galileo Constellations (figure below) with τ set at 100s are represented below:

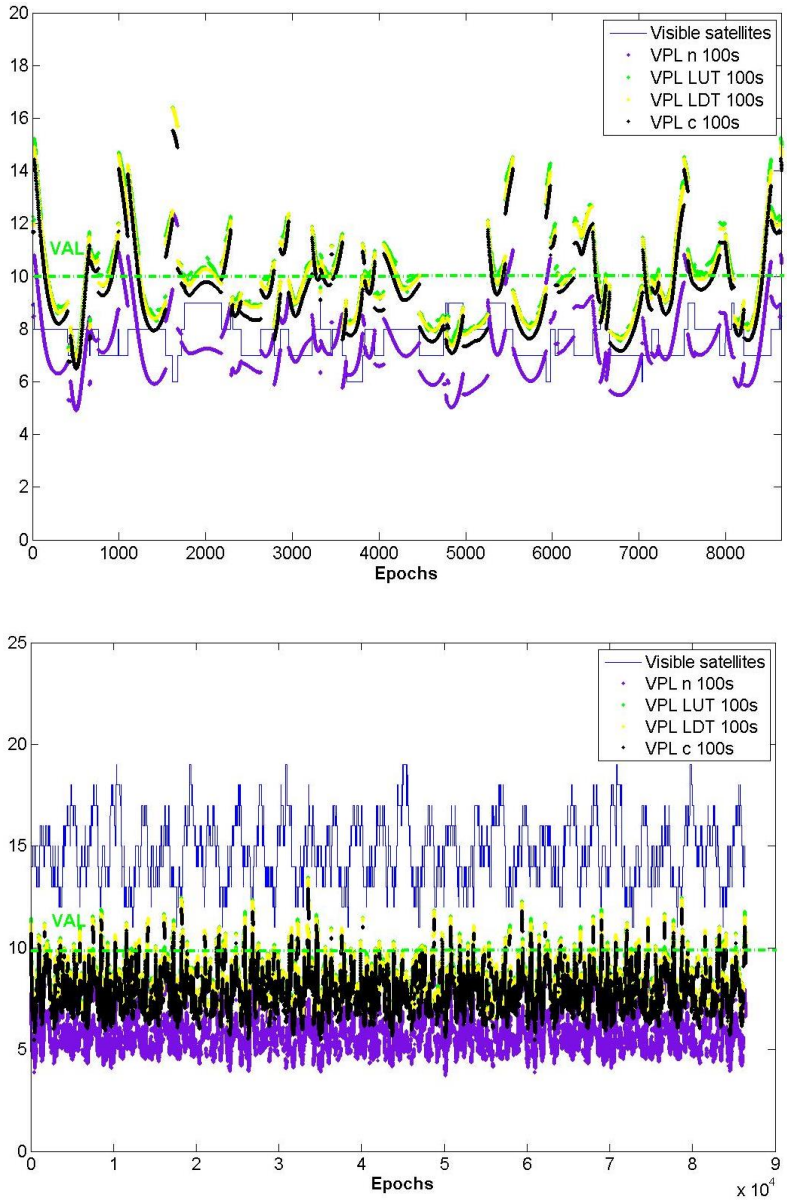

Figure 179-VPLs IF 100s Miami, GPS (left) and GPS and GAL (right), Dth10km

Results for GPS constellation (figure above) and for GPS and Galileo Constellations (figure below) with τ set at 300s are represented below:

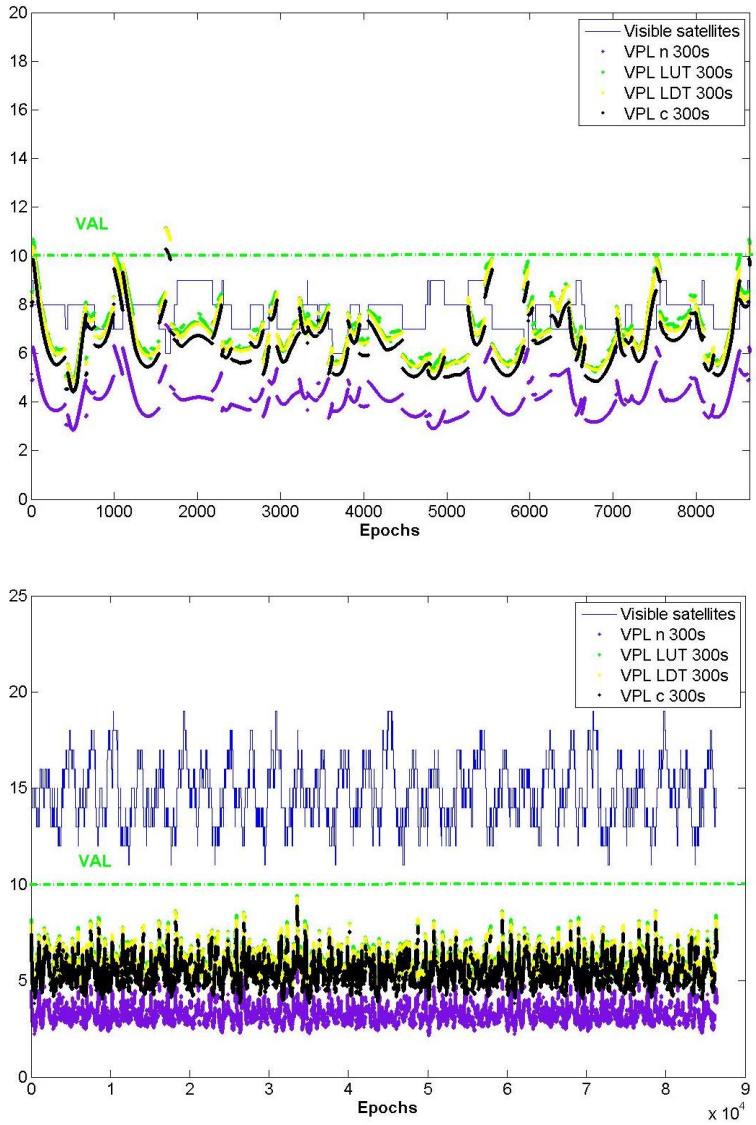

Figure 180-VPLs IF 300s Miami, GPS (left) and GPS and GAL (right), Dth10km

Results for GPS constellation (figure above) and for GPS and Galileo Constellations (figure below) with τ set at 1000s are represented below:

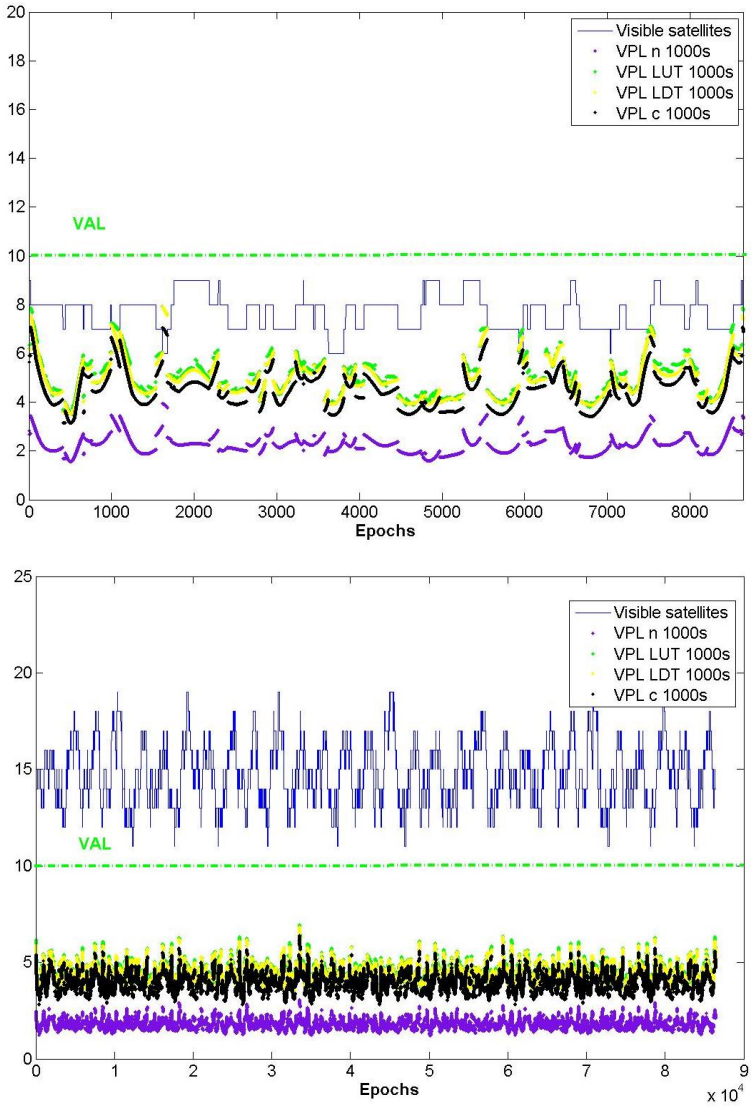

Figure 181-VPLs IF 1000s Miami, GPS (left) and GPS and GAL (right), Dth10km

C.4 Anchorage

C.4.1 Dth=5km

Results for GPS constellation (figure above) and for GPS and Galileo Constellations (figure below) with τ set at 100s are represented below:

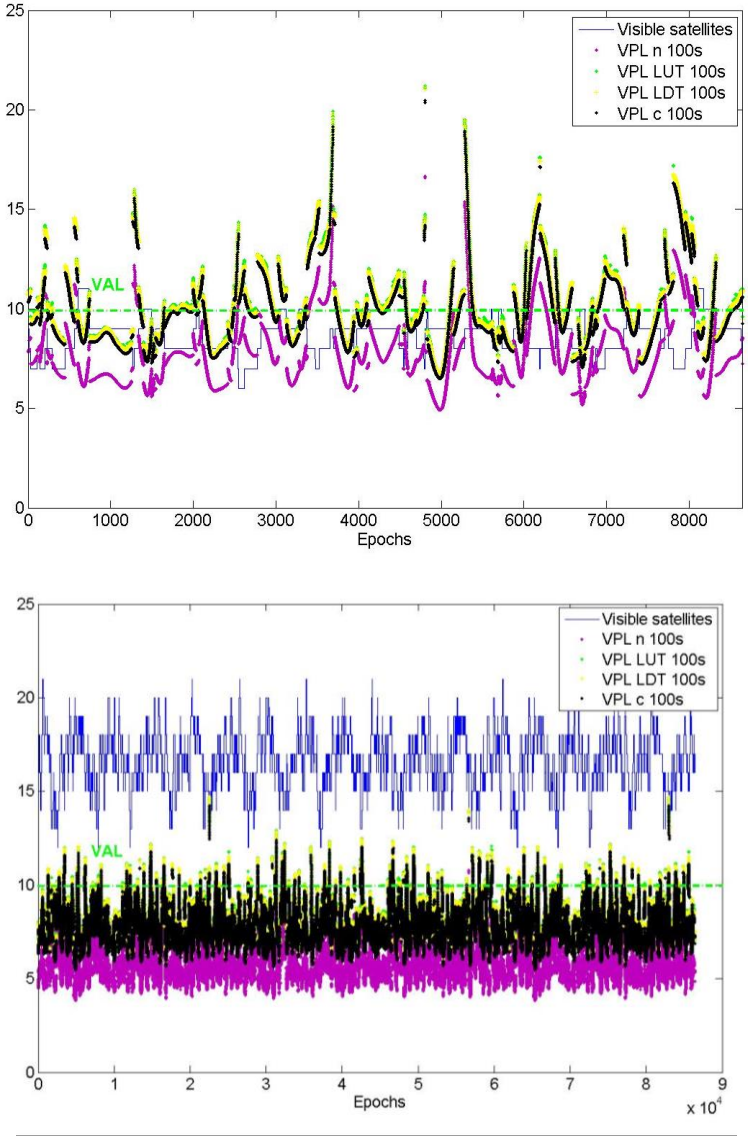

Figure 182-VPLs IF Anchorage 100s , GPS (left) and GPS and GAL (right), Dth5km

Results for GPS constellation (figure above) and for GPS and Galileo Constellations (figure below) with τ set at 300s are represented below:

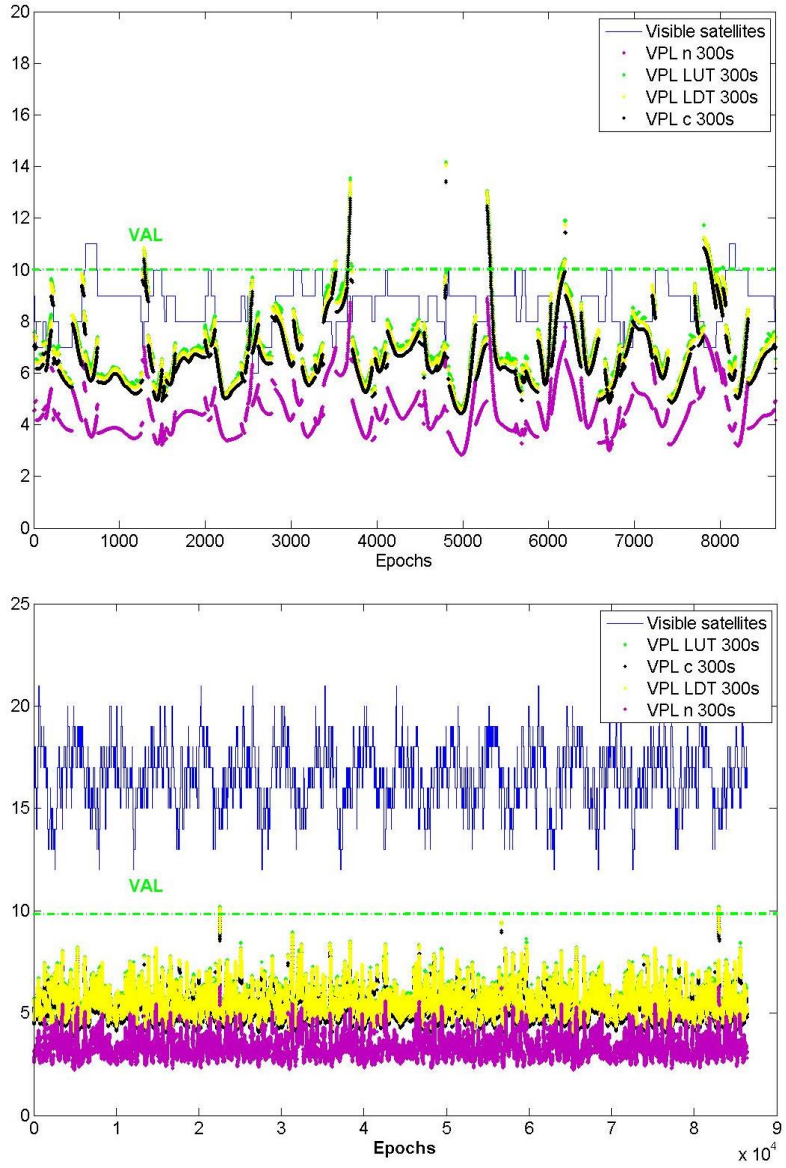

Figure 183-VPLs IF Anchorage 300s , GPS (left) and GPS and GAL (right), Dth5km

Results for GPS constellation (figure above) and for GPS and Galileo Constellations (figure below) with τ set at 1000s are represented below:

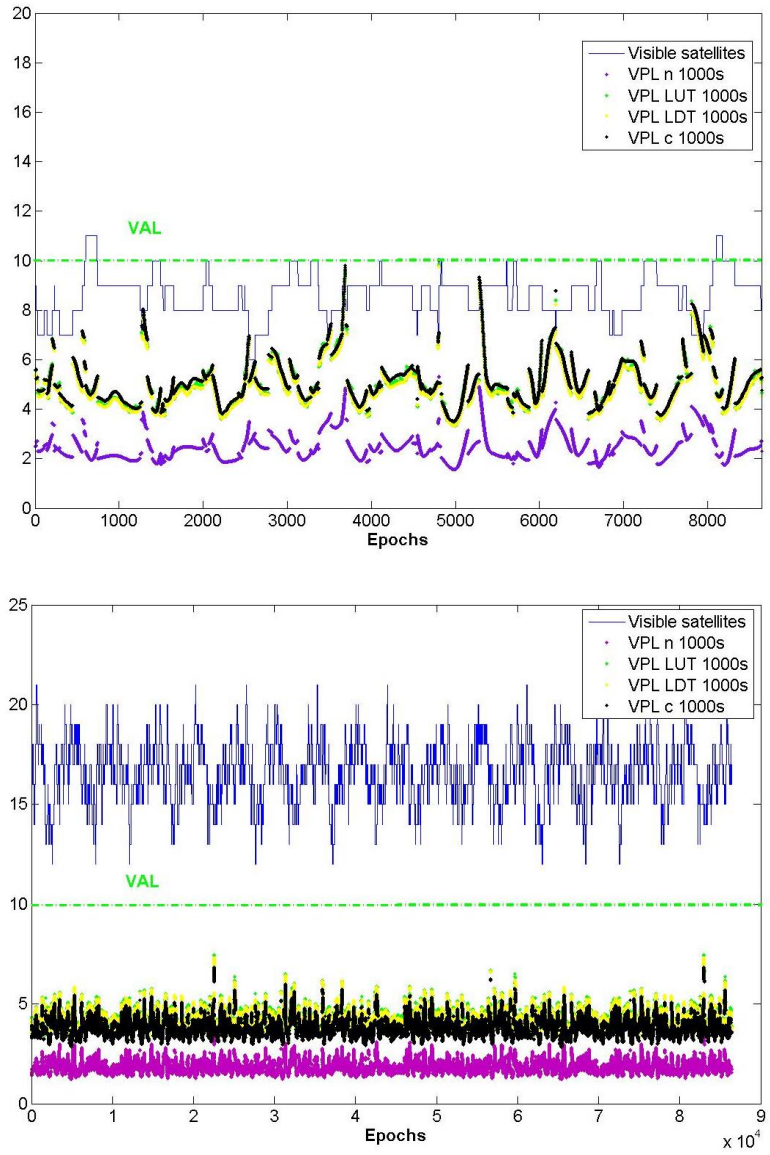

Figure 184-VPLs IF Anchorage 1000s , GPS (left) and GPS and GAL (right), Dth5km

C.4.2 Dth=10km

Results for GPS constellation (figure above) and for GPS and Galileo Constellations (figure below) with τ set at 100s are represented below:

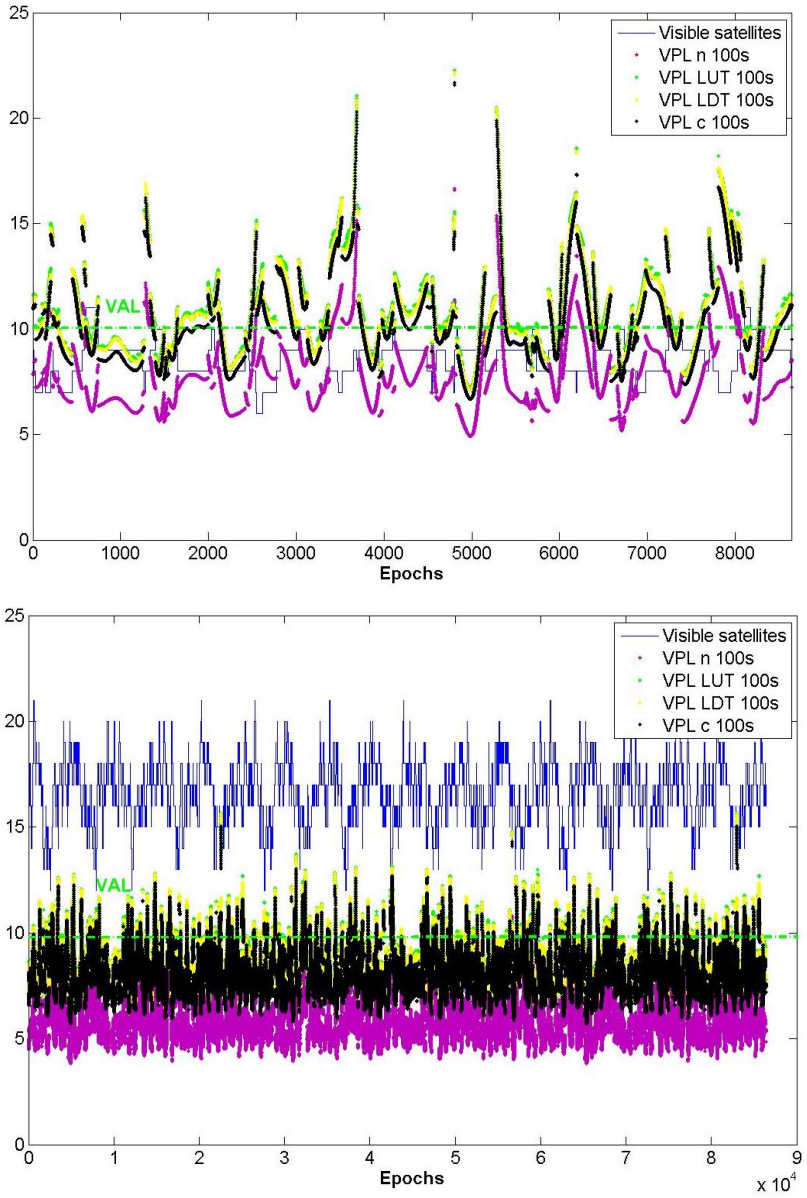

Figure 185-VPLs IF Anchorage 100s , GPS (left) and GPS and GAL (right), Dth10km

Results for GPS constellation (figure above) and for GPS and Galileo Constellations (figure below) with τ set at 300s are represented below:

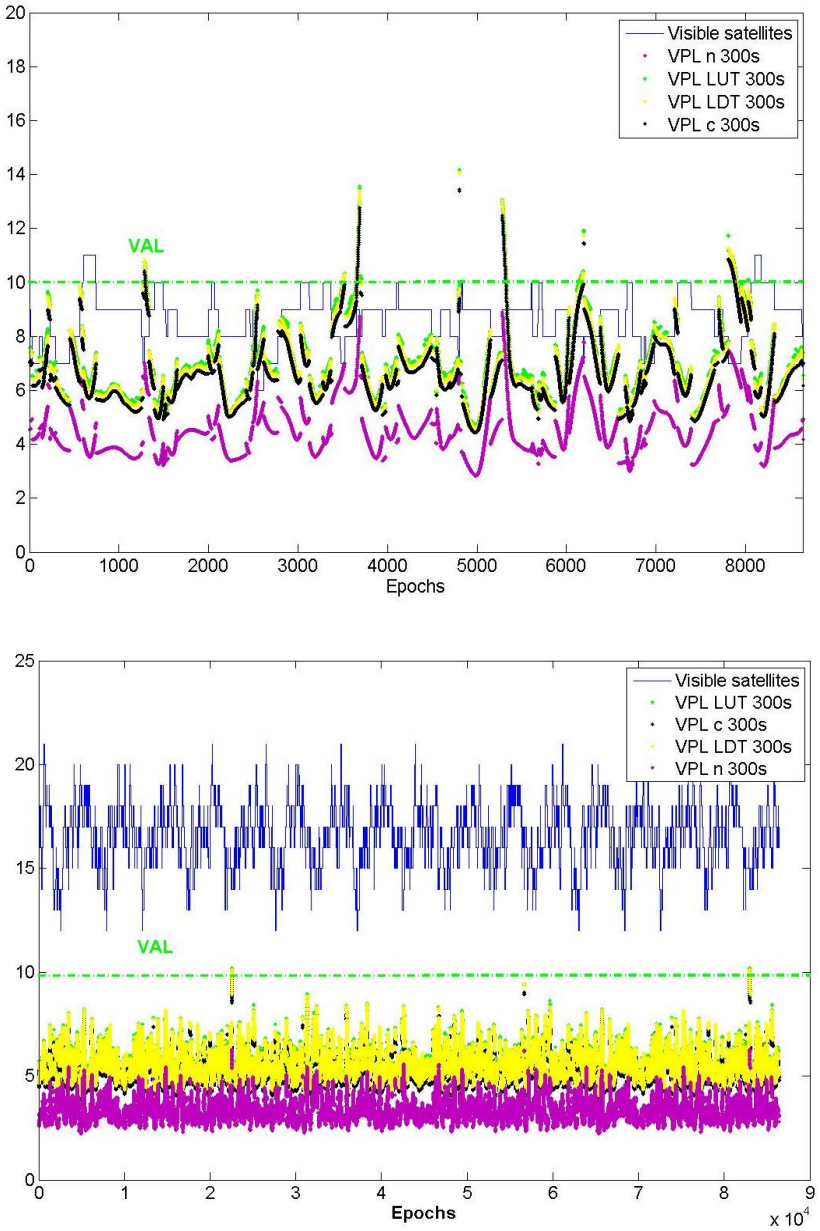

Figure 186-VPLs IF Anchorage 300s , GPS (left) and GPS and GAL (right), Dth10km

Results for GPS constellation (figure above) and for GPS and Galileo Constellations (figure below) with τ set at 1000s are represented below:

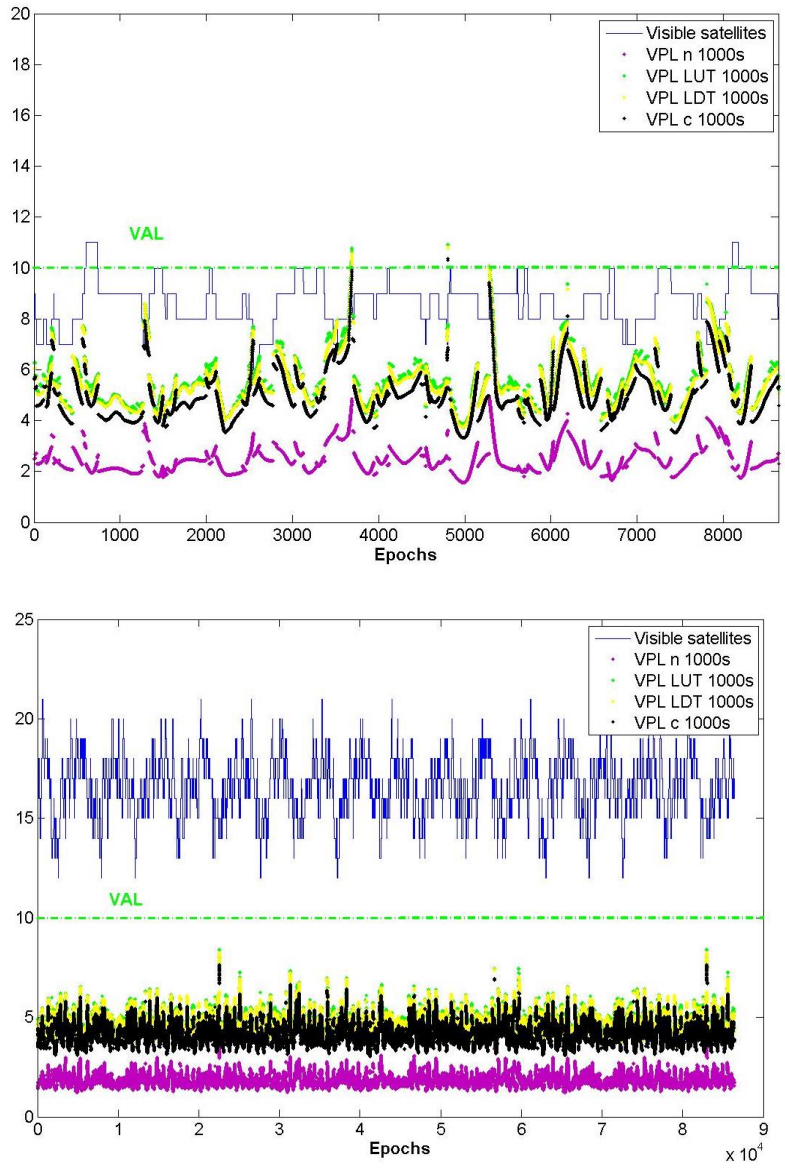

Figure 187-VPLs IF Anchorage 1000s , GPS (left) and GPS and GAL (right), Dth10km

Abstract: In the Civil Aviation domain, research activities aim to improve airspace capacity and efficiency whilst meeting stringent safety targets. These goals are met by improving performance of existing services whilst also expanding the services provided through the development of new Navigation Aids. One such developmental axe is the provision of safer, more reliable approach and landing operations in all weather conditions. The Global Navigation Satellite System (GNSS) has been identified as a key technology in providing navigation services to civil aviation users [1] [2] thanks to its global coverage and accuracy. The GNSS concept includes the provision of an integrity monitoring function by an augmentation system to the core constellations. This is needed to meet the required performances which cannot be met by the stand-alone constellations. One of the three augmentation systems developed within civil aviation is the GBAS (Ground Based Augmentation System) and is currently standardized by the ICAO to provide precision approach navigation services down to Cat I using the GPS or GLONASS constellations [3]. Studies on-going with the objective to extend the GBAS concept to support Cat II/III precision approach operations with GPS L1 C/A, however some difficulties have arisen regarding ionospheric monitoring. With the deployment of Galileo and Beidou alongside the modernization of GPS and GLONASS, it is envisaged that the GNSS future will be multi-constellation (MC) and multi-frequency (MF). European research activities have focused on the use of GPS and Galileo. The MC/MF GBAS concept should lead to many improvements such as a better modelling of **atmospheric effects** but several challenges must be resolved before the potential benefits may be realized. Indeed, this PhD has addressed two key topics relating to GBAS, the **provision of corrections data** within the MC/MF GBAS concept and the **impact of tropospheric biases** on both the SC/SF and MC/MF GBAS concepts. Due to the tight constraints on GBAS ground to air communications link, the VDB unit, a novel approach is needed. One of the proposals discussed in the PhD project for an updated GBAS VDB message structure is to separate message types for corrections with different transmission rates. Then, this PhD argues that atmospheric modelling with regards to the troposphere has been neglected in light of the ionospheric monitoring difficulties and must be revisited for both nominal and anomalous scenarios. The thesis focuses on how to compute the worst case differential tropospheric delay offline in order to characterize the threat model before extending previous work on bounding this threat in order to protect the airborne GBAS user. In the scope of MC/MF GBAS development, an alternative approach was needed. Therefore, in this PhD project, Numerical Weather Models (NWMs) are used to assess fully the worst case horizontal component of the troposphere. An innovative worst case horizontal tropospheric gradient search methodology is used to determine the induced ranging biases impacting aircraft performing Cat II/III precision approaches with GBAS. This provides as an output a worst case bias as a function of elevation for two European regions.The vertical component is also modelled by statistical analysis by comparing the truth data to the GBAS standardized model for vertical tropospheric correction up to the height of the aircraft. A model of the total uncorrected differential bias is generated which must be incorporated within the nominal GBAS protection levels. In order to bound the impact of the troposphere on the positioning error and by maintaining the goal of low data transmission, different solutions have been developed which remain conservative by assuming that ranging biases conspire in the worst possible way. Through these techniques, to protect the user against differential tropospheric ranging biases, it has been shown that a minimum of 3 parameters may be used to characterize a region's model.

Resumé : Dans le domaine de l'Aviation Civile, les motivations de recherches sont souvent guidées par la volonté d'améliorer la capacité de l'espace aérien grâce à la modernisation des moyens de navigation aérienne existants et aux nouvelles infrastructures. Ces buts peuvent être atteints en développant les services qui permettent des opérations d'approche et d'atterrissage plus robustes et plus fiables. La navigation par satellite, grâce au Global Navigation Satellite System (GNSS), a été reconnue comme un moyen performant de fournir des services de navigation aérienne [1] [2]. Le concept du GNSS requiert l'utilisation de moyen d'augmentations pour fournir une fonction de contrôle d'intégrité au vu des exigences [1] relatives aux applications critiques de type aviation civile. Un de ces moyen est le GBAS (Ground Based Augmentation System) et est standardisé par l'OACI pour fournir un service de navigation incluant les approches de précision allant jusqu'à la catégorie I incluse, en utilisant les constellations GPS ou GLONASS [3]. Des études sont en cours pour permettre d'étendre ce service jusqu'à la catégorie II/III avec le GPS L1 C/A, cependant des contraintes sont apparues lors de la surveillance de la ionosphère. Grâce à la modernisation du GPS et GLONASS et aux futures constellations Galileo et Beidou, les futurs GNSS utilisant de multiples constellations et de multiples fréquences (MC/MF) sont étudiés. Les activités de recherches européennes se sont appuyées sur la constellation GPS et sur la future constellation Galileo. Ce MC/MF GBAS devrait permettre de nombreuses améliorations comme un meilleur modèle des **retards atmosphériques**. Cependant, des challenges doivent être résolus avant d'atteindre les bénéfices potentiels. Dans ce travail de thèse, 2 principaux sujets en rapport avec le GBAS ont été traités, la **transmission des données de corrections** avec le MC/MF GBAS et **l'impact des biais troposphériques** avec le SC/SF et MC/MF GBAS. Dû aux contraintes portant sur le format des messages transmis à l'utilisateur via l'unité VDB [4], une nouvelle approche est nécessaire pour permettre l'élaboration du MC/MF GBAS. Une des solutions proposée dans cette thèse est de transmettre les corrections et les données d'intégrité à l'utilisateur dans des messages séparés à des fréquences différentes. De plus, ce travail de thèse remet en question la modélisation de l'atmosphère et particulièrement celle de la troposphère dans des conditions nominales que non-nominales en se concentrant d'abord sur le calcul du pire gradient troposphérique avant de développer les précédents travaux pour borner cette menace dans le but de protéger l'utilisateur. En vue du futur MC/MF GBAS, une nouvelle approche s'est avérée nécessaire. Ainsi, dans ce projet de thèse, des modèles météorologiques numériques (NWMs) sont utilisés pour estimer intégralement la composante horizontale du pire gradient troposphérique. Une méthode innovante pour rechercher les pires gradients troposphériques horizontaux est utilisée pour déterminer les biais qu'ils induisent impactant les avions visant une approche de Cat II/III avec le GBAS. Un modèle de ces pires biais de mesures troposphériques différentiels horizontaux dépendant de l'élévation des satellites pour 2 régions européennes est alors développé. La composante verticale est aussi modélisée grâce à une étude statistique qui compare les données réelles au modèle standard. Un modèle du biais différentiel total non corrigé est développé et doit être introduit dans le calcul des niveaux de protections sous des conditions nominales. Pour borner l'impact de la troposphère sur l'erreur de position tout en se focalisant sur le souhait d'avoir un nombre de données transmises à l'utilisateur faible, différentes solutions conservatives ont été développées où au minimum 3 paramètres, définis selon leur région géographique d'utilisation, doivent être transmis à l'utilisateur.